

# Rare Metal Technology

## 2023

### *Editors*

Takanari Ouchi  
Kerstin Forsberg  
Gisele Azimi  
Shafiq Alam  
Neale R. Neelameggham  
Hojong Kim  
Alafara Abdullahi Baba  
Hong Peng  
Athanasios Karamalidis

TMS

 Springer

# **The Minerals, Metals & Materials Series**

Takanari Ouchi · Kerstin Forsberg · Gisele Azimi ·  
Shafiq Alam · Neale R. Neelameggham ·  
Hojong Kim · Alafara Abdullahi Baba ·  
Hong Peng · Athanasios Karamalidis  
Editors

# Rare Metal Technology 2023

**TMS**

 Springer

*Editors*

Takanari Ouchi  
University of Tokyo  
Tokyo, Japan

Kerstin Forsberg  
KTH Royal Institute of Technology  
Stockholm, Sweden

Gisele Azimi  
University of Toronto  
Toronto, ON, Canada

Shafiq Alam  
University of Saskatchewan  
Saskatoon, SK, Canada

Neale R. Neelameggham  
Ind LLC  
South Jordan, UT, USA

Hojong Kim  
Pennsylvania State University  
University Park, PA, USA

Alafara Abdullahi Baba  
University of Ilorin  
Ilorin, Nigeria

Hong Peng  
University of Queensland  
Brisbane, QLD, Australia

Athanasios Karamalidis  
Pennsylvania State University  
University Park, PA, USA

ISSN 2367-1181

ISSN 2367-1696 (electronic)

The Minerals, Metals & Materials Series

ISBN 978-3-031-22760-8

ISBN 978-3-031-22761-5 (eBook)

<https://doi.org/10.1007/978-3-031-22761-5>

© The Minerals, Metals & Materials Society 2023

This work is subject to copyright. All rights are solely and exclusively licensed by the Publisher, whether the whole or part of the material is concerned, specifically the rights of translation, reprinting, reuse of illustrations, recitation, broadcasting, reproduction on microfilms or in any other physical way, and transmission or information storage and retrieval, electronic adaptation, computer software, or by similar or dissimilar methodology now known or hereafter developed.

The use of general descriptive names, registered names, trademarks, service marks, etc. in this publication does not imply, even in the absence of a specific statement, that such names are exempt from the relevant protective laws and regulations and therefore free for general use.

The publisher, the authors, and the editors are safe to assume that the advice and information in this book are believed to be true and accurate at the date of publication. Neither the publisher nor the authors or the editors give a warranty, expressed or implied, with respect to the material contained herein or for any errors or omissions that may have been made. The publisher remains neutral with regard to jurisdictional claims in published maps and institutional affiliations.

This Springer imprint is published by the registered company Springer Nature Switzerland AG  
The registered company address is: Gewerbestrasse 11, 6330 Cham, Switzerland

# Preface

*Rare Metal Technology 2023* is the proceedings volume of the tenth symposium on Rare Metal Extraction and Processing, TMS Annual Meeting & Exhibition 2023, held at the San Diego Convention Center & Hilton San Diego Bayfront, San Diego, California, USA from March 19 to March 23, 2023. This symposium is sponsored by the Hydrometallurgy and Electrometallurgy Committee and the Recycling and Environmental Technologies Committee of the TMS Extraction and Processing Division.

Rare metals have been attracting increasing attention over the past ten years; consequently, the number of participants in this symposium has been increasing. Recently, the efforts to achieve carbon neutrality have accelerated the development of clean technologies on an international level; therefore, the demand for rare metals has been increasing. However, the grade of rare metals in ores is declining, and the energy consumption and CO<sub>2</sub> emissions in mining and extraction processes are increasing. Therefore, the development of new process technologies has become an urgent requirement.

The Rare Metal Extraction and Processing Symposium has been organized to provide a forum for the discussion of the extraction process of rare metals from primary and secondary materials and residues as well as processing techniques used in rare metal production and mineral processing since 2014. The rare metals generally discussed in this symposium are antimony, bismuth, barium, beryllium, boron, calcium, chromium, gallium, germanium, hafnium, indium, manganese, molybdenum, platinum group metals, rare earth metals, rhenium, scandium, selenium, sodium, strontium, tantalum, tellurium, titanium, and tungsten, which are rare metals that are produced in low-tonnage compared to high-tonnage metals such as iron, aluminum, copper, lead, tin, zinc, and silicon.

The papers in this volume cover process development, process optimization, product characterization, environmental impacts, and plant engineering. Furthermore, the papers discuss various processing techniques for mineral beneficiation, separation, extraction, and purification of rare metals, which are based on biometallurgy, hydrometallurgy, pyrometallurgy, electrometallurgy, and other new extractive metallurgy techniques.

I would like to express my sincere gratitude to the co-organizers (co-editors) for their efforts to organize symposiums and edit the proceedings volume *Rare Metal Technology 2023*: Kerstin Forsberg, Gisele Azimi, Shafiq Alam, Neale R. Neelamegham, Hojong Kim, Alafara Abdullahi Baba, Hong Peng, and Athanasios Karamalidis. In addition, on behalf of the organizers (editors), I would like to acknowledge the TMS staff, Kelly Markel, Matt Baker, and Patricia Warren, for their assistance in assembling and publishing this proceedings book. Finally, I would like to thank all the authors, speakers, and participants of this symposium and hope that we can continue to create a good forum for discussion to advance the field of rare metal extraction and processes in the next year and beyond.

Takanari Ouchi  
Lead Organizer

# Contents

## Part I Processing for Rare Earth

<b>Rare Earth Elements Extraction from an Ionic Clay from South America</b> .....	3
Gisele Azimi, Lingyang Ding, and John Anawati	
<b>Leaching of Neodymium from Recycled NdFeB Magnet Powders Using Citric Acid</b> .....	15
Srujan Rokkam, Quang Truong, Jonas Baltrusaitis, and Manoj Silva	
<b>Separation of Rare Earth Elements from Monazite Via Sulfidation</b> .....	27
Caspar Stinn, Vasu Kaker, Zachary Kenneth Adams, and Antoine Allanore	
<b>Experimental Investigation of Liquid Metal Leaching for Rare Earth Magnet Recycling</b> .....	33
Chinenye Chinwego and Adam Powell	
<b>Recycling of Rare Earth Elements (REEs) from Scrap Nd-Fe-B Magnets</b> .....	39
Nityanand Singh, Pankaj Kumar Choubey, Rekha Panda, Rajesh Kumar Jyothi, and Manis Kumar Jha	

## Part II Processing for Precious Metals and Rare Metals/Electrochemical Processing for Rare Metals

<b>An Innovative Hydrometallurgical Process for Recovery of Critical and Rare Metals from Copper Anode Slimes</b> .....	53
Shijie Wang	

<b>Recovery and Enrichment of Platinum Group Metals from Spent Automotive Catalysts by Pyrometallurgy: A Review</b> .....	61
Jibiao Han, Xianglin Bai, Quan Yang, Biao Wang, Wangrui Ma, Yong Li, Bin Yang, Xilong Wu, and Yu Zhao	
<b>Eutectic Freeze Crystallization for Recovery of Cobalt Sulfate in the Recycling of Li-Ion Batteries</b> .....	73
Yiqian Ma, Amanda Sjögren, Michael Svärd, Xiong Xiao, James Gardner, Richard T. Olsson, and Kerstin Forsberg	
<b>Studies on the Hydrometallurgical Recovery of Metals from Used and End of Life PCBs</b> .....	83
Om Shankar Dinkar, Rekha Panda, Pankaj Kumar Choubey, Manis Kumar Jha, and Balram Ambade	
<b>Extraction of Tungsten, Yttrium, and Uranium from Tantalum–Niobium Ore from Muchinga Province in Zambia</b> .....	95
Mazwi Douglas Musowoya, Yotamu Rainford Stephen Hara, Fredrick Chileshe, Janet Mundundu, and Stephen Parirenyatwa	
<b>Production of High-Purity Mg Metal from Various MgO Resources Through a Novel Electrolytic Process Using a Cu Cathode and Vacuum Distillation</b> .....	105
Hyeong-Jun Jeung, Tae-Hyuk Lee, Youngjae Kim, Jin-Young Lee, Young Min Kim, Toru H. Okabe, Kyung-Woo Yi, and Jungshin Kang	
<b>Recovery of Copper Metal from Discarded Printed Circuit Boards (PCBs) by Hydrometallurgical and Electrometallurgical Processes</b> .....	117
Om Shankar Dinkar, Rukshana Parween, Rekha Panda, Pankaj K. Choubey, Balram Ambade, and Manis Kumar Jha	
<b>Part III New Extractant and Biometallurgical Processing</b>	
<b>New Insights on Titanium(IV) Speciation to Improve the Purification of Concentrated Phosphoric Acid</b> .....	131
Alexandre Chagnes, Lucas Mangold, Hubert Halleux, and Gérard Cote	
<b>Di-Phenols Functionalized Chitosan as Selective Adsorbents for Extraction of Germanium</b> .....	141
Madhav Patel and Athanasios K. Karamalidis	
<b>Recycling of Copper and Gold from Waste Printed Circuit Boards by Leaching Followed by Solvent Extraction</b> .....	153
Kamalesh Kumar Singh and Mudila Dhanunjaya Rao	



<b>Hydrometallurgical Extraction of Molybdenum and Rhenium from Molybdenite Flue Dust</b> .....	161
Sadia Ilyas, Rajiv Ranjan Srivastava, Hyunjung Kim, Humma Akram Cheema, and Ijaz Ahmad Bhatti	
<b>Recovery and Separation of Vanadium and Tungsten from Spent SCR Catalyst by Hydrometallurgical/Hybrid Routes</b> .....	171
Rajesh Kumar Jyothi, Ana Belen Cueva Sola, Jong Hyuk Jeon, and Jin-Young Lee	
<b>Removal of Selenium from Chloride Media Using Bioadsorbent</b> .....	179
Mohamed Abdallah and Shafiq Alam	
<b>Biosorption as a Vital Tool for Metal Recovery in Effluent Treatment: A Review</b> .....	185
Shilpa Kalamani Bawkar, Pramod K. Singh, Pankaj K. Choubey, Rekha Panda, Jhumki Hait, and Manis K. Jha	
<b>Part IV Process Development and Optimization</b>	
<b>Formation of Different Zinc Oxide Crystal Morphologies Using Cellulose as Nucleation Agent in the Waste Valorization and Recycling of Zn-Ion Batteries</b> .....	199
Billy W. Hoogendoorn, Xiong Xiao, Veerababu Poliseti, Fritjof Nilsson, Kåre Tjus, Kerstin Forsberg, and Richard T. Olsson	
<b>Production of Micro-sized Metallic Tungsten Particles from Natural Wolframite and Scheelite via Sulfide Chemistry</b> .....	209
Charles Boury, Sierra R. Green, and Antoine Allanore	
<b>Purification of an Indigenous Barite Mineral for Sustainability of Operation in the Nigerian Oil and Gas Industries</b> .....	221
Alafara A. Baba, Fausat T. Akanji, Rasheed A. Agava, Abdul Ganiyu F. Alabi, Abdullah S. Ibrahim, Kuranga I. Ayinla, Mustapha A. Raji, Seyi E. Adebeye, and Mohammed S. Haruna	
<b>Pyrolysis of Waste Printed Circuit Boards: Optimization Using Response Surface Methodology and Characterization of Solid Product</b> .....	227
Kurniawan Kurniawan, Sookyung Kim, and Jae-chun Lee	
<b>Characterization and Beneficiation of Nigerian Lithium Ore: An Overview</b> .....	239
Furqan Abdulfattah, Markus Daniel Bwala, Oladunni Oyelola Alabi, Musa Gafai Sayyadi, and Suleiman Bolaji Hassan	
<b>Tantalum Recovery Technique for Recycling of Tantalum Coated Composite Materials</b> .....	247
Akanksha Gupta and Brajendra Mishra	

<b>Reduction Volatilization Behavior of Indium Oxide in Indium-Tin Oxide (ITO) Wastes Under CO/CO<sub>2</sub> Atmosphere</b> .....	259
Zijian Su, Yan Wang, Bin Lei, and Yuanbo Zhang	
<b>Part V Poster Session</b>	
<b>Evolution Mechanism of Vanadium-Containing Phases During Sodium Roasting of Vanadium Slag with High Chromium Content</b> .....	271
Jie Cheng, Hong-Yi Li, Dong Hai, Xin-Mian Chen, Jiang Diao, and Bing Xie	
<b>Recovery of Vanadium from Vanadium Slag by Roasting with CaO-MgO Composite Additive</b> .....	279
Mingshuai Luo, Junyi Xiang, Qingyun Huang, Shengquin Zhang, and Zenghao Liu	
<b>The Behaviour of Minor Metals in BOF Slag Under Different Additives</b> .....	287
G. Haslinger, M. Leuchtenmüller, and S. Steinlechner	
<b>Author Index</b> .....	297
<b>Subject Index</b> .....	299

## About the Editors



**Takanari Ouchi** is a lecturer at the Institute of Industrial Science at the University of Tokyo. He received his Doctor of Engineering in Nanoscience and Nanoengineering from Waseda University in 2011. In this tenure, he developed electrochemical deposition processes to fabricate metal nanostructures with both well-controlled crystallinity and uniformity at a single nanometer scale and demonstrated the applicability of these processes to the fabrication of bit-patterned magnetic recording media for future hard disk drives. After completing his doctoral degree, Dr. Ouchi joined the Massachusetts Institute of Technology (MIT), where he developed liquid metal batteries, which is in principle a bi-directional electrolysis (electrorefining) cell, for application in grid scale energy storage. As a research scientist, he led a research group to systematically investigate the electrochemical properties of liquid metal electrodes in molten salt electrolytes and developed novel lithium, calcium, and sodium liquid metal batteries. Since he began working as a research associate at the University of Tokyo in 2017, he has developed new smelting and recycling processes for rare and precious metals using pyrometallurgical and electrometallurgical methods. Since August 2021, he has been appointed as a lecturer in the Department of Materials and Environmental Science, Institute of Industrial Science at the University of Tokyo. Dr. Ouchi has authored 30 peer-reviewed papers, including papers published in *Nature*, *Nature Energy*, and *Nature Communications*, nine conference proceedings, and seven review papers; he has also delivered over 100 talks at conferences. He

has constantly contributed to creating a vibrant field for metal extraction. He is currently serving as the chairperson of the Hydrometallurgy and Electrometallurgy committee and is an organizer of technical symposiums at The Minerals, Metals & Materials Society (TMS).



**Kerstin Forsberg** is Associate Professor in Chemical Engineering at KTH Royal Institute of Technology in Stockholm, Sweden. Her research is focused on separation processes, in particular crystallization. This knowledge is applied in collaborative projects concerning the recovery of resources from waste and to develop new innovative and more environmentally and economically sustainable processes. Forsberg is Head of the Division of Resource Recovery at KTH. She is also Deputy Director for the Research Platform for Industrial Transformation at KTH and director for the strategic partnership with IVL Swedish Environmental Research Institute. As a member of the Hydrometallurgy and Electrometallurgy Committee at The Minerals, Metals & Materials Society (TMS), Dr. Forsberg has contributed as a guest editor for *JOM* and by organizing technical symposia at TMS.



**Gisele Azimi** is a Professor and Canada Research Chair in Urban Mining Innovations. She is jointly appointed by the Departments of Chemical Engineering & Applied Chemistry and Materials Science & Engineering at the University of Toronto. She is also a registered Professional Engineer in Ontario. Her research program is aligned well with the “Sustainability” and “Advanced Materials and Manufacturing” research themes. In her research program, she strives to achieve a sustainable future and mitigate the adverse effects of climate change through: (1) advanced recycling and urban mining of waste electrical and electronic equipment (WEEE), utilizing innovative recycling processes based on supercritical fluids; (2) industrial solid waste reduction through waste valorization to produce strategic materials like rare earth elements; (3) development of innovative materials with unique properties with far-reaching applications in structural and energy materials sectors; and (4) energy storage focusing on the development of a new generation of rechargeable batteries made of aluminum. She received her Ph.D. in 2010 from

the Department of Chemical Engineering and Applied Chemistry at the University of Toronto. Before returning to the University of Toronto as a faculty member in 2014, she completed two postdoctoral appointments at MIT in the Departments of Materials Science and Engineering and Mechanical Engineering. She has received a number of awards including the McCharles Prize for Early Career Research Distinction, TMS EPD Young Leaders Award, Emerging Leaders Award in Chemical Engineering, Dean's Spark Professorship, Early Researcher Award, TMS Light Metals/Extraction and Processing Subject Award—Recycling, and Connaught New Researcher Award.



**Shafiq Alam** is an Associate Professor at the University of Saskatchewan, Canada. He is an expert in the area of mining and mineral processing with profound experience in industrial operations, management, engineering, design, consulting, teaching, research, and professional services. As a productive researcher, Dr. Alam has secured 2 patents and has produced over 175 publications. He is the lead/co-editor of 13 books, and an editorial board member of two mining and mineral processing journals named *Minerals* (an Open Access Journal by MDPI) and *the International Journal of Mining, Materials and Metallurgical Engineering*. He is the winner of the 2015 Technology Award from the Extraction & Processing Division of The Minerals, Metals & Materials Society (TMS), USA.

With extensive relevant industry experience as a registered professional engineer, Dr. Alam has worked on projects with many different mining industries. He is an Executive Committee Member of the Hydrometallurgy Section of the Canadian Institute of Mining, Metallurgy and Petroleum (CIM). During 2015–2017, he served as the Chair of the Hydrometallurgy and Electrometallurgy Committee of the Extraction & Processing Division (EPD) of TMS. Currently, he is the Secretary of the Recycling and Environmental Technologies Committee of TMS and is serving on the TMS-EPD Awards Committee. He is a lead/co-organizer of at least 17 symposia at international conferences through CIM and TMS. Dr. Alam is one of the founding organizers of the Rare Metal Extraction and Processing Symposium at TMS, and since 2014, he has been involved

in organizing this symposium every year with great success. In the past, he was involved in organizing the International Nickel-Cobalt 2013 Symposium and TMS 2017 Honorary Symposium on Applications of Process Engineering Principles in Materials Processing, Energy and Environmental Technologies. Dr. Alam was also a co-organizer of the 9th International Symposium on Lead and Zinc Processing (PbZn 2020), and the 2022 Energy Technologies and CO<sub>2</sub> Management Symposium. In addition to leading the 2023 Energy Technologies and CO<sub>2</sub> Management Symposium, he is involved in co-organizing the 2023 Rare Metal Extraction and Processing Symposium within the TMS 2023 Annual Meeting and Exhibition in San Diego, California. He is also a co-organizer of the PbZn 2023 conference in China and the Pressure Hydrometallurgy 2023 conference in Toronto, Canada.



**Neale R. Neelameggham** IND LLC, is involved in international technology and management licensing for metals and chemicals, thiometallurgy, energy technologies, Agricoal, lithium-ion battery, energy efficient low cost OrangeH<sub>2</sub>, Netzero sooner with Maroon gas and Pink hydrogen, rare earth oxides, etc. He has more than 38 years of expertise in magnesium production and was involved in the process development of its startup company NL Magnesium to the present US Magnesium LLC, UT until 2011, during which he was instrumental in process development from the solar ponds to magnesium metal foundry. His expertise includes competitive magnesium processes worldwide and related trade cases. In 2016, Dr. Neelameggham and Brian Davis authored the ICE-JNME award-winning paper “Twenty-First Century Global Anthropogenic Warming Convective Model.” He is working on Agricoal® to greening arid soils, and at present energy efficient Orange hydrogen, and methane abatement. He authored the ebook *The Return of Manmade CO<sub>2</sub> to Earth: Ecochemistry*. Dr. Neelameggham holds 16 patents and applications and has published several technical papers. He has served in the Magnesium Committee of the TMS Light Metals Division (LMD) since its inception in 2000, chaired in 2005, and since 2007 has been a permanent advisor for the Magnesium Technology Symposium. He has been a member of

the Reactive Metals Committee, Recycling Committee, Titanium Committee, and Program Committee for LMD and LMD council. Dr. Neelameggham was the Inaugural Chair, when in 2008, LMD and the TMS Extraction and Processing Division (EPD) created the Energy Committee and has been a Co-Editor of the Energy Technology Symposium through the present. He received the LMD Distinguished Service Award in 2010. As Chair of the Hydrometallurgy and Electrometallurgy Committee, he initiated the Rare Metal Technology Symposium in 2014 and has been a co-organizer to the present. He organized the 2018 TMS Symposium on Stored Renewable Energy in Coal.



**Hojong Kim** is an Associate Professor of Material Science and Engineering and Nuclear Engineering at Penn State University. He received a B.S. degree from Seoul National University and Ph.D. degree at MIT in the Uhlig Corrosion Laboratory. His current research focuses on electrochemical processes for the recovery and separation of energy-critical materials; large-scale energy storage systems (molten salt batteries); and the development of corrosion-resistant materials in chemically aggressive environments. He is the recipient of the NSF CAREER Award and the New Doctoral New Investigator Award from American Chemical Society. He served as Chair (2017–2019) and Vice-Chair (2015–2017) of the Hydrometallurgy and Electrometallurgy Committee of The Minerals, Metals & Materials Society.



**Alafara Abdullahi Baba** is a Professor of Analytical/Industrial and Materials Chemistry in the Faculty of Physical Sciences, University of Ilorin, Nigeria. He holds a Ph.D. in Chemistry from the University of Ilorin (2008). His dissertation entitled “Recovery of Zinc and Lead from Sphalerite, Galena and Waste Materials by Hydrometallurgical Treatments” was judged the best in the area of Physical Sciences at the University of Ilorin, Nigeria in 2009. His area of research covers analytical, industrial, and materials chemistry in general with special interests in solid minerals and materials processing through hydrometallurgical routes; reactions in solution for metallurgical applications; preparation of phyllosilicates, porous, and bioceramic materials; ore

beneficiation including indigenous barite processing for oil and gas applications with developing eco-friendly-low energy synthetic routes for industrial, technological utilities, among others. Professor Alafara has been cited in many international acclaimed journals of high impact. As an academically inclined scholar with many distinct awards, several of his research breakthroughs of more than 140 publications have been presented at both national and international conferences and workshops for wider recognition. His University of Ilorin 198<sup>th</sup> Inaugural Lecture (2021) titled “Sustainable National Development: Mineral and Material Resources to the Rescue” affirmed the use of locally sourced minerals for industries, a condition for countries to save a significant portion of foreign earnings.

Professor Alafara has occupied various positions as a chairperson, secretary, and member of relevant academic and professional committees. He was Head, Department of Industrial Chemistry of the University of Ilorin between 2017–2020; Deputy Director, Central Research Laboratories (2014–2017); University of Ilorin Senate Representative for Students’ Disciplinary Committee (2019–2021); Secretary, Hydrometallurgy and Electrometallurgy Committee of the Extraction & Processing Division (2018–2021); Co-organizer of the Rare Metal Extraction and Processing Symposium and Lead Organizer, Energy Technologies & Carbon Dioxide Management Symposium (2021); Materials Characterization–Education Committee; EPD and Best Awards Committee Representatives and appointed EPD Council (Education Representative) of The Minerals, Metals & Materials Society (TMS), USA (2021–Date). He is also the current National President of the Materials Science and Technology Society of Nigeria and Fellow of many professional societies including the Chemical Society of Nigeria and Materials Science and Technology Society of Nigeria. He has supervised and is still supervising many undergraduate and postgraduate research works and is currently serving as an External Examiner to postgraduate researchers in universities within and outside Nigeria.





**Hong Peng** is currently the Senior Research Fellow at the School of Chemical Engineering in the University of Queensland (UQ), Australia. He obtained a bachelor's degree in Minerals Engineering and a master's degree in Microbiology at Central South University, China followed by a Ph.D. in Chemical Engineering at UQ. Before joining UQ, Dr. Peng had the experience as a Chemical Engineer in its Newcastle Technology Research Center and Olympic Dam at BHP Billiton. He was the recipient of the 2020 TMS Young Leaders Professional Development Award. Dr. Peng's research focuses on the fundamental aspects of mineral processing, interfacial colloid science, crystal kinetics, and precipitation as well as molecular dynamics simulation. These projects are of interest to the nanobubbles, mine tailings, zeolite, clay minerals, and metal resource recovery.



**Athanasios Karamalidis** is an Assistant Professor of Environmental Systems Engineering of the John and Willie Leone Family Department of Energy and Minerals Engineering of the Earth and Minerals Science College at The Pennsylvania State University. Previously, Dr. Karamalidis was an Associate Research Professor of Environmental Engineering at Carnegie Mellon University and an ORISE Faculty and Post-Doctoral Fellow specialized in geochemistry at the National Energy Technology Laboratory of the US Department of Energy. He is on the managing board and one of the managing members of SCORE consortium, a designated defense manufacturing community, for the acceleration of critical element commercialization in the USA. His current academic and entrepreneurial activities focus on research and development of selective separation technologies for critical materials recovery from large volume industrial wastes, contributing to circular economy concepts.

His work has been published in books, peer-reviewed international journals, conferences, seminars, patents, and other publications. He has served as a member of national committees for research and development, and as a reviewer/panelist for many federal agencies, including NSF, DOD, and DOE. He is member of various professional societies and held the position of Member of the Board of Directors and Secretary

General of the Board of Directors of the Association of Greek Chemists for many years. As a member of the Hydrometallurgy and Electrometallurgy Committee at The Minerals, Metals & Materials Society (TMS), Dr. Karamalidis has contributed as a guest editor for *JOM* and by organizing technical symposia at TMS.

**Part I**  
**Processing for Rare Earth**

# Rare Earth Elements Extraction from an Ionic Clay from South America



Gisele Azimi, Lingyang Ding, and John Anawati

**Abstract** Ionic clays (an important resource for rare earth elements (REEs)) are formed by natural weathering of REE-bearing minerals and adsorption of liberated REEs onto the clay surface. Most ionic clays around the world including those from southern China mainly contain light REEs. Here, a unique ionic clay from south America which is rich in heavy REEs, including dysprosium (Dy), is used as the feed. A desorption process using ammonium sulfate as the lixiviant is developed. The effect of operating parameters including lixiviant concentration, pH, liquid-to-solid ratio, and temperature is investigated, and optimum conditions are determined. The characterization results show that this ionic clay comprises three modes of REEs, including ion exchanged REEs physically adsorbed on the surface, hydrolyzed REEs chemically adsorbed on the surface, and mineralized (non-desorbable) REEs within the clay. Mechanistic investigations show REE desorption/adsorption is controlled by the pH and sulfate ions in the system.

**Keywords** Ionic clay · Rare earth elements · Desorption · Ammonium sulfate

## Introduction

Rare earth elements (REEs) are a group of critical materials that are in increasingly high demand around the world. According to the United States Geological survey, in 2021, the global production of rare earth oxides (REOs) was estimated at 280,000 tons and the four top producers were China (168,000), the USA (43,000), Myanmar (Burma) (26,000), and Australia (22,000) [1]. The global production was increased by 16.6% compared with 2020 (240,000 tons REO) [1]. REEs are widely utilized

---

G. Azimi (✉) · L. Ding · J. Anawati

Laboratory for Strategic Materials, Department of Chemical Engineering and Applied Chemistry, University of Toronto, 200 College Street, Toronto, ON M5S 3E5, Canada

e-mail: [g.azimi@utoronto.ca](mailto:g.azimi@utoronto.ca)

G. Azimi

Department of Materials Science and Engineering, University of Toronto, 184 College Street, Toronto, ON M5S 3E4, Canada

in various industrial applications, including clean energy, defense, aerospace, automotive, and electronics. Manufacturing permanent magnets is the single largest and most important end use for REEs, accounting for 29% of the forecasted demand in 2020 [2]. Permanent magnets are a critical component of modern electronics used in cell phones, televisions, computers, automobiles, wind turbines, jet aircraft, and many other products. Because of their unique magnetic, catalytic, and spectroscopic properties, REEs are used in many other applications such as catalysts (20%), polishing (14%), metallurgy (9%), batteries (8%), glass (8%), ceramics (3%), phosphors (0.6%), and pigments (0.4%) [2].

Among all REEs, the demand for some like dysprosium and terbium (that are categorized under heavy rare earth elements) could become extremely challenging considering the sharp increasing demand for electric vehicles. It is predicted that dysprosium demand will rise by 2600% compared with 700% of neodymium within the next two decades. Currently, China is the sole supplier for dysprosium and terbium. Therefore, it is highly desirable to find alternative producers for these elements around the world.

Conventional REE ores contain REEs as either carbonate ((REE)(CO<sub>3</sub>)F) or phosphate ((REE)PO<sub>4</sub>) minerals. These ores require processing with concentrated acids (H<sub>2</sub>SO<sub>4</sub>, HCl) or bases (NaOH) at elevated temperatures, for example acid baking–water leaching process [3]. An alternative to conventional REE ores is a resource traditionally found in southern China, called ionic clay. Ionic clays are formed by natural weathering of REE-containing parent rocks, which results in the mobilization of REE ions, and their adsorption on the clay surface.

There are two potential mechanisms for REE adsorption on the clay surface: physisorption through cation-exchange mechanism and chemisorption through surface complexation. The former is pH- and temperature-independent in which the REE<sup>3+</sup> ions electrostatically adsorb on negative binding sites on the clay surface. These negative binding sites are produced by charge imbalances caused by the isomorphous substitutions of aluminum (Al<sup>3+</sup>) and silicon (Si<sup>4+</sup>) sites in the crystal structure of the clay which is made of aluminosilicates (Al<sub>2</sub>Si<sub>2</sub>O<sub>5</sub>(OH)<sub>4</sub>). On the other hand, the surface-complexation adsorption mechanism is pH-dependent in which the REE<sup>3+</sup> ions complex with the clay surface through a hydrolysis reaction with amphoteric hydroxyl groups ([ionic clay]–OH) at the edges of clay platelets [4]. Among the two mechanisms, the cation-exchange mechanism is the dominant mode of REE adsorption on ionic clays. The physisorbed REEs through this mechanism can be desorbed by cation exchange with lixivinat of monovalent or higher valent salts (ammonium [NH<sub>4</sub><sup>+</sup>], sodium [Na<sup>+</sup>], lithium [Li<sup>+</sup>], cesium [Cs<sup>+</sup>], and magnesium [Mg<sup>2+</sup>]). The chemisorbed REEs can be desorbed by H<sub>3</sub>O<sup>+</sup> from acid; hence, they require mild acidic conditions of pH 3–4. After desorption, REEs can be separated from the solution and purified using selective precipitation, solvent extraction, or ion exchange.

In this study, an ionic clay from South America is acquired. The clay is characterized to obtain the mineralogy and composition. A progressive acidification process is used to determine the ratio of different REE occurrence modes (physically adsorbed, chemically adsorbed, and mineralized). A desorption process using

ammonium sulfate as the lixiviant is developed. The effect of operating parameters including lixiviant concentration, pH, liquid-to-solid (L/S) ratio, and temperature is investigated, and optimum conditions are determined.

## **Materials and Methods**

### ***Reagents***

The ionic clay sample was obtained from a deposit in South America. The clay was mixed, dried, and crushed to < 2 mm. Sulfuric acid ( $\text{H}_2\text{SO}_4$ , 95.0–98.0 wt%, VWR) and ammonium sulfate ( $(\text{NH}_4)_2\text{SO}_4$  > 99.0 wt%, VWR) were used for experiments. Deionized water (0.055  $\mu\text{S}$ , millipore) was used for solution preparation. Certified multi-element standard stock solutions (inorganic ventures) were used for calibration of inductively coupled plasma–mass spectroscopy and–optical emission spectroscopy (ICP–MS/OES).

### ***Compositional and Mineralogy Characterization***

For determining the composition of the ionic clay, it was digested with lithium metaborate/tetraborate fusion ( $\text{Li}_2\text{B}_4\text{O}_7$ : $\text{LiBO}_2$ : $\text{LiBr}$  flux, 23  $\text{g}_{\text{flux}}/\text{g}_{\text{sample}}$ , 1050 °C, 9 min, Claisse LeNeo fluxer) followed by dissolution in nitric acid (5.6 wt%  $\text{HNO}_3$ , 42  $\text{mL}/\text{g}_{\text{sample+flux}}$ , 25 °C). The digests were diluted to 100 mL with deionized water and filtered with 0.45  $\mu\text{m}$  nylon syringe filters. The concentration of bulk metals (sodium, magnesium, aluminum, potassium, calcium, manganese, iron) and REEs in the digests were measured using inductively coupled plasma optical emission spectrometry (ICP-OES, PerkinElmer Optima 8000) and inductively coupled plasma mass spectrometry (ICP-MS, Thermo Scientific iCAP Q). For mineralogical characterization, the samples were characterized with X-ray diffraction (XRD— $2\theta$ : 5–70°, scan rate: 1.25°/min, Rigaku MiniFlex 600 Diffractometer).

### ***Desorption Procedure***

A sample of 5 g of the clay was analyzed with a moisture analyzer (Torbal, AST120) to determine its humidity. Then, 50 g of the clay was mixed with water and  $(\text{NH}_4)_2\text{SO}_4$  at a controlled pH (in the range of 1–3, maintained within  $\pm 0.1$  of the setpoint by periodic additions of 20%  $\text{H}_2\text{SO}_4$  solution). To determine the liquid-to-solid (L/S) ratio, the initial humidity of the clay was considered, and the amount of liquid was calculated based on the mass of the dry clay. Based on kinetic investigation performed

outside of this study, 20 min residence time was selected for all the experiments. Agitation rate was set at 200 rpm. After completion of the experiment, the slurry was vacuum filtered with Whatman grade 3 filter paper. The wet filter cake was sampled (5 g) for humidity measurement. The remaining wet filter cake was subjected to an identical desorption step (D2) with fresh  $(\text{NH}_4)_2\text{SO}_4$  and water. The water amount added was adjusted based on the retained water in the wet filter. Following D2 desorption, without removing the filter cake from the vacuum funnel, the cake was sampled for humidity measurement, and the remaining cake was washed with 200 mL of deionized water (W). The filtrate after desorption 1 (L1), desorption 2 (L2), and washing (LW) were sampled with a syringe and filtered using a syringe filter and diluted with 5 wt%  $\text{HNO}_3$  for stabilization. The concentration of REEs was measured with ICP-MS and that of impurities was measured with ICP-OES.

The elemental fractional (%) desorption (extraction) at each process step and the overall desorption (D1 + D2 + W) were calculated using the mass and humidity of feed solid, elemental composition of the feed, measured recovered volume and concentrations of the filtrates, and calculated extractions of the previous steps of the process. Desorption for each step was defined as the ratio of the mass of REE recovered in the filtrate to the mass of REE introduced into the system by the solids. The RE mass in the filtrate was determined by ICP-MS ( $C_{\text{ICP-MS}}$ ) and the recovered volume of liquor (V). The mass of the solids was determined from the mass of wet solids, the REE composition in the dry feed clay, the humidity of the wet solids, and the fractional desorption of the previous step. The desorptions in D1, D2, and W steps was combined to calculate the cumulative desorption of each step (Eqs. (1–3)). The cumulative desorption of step W corresponds to the total desorption of the process, and the absolute desorption ( $\text{mg}_{\text{RE}}/\text{kg}_{\text{dry IC}}$ ) can be determined using Eq. (4).

$$\%_{\text{extraction cumulative, D1}} = \%_{\text{extraction, D1}} \quad (1)$$

$$\%_{\text{extraction cumulative, D2}} = \%_{\text{extraction, D1}} + 100\% \times \left(1 - \frac{\%_{\text{extraction, D1}}}{100}\right) \left(\frac{\%_{\text{extraction, D2}}}{100}\right) \quad (2)$$

$$\begin{aligned} \%_{\text{extraction cumulative, W}} &= \%_{\text{extraction, D1}} + 100\% \times \left(1 - \frac{\%_{\text{extraction, D1}}}{100}\right) \left(\frac{\%_{\text{extraction, D2}}}{100}\right) \\ &+ 100\% \times \left(1 - \frac{\%_{\text{extraction, D1}}}{100}\right) \left(1 - \frac{\%_{\text{extraction, D2}}}{100}\right) \left(\frac{\%_{\text{extraction, W}}}{100}\right) \end{aligned} \quad (3)$$

$$\left[ \text{Desorption}_{\text{RE}, n} \frac{\text{mg}_{\text{RE}}}{\text{kg}_{\text{dry IC}}} \right] = \frac{\%_{\text{extraction cumulative, } n}}{100\%} \times \left[ \text{RE}_{\text{composition in dry ore}} \frac{\text{mg}}{\text{kg}} \right] \quad (4)$$

where  $\%_{\text{extraction}}$  is fractional extraction (desorption),  $C_{\text{RE}}$  is REE concentration, and  $\text{Desorption}_{\text{RE}, n}$  is absolute desorption for step  $n$  ( $n = \text{D1, D2, W}$ ).

## Results and Discussion

### *Characterization Results*

The ionic clay sample was characterized to determine its chemical composition and mineralogy. Table 1 presents the average elemental composition of the clay, and Fig. 1 presents the XRD diffractogram.

The REE elemental composition of this South American ionic clay is unique since it has high light REE content including lanthanum, cerium, and neodymium as well as yttrium. Cerium does not typically adsorb on the clay; thus, its high concentration suggests that this clay contains some non-adsorbable REEs locked within minerals such as monazite in the clay crystal structure. Another unique characteristic of this clay is that it is rich in heavy REEs such as dysprosium. The XRD results showed that the crystal structure of the clay consists of clay mineral halloysite ( $\text{Al}_2\text{Si}_2\text{O}_3(\text{OH})_8$ ), the serpentine mineral cronstedtite ( $\text{Fe}_3(\text{FeSi})\text{O}_4(\text{OH})_5$ ), and quartz ( $\text{SiO}_2$ ).

### *Desorption Results*

In this study, the effect of pH, ammonium sulfate concentration, temperature, and L/S was investigated. The baseline conditions were selected as pH 3, 0.15 M ammonium sulfate, 25 °C, and L/S of 3/1 mL/g. To investigate the effect of temperature, desorption experiments were performed at 45 °C and other conditions were kept at the baseline conditions. To investigate the effect of L/S, desorption experiments were performed at L/S of 4/1 and other conditions were kept at the baseline conditions. To investigate the effect of ammonium sulfate concentration, desorption experiments were performed at 0, 0.15, 0.25, and 0.5 M, while other conditions were kept at the baseline conditions. To investigate the effect of pH, desorption experiments were performed at pH 0, 1, 2, and 3, while other conditions were kept at the baseline conditions. The fractional desorption of total REEs in D1, D2, and W steps and total extraction efficiency for all the experiments are presented in Table 2. The corresponding values for thorium (Th) and uranium (U) are also presented.

As shown in Table 1, decreasing pH from 3 to 0 increases the total REE extraction efficiency because at lower pH, more chemisorbed REEs can be desorbed from the surface of the clay. However, decreasing pH results in higher thorium extraction because lower pH could break the crystal structure of the clay and liberates thorium from the minerals.

It can be observed that REE extraction efficiency is very low when no ammonium sulfate was in the solution since ammonium ions are required to desorb  $\text{REE}^{3+}$  ions from the clay surface. However, increasing ammonium sulfate beyond 0.15 M did not show a positive effect on the REE extraction efficiency which means 0.15 M is higher than the minimum required ammonium sulfate to extract all desorbable REEs from the clay.



**Table 1** Elemental composition of the South American ionic clay. The composition was determined by ICP-MS (REEs, U, Th) and ICP-OES (bulk metals) after alkali fusion digestion

Rare earth elements (mg/kg)																
Sc	Y	La	Ce	Pr	Nd	Sm	Eu	Gd	Tb	Dy	Ho	Er	Tm	Yb	Lu	TREE
67.4	495.3	461.8	941.0	114.0	442.9	73.7	3.5	74.0	13.4	94.1	20.6	60.3	8.9	56.4	8.1	2868
Bulk elements (wt%)																
Fe	Mg	Mn	Ca	K	Al	U	Th									
11.04	0.29	0.21	0.05	0.92	8.86	3.3	198.8									

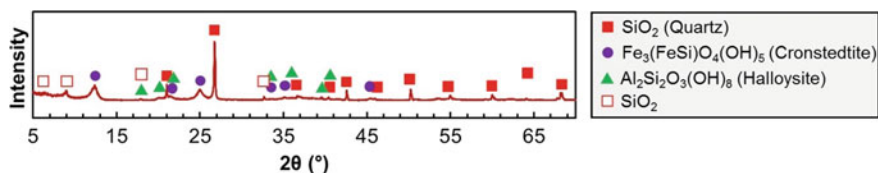


Fig. 1 XRD diffractogram of the ionic clay sample

Increasing temperature to 45 °C had a positive effect on the REEs extraction efficiency. However, running the process at temperatures higher than room temperature requires energy and increases the capital and operating costs of the process. Thus, it needs to be considered during the design process to identify the revenue gain if the process is performed at higher temperatures.

Increasing L/S ratio to 4/1 mL/g had a positive effect on the REE extraction efficiency. However, running the process at a higher L/S ratio would require larger equipment and higher reagent consumption which would also result in higher capital and operating costs. Hence, it needs to be considered during the design process to identify the revenue gain if the process is performed at higher L/S ratio.

### ***Progressive Acidification Experiment for Determination of REE Occurrence Modes***

As previously mentioned, the REEs in this ionic clay occur in three different modes, i.e., (i) electrostatically adsorbed onto permanent negative sites on the clay surface; (ii) chemically bonded (hydrolyzed) onto free hydroxyl (R-OH) sites on the clay surface; and (iii) mineralized within REE-containing minerals such as monazite.

In this study, we conducted an experiment to determine the percentage of each REE occurrence mode within the ionic clay. Two types of tests were performed, one in the presence of 0.15 M  $(\text{NH}_4)_2\text{SO}_4$  and one without  $(\text{NH}_4)_2\text{SO}_4$ . The slurry containing the clay and lixiviant in both tests was subjected to  $\text{H}_2\text{SO}_4$  addition, and the pH of the slurry was decreased from the neutral pH of clay plus lixiviant to zero. By comparing the desorption efficiencies at the two conditions, contributions from the different REE occurrence modes were calculated. Figure 2 presents the desorption efficiency of dysprosium as a representative heavy REE. In this figure, for experiment with 0.15 M  $(\text{NH}_4)_2\text{SO}_4$ , the pH 5.0 point corresponds to the clay slurry with no added acid or  $(\text{NH}_4)_2\text{SO}_4$  and the pH 4.5 point is the solution after 0.15 M  $(\text{NH}_4)_2\text{SO}_4$  addition.

The pH independent ion-exchange desorption mechanism that corresponds to physically adsorbed REEs is observed in the pH range of 5.0–4.5 where an immediate increase in desorption efficiency was observed upon addition of  $(\text{NH}_4)_2\text{SO}_4$

**Table 2** Fractional desorption results for D1, D2, and W step and total % extraction for total REEs, thorium, and uranium under various experimental conditions. The effect of temperature, L/S ratio, ammonium sulfate concentration, and pH is investigated

Sample	REE TOT extraction				Th extraction				U extraction							
	(mg/kg dry solids)		(%)		(mg/kg dry solids)		(%)		(mg/kg dry solids)		(%)					
	D1	D2	W	Total	TOT%	D1	D2	W	Total	TOT%	D1	D2	W	Total	TOT%	
<i>Effect of L/S and temperature (pH 3, 0.15 M (NH<sub>4</sub>)<sub>2</sub>SO<sub>4</sub>)</i>																
L/S = 3, T = 25 C (baseline)	433.73	62.42	6.51	502.66	17.53	0.04	0.03	0.00	0.08	0.04	0.01	0.01	0.00	0.01	0.00	0.44
L/S = 4, T = 25 C	530.65	58.13	5.50	594.28	20.72	0.06	0.05	0.00	0.11	0.05	0.01	0.01	0.00	0.01	0.00	0.45
L/S = 3, T = 45 C	511.13	78.82	8.91	598.86	20.88	0.09	0.08	0.01	0.17	0.09	0.02	0.02	0.00	0.00	0.04	1.14
<i>Effect of (NH<sub>4</sub>)<sub>2</sub>SO<sub>4</sub> concentration (25 °C, L/S = 3/1, pH 3)</i>																
0.0 M (NH <sub>4</sub> ) <sub>2</sub> SO <sub>4</sub>	4.67	2.52	2.07	9.26	0.32	0.01	0.00	0.00	0.01	0.00	0.00	0.00	0.00	0.00	0.00	0.00
0.15 M (NH <sub>4</sub> ) <sub>2</sub> SO <sub>4</sub> (baseline)	433.73	62.42	6.51	502.66	17.53	0.04	0.03	0.00	0.08	0.04	0.01	0.01	0.00	0.01	0.00	0.44
0.25 M (NH <sub>4</sub> ) <sub>2</sub> SO <sub>4</sub>	450.17	57.65	6.73	514.55	17.94	0.12	0.06	0.01	0.18	0.09	0.01	0.01	0.00	0.00	0.02	0.52
0.50 M (NH <sub>4</sub> ) <sub>2</sub> SO <sub>4</sub>	433.76	68.65	8.90	511.30	17.83	0.18	0.15	0.02	0.35	0.18	0.01	0.01	0.00	0.00	0.03	0.80
<i>Effect of pH (25 °C, L/S = 3/1, 0.15 M (NH<sub>4</sub>)<sub>2</sub>SO<sub>4</sub>)</i>																
pH = 0	616.23	99.17	14.44	729.84	25.45	8.17	5.35	0.99	14.51	7.30	0.13	0.06	0.01	0.20	5.99	
pH = 1	496.35	92.74	12.77	601.86	20.99	2.16	1.78	0.34	4.28	2.15	0.06	0.03	0.01	0.10	2.90	
pH = 2	512.95	58.30	5.30	576.55	20.10	1.04	0.43	0.04	1.52	0.76	0.03	0.01	0.00	0.05	1.51	
pH = 3 (baseline)	433.73	62.41	6.51	502.65	17.52	0.04	0.03	0.00	0.07	0.04	0.01	0.01	0.00	0.02	0.43	

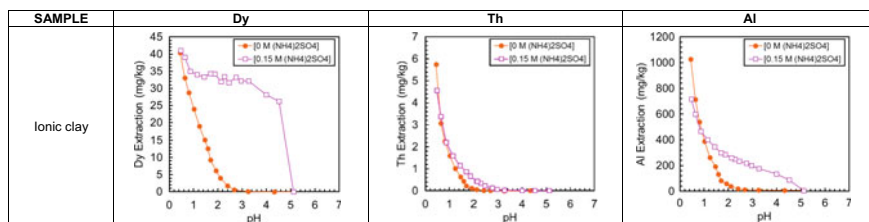


**Fig. 2** Progressive acidification plots for dysprosium, thorium, and aluminum. Dysprosium is a representative REE. Thorium is a marker for the dissolution of  $(\text{REE,Th})\text{PO}_4$  minerals, and Al represents the co-extraction of adsorbed Al and the dissolution of the clay minerals

which was not observed in the experiment with no  $(\text{NH}_4)_2\text{SO}_4$  addition. Furthermore, in addition to the REEs, very small amount of Aluminium was also electrostatically adsorbed, desorbing with  $(\text{NH}_4)_2\text{SO}_4$  addition. The dissolution of monazite  $((\text{REE,Th})\text{PO}_4)$  minerals occurred below pH 3, as shown by thorium extraction, which is not expected to adsorb on the clay surface. In the pH range of 3 to 5, the extraction of dysprosium was enhanced with decreasing pH, but only in the experiment with  $(\text{NH}_4)_2\text{SO}_4$ , which suggests that the extraction cannot be attributed to simple  $\text{H}_3\text{O}^+$  exchange. This behavior can be explained by the chemisorption mechanism and complexation with the  $\text{SO}_4^{2-}$  counter ions. The hydrolyzed  $\text{REE}^{3+}$  ions are cleaved by  $\text{H}_3\text{O}^+$ , but only when sufficient  $\text{SO}_4^{2-}$  ions are present in solution to stabilize them, forming  $\text{RE}(\text{SO}_4)^+$  and  $\text{RE}(\text{SO}_4)_2^-$  complexes, with the sulfate ion behaving as a monodentate ligand [5]. Moreover, the degradation of the clay minerals (halloysite:  $\text{Al}_2\text{Si}_2\text{O}_5(\text{OH})_4$  and cronstedtite:  $\text{Fe}_3(\text{Si}_{1.4}\text{Fe}_{0.6})\text{O}_5(\text{OH})_4$ ) to which  $\text{REE}^{3+}$  ions are adsorbed, was observed at lower pH, which resulted in co-extraction of aluminum.

The results presented in Fig. 2 show the importance of controlling pH during the desorption of this ionic clay. Decreasing pH results in higher extraction of REEs; however, pH must be kept above 3 if co-extraction of thorium must be avoided. The contributions of the three REE occurrence modes were quantified. The initial concentration of REEs in the starting solution (water + ionic clay) corresponds to the amount of water soluble REEs in the clay, which is almost zero. The proportion of physically adsorbed REEs was determined as the area between the starting solution (pH 5) and the solution with added ammonium sulfate but no pH adjustment (pH 4.5), as given in Eq. (5). The chemically adsorbed fraction was determined as the area between the solution with only ammonium sulfate (pH 4.5) and the point at which mineral dissolution started (pH 3.07) (Eq. (6)). The desorbable fraction is the sum of the physically and chemically adsorbed fractions (Eq. (7)). The mineralized fraction was determined as the area between the onset of mineral dissolution (pH 3.07) and the total REE content of the clay (Eq. (8)). It should be noted that although dissolution of the mineral phases begins at  $\text{pH} < 3$ , this dissolution accounts for a small amount of the total REEs in the clay, which require highly acidic conditions at elevated temperature to fully dissolve (for example acid baking–water leaching). The values of the three REE occurrence modes are presented in Table 3.

**Table 3** Calculated REE occurrence modes in the ionic clay for dysprosium

Sample	Dy: Total mg/kg	Dy: Physically adsorbed (%)	Dy: Chemically adsorbed (%)	Dy: Desorbable (%)	Dy: Mineralized (%)
Ionic clay	94.1	32.85	7.52	40.37	59.63

$$\text{Physically Adsorbed (\%)} = \frac{(x_{(\text{NH}_4)_2\text{SO}_4} - x_{\text{NatpH}})}{x_{\text{Max}}} \times 100\% \quad (5)$$

$$\text{Chemically Adsorbed (\%)} = \frac{(x_{\text{pH3}} - x_{(\text{NH}_4)_2\text{SO}_4})}{x_{\text{Max}}} \times 100\% \quad (6)$$

$$\text{Desorbable (\%)} = \text{Physically Adsorbed (\%)} + \text{Chemically Adsorbed (\%)} \quad (7)$$

$$\text{Mineralized (\%)} = \frac{(x_{\text{Max}} - x_{\text{pH3}})}{x_{\text{Max}}} \times 100\% \quad (8)$$

where  $x$  is extraction in mg/kg and  $x_{\text{Max}}$  is the total REE content in the clay. The mineralized (%) is based on the total amount of REEs that can be digested by alkali fusion (Table 1), and this fraction extends beyond the value presented in pH range of 0–3 in Fig. 2.

## Conclusions

A desorption process is developed to extract REEs from a South American ionic clay. Ammonium sulfate was used as the lixiviant under controlled pH using sulfuric acid. The effect of operating parameters including pH, ammonium sulfate concentration, temperature, and L/S ratio on total REE extraction was investigated. It was found that ammonium sulfate is necessary for the extraction, but beyond 0.15 M, the REE extraction remains constant which indicates 0.15 M is higher than the minimum required to extract all desorbable REEs. Decreasing pH was found to increase REE extraction; however, decreasing pH below 3 resulted in the co-extraction of thorium. In this project, the objective is to have zero radioactivity; therefore, it is decided to perform the experiments above pH 3. Increasing temperature and L/S ratio both had a positive effect on REE extraction, but they both increase the operating and capital costs, and the potential revenue gain must be considered during the design step to identify if the higher values are preferred.

**Author Contributions** G. A. conceived and supervised the research and wrote the manuscript. J. A. and L. D. designed and performed the experiments and analyzed the results.

## References

1. Cordier DJ (2022) U.S. geological survey, mineral commodity summaries—rare earths
2. Natural Canada Resources (2022) Rare earth elements facts
3. Moldoveanu GA, Papangelakis VG (2012) Recovery of rare earth elements adsorbed on clay minerals: I. Desorption mechanism. *Hydrometallurgy* 117–118:71–78
4. John Anawati GA (2022) Rare earth elements extraction from a South American ionic clay. *J Rare Earths* In Press
5. Vercouter T, Amekraz B, Moulin C, Giffaut E, Vitorge P (2005) Sulfate complexation of trivalent lanthanides probed by nanoelectrospray mass spectrometry and time-resolved laser-induced luminescence. *Inorg Chem* 44:7570–7581

# Leaching of Neodymium from Recycled NdFeB Magnet Powders Using Citric Acid



Srujan Rokkam, Quang Truong, Jonas Baltrusaitis, and Manoj Silva

**Abstract** Rare Earth Elements have grown in importance over the years because of their applications in electronics, rechargeable batteries, renewables, and the defense industry. The recycling of neodymium and dysprosium contained in NdFeB magnets from the End-of-Life electronics will improve the total supply of neodymium and dysprosium in the future. However, due to the use of expensive and hazardous acids (hydrochloric or sulfuric), no mature and economically feasible technologies have been identified for recycling NdFeB magnet powders. The extraction process utilizes a two-stage process. The NdFeB powders go through wet ball mill grinding to pretreat with sodium hydroxide (NaOH) solution to form rare earth hydroxides. The rare earth hydroxides then go through leaching in mild acids. The leaching efficiencies of HCl and citric acid were investigated. As a result, a leaching efficiency of 69% for Nd and 100% for Dy was achieved after 60 min of milling with 3.5 mL of 4.0 M NaOH and 60 min of leaching with 100 mL of 0.5 M citric acid into the solution phase. Subsequently, 100% of iron (Fe) content can be removed out of the solution. Finally, neodymium and dysprosium can be separated using multi-stage acid stripping. This work resulted from an SBIR Phase I program funded by The U.S. Defense Logistics Agency, Contract SP4701-19-P-0048, awarded to Advanced Cooling Technologies, Inc. (ACT).

**Keywords** Rare earth elements · Recover REEs · NdFeB · Permanent magnet · Industrial electronic waste · Leaching

## Introduction

Rare earth elements (REEs) have grown in importance over the years. Neodymium (Nd) and dysprosium (Dy) have become two of the most critical materials in the

---

S. Rokkam (✉) · Q. Truong  
Advanced Cooling Technologies, Inc., Lancaster, PA 17601, USA  
e-mail: [Srujan.rokkam@1-act.com](mailto:Srujan.rokkam@1-act.com)

J. Baltrusaitis · M. Silva  
Lehigh University, Bethlehem, PA 18015, USA

Rare Earth Element group because of their applications in electronics (smart phone, high-definition display), rechargeable batteries, permanent magnets, and defense applications. Over the next 25 years, Nd and Dy demands are projected to rise by 700% and 2600%, respectively [1]. Due to the absence of primary deposits and economical means of producing REEs, some of the countries are looking at recycling of REEs from industrial residues, end-of-life electronics and magnet scraps [2]. The recycling of REEs, namely Nd and Dy contained in NdFeB magnets from the End-of-Life electronics, will improve the total supply of REEs in the future and promote a circular economy of REEs by minimizing waste that is environmentally hazardous.

The state-of-the-art methods for recovery of neodymium (Nd) and other associated REEs (Pr, Dy, Tb) through different types of metallurgical processes can be categorized as: hydrometallurgical, pyro-metallurgical, or their combination [3]. Pyro-metallurgical method is a high-temperature extraction technique where the magnet scrap is treated with either a molten metal, a molten salt, or a molten oxide slag. During the process, the Nd in the magnet is dissolved, while iron and boron stay unreacted as a new molten ferrous alloy. However, most of the pyro-metallurgical methods are applicable to only highly concentrated magnet scrap. These methods involve the use of high temperatures to melt the alloys, thus making the process too energy-intensive to be environmentally sustainable. For low-concentration magnet scrap, subsequent hydrometallurgical process steps are needed [4]. For hydrometallurgical route, extraction methods for recovery REEs via leaching of NdFeB magnets, from relatively clean production scrap to complex and highly contaminated scrap, have been developed [5, 6]. In general, the magnet powders are leached in low pH acid, including hydrochloric (HCl), or sulfuric ( $H_2SO_4$ ). Such acid leaching technique provides the flexibility of magnet scrap dissolution. However, selective leaching of REEs is challenging due to large amount of Fe and other contaminants in the magnet scrap. Therefore, a high-temperature treatment is often needed to increase selectivity of REEs [7]. Hence, most of the available approaches for REE recovery have disadvantage of using strong acids and high temperature that makes the overall recovery process not economically feasible. Some recent studies on recovery of REEs and valuable elements have suggested the use of mechanochemical-assisted techniques [8, 9], ultrasound or microwave-assisted leaching [10], and solid-state chlorination [11]. Further, researchers from NETL recently reported a great improvement in REEs extraction efficiency from coal fly ash, if the feedstock was pretreated with NaOH [12].

In order to liberate REEs using organic acids which are environmentally friendly, we surveyed various available organic acids and down-selected citric acid. Carboxylic acids and diketone chelating agents have sparsely been utilized in REE extraction [13]. Only few commercial carboxylic acids, such as Versatic911/Shellsol A, have been utilized but there is very little information on their properties. However, series of REE-carboxylic acid complexes exist in the literature with well-defined crystal structures obtained via XRD with and without structural  $NO_3^-$  unit present [14]. The extraction process of REEs proceeds by complexation and cation exchange in neutral or weakly acidic medium. This basic REE organometallic chemistry provides suggestions that carboxylic acids are viable chelating agents for REE extraction.



Furthermore, these carboxylic acids are widely available industrially, also from sustainable sources such as biomass or glycerol waste product (glyceric, glyoxalic, oxalic, and tartronic) via partial oxidation [15]. Series of widely available carboxylic acids can be obtained from sustainable sources, such as biomass (citric, succinic, or valeric acid) via fermentation, extraction, and many industrial processes. The main inhibitor of their use appears to be their capacity to perform REE complexation. The deconvolution of these can be measured to evaluate their tenability as green and sustainable complexing molecules to facilitate REE extraction. In this work, citric acid is adopted as the carboxylic acid of choice for liberation of REEs, as a first step of evaluating the use of environmentally friendly options for REE recovery.

Mechanochemistry refers to solid-state chemical transformations initiated or sustained by mechanical force. In the field of material synthesis and minerals engineering, a typical mechanochemical process utilizes a ball milling or grinding to perform chemical reactions without necessarily requiring bulk dissolution of reactants [16, 17]. The advantages offered by mechanochemical routes mainly lie in the lower amount of solvent-utilization and lowered energy input to match or exceed the efficiency of conventional methods [18]. Mechanochemical processing routes typically need less energy input for the overall process and generate lower amount of waste (as the process can be solid-state or solvent free). This makes mechanochemical techniques a desirable alternative method of material processing for recovery of recyclable materials in a sustainable manner. In this work, we developed an mechanochemistry-assisted REE recovery process that investigated eco-friendly citric acid as leaching agent. The overall process utilizes reactive grinding to pretreat the NdFeB powders (to  $\sim 10 \mu\text{m}$  in diameter) with NaOH solution to form rare earth hydroxides. The rare earth hydroxides were subsequently leached in eco-friendly citric acid to form citrate. Initial optimization for the extraction process was done with the goal of maximizing Nd and Dy extraction. This combination of reactive grinding techniques and chemical processing via milder acids results in an environmentally friendly route to liberate and extract REEs, which has potential to be cost-effective.

## Experimental Leaching Process

A lab-scale ball mill reactor system suitable for wet grinding of recycled magnets to ultrafine particles was designed and fabricated. The system consists of a 3-chamber ball mill made of tungsten carbide (WC), as shown in Fig. 1. The chambers were chosen to be cylindrical jars of inside and outside diameters of 115 mm and 130 mm, respectively. Due to the strong magnetic property of NdFeB powders, the material of milling jars and balls should be non-magnetic. In view of these desired non-magnetic properties and mechanical behavior of jars and milling balls, tungsten carbide was chosen as the material choice. The reactor dimensions were chosen, keeping in view the off-the-shelf available cylinders. It should be noted that zirconia would not be strong enough to directly mill large chunk of NdFeB magnet and

difficult to manufacture. Stainless steel on the other hand has the desired strength, but would attract the magnet powders to the wall. Hence, titanium plates are used as end caps as well as protection for the screens in between chambers. The screens are 44- and 10-micron mesh in nylon, which is compatible with magnet powders. The titanium plate between chambers were cut to allow finer powders to flow from one chamber to another.

The lab-scale ball mill system is shown in Fig. 2. The ball mill sits on a two-piece shaft coupling connecting to a speed-control motor (120 V AC, NEMA 34, 1/5 hp). The motor has a maximum speed of 1750 rpm. The support frame was designed to be able to tilt at an angle from  $0^\circ$  to  $15^\circ$ . During operation, the ball mill is set at  $5^\circ$  angle, allowing the magnet powders to move downstream.

Magnets recycled from hard disk drives (HDDs) were used as feedstock for the experiments. These as received magnets were too large for lab-scale ball mill or direct grinding. Hence, as a preparatory step, they were grounded the magnet to larger chunk first, as shown in Fig. 3a. In the second step, the large chunk of magnets

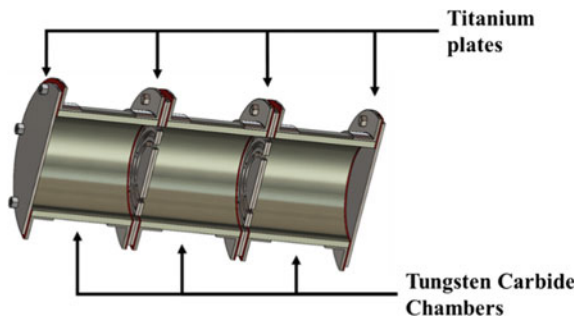


**Fig. 1** Cut view of the internal structure of the 3-chamber ball mill: the jars are tungsten carbide; the plates are titanium; in between the plates are nylon mesh

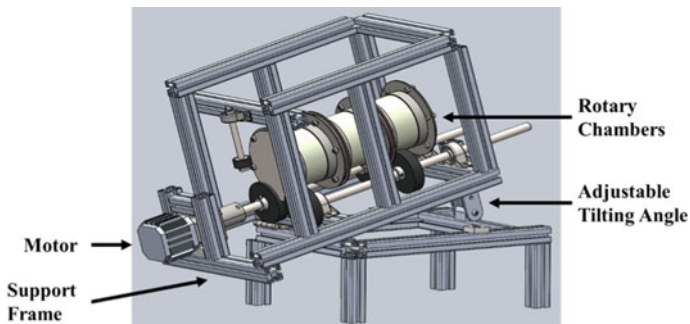


**Fig. 2** CAD model of the lab-scale ball mill system. The system consists of a 3-chamber ball mill made of tungsten carbide. The system is designed to have an adjustable tilting angle for the magnet powders to move through all chambers easily

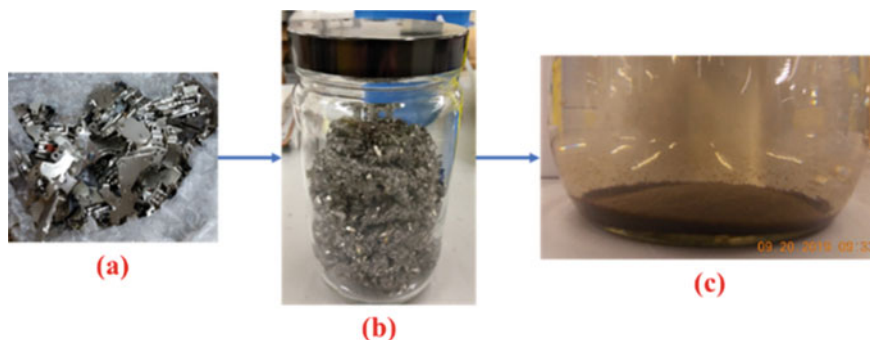


**Fig. 3** Recycled magnet through each stage at ACT: **a** original magnet recycled from HDDs, **b** large chunk of magnet ground by hammering, **c** fine magnet powders in water solution ground by custom ball mill grinder

was then subject to the wet grinding in water by the custom-built grinder to obtain fine powder solution, as shown in Fig. 3 (from b to c). Three sizes of the milling balls were tested to determine the optimal size for wet grind magnet powder, including 6, 10, and 20 mm. We found that 10 mm tungsten carbide balls were most suitable for grinding NdFeB powder to less than 10  $\mu\text{m}$ . This fine powder solution was then subject to reactive grinding in NaOH, using a smaller tabletop setup and leached in different acids.

In the bench-scale milling setup, a total of 200–400 mg sample of magnetic scraps, at  $\sim 10$  microns, and sodium hydroxide solution were loaded into a 15 mL zirconia jar (*Form-Tech Scientific*) together with two 7 mm zirconia balls and milled for the respective period of time at 21 Hz in a *Retsch MM300* mixer mill. Liquid-assisted grinding (LAG) was utilized due to the solid–liquid extraction. The resulting slurry was mixed with citric acid and allowed to react for the desired amount of time. Stock solution of 4.0 mol/L NaOH (from *Merck*) was made by adding solid NaOH to deionized water (from *Millipore*) in a volumetric flask. Citric acid (from *Millipore-Sigma*) was used in all extractions. All 1000 ppm standards for atomic absorption spectroscopy (AAS) were purchased from *Perkin-Elmer*. *Perkin-Elmer AAnalyst200* AAS was utilized to measure metal concentrations in aqueous solutions. All AAS hollow cathode lamps were purchased from *Perkin-Elmer*.

## Results and Discussion

The initial content of NdFeB powders was investigated. As shown in Table 1, new NdFeB powder from Chinese manufacturer and recycled NdFeB powder from HDDs were tested. The magnetic powder was dissolved in a mixture of 70% nitric acid and hydrochloric acid. After 4 h of reaction time, the solution was diluted to 100 mL with deionized water in a volumetric flask. This solution was directly used for dysprosium

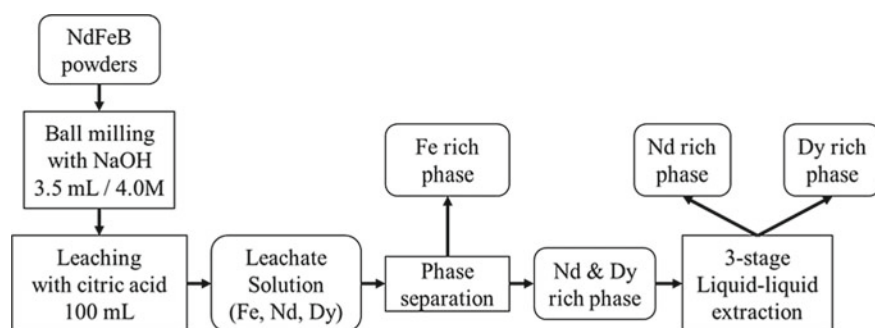
**Table 1** Initial content of Fe, Nd, and Dy (%wt) in NdFeB magnet powders: new vs recycled (from HDDs)

	Iron (Fe) (%)	Neodymium (Nd) (%)	Dysprosium (Dy) (%)
New powders	67.3	24.3	0.6
Recycled powders (from HDDs)	59.7	11.4	0.9

measurements, neodymium, and iron were measured by using a  $\times 10$  diluted solution. The summary of the initial content in NdFeB magnets is shown in Table 1 focusing on three critical elements: Fe, Nd, and Dy. We note that the recycled magnet has a lower Nd weight percent compared to the new magnet powder. The recycled magnet contains small fractions of other materials (such as Ni plating) that lowers the initial weight percentages compared to the new magnet powders. The new magnet powders were obtained from the original NdFeB manufacturer and had not been through modification for specific applications.

The new NdFeB powder was used to investigate optimal milling conditions in order to achieve the highest Nd extraction efficiency. Figure 4 presents the schematic of the proposed REEs extraction process. A baseline case was performed to show the effect of different leaching reagents without any milling or grinding. Leaching of Nd from new NdFeB powder was performed to compare the leaching efficiency of several reagents: 0.4 M  $H_2SO_4$ , 0.2 M NaOH, 0.2 M HCl, and 0.2 M citric acid. Without any pretreatment or milling, hydrochloric acid is the best acid to leach REEs out of NdFeB powder. The leaching efficiency is shown in Table 2 and Nd concentrations obtained are shown in Fig. 5, where citric acid leached only 42.3% of Nd, about half of the amount that HCl acid leached (82.7%).

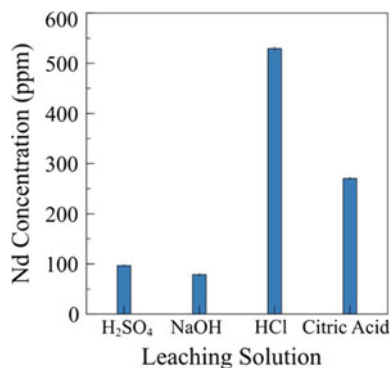
As stated previously, HCl is a strong acid, and using HCl in an industrial process leads to high cost of HCl itself as well as acid treatment and safety equipment. Thus, we proposed using citric acid as leaching reagent. Further, we performed reactive grinding/milling to improve the leaching efficiency of citric acid. The new NdFeB powder was used to investigate optimal milling conditions in order to achieve the

**Fig. 4** Schematic of the proposed REEs extraction process, including: milling, acid leaching, and liquid-liquid extraction stages

**Table 2** Leaching efficiency of different reagents (for baseline case). HCl is the best leaching reagent. Citric acid can only leach half of the amount that HCl (baseline: without any improvements via reactive grinding)

Leaching solution	Nd extraction (%)
H <sub>2</sub> SO <sub>4</sub>	15.1
NaOH	12.3
HCl	82.7
Citric acid	42.3

**Fig. 5** Leaching of Nd from new NdFeB powders using different reagents: H<sub>2</sub>SO<sub>4</sub>, NaOH, HCl, and citric acid



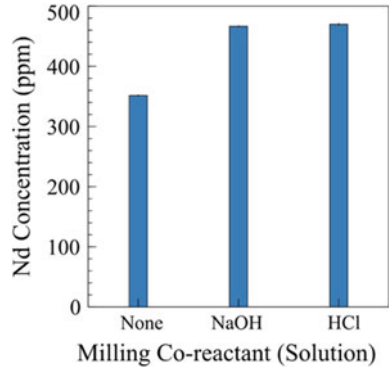
highest Nd extraction efficiency. The parameters investigated in this study were milling time, leaching time, and co-reactant species.

Figure 6 shows the leaching efficiency of citric acid when the powder went through reactive grinding with: no co-reactant, NaOH, and HCl, while the use of no co-reactant resulted in 54.9% extraction, using NaOH resulted in 72.9% and use of HCl resulted in 77.0% extraction. As a result, NaOH would be a good reagent for milling because it has equivalent extraction efficiency of HCl but is less hazardous. Figure 7 shows the effect of milling time when milling with 3.5 mL of 4.0 M NaOH and leaching in 100 mL of citric acid. Longer milling times led to more mobilization of metal ions from the powder due to more reaction time with NaOH.

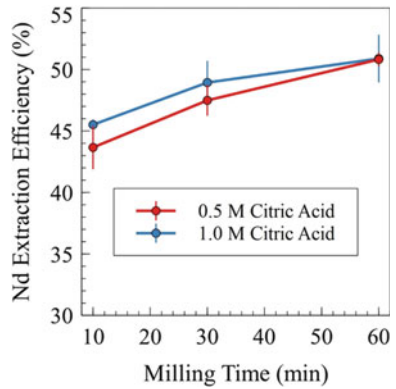
In this study, two concentrations of citric acid were used: 0.5 and 1.0 M. As shown in Fig. 7, there is an increase in Nd recovery efficiency for both 0.5 and 1.0 M citric acid concentrations after 10 min of extraction time, but the extraction plateaus after the 60 min mark. Therefore, 60 min is the optimal milling time with NaOH.

Figure 8 shows the effect of leaching time when milling with 3.5 mL of 4.0 M NaOH and leaching in 100 mL of citric acid. A 97% Nd extraction efficiency was observed at 60 min of leaching time for both 0.5 M and 1.0 M citric acid concentrations, while 0.2 M acid underperforms the 0.5 M and 1.0 M concentrations after 30 min. Moreover, the improvement of Nd extraction efficiency when citric acid concentration was increased from 0.5 to 1.0 M was not significant. Consequently, we concluded that the optimal concentration of citric acid and leaching time are

**Fig. 6** Nd extraction variation, when milling with different co-reactants. In all cases, NdFeB powder went through reactive grinding/milling, then leaching in citric acid



**Fig. 7** Nd extraction variation as a function of milling time. In all cases, NdFeB powder went through reactive grinding/milling, then leaching in citric acid. All experiments were done in duplicate, and average results are presented with error bars



(100 mL of) 0.5 M and 60 min. In summary, the optimal conditions for reactive grinding/milling and citric acid leaching of NdFeB powders are: milling in 3.5 mL of 4.0 M NaOH for 60 min, then leaching in 100 mL of 0.5 M citric acid for 60 min.

**Fig. 8** Nd extraction variation as a function of leaching time. In all cases, NdFeB powder went through reactive grinding/milling, then leaching in citric acid. All experiments were done in duplicate, and average results are presented with error bars

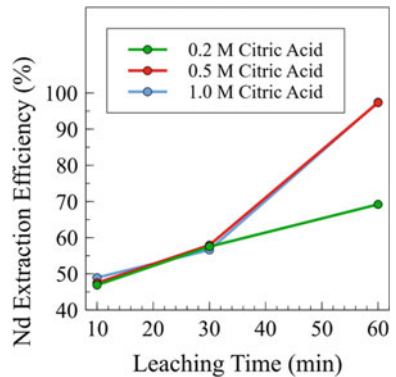


**Table 3** Leaching efficiency when milling in NaOH and leaching in citric acid

	Iron (Fe) (%)	Neodymium (Nd) (%)	Dysprosium (Dy)
New powders	67	97	N/A
Recycled powders (from HDDs)	30	69	100%

Following the optimization done with the new powder, the recycled magnet powder was subjected to the same extraction procedure: milling with 3.5 mL 4.0 M NaOH for 60 min (at 21 Hz frequency), and extraction with 100 mL 0.5 M citric acid for 60 min. Table 3 presents the percentage of Fe, Nd, and Dy extracted from both new and recycled powders when subjected to the optimal milling and leaching conditions. In new magnet powders, the leaching efficiency of Nd is 97%, Fe is 67%. The initial content of Dy is too low to be accurately determined.

Since leaching of Fe is not preferable, the recycled magnet was left in air and water, allowing for light oxidation. Iron oxide is less soluble in acid compared to the untreated form in the magnetic powder, leading to low leaching efficiency of Fe. On the other hand, neodymium oxide is easily dissolved in strong acid, but weakly dissolved in citric acid. Therefore, the extraction efficiency of Nd is lower than that of new magnet, although still at 69%. However, the leaching of Fe is successfully reduced to 30%. In addition, due to slightly higher initial content of Dy, the leaching efficiency of Dy was found to be 100%.

However, in both type of magnet, Fe was also leached alongside with the REEs. In addition, Nd and Dy have similar physical properties, including solubility, making it difficult to separate them. Further phase separation steps, and liquid–liquid extraction steps can be added to obtain Nd and Dy individually [19].

## Conclusions

This study successfully demonstrated feasibility of Nd and Dy extraction via reactive grinding/milling with NaOH, and citric acid leaching from NdFeB magnet recycled from HDDs. Due to the strong magnetic nature of NdFeB magnet, a large and weakly-magnetic ball mill is required to grind to fine powder. A leaching efficiency of 69% for Nd and 100% for Dy, and 30% for Fe was achieved via a two-stage process:

- 60 min of milling with 3.5 mL of 4.0 M NaOH.
- 60 min of leaching with 100 mL of 0.5 M citric acid into the solution phase.

Since leaching of iron (Fe) is not preferable, the recycled magnet was left in air and water, allowing for light oxidation. Iron oxide is less soluble in acid, leading to low leaching efficiency of Fe. On the other hand, neodymium oxide is easily dissolved in strong acid, but weakly dissolved in citric acid. Therefore, the extraction efficiency of Nd is lower than that of Dy, although still at 69%. Overall, the small extraction of Fe is preferred to reduce cost of Fe removal in liquid–liquid extraction.

**Acknowledgements** The funding for this work came from a SBIR phase I program funded by The U.S. Defense Logistics Agency. Contract SP4701-19-P-0048 was awarded to Advanced Cooling Technologies, Inc. (ACT). Dr. Rokkam was the principal investigator. Mr. Truong was the primary project engineer who undertook the project work. Dr. Baltrusaitis (Associate Professor at Lehigh University) and Mr. Silva (Graduate Student) undertook the project tasks at Lehigh. The authors would like thank the discussions with and support of the DLA program manager, Vaibhav Jain.

## References

1. Alonso E, Sherman AM, Wallington TJ, Everson MP, Field FR, Roth R, Kirchain RE (2012) Evaluating rare earth element availability: a case with revolutionary demand from clean technologies. *Environ Sci Technol* 46(6):3406–3414
2. Lixandru P, Venkatesan C, Jönsson I, Poenaru B, Hall Y, Yang A, Walton K, Güth R, Gauß OG (2017) Identification and recovery of rare earth permanent magnets from waste electrical and electronic equipment. *Waste Manage* 68:482–489
3. Tian Y, Liu Z, Zhang G (2019) Recovering REEs from NdFeB wastes with high purity and efficiency by leaching and selective precipitation process with modified agents. *J Rare Earths* 37(2):205–210
4. Firdaus M, Rhamdhani MA, Durandet Y, Rankin WJ, McGregor K (2016) Review of high-temperature recovery of rare earth (Nd/Dy) from magnet waste. *J Sustain Metall*
5. Ónal MAR, Borra CR, Guo M, Blanpain B, Gerven TomVan (2017) Hydrometallurgical recycling of NdFeB magnets: complete leaching, iron removal and electrolysis. *J Rare Earths* 35(6):574–584
6. Liu Q, Tua T, Guo H, Cheng H, Wang X (2020) High-efficiency simultaneous extraction of rare earth elements and iron from NdFeB waste by oxalic acid leaching. *J Rare Earths*. <https://doi.org/10.1016/j.jre.2020.04.020>
7. Yang Y et al (2017) REE recovery from end-of-life NdFeB permanent magnet scrap: a critical review. *J Sustain Metall* 3:122–149
8. Van Loy S, Binnemans K, Van Gerven T (2018) Mechanochemical-assisted leaching of lamp phosphors: a green engineering approach for rare earth recovery. *Engineering* 4(3):398–405, ISSN 2095-8099. <https://doi.org/10.1016/j.eng.2018.05.015>
9. Zhang ZY, Zhang FS, Yao T (2017) An environmentally friendly ball milling process for recovery of valuable metals from e-waste scraps. *Waste Manage* 68:490–497. <https://doi.org/10.1016/j.wasman.2017.07.029>
10. Behera SS, Panda SK, Mandal D, Parhi PK (2019) Ultrasound and microwave assisted leaching of neodymium from waste magnet using organic solvent. *Hydrometallurgy* 185:61–70, ISSN 0304-386X. <https://doi.org/10.1016/j.hydromet.2019.02.003>
11. Tom Lorenz, Martin Bertau. (2020) Recycling of rare earth elements from SmCo5-Magnets via solid-state chlorination, *Journal of Cleaner Production*. Volume 246, 118980. <https://doi.org/10.1016/j.jclepro.2019.118980>
12. Granite E et al (2017) Overview and accomplishments of R&ICs rare earth elements from coal & coal by-products. Project Rev. Meeting for Crosscutting Research, Gasification Systems & REEs Research
13. Xie F et al (2014) A critical review on solvent extraction of rare earths from aqueous solutions. *Miner Eng* 56:10–28. <https://doi.org/10.1016/j.mineng.2013.10.021>
14. Bünzli J-CG (2014) Review: lanthanide coordination chemistry: from old concepts to coordination polymers. *J Coord Chem* 67(23–24):3706–3733
15. Brainer JEN, Sales DCS, Medeiros EBM, Lima Filho NM, Abreu CAM (2014) Wet oxidation of glycerol into fine organic acids: catalyst selection and kinetic evaluation. *Braz J Chem Eng*:913



16. Do JL, Frišćić T (2017) Mechanochemistry: a force of synthesis. *ACS Cent Sci* 3(1):13–19. <https://doi.org/10.1021/acscentsci.6b00277>
17. Balaz P (2008) Mechanochemistry in minerals engineering. *Mechanochemistry in nanoscience and minerals engineering*, pp. 257–296. Springer, Berlin, Heidelberg. [https://doi.org/10.1007/978-3-540-74855-7\\_5](https://doi.org/10.1007/978-3-540-74855-7_5)
18. James SL, Adams CJ, Bolm C, Braga D, Collier P, Friščić T, Friščić F, Grepioni, F, Harris KDM, Hyett G et al (2012) Mechanochemistry: opportunities for new and cleaner synthesis. *Chem Soc Rev* 41, 413–447. <https://doi.org/10.1039/c1cs15171a>
19. Panda N, Devi N, Mishra S (2012) Solvent extraction of neodymium (III) from acidic nitrate medium using Cyanex 921 in kerosene. *J Rare Earths* 30(8):794–797

# Separation of Rare Earth Elements from Monazite Via Sulfidation



Caspar Stinn, Vasu Kaker, Zachary Kenneth Adams, and Antoine Allanore

**Abstract** Rare earth elements are critical for sustainability applications, yet their extraction, separation, and smelting remain environmentally and economically tedious. Conventional rare earth processing consists of a sequence of physical beneficiation, hydrometallurgical, and metallothermic or electrolytic processes to produce pure metals and alloys. Environmental impacts are concentrated in impurities management and material separation. Recently, sulfide-based separation chemistries have been shown to offer higher separation effectiveness than legacy hydrometallurgical methods at a fraction of the cost and energy usage. However, previous experimental studies have only employed synthetic feedstocks of mixed rare earth oxides or FeNdB magnets. Herein, we consider rare earth element separation from monazite mineral using sulfidation. We explore the use of iron and alkaline-earth compounds as separation additives to enable separation of rare earth elements and sequestration of normally occurring radioactive materials in parallel with de phosphorylation. Preliminary experimental results indicate that the addition of iron during rare earth mineral sulfidation is a promising method to promote selectivity, potentially enabling targeted rare earth element extraction and production.

**Keywords** Rare earth · Monazite · Sulfidation · Neodymium

## Introduction

The lanthanides (Ln) along with scandium and yttrium constitute the “rare earth” metals, a group of elements utilized in applications ranging from catalysis to magnets to desulfurization of steels [1]. The most commercially relevant rare earth minerals are bastnaesite ( $\text{LnCO}_3\text{F}$ ) and monazite/xenotime ( $\text{LnPO}_4$ ) [2]. In these minerals,

---

C. Stinn · Z. K. Adams · A. Allanore (✉)  
Department of Materials Science and Engineering, Massachusetts Institute of Technology,  
Cambridge, MA, USA  
e-mail: [allanore@mit.edu](mailto:allanore@mit.edu)

V. Kaker  
Department of Electrical Engineering and Computer Science, Massachusetts Institute of  
Technology, Cambridge, MA, USA

© The Minerals, Metals & Materials Society 2023  
T. Ouchi et al. (eds.), *Rare Metal Technology 2023*, The Minerals, Metals  
& Materials Series, [https://doi.org/10.1007/978-3-031-22761-5\\_3](https://doi.org/10.1007/978-3-031-22761-5_3)

the lanthanides are always found together, substituting for one another in minerals due to their similar size and valence electronic structure [3]. Normally occurring radioactive elements (NORMs) uranium and thorium are also present. Together, these realities have several implications. Rare earth elements are currently extracted and processed together, causing all rare earth elements to exist as a co- and by-products [4]. During rare earth concentrate production, NORMs must be removed prior to rare earth element separation to avoid radioactive contamination of downstream separation circuits and enrichment of source material [5]. Rare earth element demand is in practice driven by several high value elements, such as neodymium, creating a “balance problem” where other rare earth elements are available for the market in excess or shortage [6]. These market factors are complicated by the geographic concentration of rare earth mineral processing [7]. Across different criticality indices, rare earth supplies are reported to be at risk of geopolitical disruption, with potentially far reaching economic and security implications [8]. Meeting this collection of market, supply chain, and geopolitical challenges requires a paradigm shift in rare earth element extractive metallurgy and recycling.

Rare earth elements are currently produced from primary sources using a series of hydrometallurgical processing steps [3]. Following mining and physical beneficiation, rare earth minerals are digested or “cracked” using alkaline fusion or acid roasting to produce soluble rare earth compounds [2]. These compounds are then dissolved in acidic solution for aqueous-organic liquid-liquid solvent extraction. Cracking of rare earth minerals is operated as the only “targeted” process in the pathway, aiming to sequester thorium and a significant fraction of cerium in insoluble compounds prior to leaching and downstream solvent extraction [3]. Currently, environmental impacts are concentrated in cracking, dissolution, and solvent extraction steps [9]. Technical improvements have been proposed to reduce the intensity of hydrometallurgical routes [10]; yet, significant economic and environmental burdens remain. Different primary separation pathways have also been proposed, ranging from halogenation with chemical vapor transport [11] to borate crystallization [12] to selective reduction of rare earth oxides [13]. Sulfide-based separation chemistries are promising alternatives, potentially able to greatly reduce environmental impact and processing costs [14].

Merritt et al. demonstrated sulfidation of rare earth phosphate minerals with hydrogen sulfide in the presence of alkaline and alkaline-earth compounds [15]. They found that phosphorous could be sequestered in alkaline and alkaline-earth compounds, NORMs in oxide phases, and rare earth elements in oxysulfide phases. More recently, Stinn and Allanore demonstrated that sulfidation of lanthanum phosphate and calcium carbonate with elemental sulfur enabled similar sequestration of phosphorous and oxysulfide formation [14]. Stinn and Allanore also found that sulfidation was selective between rare earth elements during sulfidation of mixed rare earth oxides [14, 16]. During sulfidation of calcined iron-neodymium-boron rare earth magnets, the presence of iron improved sulfidation selectivity for light versus heavy rare earth elements, potentially enabling single-stage separation for rare earth element pairs [14]. However, selective sulfidation was not previously attempted on a natural rare earth mineral. Herein, we conduct the selective sulfidation of natural rare earth

monazite in the presence of iron oxide, with or without calcium carbonate as a phosphorous collector. We explore the possibility of utilizing sulfidation to enable targeted extraction of individual rare earth elements without complete hydrometallurgical dissolution.

## Methods

Monazite mineral ( $<63 \mu\text{m}$ ), iron oxide ( $\text{Fe}_2\text{O}_3$ ,  $<5 \mu\text{m}$ ,  $>99\%$ , Sigma Aldrich), and calcium carbonate ( $\text{CaCO}_3$ ,  $32\text{--}106 \mu\text{m}$   $99\%$ , Alfa Aesar) were utilized as sulfidation precursors. Vaporized elemental sulfur ( $99.5\%$ , Acros Organics) was utilized as a sulfur source in an argon carrier gas at a partial pressure of  $0.1\text{--}0.5$  atm with a total pressure of 1 atm. The carrier gas flowrate was 500 sccm. Two blends of materials were sulfidized in separate reactors: one containing equal parts by mass of monazite and iron oxide and one containing monazite, iron oxide, and calcium carbonate in a 3:3:2 mass ratio. Sulfidation was conducted in an alumina packed bed reactor at a temperature of  $1200^\circ\text{C}$  for two hours using procedures and apparatuses described previously [14]. Following sulfidation, the sulfidized products from each reactor were analyzed via scanning electron microscopy with energy dispersive x-ray spectroscopy (SEM-EDS).

## Results and Discussion

Micrographs illustrating the products of sulfidation are shown in Fig. 1, with the SEM/EDS compositions of major phases reported in Table 1. During sulfidation of the mixed monazite and iron oxide, iron oxide phases were observed to sulfidize to iron sulfide with some solubility for rare earth elements, while monazite phases remained as rare earth-rich phosphates. In the presence of calcium carbonate as a phosphorous collector, a thiophosphate of iron, calcium, and the rare earth elements was observed via SEM/EDS in addition to iron sulfide and unreacted monazite phases. X-ray diffraction analysis is necessary, however, to determine the crystalline nature of product phases. Some solubility for iron was observed in the rare earth phosphate following sulfidation without calcium carbonate. At a sulfidation temperature of  $1200^\circ\text{C}$  in the absence of a phosphorous collector, decomposition of rare earth phosphate to oxysulfide was hindered by either thermodynamic or kinetic effects. Kinetically, the sulfidation of rare earth phosphate is slower than the oxide [14]. In the absence of a dedicated condensed collector for phosphorous, gaseous phosphorous sulfidation products are likely diphosphorous pentoxide or diphosphorous pentasulfide gasses. These are relatively large molecules, which may be entropically unfavorable products due to their possession of fewer degrees of freedom per atom of contained sulfur compared to reactant diatomic sulfur gas. Further work is necessary,

however, to understand the differences in sulfidation rate and affinity between oxide and phosphate species.

Some selectivity was observed between the partitioning of rare earth elements in product phases via SEM/EDS. However, these results should be interpreted as preliminary at best due to the challenge of differentiating low concentrations of individual rare earth elements via SEM/EDS. Further, mapping of elements between phases using more sensitive methods, such as electron microprobe analysis and wavelength dispersive X-ray spectroscopy (EPMA/WDS), will be necessary to draw definitive conclusions on rare earth sulfidation selectivity. With these considerations in mind, neodymium was observed to sulfidize selectively compared to cerium and lanthanum with and without calcium carbonate as a phosphorous collector. Considering the results from the selective sulfidation of rare earth magnets, the sulfidation selectivity for heavy rare earth elements may also be substantial, yet further analysis is needed. The solubility of iron observed in the rare earth phosphate phase may be due to iron

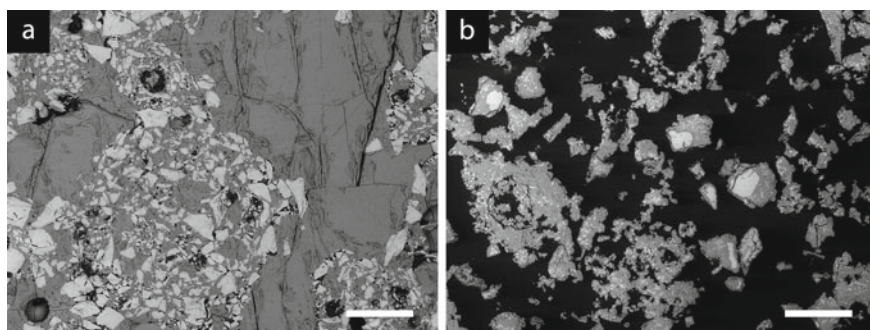


**Fig. 1** Sulfidation products of monazite and iron oxide (SEM backscatter electron composite image). Panel a corresponds to sulfidation without calcium carbonate, where light phases correspond to phosphate and dark phases correspond to sulfide (Table 1). Panel b corresponds to sulfidation with calcium carbonate, where large light phases correspond to phosphate, small white phases correspond to thiophosphate, and dark phases correspond to sulfide (Table 1). Scale bar: 200  $\mu\text{m}$

**Table 1** SEM/EDS composition by mass of sulfidized product phases

	Sample phase	La	Ce	Nd	Fe	Ca	O	P	S
No CaCO <sub>3</sub>	Phosphate	14.0% ( $\pm 1.1$ )	32.1% ( $\pm 1.3$ )	7.0% ( $\pm 0.9$ )	10.7% ( $\pm 0.8$ )	na	18.2% ( $\pm 1.0$ )	11.2% ( $\pm 0.4$ )	7.0% ( $\pm 0.6$ )
	Sulfide	0.3% ( $\pm 0.1$ )	1.4% ( $\pm 0.3$ )	0.5% ( $\pm 0.2$ )	60.4% ( $\pm 0.9$ )	na	3.6% ( $\pm 0.5$ )	0.7% ( $\pm 0.2$ )	33.1% ( $\pm 0.4$ )
With CaCO <sub>3</sub>	Phosphate	13.7% ( $\pm 0.6$ )	32.3% ( $\pm 0.9$ )	7.4% ( $\pm 0.6$ )	4.3% ( $\pm 0.4$ )	4.3% ( $\pm 0.2$ )	20.3% ( $\pm 0.7$ )	12.5% ( $\pm 0.2$ )	5.1% ( $\pm 0.2$ )
	Thiophosphate	8.2% ( $\pm 0.9$ )	18.6% ( $\pm 1.0$ )	4.8% ( $\pm 0.5$ )	7.0% ( $\pm 1.6$ )	16.7% ( $\pm 1.2$ )	21.3% ( $\pm 0.9$ )	12.8% ( $\pm 0.7$ )	10.5% ( $\pm 0.8$ )
	Sulfide	2.0% ( $\pm 0.4$ )	4.6% ( $\pm 0.4$ )	1.3% ( $\pm 0.3$ )	43.8% ( $\pm 1.4$ )	4.9% ( $\pm 0.3$ )	11.0% ( $\pm 1.0$ )	3.3% ( $\pm 0.3$ )	29.4% ( $\pm 0.7$ )

exhibiting some affinity for phosphorous sequestration during sulfidation. Detailed thermodynamic analysis is necessary to support this claim. Meanwhile, the role of iron in accentuating chemical differences between rare earth elements as sulfides is thermodynamically unexplored. Analysis of solar system versus crustal abundances of rare earth elements may inform the relative siderophilicity of individual rare earth elements in the presence of sulfur through insight into the preferential partitioning of individual rare earth elements to the earth's core.

These results, while preliminary, suggest that sulfidation of rare earth minerals may be conducted selectively, aided by the presence of iron compound collector phases. If selectivity between rare earth elements is confirmed via subsequent analysis, sulfidation with iron or transition metal-based collector phases may provide a means to selectively target and extract high value rare earth elements prior to mineral cracking and complete dissolution. Following sulfidation, iron sulfide containing target rare earth elements could be physically separated from the remaining rare phosphate/thiophosphate via conventional methods such as flotation. Once the sulfide phases were isolated, rare earths could be separated from iron via selective desulfidation [16] or other methods. This could alleviate market challenges surrounding the rare earth "balance problem" by unwinding the nested web of co- and by-products in rare earth element extraction.

## Conclusions

Rare earth elements exhibit complex market dynamics and tedious processing pathways due to their nature as by- and co-products of one another. Sulfide chemistry is a promising alternative to reduce costs and environmental impact while enabling targeted extraction of high value rare earth elements. Herein, we conduct sulfidation of monazite in the presence of iron oxide and calcium carbonate. Preliminary results suggest that sulfidation is selective for individual rare earth elements from monazite, where iron sulfide may be utilized as a collector phase to aid in recovery and selectivity. Further analysis is necessary, however, to confirm rare earth element partitioning between phases. Additionally, thermodynamic study may be employed to understand sulfide-phosphate interactions and the role of iron in differentiating the chemical behavior of individual rare earth elements.

**Acknowledgements** A portion of this work was funded by the MIT Undergraduate Research Opportunities Program (UROP).

## References

1. Cheisson T, Schelter EJ (2019) Rare earth elements: Mendeleev's bane, modern marvels. *Science* 363(6426):489–493. <https://doi.org/10.1126/science.aau7628>
2. Jordens A, Cheng YP, Waters KE (2013) A review of the beneficiation of rare earth element bearing minerals. *Miner Eng* 41:97–114. <https://doi.org/10.1016/j.mineng.2012.10.017>
3. Zhao B, Zhang J, & Schreiner B (2016) Separation hydrometallurgy of rare earth elements. Springer International Publishing, AG Switzerland
4. K Lee JC, Wen Z (2018) Pathways for greening the supply of rare earth elements in China. *Nat Sustain*. 1:598–605. <https://doi.org/10.1038/s41893-018-0154-5>
5. Findeiß M, Schäffer A (2017) Fate and environmental impact of thorium residues during rare earth processing. *J Sustain Metall* 3(1):179–189. <https://doi.org/10.1007/s40831-016-0083-3>
6. Binnemans K, Jones PT, Müller T, Yurramendi L (2018) Rare earths and the balance problem: how to deal with changing markets? *J Sustain Metall* 4(1):126–146. <https://doi.org/10.1007/s40831-018-0162-8>
7. Goldman JA (2014) The U.S. rare earth industry: Its growth and decline. *J Policy Hist* 26(2):139–166. <https://doi.org/10.1017/S0898030614000013>
8. Erdmann L, Graedel TE (2011) Criticality of non-fuel minerals: a review of major approaches and analyses. *Environ Sci Technol* 45(18):7620–7630. <https://doi.org/10.1021/es200563g>
9. Bailey G, Joyce PJ, Schrijvers D, Schulze R, Sylvestre AM, Sprecher B, Vahidi E, Dewulf W, Van Acker K (2020) Review and new life cycle assessment for rare earth production from bastnäsite, ion adsorption clays and lateritic monazite. *Resour Conserv Recycl* 155:104675. <https://doi.org/10.1016/j.resconrec.2019.104675>
10. Li XZ, Zhou LP, Yan LL, Dong YM, Bai ZL, Sun XQ, Diwu J, Wang S, Bünzli JC, Sun QF (2018) A supramolecular lanthanide separation approach based on multivalent cooperative enhancement of metal ion selectivity. *Nat Commun* 9:547. <https://doi.org/10.1038/s41467-018-02940-7>
11. Wang ZC, Zhang LQ, Lei PX, Chi MY (2002) Rare earth extraction and separation from mixed bastnaesite-monzite concentrate by stepwise carbochlorination-chemical vapor transport. *Metall Mater Trans B* 33(5):661–668. <https://doi.org/10.1007/s11663-002-0018-1>
12. Yin X, Wang Y, Bai X, Wang Y, Chen L, Xiao C, Diwu J, Du S, Chai Z, Albrecht-Schmitt TE, Wang S (2017) Rare earth separations by selective borate crystallization. *Nat Commun* 8. <https://doi.org/10.1038/ncomms14438>
13. Nakanishi BR, Allanore A (2019) Electrochemical investigation of molten lanthanum-yttrium oxide for selective liquid rare-earth metal extraction. *J Electrochem Soc* 166(13):E420–E428. <https://doi.org/10.1149/2.1141913jes>
14. Stinn C, Allanore A (2022) Selective sulfidation of metal compounds. *Nature* 602:78–83. <https://doi.org/10.1038/s41586-021-04321-5>
15. Merritt RR (1990) High temperature methods for processing monazite: II. Reaction with sodium carbonate. *J Less-Common Met* 166:211–219
16. Stinn C, Allanore A (2022) Selective sulfidation for rare earth element separation. In: Ouchi T (ed) *Rare metal technology 2022*, pp 259–278. Springer, Cham

# Experimental Investigation of Liquid Metal Leaching for Rare Earth Magnet Recycling



Chinenye Chinwego and Adam Powell

**Abstract** The importance of rare earth metals for clean energy technology and the threat to their supply has prompted several researchers to consider alternative techniques to mining. One strategy that is gaining traction in this area is recycling. Various studies have shown that the magnet-to-metal method, in which rare earth metal is leached from the magnet, is a potential way to obtain recycled mixed rare earth metal that may be used as a precursor for the manufacturing of rare earth magnets. This study will evaluate the leaching behavior of rare earth magnets in a liquid metal leaching and distillation recycling method. These data and prior leaching studies will form the basis of a model of leaching mass transfer kinetics. Models of distillation for magnesium and one other leaching agent can be used for scale-up reactor engineering.

**Keywords** Rare earth metals · Recycling

## Introduction

The recycling of rare earth magnets is gaining ground because of their importance to clean energy applications and the supply risk they pose, as mining and refining these metals is carried out in a few countries. Several research studies have explored extraction methods for rare earth magnet scraps, such as solvent extraction [1, 2], hydrogen decrepitation [3], and bioleaching [4]. Solvent extraction recovers the rare earth in oxide form, and hydrogen decrepitation is a magnet-to-magnet approach that still requires the addition of pure rare earth metals to avoid downgrading the final product. Liquid metal leaching and distillation is a potential method to obtain pure rare earth metal that can serve as a precursor for magnet production [5, 6].

This study explored the effect of particle size on the leaching behavior of rare earth magnets using magnesium as the leaching agent.

---

C. Chinwego (✉) · A. Powell  
Worcester Polytechnic Institute, Worcester, MA, USA  
e-mail: [cachinwego@wpi.edu](mailto:cachinwego@wpi.edu)



## Research Methodology

The leaching was carried out in a Mellen furnace at 900 °C for 2 h. Magnesium rods purchased from Strem were cut into smaller pieces. The rare earth magnets obtained were demagnetized at 350 °C, and the coatings were removed. The uncoated magnets were crushed to particle sizes ranging from 250 microns to 1 mm; thus, these were differentiated in terms of small, medium, and large particle sizes. The magnesium to magnet ratio variation used for the experiment was 3:1. The magnesium and magnet particles were placed in the graphite crucible as shown in Fig. 1a.

Characterization of the samples was carried out using ICP-MS/OES and SEM/EDX. The Nd to Mg ratios for the top section, midsection, interface, and bottom section of the leached sample were determined by icp-oes, as shown in Table 1. The praseodymium and other traces of heavy rare earth metals were also analyzed using ICP-MS, as shown in Table 2. In the bottom section, the large, medium, and small particle sizes were also characterized.

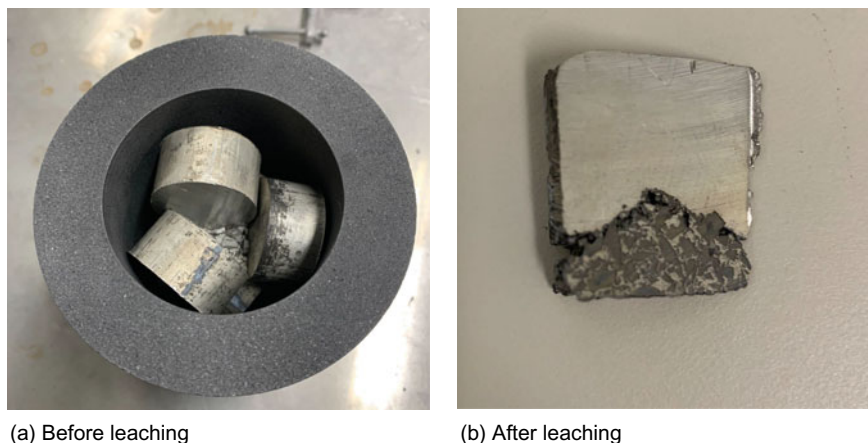


**Fig. 1** Magnesium and magnet samples before and after leaching

**Table 1** Neodymium-to-magnesium ratio of sample section based on ICP-OES analysis

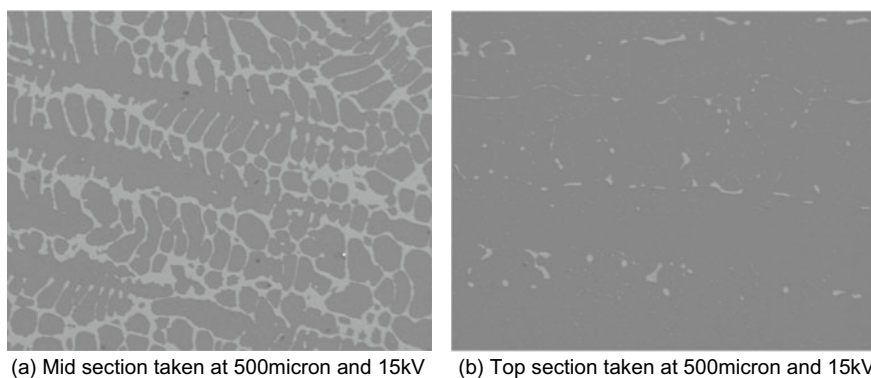
	Top	Mid	Interface	Bottom (small particle size)	Bottom (medium particle size)	Bottom (large particle size)
Nd/Mg ratio	0.004	0.014	0.133	0.311	0.267	0.234

**Table 2** Elemental analysis of other rare earth elements present using ICP-MS

	Pr (%)	Dy(%)	Tb(%)
Top	0.14	0	0
Mid	0.47	0	0
Interface	2.91	0.02	0.02
Bottom (small particle size)	1.08	0.01	0
Bottom (medium particle size)	1.69	0.02	0.01
Bottom (large particle size)	1.63	0.02	0.01

## Results and Discussion

The Nd-to-Mg ratio is highest at the bottom of the sample for the small particle size than the medium and large particle sizes. It is lowest at the top of the sample, indicating that some of the Nd were leached. At the interface, where there is a clear distinction between the magnet particles and the solid magnesium, we can see a relatively higher Nd/Mg ratio than the mid and top sections. In an attempt to identify trace rare earth elements, ICP mass spectroscopy was carried out. It was observed that some of the praseodymium was leached into the magnesium, as shown in Table 2, but no observable amounts of Dy or Tb entered the Mg alloy. This observation was supported by the EDS analysis of the top section sample, as shown in Fig. 2. That figure shows very high Nd concentration in regions with strong electron x-ray signals, indicating that Nd concentrates in intermetallic precipitates in the alloy. The large area spectrum indicates average Nd content of about 2–3 wt%, which is not far from the 3.5 wt% Nd concentration indicated by ICP-OES characterization. The SEM images in Fig. 2 carried out on the midsection and top of the sample show the presence of Mg-Nd alloy, indicating that leaching occurred (Fig. 3).

**Fig. 2** SEM images of the mid- and top sections after leaching

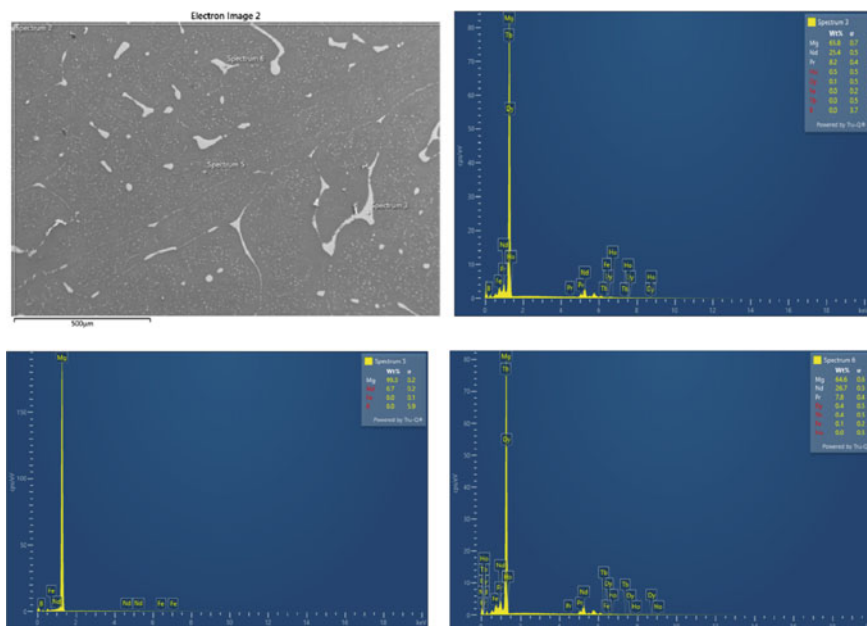


**Fig. 3** EDS analysis of Mg alloy top sample after leaching: (top left) backscatter image showing locations of EDS analysis (Spectrum 2 covers the whole field of view); (top right, bottom left and right) EDS spectra 3, 5, 6 showing 25%, 0.7%, and 26% Nd, respectively

## Conclusion

Liquid metal leaching using magnesium is a suitable way for recovering rare earth elements from magnet scrap. The magnesium-rare earth alloy formed afterward can be distilled to obtain the rare earth metal. Reducing the particle sizes of the scrap magnet can increase the leaching efficiency.

**Acknowledgements** This work was funded by the US DEVCOM Army Research Laboratory, Co-operative agreement W911NF-19-2-0108.

## References

1. Deshmane VG, Islam SZ, Bhawe RR (2019) Selective recovery of rare earth elements from a wide range of E-waste and process scalability of membrane solvent extraction. *Environ Sci Technol* acs.est.9b05695. <https://doi.org/10.1021/acs.est.9b05695>
2. Xie F, Zhang TA, Dreisinger D, Doyle F (2014) A critical review on solvent extraction of rare earths from aqueous solutions. *Miner Eng* 56:10–28. <https://doi.org/10.1016/j.mineng.2013.10.021>

3. Zakotnik M, Afunoy, P, Dunn S, Tudor CO (2020) Magnet recycling to create Nd-Fe-B magnets with improved or restored magnetic performance. 9,044,834. Accessed Mar 19, 2020. [Online]. Available: <https://patents.google.com/patent/US9044834B2/en>
4. Thompson VS et al (2018) Techno-economic and life cycle analysis for bioleaching rare-earth elements from waste materials. ACS Sustain. Chem. Eng. 6(2):1602–1609. <https://doi.org/10.1021/acssuschemeng.7b02771>
5. Ott RT, McCallum RW (2021) Recovering rare earth metals from magnet scrap,” U.S. Patent 10,323,299. Accessed: May 17, 2021. [Online]. Available: <https://patents.google.com/patent/US10323299B2/en>
6. Chinwego C, Wagner H, Giancola E, Jironvil J, Powell A (2022) Technoeconomic analysis of rare-earth metal recycling using efficient metal distillation. JOM 74(4):1296–1305. <https://doi.org/10.1007/s11837-021-05045-7>

# Recycling of Rare Earth Elements (REEs) from Scrap Nd-Fe-B Magnets



Nityanand Singh, Pankaj Kumar Choubey, Rekha Panda,  
Rajesh Kumar Jyothi, and Manis Kumar Jha

**Abstract** Nd-Fe-B magnets find a wide range of applications due to their high magnetic properties. At their end-of-life, a huge quantity of scrap Nd-Fe-B magnets are generated, which are a promising alternative resource for rare earth elements (REEs). Recycling of scrap Nd-Fe-B magnets will mitigate the demand supply gap of REEs. Thus, the present paper reports development of feasible hydrometallurgical flow sheet to recover REEs from Nd-Fe-B magnets. The process consists of roasting of magnets with 20% NaCl at 750 °C for 2 h followed by water leaching of the roasted mass at 75 °C for 60 min to produce REEs containing leach liquor. About 99.9% REEs was recovered, and the left residue contained Fe, which was further calcined at 600 °C for 2 h to get red oxide pigment.

**Keywords** Scrap Nd-Fe-B magnets · Hydrometallurgy · Roasting · Leaching · REEs

## Introduction

Neodymium-iron-boron (Nd-Fe-B) magnets are the most important magnets and have an essential range of applications such as electric vehicles due their high power and torque density [1], 1000–2000 kg in wind turbine generators [2], and computer hard disk drives [3]. Sintered Nd-Fe-B magnets have been widely used and continue to develop since they were invented because of their high performance and low cost. The average annual production growth in China and the world was 6310 tons and 6920 tons, respectively [4]. After the life circle of these devices is over, these rare earth magnets are being thrown away rapidly or dump in the land fill illegally. Present rare earth element in the permanent magnets gets dissolve and mixed in the water

---

N. Singh · P. K. Choubey · R. Panda · M. K. Jha (✉)  
Metal Extraction and Recycling Division, CSIR-National Metallurgical Laboratory,  
Jamshedpur 831007, India  
e-mail: [mkjha@nmlindia.org](mailto:mkjha@nmlindia.org)

R. K. Jyothi  
Convergence Research Center for Development of Mineral Resources, Korea Institute of  
Geoscience & Mineral Resources (KIGAM), Daejeon 34132, South Korea

© The Minerals, Metals & Materials Society 2023  
T. Ouchi et al. (eds.), *Rare Metal Technology 2023*, The Minerals, Metals  
& Materials Series, [https://doi.org/10.1007/978-3-031-22761-5\\_5](https://doi.org/10.1007/978-3-031-22761-5_5)

and soil, respectively. This causes severe diseases to the human life such as liver infection, difficulty in breathing, etc. The rapid industrialization and advancement of technology in EEE, electrical vehicle, and the turbines has increased demand of these permanent magnets rapidly [5]. The availability of rare earth Metals (REMs) in the earth is limited, and its mining process produce many essential difficulties especially with regard to the environment as REEs minerals containing some traces of radioactive elements such as uranium (U) and thorium (Th) [3]. The problem raising due to the unavailability of rare earth metals and decreasing primary resources by direct mining of rare earth metals has led to dependence on the secondary resources for the recovery of Rare earth metals. The spent Nd-Fe-B magnets after their end-of-life can be consider as the major source of rare earth elements.

A number of processes have been reported by many authors for the recovery of rare earth elements from spent Nd-Fe-B magnets by pyro-, hydro-, and electrometallurgy routes. Markarwa et al. [6] reported one step of REEs recovery with purity up to 93% from spent Nd-Fe-B magnets by electro-leaching with sulfuric acid and precipitation of REEs as oxalate with oxalic acid with same concentration 0.5 mol/L [6].

In addition, oxidative roasting carried out followed by organic acid leaching has been used to extract the REMs from Nd-Fe-B magnet. The Nd-Fe-B magnet was heated at 900 °C for 480 min to oxidize into acid susceptible species. The roasted materials were dissolved in a mix solution of malic and citric acids at 90 °C to leach more than 90% REEs [7]. Kumari et al. reported the extraction of neodymium by sulfuric acid leaching followed by precipitation using ammonia to recover the neodymium hydroxide. Almost ~ 99.99% recovery of REMs (Nd, Pr, Dy) [8]. Makarova et al. [9] was shown in their work, electrochemical leaching of rare earth elements of spent Nd-Fe-B magnets [9]. Ali et al. [10] reported nitration, calcinations, water leaching; ~ 95% REEs were recovered [10]. Lee et al. [11] proposed physical and chemical treatment of like demagnetization, grinding, screening, and leaching of Nd-Fe-B magnets [11]. In subsequent study, the precipitation and solvent extraction have also been studied to extract the rare earth metals from leach liquor of Nd-Fe-B magnet. Rabatho et al. [12] leached 81% of Dy and 98% of Nd in 1 M HNO<sub>3</sub> at 25 °C by using of 0.3 M H<sub>2</sub>O<sub>2</sub>, without affecting Fe which was remained in the residue. Further, 91.5% of Nd and 81.8% of Dy were recovered by precipitation using oxalic acid (H<sub>2</sub>C<sub>2</sub>O<sub>2</sub>) in a range of pH 8 at room temperature.

Due to similarity of REEs, it hard to target to maximize the selectivity and feasibility of all the process used to recover REEs from Nd-Fe-B magnets, and they have many demerits such as high cost, high energy consumptions, and many more.

In a view of the above aspect, the present study focused on the hydrometallurgical extraction of rare earth elements (Nd, Pr, and Dy) from discarded Nd-Fe-B magnet of hard disk. At first, magnet was demagnetized at elevated temperature; thereafter, roasting of crushed magnets was carried out with sodium chloride (NaCl) for the selective leaching of rare earth elements, and then, water leaching was carried out. To optimize the conditions for extraction of REEs, leaching studies were carried out at different parameters such as reaction time, temperature, and pulp density to recover the REEs from scrap Nd-Fe-B magnet. Further, the leached liquor contains REEs (Nd, Dy, and Pr) which undergoes evaporation to get the REEs salt.

## Experimental

### *Materials*

The waste computer CPU was collected from the local market and dismantled to separate hard disk drive and then magnet which treated for recovery of metals from it. The entire chemicals used in this study such as sulfuric acid, hydrogen peroxide, calcium hydroxide, nitric acid, and NaOH are analytical grade (AR) supplied by Rankem, India. Apart from concentrated chemical, all the dilute solutions were used in this study was prepared by using distilled water.

### *Pre-treatment and Characterization of Waste Hard Disk Drive*

At first the waste hard disk is dismantled manually to separate magnet present inside it, the separated magnet from spent hard disk are collected into a crucible which subjected to demagnetized by heating at 310 °C for 2 h to sour their magnetic strength. The demagnetized magnets crushed and ground manually to reduce their size up to 100 meshes to convert the material into homogenous form, which helps to increases efficiencies of leaching of REEs. The flowchart showing pre-treatment of waste hard disk is shown in Fig. 1.

The demagnetized-crushed magnets are characterized by dissolving in a mixture of three parts HCl to one part HNO<sub>3</sub> (Aqua regia) which is also summarized in Table 1 showing the total composition of metals present in Nd-Fe-B magnets determined by Induced Coupled Plasma-Optical Emission Spectrophotometer (ICP-OES). It is found that the excess of iron present in the magnet, some of them are associated with cobalt to improve corrosion properties of the magnets and the surface of magnets are coated by an electrochemical layer of nickel or some plastics [2].

### *Roasting Procedure*

Roasting of Nd-Fe-B magnets was carried out for the effective liberation of rare earth metals (REMs) by using cylindrical alumina crucible. At first, the demagnetized-crushed magnets are mixed with 20% sodium chloride (NaCl) in the ratio of 1:4 by the help of spatula. Then, the homogenous mixture was roasted in a pre-heating muffle furnace at the range of temperature between 500 and 800 °C for 30–180 min. After the completion of roasting experiment, the crucible was taken out of the furnace and left the material in air for cooling. Since the material was not converted in paste, it was easily ground by the help of mortar pistol. Now, the material roasted undergoes leaching procedure with various leachants such as water, sulfuric acid, hydrogen peroxide, and nitric acid.

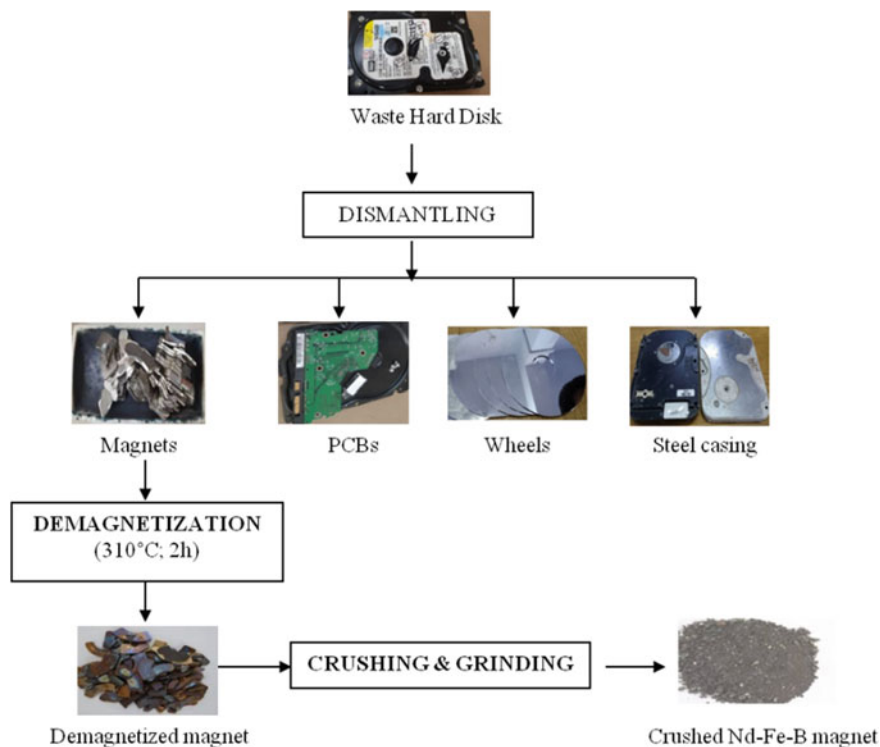


**Fig. 1** Flow diagram showing pre-treatment of waste hard disk from personal computers

**Table 1** Wt. % of metals in Ne-Fe-B magnets

Nd	Dy	Pr	Fe	Ni	Co
24.74	1.25	2.5	55.8	3.9	3.3

### *Leaching Procedure*

Leaching process was carried out to recover rare earth metals from scrap magnets of hard disk. At first, the glass Pyrex leaching reactor (250 mL) was well setup with reflux condenser to neglect the loss of liquid in the form of vapor at elevated temperature and placed in temperature-controlled hot plate to maintain the optimized temperature throughout the experiments, and a constant stirring was provided to the whole setup by using magnetic stirrer. Sampling was done at regular time interval to optimize the suitable parameters. The leach liquor was separated from the residue by using vacuum filtration unit. The obtained leach liquor which contains REMs was further subjected to evaporation process at high temperature to get REMs salt, whereas the residue left which contains other non-ferrous metals such as Fe, Co, and



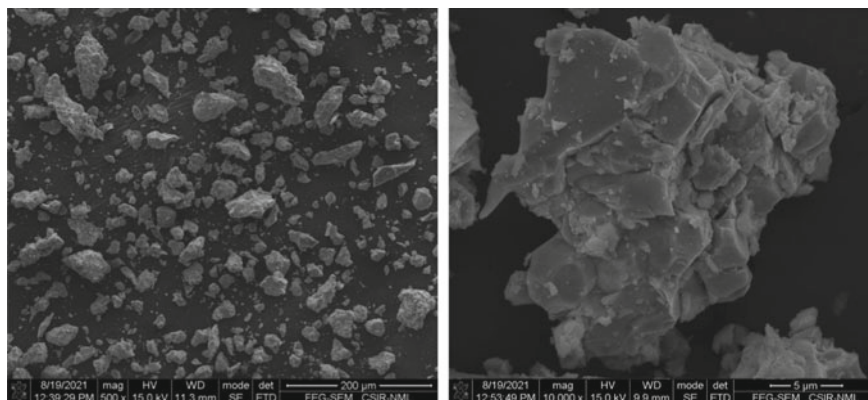


**Fig. 2** SEM image of demagnetized-crushed Nd-Fe-B magnet

Ni was washed and dried in a vacuum oven at 110 °C for 1 h, which can be further used to recover it by hydrometallurgical process.

### ***Analytical Procedure***

The demagnetized-crushed materials of spent permanent magnets of discarded hard disk drive are first analyzed in XRD for their phase detection, and then, the morphology of Nd-Fe-B magnets is studied by using SEM–EDS JXA-8230 Electron Probe Micro Analyzer (JEOL, Japan) with the same to know the accurate composition and morphology of metals present in the crushed materials of waste magnets (Figs. 2 and 3). The concentration of all metals (REEs, Fe, Co, Ni, B, etc.) present in the leach liquor was analyzed using Induced Coupled Plasma-Optical Emission Spectrophotometer (ICP-OES) (VISTA-PMX, CCD Simultaneous; Make: Australia) and Atomic Absorption Spectrophotometer (AAS) (Perkin Elmer model, Analyst 200; USA).

## **Results and Discussion**

### ***Pre-treatment of Nd-Fe-B Magnets***

Initially, spent hard disk drives of personal computers were dismantled manually and separated the required magnet for the recovery of REMs and the other parts, viz. steel frames, PCBs, platter, actuator, etc., are also separated. The magnets are demagnetized to diminish their magnetic strength at elevated temperature 310 °C

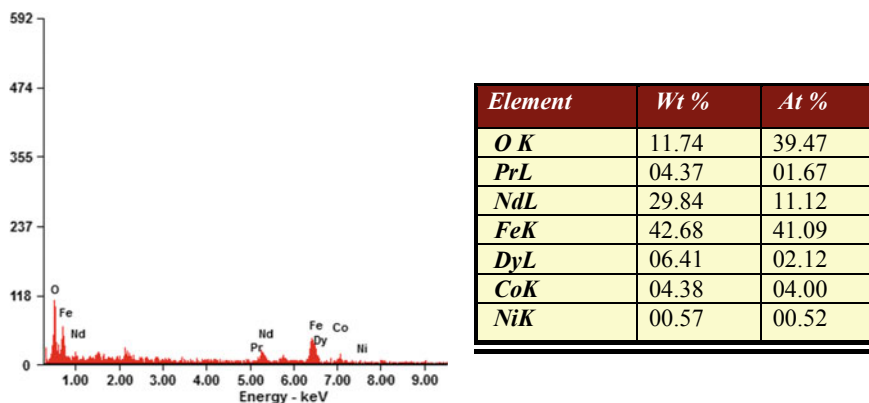


**Fig. 3** EDS pattern of demagnetized-crushed Nd-Fe-B magnet

for 2 h. Further, the demagnetized magnets are pulverized up to 100 mesh size. Figure 1 shows the systematic flowchart for pre-treatment of spent Nd-Fe-B magnets of hard disk drives. The pulverized materials of magnets were chemically digested and analyzed. About 24.74% of Nd, 2.5% of Pr, 1.25% of Dy, 55.8% of Fe, along with other traces metals, was present in the demagnetized-crushed magnets shown in Table 1.

### ***Roasting Studies of Nd-Fe-B Magnets***

Roasting study was carried out for selective recovery of rare earth metals from the Nd-Fe-B magnets by mixing with calcium hydroxide at optimal temperature. The roasting process was optimized for effectiveness at varying parameters as selection of additive, effect of concentration of sodium chloride, temperature, time, etc.

#### **Selection of Additive**

The roasting experiments were conducted with various additives, viz. calcium hydroxide, sodium hydroxide, sodium chloride, calcium carbonate, etc.; the concentration of the additive for each experiments remains the same which is 20%, and the pulverized materials of permanent magnets are mixed with the additive in the ratio of 1:4 for 1 h. The result obtained is shown in Table 2.

**Table 2** List of additive used for subsequent study of roasting of Nd-Fe-B magnets

Additive	Nd (%)	Pr (%)	Dy (%)	Fe (%)
CaCO <sub>3</sub>	43.6	33.7	31.0	–
Ca(OH) <sub>2</sub>	78	62	44.83	21.8
NaOH	66.31	53.5	48.5	19.5
NaCl	93.4	88.4	90.4	–

### Effect of Temperature

To demonstrate the effect of temperature on roasting of Nd-Fe-B magnets, various set of roasting experiments were carried out viz. 500, 600, 700, 750, and 800 °C for 1 h. At first, the crushed materials are well mixed with paste of sodium chloride and then placed into muffle furnace by putting it in an alumina crucible. At 500 °C, no weight loss has been found after roasting; it is because the sample needs more temperature to fracture the internal caging of samples. On moving toward 600 °C, at this the REEs are leached in water with low leaching efficiency which is 43%. But, in case of 700 °C roasting temperature, leaching efficiency of REEs increased from 43 to 78%, and at 750 °C, complete recovery of rare earth elements has been found which is shown in Fig. 3.

### Leaching Studies

#### Effect of Pulp Density

For more dissolution of metals, one factor pulp density plays significant role; as pulp density increases, it helps to increase the solution's surface area per unit volume, which increases the reaction rate; pulp density also affects the leaching rate of REEs from Nd-Fe-B of hard disk. For knowing the better optimized condition, various sets were practiced with different pulp densities such as 25, 50, 75, 100, and 150 g/L. Results indicates that the leaching percentage at 100 g/L is maximum, and it became constant at 150 g/L and so on; it is because the pulp density is inversely proportional to the leaching rate, and it may be due to the sample requiring more amount of acid solution as we increase the amount of samples [13]. 100 g/L pulp density was considered as best optimized condition for the further experiments after practicing various sets of leaching with different pulp density with same condition (Fig. 5).

## Effect of Temperature

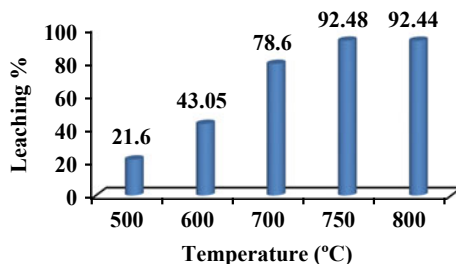
As the temperature of the reaction increases, the rate of reaction increases and vice versa [14]. Therefore, to study the effect of temperature on leaching of roasted Nd-Fe-B magnets, many sets leaching experiment were practiced at different temperature such as 25, 60, 75, and 90 °C with pulp density 100 g/L and time 30 min. After analysis, results indicate that increase in temperature increases leaching efficiency of REMs contained in the solid materials, but at high temperature, it becomes constant, and at 75 °C, the leaching percentage of REMs was found maximum, while at 90 °C it seems almost constant. Therefore, further leaching experiments were carried out at 60 °C as optimized leaching temperature at this temperature leaching of REMs was found 99.9% (Fig. 6).

## Effect of Time

To investigate the effect of time in the dissolution of REMs from Nd-Fe-B magnets of computers, the roasted products were leached in water at 75 °C by maintaining 100 g/L pulp density; various leaching sets were practiced such as 10, 15, 20, 30, 45, 60, and 75 min. Results show that the leaching efficiency of REEs reached ~ 57% in 30 min and the maximum recovery (~ 92%) was obtained in 60 min. which is shown in Fig. 4. The residue obtained after filtration contains iron was further calcined at 600 for 2 h.

After 10 min of the experiment, the leach liquor was taken in a test tube bottle {bottle (a) in Fig. 2} and analyzed which indicates 19.6% recovery. Further, after 30 min, it was increased by ~ 57.3% {bottle (b) in Fig. 2}. In addition, after 45 min and 60 min, the recovery rate of REEs was continuously increased by 69.8% and 93.4% {bottle (c) and (d)}. But, after 60 min of the reaction, the results show that the dissolution of iron started along with the REEs {bottle (e) in Fig. 2}; therefore, 60 min mixing time was considered as suitable parameter for further experiments (Fig. 7). The complete process flow sheet for extraction of REMs is presented in Fig. 8.

**Fig. 4** Effect of temperature on roasting of Nd-Fe-B magnets with 20% NaCl paste (solid: 80 g Nd-Fe-B magnet + 20 g NaCl (liquid); temperature: 500–800 °C; time: 60 min)



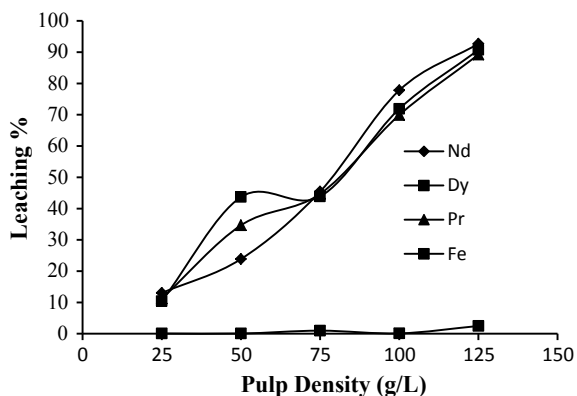


**Fig. 5** Effect of pulp density on leaching of REEs from roasted Nd-Fe-B magnets (Experimental condition: solid—25–125 g/L; temperature—75 °C; time—60 min)

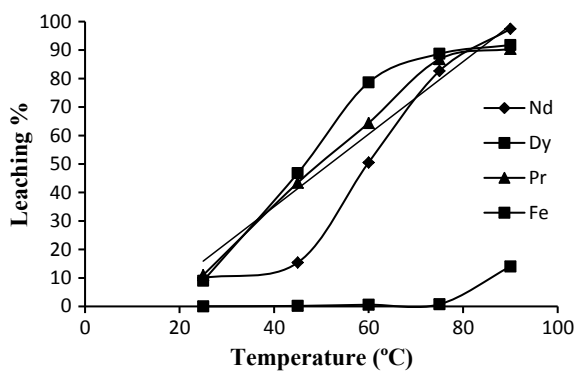


**Fig. 6** Effect of temperature on leaching of REEs from roasted Nd-Fe-B magnets (Experimental condition: solid—100 g/L; Temperature—25–75 °C; Time—60 min)

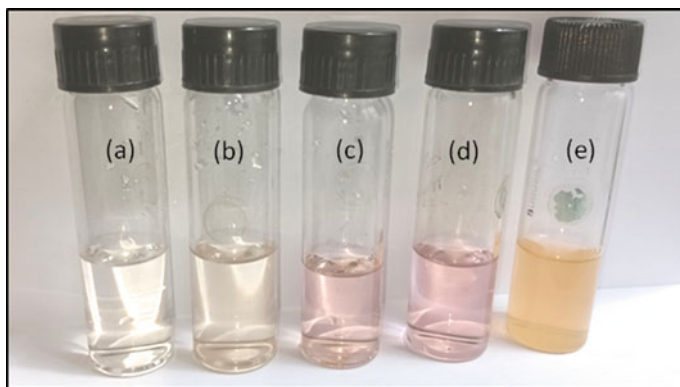


**Fig. 7** Effect of mixing time on leaching of REEs from roasted Nd-Fe-B magnets

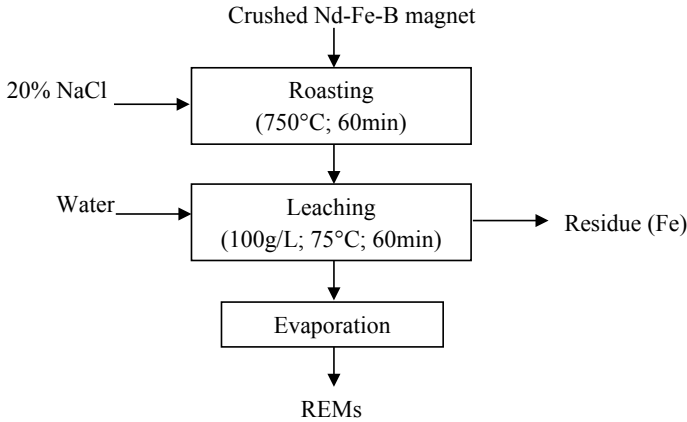


**Fig. 8** Flow diagram showing selective recovery of REMs from Nd-Fe-B magnets

## Conclusions

Based on the above experimental results, the following conclusions have been made.

- The Nd-Fe-B magnets can be demagnetized by heat treatment at 310 °C in 2 h.
- The complete conversion of REEs in water-soluble species occurred at 750 °C by mixing with 20% of NaCl paste placed in muffle furnace.
- Roasted magnets was leached in water at 75 °C by 60 min mixing time, maintaining 100 g/L. Results indicates complete dissolution of REMs by water leaching.
- The leach liquor of discarded magnet can be evaporated at high temperature to get REEs salts.
- Finally, the residue left which contains Fe was calcined 600 °C for 2 h to convert it as Fe-pigment red oxide.

**Acknowledgements** The authors are thankful to Director, CSIR-National Metallurgical Laboratory, Jamshedpur, India, for kind permission to publish the paper.

## References

1. Luk PCK, Abdulrahem HA, Xia B (2020) Low-cost high-performance ferrite permanent magnet machines in EV applications: a comprehensive review. *Transportation* 6:100080
2. Gruber V, Carsky M (2020) New technology for lanthanide recovery from spent Nd-Fe-B magnet. *S Afr J Chem Eng* 33:35–38
3. Nababan DC, Mukhlis R, Durandet Y, Pownceby MI, Prentice L, Rhamdhani MA (2021) Mechanism and microstructure evolution of high temperature oxidation of end-of-life NdFeB rare earth permanent magnets. *Corros Sci* 182:109290
4. <https://www.statista.com/statistics/270277/mining-of-rare-earths-by-country/>

5. Lu X, Wu Y, Lian J, Zhang Y, Chen C, Wang P, Meng L (2020) Energy management of hybrid electric vehicles: a review of energy optimization of fuel cell hybrid power system based on genetic algorithm. *Energy Convers Manage* 205:112474
6. Makarova I, Rylb J, Sunc Z, Kurilod I, Górnickae K, Laatikainen M, Repoa E (2020) One-step recovery of REE oxalates in electro-leaching of spent NdFeB magnets. *Sep Purif Technol* 251:117362
7. Kumari MK, Jha DD, Pathak (2020) An innovative environmental process for the treatment of scrap Nd-Fe-B magnets. *J Environ Manage* 273:111063
8. Makarova I, Soboleva E, Osipenko M, Kurilo I, Laatikainen M (2020) Electrochemical leaching of rare-earth elements from spent NdFeB magnets. *Hydrometallurgy* 192:105264
9. Onal MAR, Aktan E, Borra CR, Blanpain B, Gerven TV, Guo M (2017) Recycling of NdFeB magnets using nitration, calcination and water leaching for REE recovery. *Hydrometallurgy* 167:115–123
10. Reisdorfer G, Bertuol D, Tanabe EH (2019) Recovery of neodymium the magnets of hard disk drives using organic acids. *Miner Eng* 143:105938
11. Lee CH, Chen YJ, Liao CH, Popuri RS, Tsai SL, Hung CE (2013) Selective leaching process for Neodymium recovery scrap Nd-Fe-B magnet. *Metall Mater Trans A* 44:5825–5833
12. Rabatho JP, Tongamp W, Takasaki Y, Haga K, Shibayama A (2013) Recovery of Nd and Dy from rare earth magnetic waste sludge by hydrometallurgical process. *J Mater Cycles Waste Manag* 15:171–178
13. Jha MK, Kumari A, Choubey PK, Lee JC, Kumar V, Jeong J (2012) Leaching of lead from solder material of waste printed circuit boards (PCBs). *Hydrometallurgy* 121–124:28–34
14. Choubey PK, Singh N, Panda R, Jyothi RK, Yoo K, Park I, Manis Kumar Jha (2021) Development of hydrometallurgical process for recovery of rare earth metals (Nd, Pr, and Dy) from Nd-Fe-B Magnets. *Metals* 11:1987

**Part II**  
**Processing for Precious Metals and Rare**  
**Metals/Electrochemical Processing**  
**for Rare Metals**



# An Innovative Hydrometallurgical Process for Recovery of Critical and Rare Metals from Copper Anode Slimes



Shijie Wang

**Abstract** During electrorefining, copper is purified from impure anodes by dissolving the anodes in an electrolyte and plating on the cathodes. All insoluble components are precipitated to the bottom of electrolytic cells in the tankhouse or cellhouse. These settled insoluble components are called anode slimes. They contain copper, tellurium, selenium, bismuth, silver, gold, and traces of platinum group metals, such as platinum and palladium. Traditionally, these valuable metals are recovered in partial pyro- and hydrometallurgical processes. This paper presents an innovative 100% hydrometallurgical process: Wang's process. It can be tailored to target the recovery of specific critical metals. This novel process would not only eliminate all by-products from current precious metals plants, but also significantly increase revenues from copper electrorefinery operations.

**Keywords** Anode slimes · Bismuth · Gold · Hydrometallurgy · Palladium · Platinum · Selenium

## Introduction

Chalcopyrite is an abundant copper-bearing mineral: It accounts for approximately 70% of the world's known copper reserves. Precious metals, platinum group metals, rare metals, and p-block elements are associated with copper in chalcopyrite. During the copper electrorefining process, precious metals (gold and silver), platinum group metals (palladium and platinum), rare metals (selenium and tellurium), bismuth arsenate, and antimony arsenate are insoluble in sulfuric acid. (Bismuth and antimony arsenate form when arsenic is added to control their solubilities in the tankhouse). These settle and concentrate in copper anode slimes.

Most copper refineries still use conventional pyrometallurgical processes to recover precious metals from copper anode slimes, [1, 2] where it typically takes forty-five (45) days to produce gold and silver ingots from raw anode slimes. In

---

S. Wang (✉)  
Coeur Mining, Inc., 104 S. Michigan Ave., Chicago, IL 60603, USA  
e-mail: [swang@coeur.com](mailto:swang@coeur.com)

addition to being time-consuming, these operations are associated with high-energy consumption and negative environmental impacts. Due to the need to comply with increasingly stringent environmental regulations, and in the face of growing global metal demand, hydrometallurgical processing has become an attractive alternative.

An innovative hydrometallurgical process (Wang's process) was developed to recover critical metals based on their physical and chemical properties. This novel process involves a series of hydrometallurgical separations. It is economically viable and robust for recovery of many metals, including relatively inert metals such as gold and platinum group metals. It is also able to produce gold and silver ingots from raw anode slimes in only five (5) days.

## Process Development

The goal of the novel hydrometallurgical process is to maximize metal recovery and eliminate some of the issues that pose challenges to major copper refineries in particular. Minimizing value loss and avoiding cross-contamination are other critical objectives in precious and rare metals operations.

Typical gold-bearing solutions, such as raffinate from gold leaching and solution purification, contain entrapped gold as well as co-extracted platinum group metals, selenium, bismuth, and tellurium. In pyrometallurgical operations, these elements all accumulate in the precipitated crude selenium and discharging solution, resulting in value loss and penalty in selenium sales.

This novel, innovative hydrometallurgical process was developed for recoveries of gold, palladium, selenium, and bismuth in series (Fig. 1). The final discharge solution is sent to the water treatment plant. The combination of  $\text{Au} \rightarrow \text{Pd} \rightarrow \text{Se} \rightarrow \text{Bi}$  in series is very attractive for major copper refineries when a fully hydrometallurgical process is chosen for anode slimes processing.

### *Step 1: Gold Recovery*

In commercial practice, poor organic/aqueous separation in the gold solvent extraction circuit often results in increased gold reporting to the crude selenium. This reduces the saleability of selenium to the customer because residual dibutyl carbitol (organic used in solvent extraction) produces an obnoxious odor. Producing a clean crude selenium is of critical importance [3, 4].

Activated carbon can effectively adsorb substances and organics from solution due to its large number of cavernous pores. Pilot tests have shown that activated carbon adsorbed approximately 99% of the gold from the raffinate at room temperature in 30 min. Considering that 100% removal of organics from water and other liquids was attained, a carbon column was designed to maximize gold recovery and eliminate residual dibutyl carbitol in crude selenium products (Fig. 2).

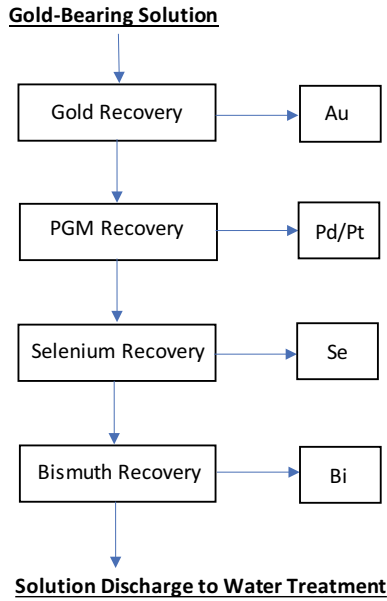


Fig. 1 Flow diagram for innovative hydrometallurgical process to recover Au, Pd, Se, and Bi

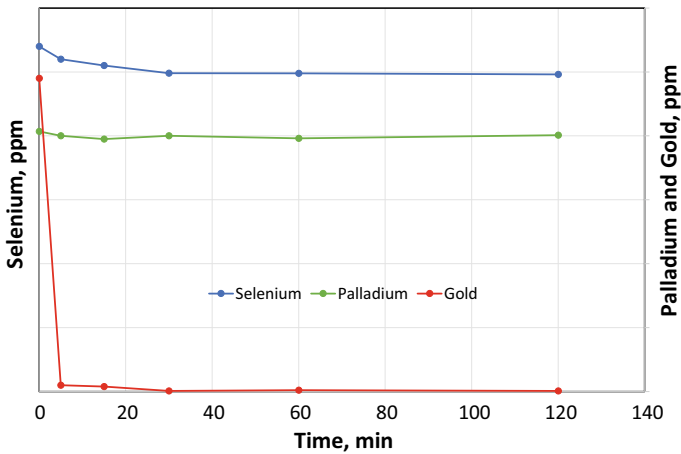
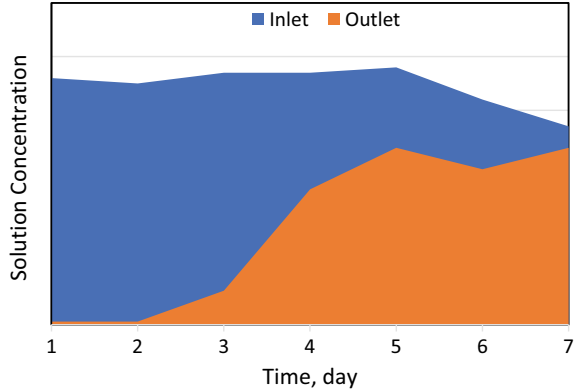


Fig. 2 Gold adsorption by activated carbon

### Step 2: Palladium and Platinum Recovery

The palladium and platinum selective process was designed to be flexible and robust in converting Pd and Pt from an input stream that can vary in concentration by 60% and 110%, respectively, of the normal plant feed rate [5]. Palladium absorption

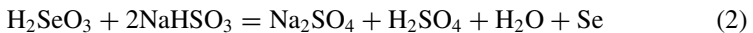
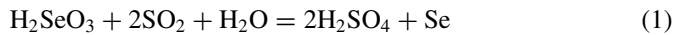
**Fig. 3** Palladium absorption in selective resin



reached to its capacity of 78.6% in the first pass (Fig. 3). The platinum concentration was below the detection limit. Results indicate that this resin can recover palladium after gold recovery is complete.

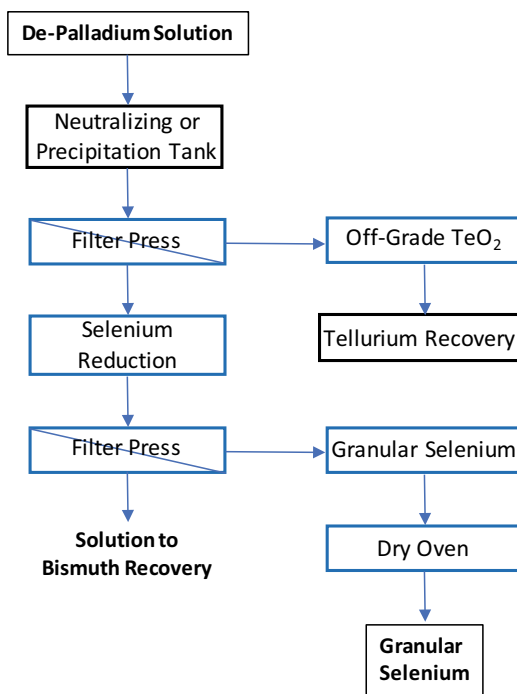
### ***Step 3: Selenium Recovery***

After gold and palladium are recovered, the selenium solution is transferred to the selenium circuit for reduction and recovery. In the original process, selenium reduced and collected precious metals, palladium, and platinum as it was reduced and precipitated itself. In the new process, although the conditions under which selenium is precipitated are similar to those used in the original process, sodium bisulfite ( $\text{NaHSO}_3$ ) replaces sulfur dioxide ( $\text{SO}_2$ ) as the reductant (compare reaction 2 to reaction 1 below). The effluent containing recoverable + 4 valent selenium is treated directly with sodium bisulfite, which reduces + 4 Se to elemental Se as a precipitate. This granular selenium is filtered out, and the filtrate is further treated for bismuth recovery in the bismuth circuit.



Changing from sulfur dioxide to sodium bisulfite is advantageous with respect to storage, environmental considerations, ease of use, and precise control of reductant addition. This selenium refining circuit may need one additional stage to remove nearly all remaining tramp tellurium, as shown in Fig. 4 [6].

**Fig. 4** Additional stage for selenium refining



#### ***Step 4: Bismuth Recovery***

In this fourth and final stage in the metal recovery series, bismuth is removed from the selenium reduction discharge solution. It is critically important to remove and recover bismuth in order to avoid it being eventually re-smelted and recycled in copper anodes [7].

In this step, a SuperLig<sup>®</sup>83 (IBC Advanced Technologies) column is used (Fig. 5), which contains a proprietary chelating molecule that is very selective for the Bi<sup>3+</sup> cation. The bismuth-chelating molecules are covalently bound to silica beads of approximately 0.25–0.5 mm diameter. The Bi<sup>3+</sup> captured in the SuperLig<sup>®</sup>83 can be eluted by sulfuric acid at an elevated temperature and precipitated as Bi(HSO<sub>4</sub>)<sub>3</sub> when it cools naturally to room temperature. SuperLig<sup>®</sup>83 is capable of working in both acidic sulfate and some chloride-containing solutions.

SuperLig<sup>®</sup>83 has been commercially applied for bismuth removal in sulfuric acid media from tankhouse electrolyte. However, this is the first time that it has been used to load bismuth from HCl media, which was then eluted by 9 M H<sub>2</sub>SO<sub>4</sub> for bismuth sulfate recovery. Pilot test results were encouraging; consequently, the SuperLig<sup>®</sup>83 is employed for removal and recovery of bismuth from selenium reduction solution in the novel hydrometallurgical process (Fig. 6).

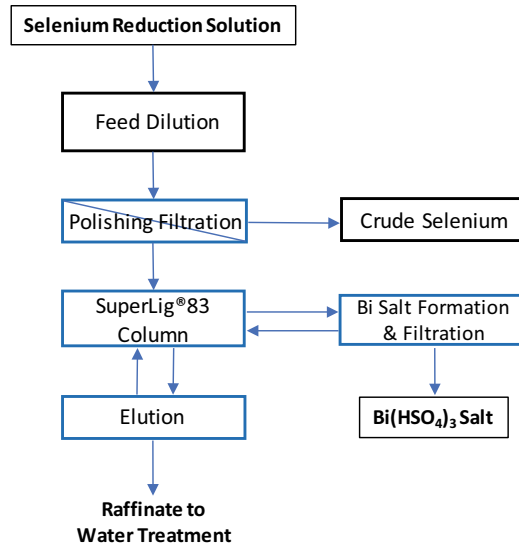


**Fig. 5** Block flow diagram for bismuth recovery with SuperLig<sup>®</sup>83

## Conclusions

- The need to comply with increasingly stringent environmental regulations has made hydrometallurgical processing an attractive method for recovery of many metals from copper anode slimes.
- This paper describes an innovative, four-step, hydrometallurgical process for gold, palladium, platinum, selenium, and bismuth recovery and refining.
- The combination of  $\text{Au} \rightarrow \text{Pd} \rightarrow \text{Se} \rightarrow \text{Bi}$  in series is attractive for applications in major copper refineries where a fully hydrometallurgical process is chosen for anode slimes processing.

Recovery of these elements is not only desirable, but economically viable and environmentally sound.

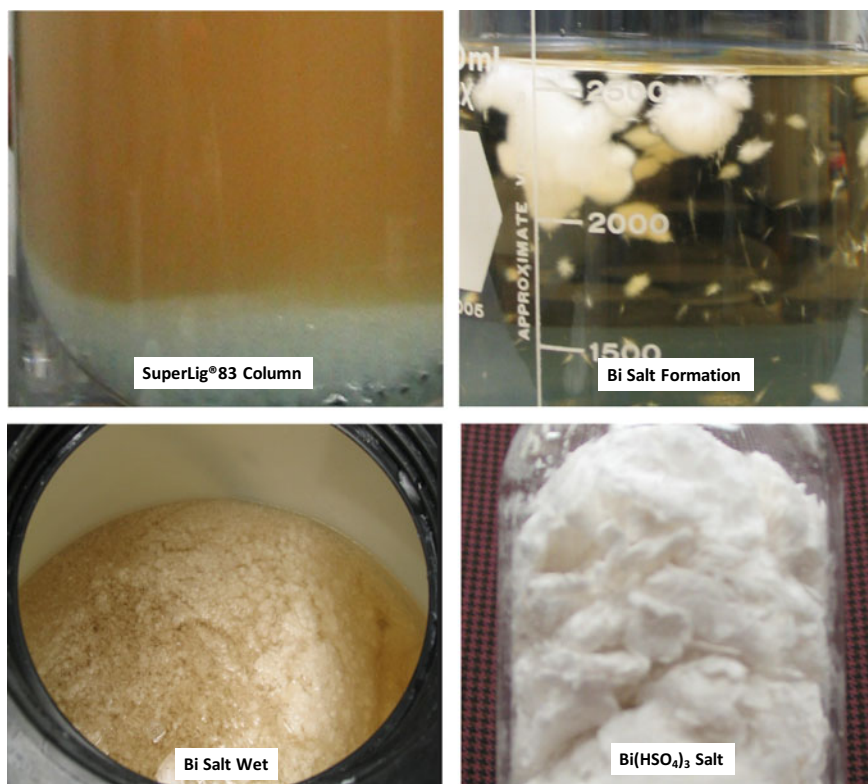


**Fig. 6** Bismuth recovery using SuperLig®83

## References

1. Wang S, Wesstrom B, Fernandez J (2003) Removal and recovery of tellurium/selenium from copper slimes leachate. In: Schlesinger ME (ed) EPD Congress 2003, TMS
2. Wang S, Kim D, Brees D (2010) Sustainable developments in copper anode slimes—wet chlorination-processing. Copper 2010 conference. Hamburg, Germany
3. Wang S (2005) Selenium removal in precious metals operations
4. Wang S (2005) Selenium reduction—selenium treatment technologies. Company Internal Research Report
5. Wang S (2012) PGM recovery features. Company Internal Research Report
6. Wang S (2023) Research and industrial applications of selenium and tellurium recovery processes. An extraction & processing division symposium in honor of Patrick R. Taylor. TMS
7. Wang S, Kim D (2008) Bismuth recovery from hydrochloric acid solution. *Can Metall Q* 47(3):317–326

# Recovery and Enrichment of Platinum Group Metals from Spent Automotive Catalysts by Pyrometallurgy: A Review



Jibiao Han, Xianglin Bai, Quan Yang, Biao Wang, Wangrui Ma, Yong Li, Bin Yang, Xilong Wu, and Yu Zhao

**Abstract** The world platinum group metals (PGMs) reserves and the recovery of PGMs secondary resources are discussed in this review. For many countries, the low reserves, large consumption, and high external dependence of PGMs are common problems nowadays. Therefore, the recycling of catalysts which contain PGMs has become an important method to alleviate the shortage of resources. This paper mainly introduces the pyrometallurgical recovery and enrichment process of spent automotive catalysts, including plasma melting and metal capture method, which has the advantages of high enrichment rate, large-scale, and short process, and iron, copper, and lead are often used as metal collectors to capture and recover PGMs. The advantages and disadvantages of different technologies are summarized, and the improvement and progress of PGMs recovery process are prospected, which provide a new idea for green and efficient recovery of spent automotive catalysts.

**Keywords** Platinum group metals (PGMs) · Spent automobile catalyst · Pyrometallurgy recovery · Metal capture method · Enrichment

## Introduction

Platinum group metals (PGMs) include platinum, palladium, rhodium, iridium, ruthenium, and osmium. They are widely used in automotive catalysts, petrochemical industry, national defense construction, electronic industry, jewelry, pharmaceutical,

---

J. Han · X. Bai · Q. Yang · B. Wang · W. Ma · Y. Li · X. Wu (✉) · Y. Zhao (✉)  
Sino-Platinum Metals Resources (Yimen) Co. Ltd., Yuxi 653100, China  
e-mail: [291283488@qq.com](mailto:291283488@qq.com)

Y. Zhao  
e-mail: [306736970@qq.com](mailto:306736970@qq.com)

J. Han · X. Bai  
Precious Metal Laboratory Co., Ltd. of Yunnan, Kunming 650000, China

J. Han · B. Yang  
National Engineering Lab for Vacuum Metallurgy, Kunming University of Science and Technology, Kunming 650093, China



and other fields because of unique catalytic properties, high melting point, and corrosion resistance. PGMs also have increasingly important applications in new energy, materials, and other frontier industries, such as hydrogen energy industry, new energy vehicles, and environmental protection materials, and have become an important metal material to promote the development of science and technology [1–5].

PGMs play an important role in national development and life, but extremely scarce mineral reserves and unevenly distributed mineral resources have become the reasons that restrict their rapid development. According to the data of the United States Geological Survey (USGS), the global PGMs reserves are about 70,000 tons in 2021. The platinum group metal resources in South Africa, Russia, and Zimbabwe account for more than 98% of the total global resources that the distribution is very concentrate [6]. The reserves of PGMs in other countries are very scarce, the USA accounts for about 1.28% of the world, while China only accounts for about 0.58%. Most countries in the world rely on imports of PGMs. The demand for Pt, Pd, and Rh has decreased due to the COVID-19 epidemic, but with the continuous development and progress of social economy, PGMs has shown an overall upward trend [7].

The total consumption of PGMs in China has become the first in the world and has increased year by year since 2009. The consumption of platinum and palladium reached 165 t in 2019, accounting for more than 27% of the world's, which is mainly used in the field of automotive catalysts. Car ownership of China has also ranked first in the world for many years. According to the data of China's National Bureau of Statistics, car ownership of China has reached 310 million by June 2022 [8]. A large number of cars were scrapped when they reached their service life. The recycling volume of scrapped cars was 15 million in China in 2020, including about 10 million spent automobile catalysts. Based on the average 2 g of PGMs per car, China will have 20 tons of PGMs rich automotive catalysts scrapped for recycling every year. Although the automobile catalyst is classified as hazardous waste, the content of platinum group metals in spent automobile catalyst is more than 2000 g/t, which is hundreds of times than platinum group ore. It will not only cause environmental pollution, but also cause a waste of resources if discarded or stacked [9, 10]. The efficient recovery and utilization of waste automobile catalyst will have long-term economic benefits and social value and reduce the contradiction caused by the uneven supply and demand relationship and distribution of Pt.

Nowadays, automotive catalysts are mainly composed of carrier, coating, active components, etc.; the carrier is mainly cordierite, and the coating is  $\gamma$ -Al<sub>2</sub>O<sub>3</sub> which also adds lanthanum, cerium, praseodymium, neodymium, and other rare earth elements to reduce the addition of PGMs. Under the synergistic effect of these PGMs and rare earth, they catalyze and purify automobile exhaust [11]. The methods of recovering platinum, palladium, and rhodium from spent automobile catalysts mainly include pyrometallurgical process, hydrometallurgical process and biohydrometallurgy process, and even microwave enhanced method is used [12–17]. Pyrometallurgical process has become the main process flow for the treatment of spent automobile catalysts with its unique advantages, includes metal collection method and chlorination evaporation method. Its principle is to separate the active components from

other components and enrich them to obtain precious metals. According to the calculation of China's car ownership, the content of PGMs far exceeds China's reserves, and under the background of rapid development of electric vehicles, more and more spent catalyst will be produced. It is great significance to carry out the comprehensive utilization of spent automotive catalyst secondary resources to promote the sustainable development of industries.

This paper summarized the current situation and consumption of PGMs mineral resources in the world and the recovery of spent automotive catalysts, focused on the capture mechanism, recovery and enrichment technology of PGMs, discussed the direction and development of platinum group metal recovery process, so as to provide reference for the comprehensive utilization of secondary PGM resources.

## Current Situation and Consumption of PGM Resources

### *PGM Resources*

The world's PGMs resources and reserves are mainly concentrated in South Africa, Russia, Zimbabwe, the USA, and other countries. South Africa has the most abundant mineral reserves, which accounting for more than 90% of the world.

The output of Pt was about 180 tons in 2021 (Fig. 1), an increase of 8.4% compared with 166 tons in 2020. The output of palladium was 200 tons in 2021 (Fig. 2), a decrease of 7.8% compared with 217 tons in 2020, and the output of platinum and palladium WAS 178 tons and the 213 tons, respectively, in 2019, which maintained at a certain level.

**Fig. 1** World mineral production of platinum in 2021

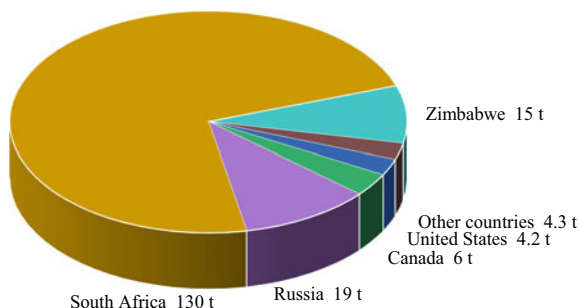
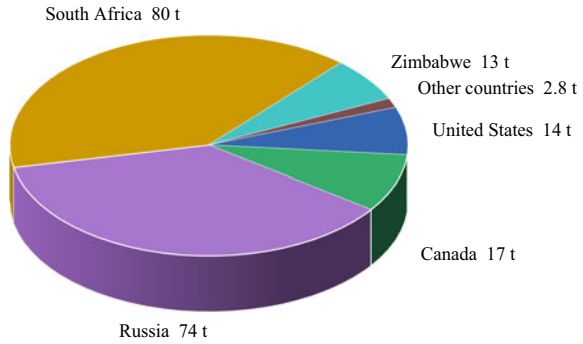


**Fig. 2** World mineral production of palladium in 2021



### Global PGM Supply and Consumption

The global supply of PGMs mainly comes from mineral resources. However, due to the scarcity and high price of PGM resources, the renewable output of secondary resources has also increased year by year. According to the International Platinum Investment Association, Johnson Matthey and other public information show that the secondary resource recovery of Pt accounts for more than 25% of the total output and shows an increasing trend year by year (Fig. 4). The secondary resource recovery of Pt reached 69t in 2019 (Fig. 3). The recovery of Pd accounts for more than 30% of the total output, and the recovery of palladium has been close to 100 t since 2018 (Fig. 3). It can be seen that the output from secondary resource recovery accounts for a large proportion of the global supply of platinum and palladium. PGMs are mainly used in petrochemical, automobile manufacturing, jewelry, and other industries, among which the automotive and chemical industry catalysts are the most widely used which accounting for more than 60%, and the consumption field is relatively concentrated (Fig. 4) [18]. The recycling of PGMs from secondary resources is of strategic significance for the application and development, and the

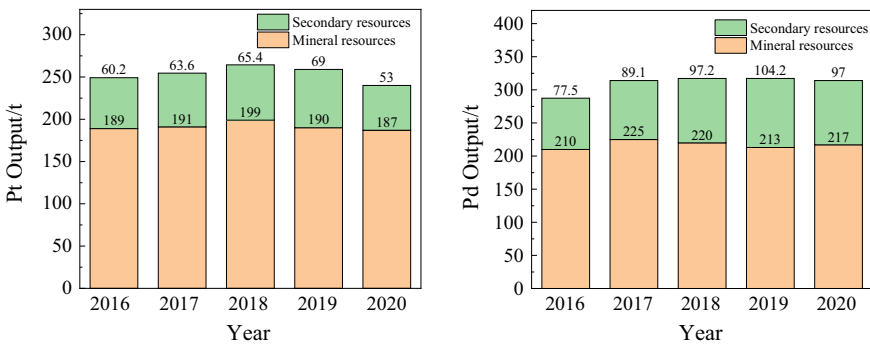


**Fig. 3** Supply of Pt and Pd resources in from 2016 to 2020

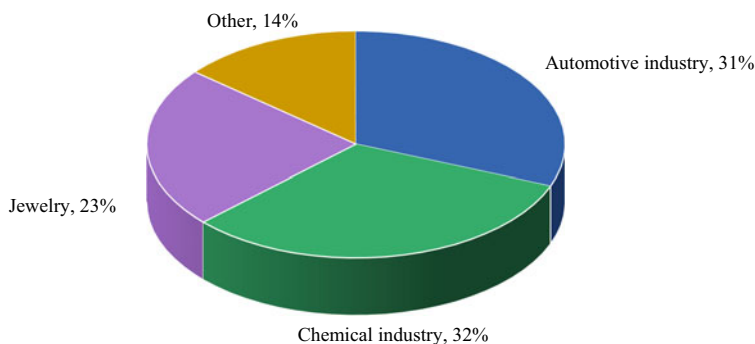


**Fig. 4** Application fields of platinum group metals

field of recycling precious metals today is mainly based on the recycling of spent catalysts.

## **Metal Capture Method**

Metal capture method is one of the most commonly used methods to recover precious metals from spent automobile catalysts by pyrometallurgy. It has the advantages of large treatment capacity, simple process, strong adaptability of materials, and no wastewater. Many companies in the world use this method to recover PGMs from spent catalysts, such as Johnson Matthey (UK), Umicore (Belgium), Sabinmetal (USA), Tanaka precious metals (Japan), Badische anilin und soda Fabrik (Germany), and Sino-platinum Metals (China), which have been used in the production process [14, 19]. Pyrometallurgical recovery process includes plasma smelting method, metal capture method, and chlorination volatilization method. Plasma smelting method also belongs to metal capture method because it uses metal iron to capture PGMs. The overall process of pyrometallurgy generally includes shearing, crushing, grinding, batching, ball pressing, smelting, and enrichment, refining and other processes (Fig. 5), in which Fe, Cu, Pb, and other kinds of collectors are generally used.

## ***Iron Capture Method***

Plasma smelting method uses plasma arc to melt and enrich precious metals. Although smelting has its particularity, it also belongs to the category of metal capture method (Fig. 6). In the process, iron is generally used to capture PGMs. Spent automobile catalyst, reductant, capturing agent, and slag forming agent are added to the furnace at a temperature above 1500 °C, PGMs and Fe have the same crystal structure and similar atomic radius, and Fe has strong affinity for PGMs, Fe

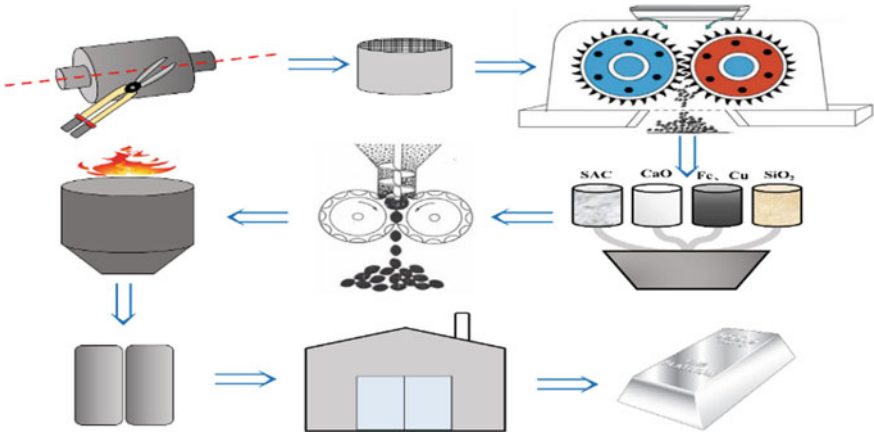


Fig. 5 Overall process steps of metals collection method

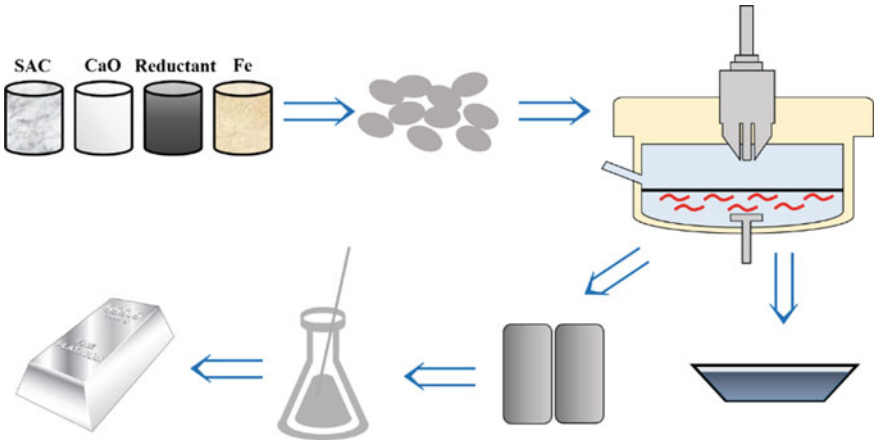


Fig. 6 Process of iron capture and recovery of PGMs by plasma smelting

can form a continuous solid solution with PGMs under high temperature conditions, so that the PGMs in the spent automobile catalyst can quickly enter the metal phase to achieve the effect of separation, and Fe is also a very low-cost collector, which is beneficial to industrial production. By plasma smelting and enrichment, the recoveries of Pt, Pd, and Rh can reach more than 98%, 98%, and 97%, respectively. The total content of PGMs in the slag is about 10 g/t, which has high commercial value.

The capturing mechanism is that PGMs are deposited into the alloy phase due to the influence of the gravity of particles in the recovery process. Metal droplets pass through the slag and precipitate in the metal phase under the action of gravity to form PGMs rich alloys. Benson analyzed the mechanism of extracting PGMs from raw material slag based on the hydrodynamic model and proposed a method that can

estimate the drop rate. It is not a simple gravity effect, but related to the affinity of Fe and PGMs, only when the particles in the catalyst are greater than 200 microns, can be enriched by gravity sedimentation. The capture of PGMs can only be achieved through the adsorption agglomeration sedimentation of Fe. After calculation, it is concluded that the optimal capture diameter of Fe droplets is 0.1–0.3 mm, and the recovery rate of Pt can reach more than 90%. In the experiment, the overall recovery rate of PGMs are more than 95% [20, 21].

Sino-platinum Metals Co., Ltd has introduced a plasma furnace and smelted spent automobile catalyst in China. Li studied  $\text{Fe}_3\text{O}_4$  as a collector to recover PGMs and carried out industrial exploration. The experimental results showed that the comprehensive recovery of PGMs was more than 97%, and the total amount in the slag was 10.9–12.9 g/t [20, 21]. Plasma smelting Fe capture method has the advantages of high metal recovery rate, wide applicability, and high production efficiency, but there are also expensive equipment and large demand for consumables. During the smelting process, silicon dioxide caused by local high temperature is reduced to silicon, making the alloy generate high silicon iron that is difficult to dissolve in acid and alkali, affecting the subsequent separation process.

In order to reduce the temperature and avoid the formation of high silicon iron, Dong studied to recover the secondary resources of PGMs and developed the low-temperature solid-state iron capturing technology. Under the condition of reduction temperature of 1220 °C and reduction time of 6 h, the recovery rates of Pt, Pd, and Rh were 98.6%, 91.7%, and 97.6%, respectively, and the analysis results showed that PGMs were preferentially converted into atomic states or atomic clusters in the process of solid-state reduction. It is bonded with free electrons in the new metal Fe to form a PGMs containing ferroalloy to realize separation [22]. Ding used low melting point flux to realize liquid iron capture at 1300–1400 °C, and the process was carried out at low temperature, avoiding the formation of high silicon iron, and then obtained ferroalloy containing PGMs through the smelting [23].

### ***Copper Capture Method***

The method of capturing PGMs with copper was developed earlier, and the process of recovering with copper capture was first adopted by Umicore Company in Belgium, the recovery rate of PGMs could reached more than 95% [24, 25]. Spent automobile catalyst, copper or copper oxide, reductant, and flux are added to the smelting furnace, usually electric arc furnace to smelting (Fig. 7).

Yamada used copper capture method to recover Pt containing materials, and the total content of PGMs in its smelting slag was reduced to 1 g/t, with obvious enrichment effect [26]. Nippon Company of Japan used copper capture PGMs for industrial production, then obtained copper alloy, the copper alloy could be blown into a concentrate with a content of 30% PGMs through oxygen blowing, and the copper oxide obtained by blowing could be returned to the smelting process for further use. The Serbian Research Institute proposed a process to cast the smelted copper alloy into

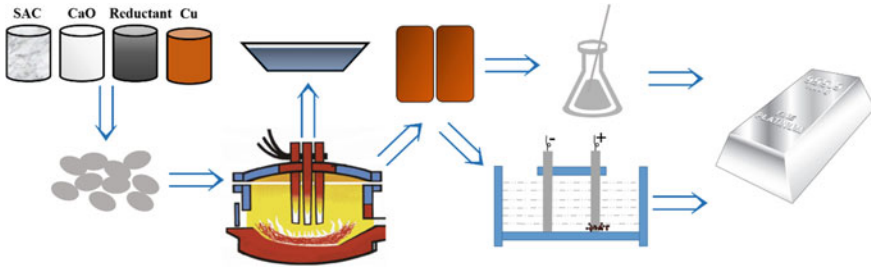


**Fig. 7** Recovery of PGMs by copper capture in electric arc furnace smelting

an anode plate with a content of 1% PGMs. After electrolytic refining, PGMs were deposited in the anode mud for recycling. The cathode copper plate could be reused, and the overall recovery rate of PGMs were as high as 99% [27, 28]. Kolliopoulos studied the recovery behavior of copper in the capture and recovery of spent automobile catalyst. They believed that there were two recovery mechanisms in the capture process: one was the infiltration adsorption process, that is, PGMs particles were adsorbed on the copper droplets, which entered the metal phase through the slag, and the other was to form a solid solution with copper at the bottom in the form of sedimentation through the slag, because the relative atomic mass of platinum is heavy, it has a high sedimentation rate, so it has a high recovery rate [29]. Zhang studied the capturing of Pd by copper alone, and using energy spectrum, X-ray photoelectron spectroscopy, and first principle calculation, it was clear that Pd not only migrated into the metal phase, but also replaced copper atoms into the copper lattice to form a Cu-Pd alloy [30]. The smelting temperature of copper capture is low and the recovery rate of PGMs is high. It can not only be industrialized, but also can be recycled. Using copper as a collector also has great advantages, but the subsequent separation process has limited its development, because the subsequent purification and impurity removal process produces a large amount of wastewater, causing pollution, and the process flow is long, which directly affects economic benefits.

### ***Lead Capture Method***

Lead is an excellent collector of PGMs. Developed countries began to use lead to capture and recover PGMs as early as 1980. This is the oldest pyrometallurgical method for treating spent automobile catalysts and detecting PGMs. Lead capture is generally used in electric furnace. PGMs are separated from the carrier to obtain crude lead containing PGMs at high temperature, and then lead is oxidized in ash blowing furnace or converter to obtain PGMs enrichment (Fig. 8). Compennolle used the spent automobile catalyst after crushing, added lead oxide and other fluxes, smelted at 1100 °C for 2 h, and the lead button obtained after smelting was soot blown at 1000 °C, resulting in the volatilization of some lead [31]. In order to reduce

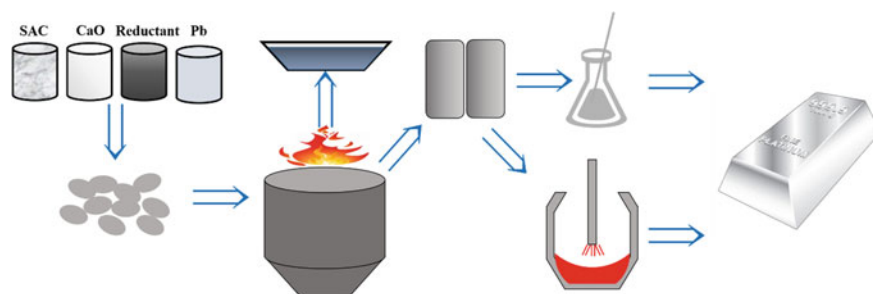


**Fig. 8** Recovery of PGMs by lead capture in electric furnace smelting

the loss of lead buckle in the process of soot blowing, gold and silver can be used as a protective agent to reduce the loss and increase the recovery rate. For example, Zhu used silver as a protective agent to recover Pt and Pd, and the recovery rate could reach more than 92.5% [32, 33]. Ni used lead assays to capture PGMs in ores at 1080–1100 °C, which could enrich Pt, Pd, Rh, Ir in lead particles [34].

### ***Other Capture Method***

Experts and scholars have also carried out a variety of research methods, such as using metal Bi for capture, or using waste printed circuit boards for capture, and even using cyanide tailings and other wastes for capture. Zhang used metal Bi as the collector. Under the condition of smelting at 1100 °C for 10 min, the recoveries of Pt, Pd, and Rh were 95.02, 98.90, and 97.00%, respectively. PGMs preferentially entered the Bi phase, reducing the free energy of the system and formed metal droplets to converge and settled into the metal phase [35]. The waste circuit board was used as the capture agent, the carrier material was used as the slag-forming agent, and the melting could be carried out by adding the flux and reducing agent. After melting, the automobile catalyst and the gold, Pt, Pd, Rh in the waste circuit board could be comprehensively recovered, which were enriched in the Cu-Sn alloy. The PGMs had a high distribution ratio at the slag gold interface. This process was simple, and the spent automobile catalyst and waste circuit board could also be comprehensively recovered to achieve the purpose of treating waste with waste. However, the volatilization of toxic and harmful gases in the process limits its development [36, 37]. Liu provided an economic and environmental protection technology for treating spent automobile catalyst with cyanide tailings, in which Fe collector is produced by carbothermal reduction process, the melted PGMs enter the alloy phase, while Pb, Cr and other elements were fixed in the slag, and the process cost was low, and had high trapping efficiency [38].



## Conclusion and Prospect

The spent automobile catalyst will be accompanied by the arrival of the service life which increases year by year. As an important secondary resource, the efficient and comprehensive utilization of waste automobile catalysts is an important way to solve the contradiction between supply and demand of PGMs and can bring huge economic value and environmental benefits. In view of the current research progress of pyrometallurgy recovery technology, it has the effects of large processing capacity, high efficiency, high capture rate, and easy production, but there are still some problems, such as high temperature, high energy consumption and low recovery rate for specific metals. On the whole, Fe capture has better economic benefits. Although the technology of pyrometallurgy recovery of PGMs has made great progress in general, there are still many problems, and if the recovery rate, efficiency, or energy consumption can be changed by changing the process route, or reducing the temperature with appropriate flux, changing the type of collector or slag composition, it will provide a new technical idea for the recovery of PGMs from spent automobile catalysts and realize the sustainable development of platinum group metal resources.

## References

1. Chaudhari N, Joo J, Kwon H et al (2018) Nanodendrites of platinum-group metals for electrocatalytic applications. *Nano Res* 11(12):6111–6140
2. Dong H, Zhao J, Chen J et al (2015) Recovery of platinum group metals from spent catalysts: a review. *Int J Miner Process* 145:108–113
3. Dimitrijevi M, Mili S, Slaana A et al (2014) Recovery of platinum-group metals (PGMs) from spent automotive catalysts: Part I: the primary and secondary sources of PGMs and their use. *Reciklaža i održivi razvoj* 7:9–21
4. Dimitrijevi M, Mili S, Slaana A et al (2015) Recovery of platinum-group metals (PGMs) from spent automotive catalysts: Part II: automotive catalysts: Structures and principle of operation. *Reciklaža i održivi razvoj* 8(1):1–11
5. Demarco J, Cadore J, Veit H, et al (2020) Leaching of platinum group metals from spent automotive catalysts using organic acids. *Min Eng* 159:106634
6. United States Geological Survey. Mineral commodity summaries 2022. Available online: <https://pubs.er.usgs.gov/publication/mcs2022>. Accessed on 31 January 2022
7. Zhang F, Lu S (2021) Research progress on recovery of platinum group metals from spent automotive catalysts supported on cordierite. *Rare Metal Mater Eng* 50(9):3388–3398
8. China's National Bureau (2022) Available online: [https://www.cqn.com.cn/auto/content/2022-07/19/content\\_8843963.htm](https://www.cqn.com.cn/auto/content/2022-07/19/content_8843963.htm). Accessed on 19 July 2022
9. Lloyd S, Lave L, Matthews H (2005) Life cycle benefits of using nanotechnology to stabilize platinum-group metal particles in automotive catalysts. *Environ Sci Technol* 39(5):1384–1392
10. Fornalczyk A, Golak S, Saternus M (2013) Model of Infiltration of spent automotive catalysts by molten metal in process of platinum metals recovery. *Math Probl Eng* 76(13):255–60
11. Li L, Zhang N, Wu R et al (2020) comparative study of moisture-treated Pd@CeO<sub>2</sub>/Al<sub>2</sub>O<sub>3</sub> and Pd/CeO<sub>2</sub>/Al<sub>2</sub>O<sub>3</sub> catalysts for automobile exhaust emission reactions: effect of core-shell interface. *ACS Appl Mater Interfaces* 12(9):10350–10358
12. Saitoh N, Nomura T, Konishi Y (2017) Biotechnological recovery of platinum group metals from leachates of spent automotive catalysts. In: *Rare metal technology 2017*, pp 129–135

13. Karim S, Ting Y (2021) Recycling pathways for platinum group metals from spent automotive catalyst: a review on conventional approaches and bio-processes. *Resour Conserv Recycl* 170:105588
14. Jha M, Lee J, Kim M et al (2013) Hydrometallurgical recovery/recycling of platinum by the leaching of spent catalysts: a review. *Hydrometallurgy* 133:23–32
15. Nakahiro Y (2009) Recent development on recycling technology of platinum group metals from spent catalysts. *Resour Process* 40(4):161–165
16. Peng Z, Li Z, Lin X et al (2018) Thermodynamic analysis of smelting of spent catalysts for recovery of platinum group metals. In: 9th International Symposium on high-temperature metallurgical processing, pp 215–223
17. Liu C, Sun S, Zhu X, et al (2020) Research, metals smelting-collection method for recycling of platinum group metals from waste catalysts: a mini review. *Waste Manage Res* 39(1):0734242X2096979
18. Pietrelli L, Fontana D (2013) Automotive spent catalysts treatment and platinum recovery. *Waste Manage* 2(2):222–232
19. Peng Z, Li Z, Lin X et al (2017) Recovery of platinum group metals from spent catalysts. *Int J Miner Process* 69(9):1553–1562
20. He X, Li Y, Wu X et al (2016) Study on the process of enrichment platinum group metals by plasma melting technology. *Precious Met* 37(1):1–5
21. He X, Wang H, Wu X et al (2012) Study on the recovery of rhodium from spent organic rhodium catalysts of acetic acid industry using pyrometallurgical process. *Precious Met* 33(A01):24–27
22. Dong H, Zhao J, Chen J et al (2014) Recovery of platinum group metal secondary resource by iron trapping method based on solid state. *Chin J Nonferrous Met* 24(10):2692–2697
23. Ding Y, Zheng H, Zhang S et al (2020) Highly efficient recovery of platinum, palladium, and rhodium from spent automotive catalysts via iron melting collection. *Resour Conserv Recycl* 155:104644
24. Hagelüken C (2006) Recycling of electronic scrap at Umicore precious met refining. *Acta Metallurgica Slovaca* 12:111–120
25. Hoffmann J (1988) Recovery of platinum-group metals from gabbroic rocks metals from auto catalysts. *JOM* 40(6):40–44
26. Yamada K, Seiko K, Ezawa N, et al (2003) Method and device for recovering platinum group elements. CN. Patent 200710153756.X. 4 August 2003
27. Fornalczyk A, Saternus M (2009) Removal of platinum group metals from the used auto catalytic converter. *Metallurgija* 48(2):133–136
28. Agnieszka F, Mariola S, Agnieszka F et al (2013) Vapour treatment method against other pyro-and hydrometallurgical processes applied to recover platinum from used auto catalytic converters. *Acta Metall Sin* 26(3):247–256
29. Kolliopoulos G, Balomenos E, Giannopoulou I, et al (2014) Behavior of platinum group metals during their pyrometallurgical recovery from spent automotive catalysts. *Open Access Libr J* 1(e736)
30. Zhang L, Song Q, Liu Y et al (2019) Novel approach for recovery of palladium in spent catalyst from automobile by a capture technology of eutectic copper. *J Clean Prod* 239:118093
31. Compennolle S, Wambeke D, De Raedt I et al (2011) Direct determination of Pd, Pt and Rh in fire assay lead buttons by laser ablation-ICP-OES: automotive exhaust catalysts as an example. *J Anal At Spectrom* 26(8):1679–1684
32. Zhu K, Mao J (2017) Determination of platinum and palladium in geochemical samples by inductively coupled plasma mass spectrometry with minified lead fire assay. *Precious Met* 38(3):61–65
33. Mao Y, Zhu K, Zou J (2017) Determination of platinum and palladium in geochemical samples by low Pb fire assay enrichment-inductively coupled plasma mass spectrometry. *Gold* 38(3):79–82
34. Ni W, Meng Y, Yao M, et al, Determination of platinum, palladium, rhodium and iridium in mineral samples by Zeeman graphite furnace atomic absorption spectrometry after the preconcentration with lead fire assaying. *Metall Anal* 30(3):23–26

35. Zhang F, Zhang G, Xu L, et al, Enrichment of Pd, Pt and Rh from spent automotive catalyst by pyrometallurgical bismuth capture. *Chin J Nonferrous Met* 30(9):2162–2170
36. Kim B, Lee J, Seo S et al (2004) A process for extracting precious metals from spent printed circuit boards and automobile catalysts. *JOM* 56(12):55–58
37. Kim B, Lee J, Jeong J et al (2013) A novel process for extracting precious metals from spent mobile phone PCBs and automobile catalysts. *Express Regul Article* 54(6):1045–1048
38. Liu C, Sun S, Tu G et al (2021) Co-treatment of spent automotive catalyst and cyanide tailing via vitrification and smelting-collection process for platinum group metals recovery. *J Environ Chem Eng* 9(5):105823

# Eutectic Freeze Crystallization for Recovery of Cobalt Sulfate in the Recycling of Li-Ion Batteries



Yiqian Ma, Amanda Sjögren, Michael Svärd, Xiong Xiao, James Gardner, Richard T. Olsson, and Kerstin Forsberg

**Abstract** Crystallization of cobalt sulfate within a typical hydrometallurgical process for the recycling of Ni-Mn-Co oxide or Ni-Co-Al oxide Li-ion batteries has been investigated. The cobalt sulfate salt was obtained by eutectic freeze crystallization (EFC) from a synthetic acidic cobalt strip liquor after solvent extraction. The ternary phase diagram of  $\text{CoSO}_4\text{-H}_2\text{SO}_4\text{-H}_2\text{O}$  was first established by the mixed-solvent electrolyte (MSE) model to predict and reveal the changes in the system during the freezing process and to assess the conditions required for EFC. Batch EFC experiments were then conducted for the cobalt strip liquor, which contained a low concentration of impurities. It is shown that with suitable control of supersaturation, seeding, and stirring, pure ice and salt crystals can be recovered as separate phases at the eutectic temperatures, with the crystalline salts in the form of a heptahydrate. The crystallization process can be described using the ternary phase diagram, but with certain deviations. The deviations might be related to insufficient data at the low temperatures in the MSE model and acid entrapment in crystals during the crystallization process. Finally, the performance of the EFC process has been compared to that of an evaporative crystallization (EC) using the same strip liquor. It was found that the  $\text{CoSO}_4\cdot 7\text{H}_2\text{O}$  product obtained by EFC was of slightly higher quality considering purity and crystal shape compared to that from EC.

**Keywords** Eutectic freeze crystallization ·  $\text{CoSO}_4$  · Li-ion batteries · Hydrometallurgy · Recycling

---

Y. Ma (✉) · A. Sjögren · M. Svärd · K. Forsberg  
Department of Chemical Engineering, KTH Royal Institute of Technology, Teknikringen 42,  
11428 Stockholm, Sweden  
e-mail: [yiqianm@kth.se](mailto:yiqianm@kth.se)

X. Xiao · R. T. Olsson  
Department of Fiber and Polymer Technology, KTH Royal Institute of Technology, Teknikringen  
56, 11428 Stockholm, Sweden

J. Gardner  
Department of Chemistry, KTH Royal Institute of Technology, Teknikringen 30, 11428  
Stockholm, Sweden

## Introduction

The recycling of Li-ion batteries (LiBs) is essential from an economic and environmental perspective. After mechanical and thermal treatment of spent Li-ion batteries, hydrometallurgy is considered the best way to recover the most valuable metals Li, Ni, Co, and Mn from the cathode material due to high recovery efficiency, low energy consumption, and minimal gas emission [1, 2]. Various acids have been proposed for the leaching step in hydrometallurgical processing; yet,  $\text{H}_2\text{SO}_4$  is the most used, owing to the advantages of low cost and high leaching efficiency at moderate concentration [3]. After obtaining the acid leach solution, various processes, usually including chemical precipitation and solvent extraction methods, have been developed for the separation and purification stage [4]. Precipitation removes Fe, Al, and Cu from the acid leach solution, while solvent extraction is selective for separation and recovery of the remaining metals in different fractions [5].

Solvent extraction using Cyanex 272, Cyanex 302, PC-88A, TOA, and D2EHPA for the fractionation of Ni, Co, and Li from acidic solution in the recycling of LiBs has been reported in the literature [6]. These extractants can extract  $\text{Co}^{2+}$  over  $\text{Ni}^{2+}$  and  $\text{Li}^+$  due to their excellent Co/Ni and Co/Li selectivity. After the extraction step, Co is usually stripped using sulfuric acid and recovered as  $\text{CoSO}_4 \cdot 7\text{H}_2\text{O}$  by crystallization [7]. For example, Kang et al. [8] reported  $\text{CoSO}_4$  recovery from the spent LiBs using precipitation, solvent extraction, and crystallization. Cyanex 272 was used to selectively extract Co from the solution after the precipitation of Cu, Fe, and Al. Stripping of the loaded organic phase with 2 M  $\text{H}_2\text{SO}_4$  produced a solution of 96 g/L Co. Finally, pure pigment grade  $\text{CoSO}_4$  was obtained by evaporative crystallization of the Co-enriched solution.

For the isolation of salts from an aqueous salt stream, eutectic freeze crystallization (EFC) is an alternative method. This technique is based on cooling the salt solution down to the eutectic point of the respective system, where ice and salt crystals are formed simultaneously [9]. Eutectic freeze crystallization is strongly preferred to evaporative crystallization, as it requires less energy. In addition, eutectic freeze crystallization has an advantage in treating corrosive streams due to the low temperatures employed [10]; thus, it is very suitable for salt recovery from acidic strip liquors. EFC is effective for the desalination of brines generated from reverse osmosis, and EFC has been tested for the recovery of metal salts in hydrometallurgy [11].

The present study focuses on the  $\text{CoSO}_4$  recovery from a strip liquor in the recycling of LiBs. Binary and ternary phase diagrams of the  $\text{CoSO}_4\text{-H}_2\text{SO}_4\text{-H}_2\text{O}$  system have been established by employing the mixed-solvent electrolyte (MSE) model. Batch crystallization experiments have then been performed to recover  $\text{CoSO}_4$  from the acidic strip liquor and to evaluate the EFC process. Finally, EFC for  $\text{CoSO}_4$  recovery is further assessed by comparing it with EC using the same feed solution.

## Materials and Methods

### *Development of Phase Diagrams Using the MSE Model*

Phase diagrams are used to show the thermodynamic equilibrium behavior of the  $\text{CoSO}_4\text{-H}_2\text{SO}_4\text{-H}_2\text{O}$  system in this study. The MSE model, embedded in the OLI Stream Analyzer software [12], was employed to develop a binary phase diagram of  $\text{CoSO}_4\text{-0.5 mol/kg H}_2\text{SO}_4$  and ternary phase diagram of  $\text{CoSO}_4\text{-H}_2\text{SO}_4\text{-H}_2\text{O}$  which includes the eutectic (or cotectic) curves of ice and salt crystals.

### *Feed Solution and Analysis*

Analytical grade reagents  $\text{H}_2\text{SO}_4$ ,  $\text{CoSO}_4\cdot 7\text{H}_2\text{O}$ ,  $\text{MnSO}_4\cdot \text{H}_2\text{O}$ ,  $\text{Li}_2\text{CO}_3$ ,  $\text{NiSO}_4\cdot 7\text{H}_2\text{O}$ ,  $\text{Fe}_2(\text{SO}_4)_3$ ,  $\text{Al}_2(\text{SO}_4)_3$ ,  $\text{CaSO}_4$ ,  $\text{CuSO}_4\cdot 5\text{H}_2\text{O}$ , and  $\text{Na}_2\text{SO}_4$  were used to prepare an acidic strip liquor. The solution was prepared using deionized water. Table 1 shows the composition of the synthetic strip liquor. After batch eutectic freeze crystallization or evaporative crystallization experiment and filtration, cobalt sulfate hydrates could be obtained. Optical microscopy was used to observe the color and shape of the resulting crystals. The chemical phases of the crystals were determined by X-ray powder diffraction (XRD). Inductively coupled plasma-optical emission spectrometry (ICP-OES) was used to measure the total concentration of elements present in solution samples. The composition of the crystals was determined after complete dissolution in water.

### *Eutectic Freeze Crystallization (EFC) Experiments*

EFC experiments were performed in a jacketed 250 mL glass vessel equipped with a mechanical stirrer. A schematic overview of the setup is shown in Fig. 1. A 30-vol% ethylene glycol/water solution was used to indirectly cool the crystallizer, with coolant cooled and circulated through the jacket of the crystallizer by a cryostatic water bath (FP50-HP refrigerated/heating circulator, Julabo, Allentown, PA, USA). A temperature monitor (KST 5-inch Paperless Recorder, Keshun Instrument Co. Ltd, Ningbo, China) was connected to PT-100 sensors (Omega Engineering Inc., Norwalk, CT, USA) with an accuracy of 0.1 °C, and used to record temperature data

**Table 1** Composition of a cobalt strip liquor

Metal (mg/L)	Co	Ni	Mn	Li	Cu	Na	Fe	Al	Ca	$\text{H}_2\text{SO}_4$
Synthetic strip liquor	96,000	2	22	4	1	11	2	4	4	36,300

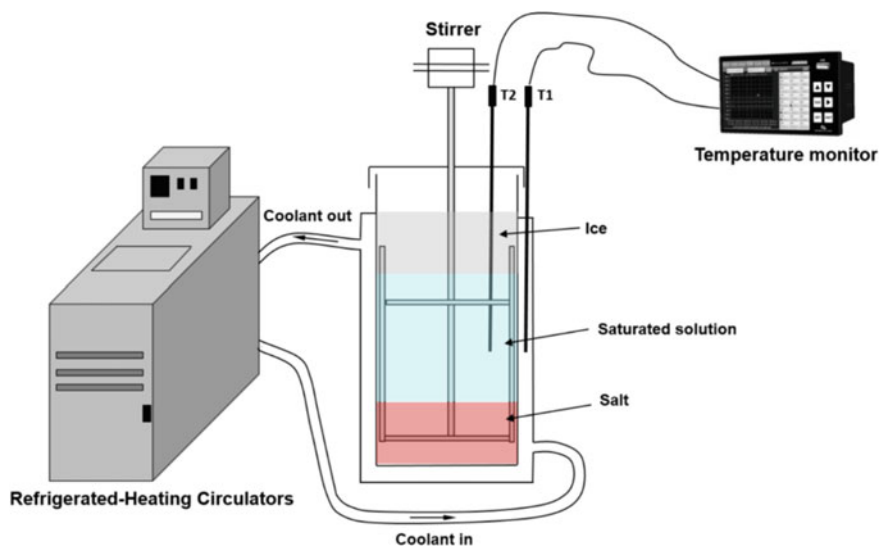


Fig. 1 Experimental setup for eutectic freeze crystallization

every 30 s. One sensor was used to measure the crystallizer temperature, while the other sensor measured the coolant temperature. For each batch experiment, 200 g synthetic strip solution was used. The agitator speed was kept at 50 rpm. After EFC of ice and salt, filtration was conducted to obtain the salt crystals.

## Results and Discussion

### *Phase Diagrams*

Binary phase diagrams of  $\text{CoSO}_4$  dissolved in pure  $\text{H}_2\text{O}$  and aqueous 0.5 mol/kg  $\text{H}_2\text{SO}_4$  solution over the temperature range  $-20$  to  $60$  °C are presented in Fig. 2. The results show that  $\text{CoSO}_4 \cdot 7\text{H}_2\text{O}$  is the stable crystalline phase at low temperature.  $E_1$  and  $E_2$  are the predicted eutectic points in  $\text{H}_2\text{O}$  and 0.5 mol/kg  $\text{H}_2\text{SO}_4$  solution, respectively. Both the eutectic temperature and concentration of the  $\text{CoSO}_4$ -0.5 mol/kg  $\text{H}_2\text{SO}_4$  system are below those of the  $\text{CoSO}_4$ - $\text{H}_2\text{O}$  system.

Figure 3 is the calculated ternary phase diagram of  $\text{CoSO}_4$ - $\text{H}_2\text{SO}_4$ - $\text{H}_2\text{O}$  with simulated lines. In the ternary phase diagram, solid line EP in Fig. 3 represents the eutectic solubility line for  $\text{CoSO}_4 \cdot 7\text{H}_2\text{O}$  and ice.

For the EFC of  $\text{CoSO}_4$  in dilute  $\text{H}_2\text{SO}_4$  solution, the composition and temperature of the eutectic points gradually shift along the solubility eutectic line after the solution has reached the eutectic condition.

**Fig. 2** Calculated binary phase diagram of  $\text{CoSO}_4\text{-H}_2\text{O}$  and  $\text{CoSO}_4\text{-0.5 mol/kg H}_2\text{SO}_4$  systems

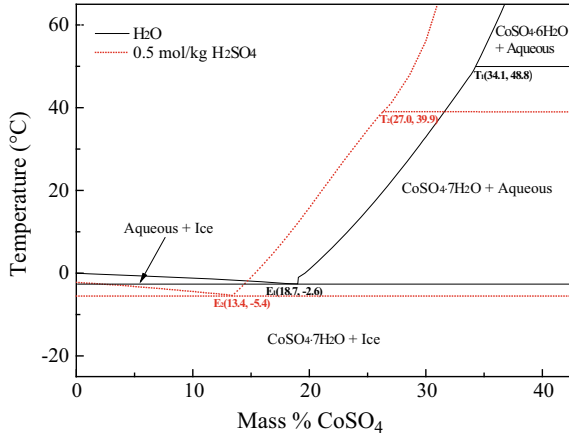
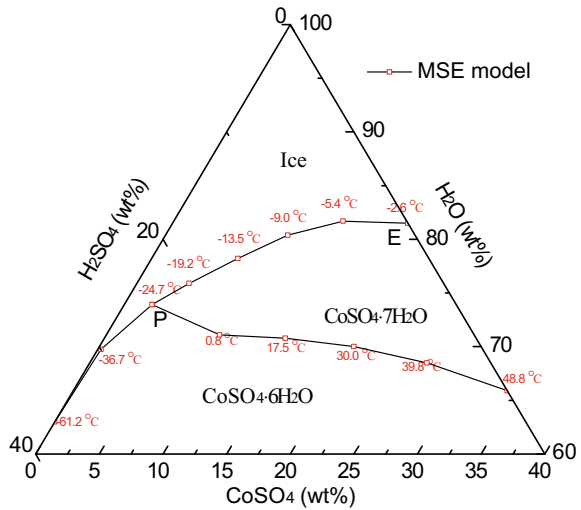


**Fig. 3** Calculated ternary phase diagram of  $\text{CoSO}_4\text{-H}_2\text{SO}_4\text{-H}_2\text{O}$  from MSE model



**Behavior of Solution Temperature and Composition During EFC**

From several EFC batch experiments of the synthetic solution, the first eutectic temperature was observed at  $-4.7^\circ\text{C}$ , at which simultaneous crystallization of ice and salt commenced. However, as shown in Fig. 4, as the solution entered eutectic conditions, the eutectic temperature continued to slowly decrease to  $-6.8^\circ\text{C}$  for a period of 70 min.

The decrease in temperature can be explained by the increasing concentration of sulfuric acid in the remaining mother liquor, caused by the crystallization of ice and



**Fig. 4** Temperature curve obtained after EFC of the synthetic acidic strip solution

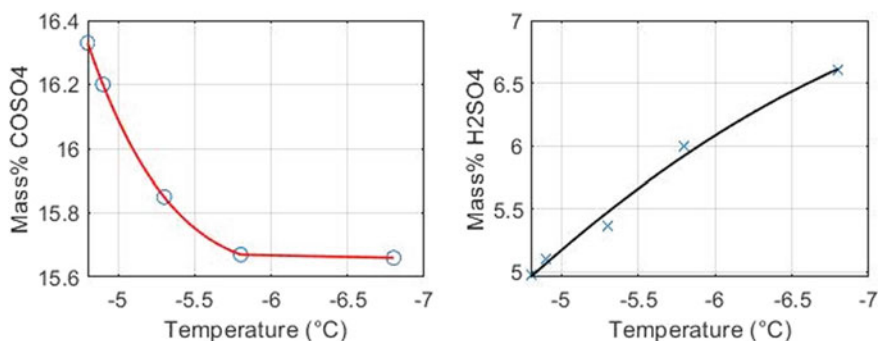
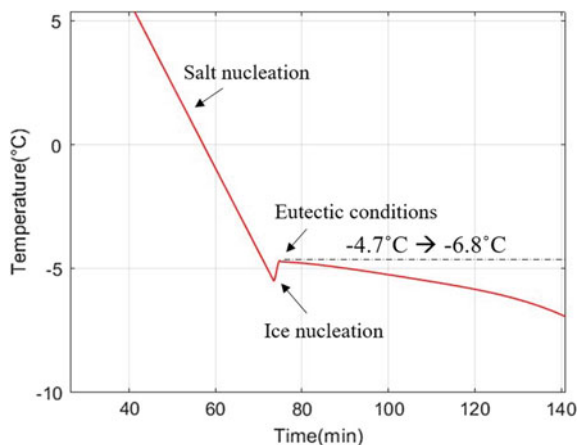


**Fig. 5** Evolution of CoSO<sub>4</sub> and H<sub>2</sub>SO<sub>4</sub> concentrations at the eutectic conditions

CoSO<sub>4</sub> · 7H<sub>2</sub>O. Figure 5 illustrates the composition of the mother liquor at eutectic conditions; each marked data corresponds to a collected sample.

### *The Comparison of EFC and Evaporative Crystallization (EC)*

XRD analysis results (Figs. 6 and 7) confirmed that the crystals obtained from both EFC and EC were in the heptahydrate form.

For the batch experiments, the crystallization yields of the EFC and EC were controlled at comparable levels of ~ 55% and ~ 47%, respectively. Tables 2 and 3 list the composition of crystals obtained in the EFC and EC batch experiments, respectively. As seen, the purity level of the CoSO<sub>4</sub> · 7H<sub>2</sub>O product was comparable for EC and EFC. the Na and Fe content is overall higher in the crystals from EC than in the crystals from EFC. This can be explained by the evaporation of water; the

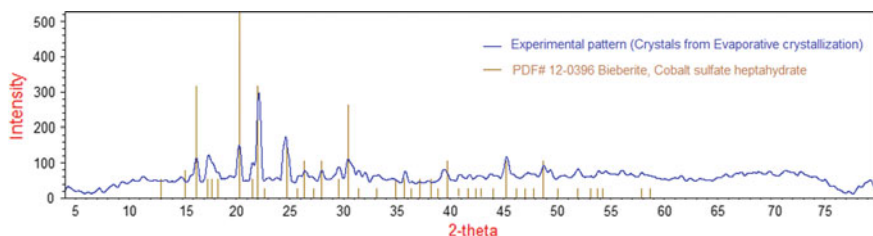


**Fig. 6** XRD pattern of crystals from EC (blue), compared to a standard card of  $\text{CoSO}_4 \cdot 7\text{H}_2\text{O}$  (orange)

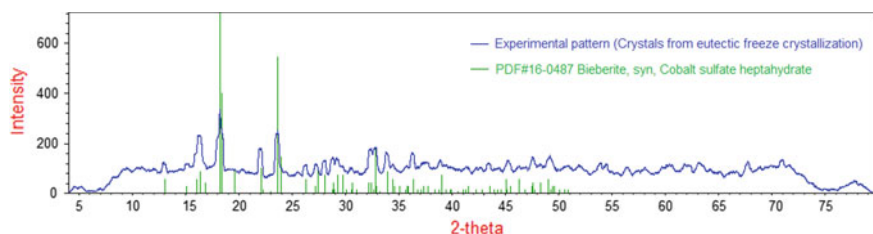


**Fig.7** XRD pattern of crystals from EFC (blue), compared to a standard card of  $\text{CoSO}_4 \cdot 7\text{H}_2\text{O}$  (green)

**Table 2** Composition of salt crystals from EFC

Metal in salt crystals	Co (wt%)	Ni (ppm)	Mn (ppm)	Li (ppm)	Cu (ppm)	Na (ppm)	Fe (ppm)	Al (ppm)	Ca (ppm)
Unwashed crystals	21.1	87	16	0.7	5.9	2.8	7.2	0.2	0
Washed with cold water	21.1	82	14	0.5	5.5	0.7	6.4	0	0

**Table 3** Composition of salt crystals from EC

Metal in salt crystals	Co (wt%)	Ni (ppm)	Mn (ppm)	Li (ppm)	Cu (ppm)	Na (ppm)	Fe (ppm)	Al (ppm)	Ca (ppm)
Unwashed crystals	21.1	94	24	2.1	5.3	14	18	1.8	1.3
Washed with cold water	21.1	88	18	0.7	5.2	3	17	0.2	0

remaining mother liquor becomes more concentrated; consequently, the impurities will get trapped more frequently in the salt crystals while part of the impurities might be trapped in the ice for EFC. The mechanisms and extent of incorporation of impurities in the salt and ice phases requires further investigation.

The morphology of the crystals from EFC and EC in Fig. 8 differs significantly. The EFC crystals have a more regular and spherical surface compared to the irregular EC crystals. The largest crystals from EFC batch experiments have a diameter of 30  $\mu\text{m}$ , while the smallest have a diameter of 10  $\mu\text{m}$ . The determination of the size

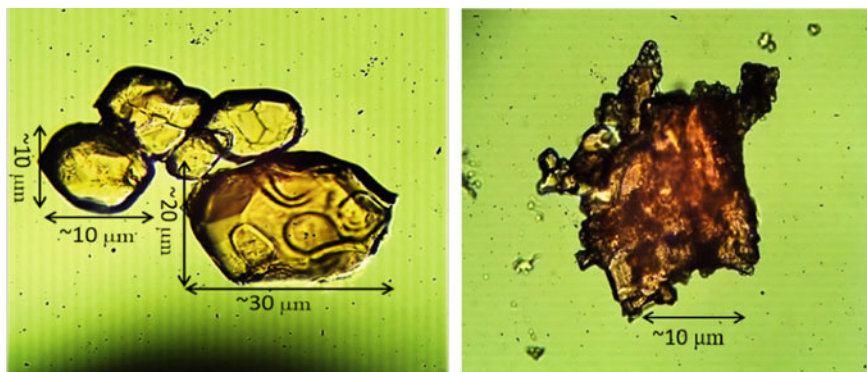


**Fig. 8** Crystals of  $\text{CoSO}_4 \cdot 7\text{H}_2\text{O}$  from EFC (left) and EC (right) experiments

of the EC crystals was difficult considering the irregular structure. The rapid crystal growth at room temperature can explain the disorganized shape of these crystals. It can be stated that batch experiments of EFC resulted in more desirable crystals than those from EC.

## Conclusion

The predicted phase diagrams of  $\text{CoSO}_4\text{--H}_2\text{SO}_4\text{--H}_2\text{O}$  system indicate that  $\text{CoSO}_4 \cdot 7\text{H}_2\text{O}$  can crystallize along with ice from the strip liquor using EFC, and the binary eutectic temperature decreases as the concentration of acid increases. The crystals of  $\text{CoSO}_4 \cdot 7\text{H}_2\text{O}$  were then obtained successfully using EFC with suitable conditions. The crystallization process can be described using the ternary phase diagram, but with certain deviations. After washing, the impurity content of the  $\text{CoSO}_4 \cdot 7\text{H}_2\text{O}$  obtained using EFC is very low.

**Acknowledgements** This study was carried out within the Processes for Efficient Recycling of Lithium Ion Batteries (PERLI) project. The authors are indebted to the Swedish Energy Agency for financial support (grant number 48228-1).

## References

1. Neumann J, Petranikova M, Meeus M, Gamarra JD, Younesi R, Winter M, Nowak S (2022) Recycling of lithium-ion batteries—current state of the art, circular economy, and next generation recycling. *Adv Energy Mater* 12(17):2102917
2. Ma Y, Svärd M, Xiao X, Gardner J, Olsson RT, Forsberg K (2020) Precipitation and crystallization used in the production of metal salts for li-ion battery materials: a review. *Metals* 10(12):1609

3. Tao R, Xing P, Li H, Sun Z, Wu Y (2022) Recovery of spent LiCoO<sub>2</sub> lithium-ion battery via environmentally friendly pyrolysis and hydrometallurgical leaching. *Resour Conserv Recycl* 176:105921
4. Zhang K, Liang H, Zhong X, Cao H, Wang R, Liu Z (2022) Recovery of metals from sulfate leach solutions of spent ternary lithium-ion batteries by precipitation with phosphate and solvent extraction with P507. *Hydrometallurgy* 210:105861
5. Latini D, Vaccari M, Lagnoni M, Orefice M, Mathieux F, Huisman J, Tognotti L, Bertei A (2022) A comprehensive review and classification of unit operations with assessment of outputs quality in lithium-ion battery recycling. *J Power Sources* 546:231979
6. Lei S, Sun W, Yang Y (2022) Solvent extraction for recycling of spent lithium-ion batteries. *J Hazard Mater* 424:127654
7. Hu J, Zhang J, Li H, Chen Y, Wang C (2017) A promising approach for the recovery of high value-added metals from spent lithium-ion batteries. *J Power Sources* 351:192–199
8. Kang J, Senanayake G, Sohn J, Shin S (2010) Recovery of cobalt sulfate from spent lithium ion batteries by reductive leaching and solvent extraction with Cyanex 272. *Hydrometallurgy* 100:168–171
9. Ma Y, Svärd M, Xiao X, Sahadevan SA, Gardner J, Olsson RT, Forsberg K (2022) Eutectic freeze crystallization for recovery of NiSO<sub>4</sub> and CoSO<sub>4</sub> hydrates from sulfate solutions. *Sep Purif Technol* 286:120308
10. Lu H, Wang J, Wang T, Wang N, Bao Y, Hao H (2017) Crystallization techniques in wastewater treatment: an overview of applications. *Chemosphere* 173:474–484
11. Lu X (2014) Novel applications of eutectic freeze crystallization. PhD Thesis, Technische Universiteit Delft, ISBN: 9789461863416
12. OLI Systems, Inc (2020) OLI Stream Analyser [Computer software], Version 10.0.2.1., Morris Plains, New Jersey, USA

# Studies on the Hydrometallurgical Recovery of Metals from Used and End of Life PCBs



Om Shankar Dinkar, Rekha Panda, Pankaj Kumar Choubey,  
Manis Kumar Jha, and Balram Ambade

**Abstract** In this era of modernisation, the demand for metals is increasing and the limitation of primary resources has created a huge gap between demand and supply. In this connection, an attempt has been made to recover Pb, Sn, and Cu from waste PCBs of computer hard disc using pre-treatment followed by hydrometallurgical techniques. In PCBs, encapsulation of epoxy sheets hinders dissolution of metals. Therefore, initially PCBs were depopulated, and then, using pre-treatment techniques, i.e. size reduction and wet gravity separation, mix metal concentrate was obtained. This obtained concentrate was used further for developing various metal recovery processes and optimisation of various process parameters. The experimental results indicate ~ 99% recovery of metals using suitable leachates. The obtained data is presented and validated to develop a process flow-sheet. This work will be productive for the researchers, students, and industrialists working in this area.

**Keywords** Hydrometallurgy · Leaching · PCBs · Copper · Lead · Tin · Separation

## Introduction

Rapid technological advancement, especially in the electronics industry, has accelerated the manufacturing of new advanced sophisticated electronic gadgets for the sale in market with continuous replacement of the older ones. It has reduced the life span of electronic gadgets and resulted in generation of huge amount of waste electrical and electronic equipments (WEEEs) [1–4]. The worldwide generation of WEEEs is 20–50 million tons per year which is three times faster in comparison with other wastes [4, 5]. As per global e-waste monitor (2020), 52.7 million tons of e-waste was generated in 2015, which is expected to reach 74.4 million tons by

---

O. S. Dinkar · R. Panda · P. K. Choubey · M. K. Jha (✉)  
Metal Extraction and Recycling Division, CSIR-National Metallurgical Laboratory,  
Jamshedpur 831007, India  
e-mail: [mkjha@nmlindia.org](mailto:mkjha@nmlindia.org)

O. S. Dinkar · B. Ambade  
Department of Chemistry, National Institute of Technology, Jamshedpur 831014, India

the end of 2030. These WEEEs constitute household appliances, IT equipments, telecom devices, medical devices, etc. In all these EEEs, PCBs are the important and common component, which is made up of metals, plastics, and ceramics [1, 6, 7]. The metal forms 40% of the total weight of PCBs. PCBs form 3% (wt.) out of total WEEEs produced [3, 6, 8]. The waste PCBs (WPCBs) possess varieties of metals and materials, viz. aluminum (Al), copper (Cu), iron (Fe), nickel (Ni), lead (Pb), tin (Sn), gold (Au), silver (Ag), platinum (Pt), palladium (Pd), glass fiber, and epoxy resin [3, 9, 10] based on application or type.

In this era of metals crises, WPCBs/WEEEs have been considered as alternative resources to fulfill the demand and supply of metals up to certain extent. Development of feasible recycling processes to recover metals from WPCBs will not only decrease the environmental pollution but also conserve the natural resources and lead towards sustainable development.

In this regard, PCBs of various sources have been reported for the recovery of metals. Kumar et al., 2014, reported about 90% and 65% of total metal recovery from PCBs of VC and DVD by froth flotation and pneumatic separation [11]. Arshadi et al., 2018, reported content evaluation of computer PCBs, central processing units (CPUs) PCBs, TV PCBs, fax machine PCBs, and copy machine PCBs for the enhancement of base metals recovery [12]. Lu et al., 2017, reported gold recovery from waste memory module using chlorination process [13], personal computer PCBs [14], precious metals recovery from mobile phone PCBs [15], selective copper recovery from mobile phone PCBs [16], and copper and gold recovery from laptop PCBs using bioleaching [17].

In addition to these, another significant source of metals is PCBs of hard disk drives. However, some works are also reported on this. Fujita et al., 2014, proposed heat treatment and physical separation for the evaluation of recycling process of hard disc drive PCBs [18]. Peiro et al., 2019, examined the urban mining feasibility of hard disc drive [19] including PCBs. Tanvar et al., 2019, reported evaluation and characterization studies of hard discs to recover copper and rare earth metals [20]. But all these processes were found to be of initial stage as per the literature review and indicated lack of proper recycling process for hard disc drive PCBs. Therefore, need of proper and feasible process to recover metals value from the PCBs of hard disc drive was observed.

Therefore, the present paper reports the attempts made focusing on the optimization of process parameters for the separation and recovery of metals from PCBs of hard disc drive in proper and feasible manner including combination of pre-treatment for the removal of epoxy sheets and hydrometallurgical metal dissolution processes.

## **Experimental**

### ***Materials***

Source material used for this experimental work was depopulated PCBs of obsolete and discarded hard disc drives which contain relatively significant quantity of copper along with lead and tin. All the reagents such as sulfuric acid, hydrochloric acid, and nitric acid supplied by Merck were of analytical grade, and distilled water was used for acid solution preparation and washing purpose.

### ***Method***

As the encapsulation of epoxy sheets hinders hydrometallurgical metal dissolution process, hence, its removal was necessarily required. For this purpose, initially mix metal concentrate sample of less than 14 mesh size containing 94.46% Cu, 0.57% Pb, and 0.85% Sn was obtained from depopulated PCBs using size reduction and wet gravity separation pre-treatment techniques. Then, the leaching experiments for the dissolution and separation of the metals from obtained concentrate were performed in a glass leaching reactor. The desired ratio of sample and leachate was put in a three neck glass flask and heated to a set temperature using a temperature controller and hot plate with inbuilt magnetic stirring function. Required samples were collected from the glass flask at regular time intervals to examine the leaching performance of the metals in a particular leachate. After completion of the leaching process, the tin salt left as residue was dried using a vacuum oven and kept for further examination. Further, metal content in collected samples during the various experiments was analyzed using an AA400 Atomic Absorption Spectrometer, Make: Perkin Elmer, and AA240 (Varian, Agilent). The obtained results indicated the satisfactory mass balance for each set of leaching process.

## **Results and Discussion**

Leaching studies were carried out for the recovery and separation of different metals present in the obtained metal concentrate of hard disc drive PCBs. The selection of suitable acid solution for dissolution of metals and optimization of various process parameters such as effect of acid concentration, time, and temperature using selected acid solution were carried out to examine the leaching and separation of metals.

## ***Selection of Suitable Acid for Metal Dissolution***

Experiments were conducted using a different acid solution to select the effective acid solution for the optimization of process parameters to separate metals using hydrometallurgical metal dissolution processes from mix metal concentrate obtained by pre-treating the PCBs of hard disc drives in proper and feasible manner.

### **Sulfate Based Acid Solution**

The initial dissolution behavior of metals present in the obtained metallic concentrate was checked using  $\text{H}_2\text{SO}_4$  solution. Less than 14 mesh size of sample was used for the experimental purpose. The 100 mL of dilute 4 M  $\text{H}_2\text{SO}_4$  solution was taken in three necked 250 mL flask and heated up to 90 °C. Then, 10 g of sample was immersed after reaching the temperature to maintain 100 g/L pulp density, and 90 °C of solution temperature was maintained up to the completion of the experiment. After completion of the experiment, obtained solution was analyzed and indicated very poor dissolution of all metals except tin. However, oxidizing agents may also be used with sulfuric acid solution to enhance the dissolution efficiency but the use of oxidizing agents not only increases the dissolution efficiency of copper but also increases the dissolution of other metals [16], which makes process nonselective in terms of separation. Hence, sulfuric acid solution was not found suitable for the said purpose.

### **Chloride Based Acid Solution**

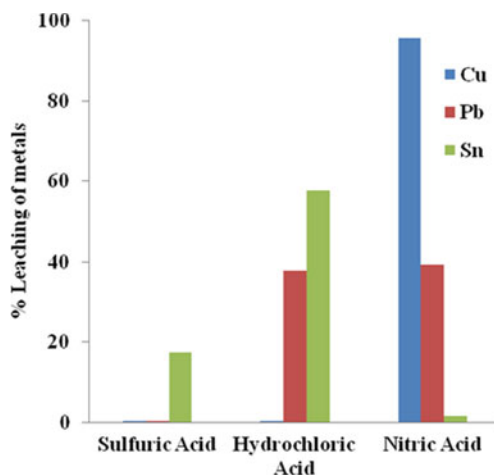
Further, the dissolution study for mix metallic concentrate was performed in hydrochloric acid (HCl) solution to check the dissolution behavior of metals. The dissolution was performed similar to the above condition, 100 mL 4 M HCl in 250 mL flask, heating temperature 90 °C, and 100 g/L of pulp density. Further obtained leached solution was analyzed and results indicated an increase in the dissolution of all metals; however, this increase was not sufficient as lead and tin leaching were found just 38 and 40 percent, respectively, and in the case of copper very poor result obtained may be due to lower  $\text{H}^+$  ion oxidation potential than pure metallic copper.

### **Nitrate Based Acid Solution**

In continuation of suitable leachate selection, obtained mix metallic concentrate of less than 14 mesh size was treated with nitric acid ( $\text{HNO}_3$ ) solution under the similar experimental condition, i.e. 100 mL volume, 4 M solution concentration in 250 mL flask maintaining 100 g/L pulp density and 90 °C of temperature to check the dissolution behavior of metal's value present in the concentrate. After reaching the



**Fig. 1** Selection of suitable acid solution [Acid solution: 4 M, Pulp density: 100 g/L Temp.: 90 °C]



temperature, when concentrate sample was added to the acid solution, the reaction was very fast and vigorous. The obtained results indicated increasing dissolution of Cu and Pb which was about 95.59% and 39%, respectively, while the dissolution behavior of Sn was very poor under this condition and acid solution. May be poor dissolution of Sn was due to the redial dissolution and hydrated stannic oxide ( $\text{SnO}_2$ ) formation. Figure 1 presents the dissolution of metals in sulfate, chloride, and nitrate acid solution. As Cu and Pb dissolution was found to be increasing in  $\text{HNO}_3$  solution, hence  $\text{HNO}_3$  was selected for further experimental purpose.

### Effect of Acid Concentration

As nitric acid solution was found suitable for both copper and lead therefore, further dissolution studies were carried out on different concentrations of nitric acid. Initially by targeting lead, low concentrations 0.05, 0.1, and 0.2 M were applied by taking 10 g of obtained metallic concentrate less than 14 mesh size in 100 mL of volume maintaining 100 g/L pulp density at 90 °C for 90 min to check the dissolution behavior of lead and copper. As Fig. 2 indicates, dissolution of lead was increasing with increase in acid concentration and almost complete dissolution of lead was achieved using 0.1 M nitric acid solution by maintaining 100 g/L of pulp density at 90 °C with very little dissolution of copper. Further obtained residue containing tin and copper was treated with enhanced concentrations 1, 3, and 5 M of nitric acid targeting copper dissolution. Figure 3 indicates that copper dissolution was increasing with increase in acid concentration and almost complete dissolution 99.99% of cooper was achieved with 5 M of nitric acid concentration at 90 °C maintaining 100 g/L of pulp density in 90 min leaving tin in the residue due to salt formation.

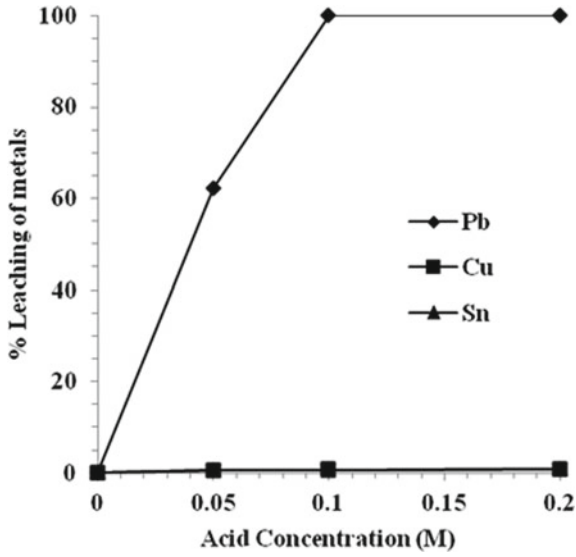


**Fig. 2** Effect of nitric acid concentration on lead dissolution [Pulp density: 100 g/L, Temp.: 90 °C, Time: 90 min]

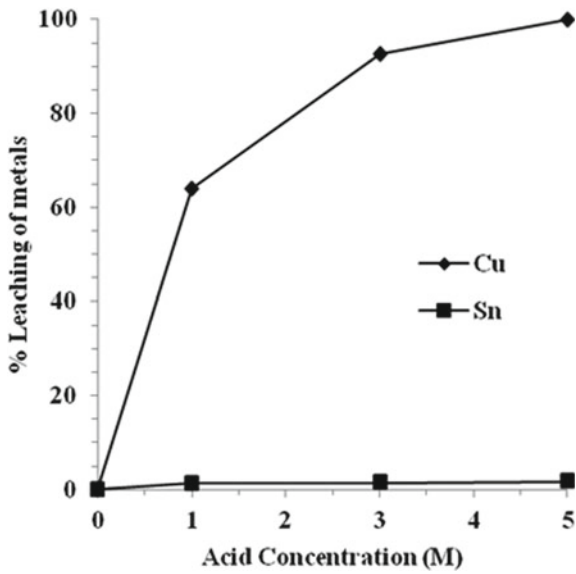


**Fig. 3** Effect of nitric acid concentration on copper dissolution [Pulp density: 100 g/L, Temp.: 90 °C, Time: 90 min]

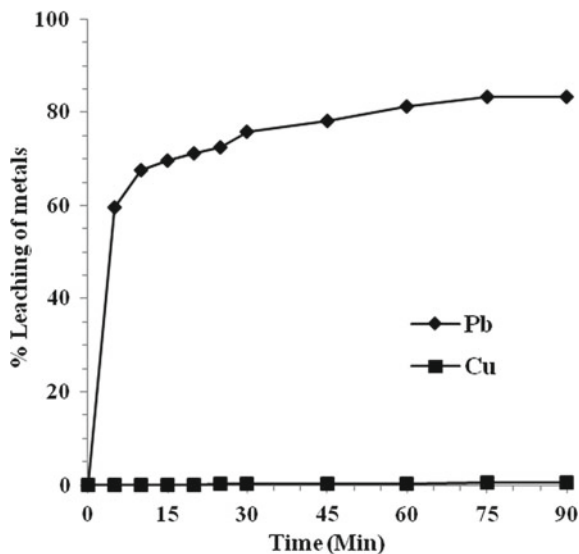
## Effect of Temperature and Time on Pb and Cu Dissolution

Further studies were carried out to check the leaching behavior of lead and copper by varying the temperature to 75 and 90 °C maintaining pulp density 100 g/L. As shown in Figs. 4 and 5, dissolution of lead and copper was increasing with increase in temperature and time from 59.47 to 83.38% and 0.11 to 0.55%, respectively, on 75 °C and 71.37 to 99.99% and 0.13 to 0.66%, respectively, on 90 °C using 0.1 M nitric acid solution. As mentioned above, residue after complete lead dissolution was further put in second dissolution targeting copper. Figures 6 and 7 indicate the dissolution of copper was also increasing with increase in time and temperature from 39.8 to 93.83% on 75 °C and 47.32 to 99.99% on 90 °C using 5 M nitric acid solution. This study indicated that 90 °C was suitable temperature for almost complete dissolution of lead and copper.

### *Kinetic Study for Lead and Copper*

The results obtained were used to study the dissolution kinetics of lead and copper for both dissolutions. Initially, mix metallic concentrate of hard disc drive PCBs using 0.1 M and residue obtained after total lead dissolution from mix metallic concentrate using 5 M nitric acid varying time and maintaining 100 g/L pulp density at 90 °C. The obtained data was tested with different standard equations to understand the mechanism of dissolution of lead and copper with nitric acid. In the case of lead, the data obtained from dissolution of mix metallic concentrate sample at lower acid

**Fig. 4** Effect of time [0.1 M nitric acid, Pulp density: 100 g/L, Temp.: 75 °C, Time: 90 min]



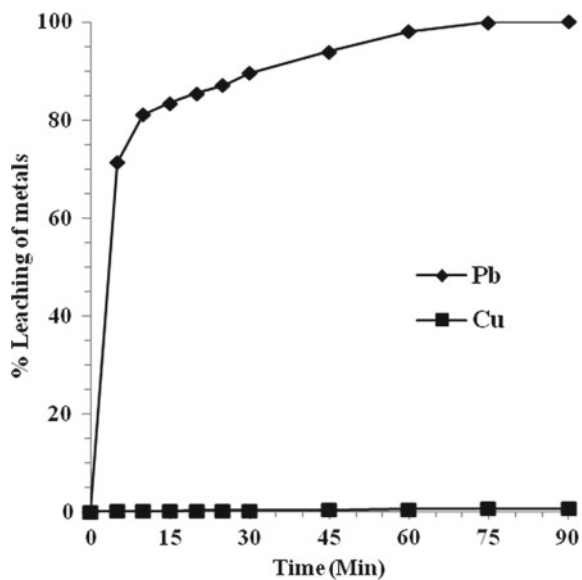


Fig. 5 Effect of time [0.1 M nitric acid, Pulp density: 100 g/L, Temp.: 90 °C, Time: 90 min]

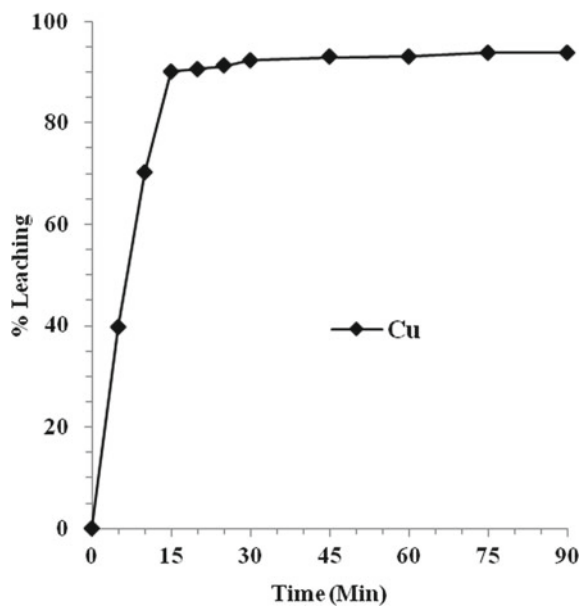


Fig. 6 Effect of time [5 M nitric acid, Pulp density: 100 g/L, Temp.: 75 °C, Time: 90 min.]

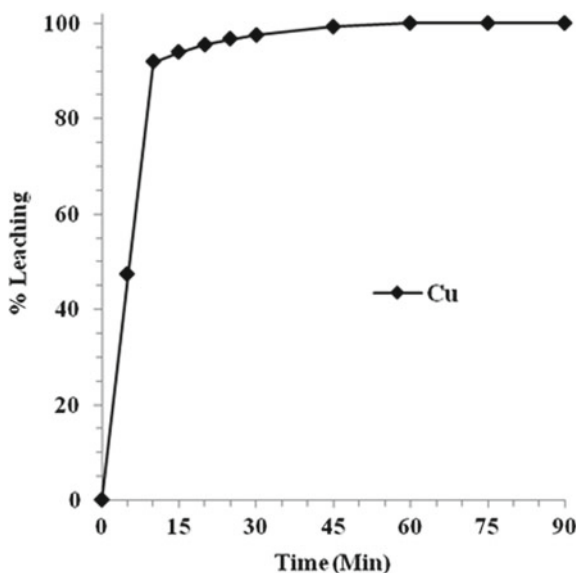


Fig. 7 Effect of time [5 M nitric acid, Pulp density: 100 g/L, Temp.: 90 °C, Time: 90 min.]

concentration, i.e. 0.1 M on 90 °C, was fitted with the equation  $1-(1-X)^{1/3} = K_c t$ , (Shrinking spheres), where X = fraction of lead reacted (% lead dissolution/100),  $K_c$  = reaction rate constant per minute, t = time in minute and presented in Fig. 8. The obtained result of copper dissolution from the residue produced after lead dissolution using 05 M nitric acid concentration at 90 °C was fitted with the equation  $1-3 * (1-X)^{2/3} + 2 * (1-X)$  (Ash diffusion control dense constant size-spherical particles) and presented in Fig. 9. The value of constant K was calculated and validated with reaction model, and calculated value of K was found almost constant.

## Conclusion

Studies were carried out on laboratory scale using nitric acid solutions for the separation and recovery of lead and copper from mix metallic concentrate obtained from depopulated hard disc PCBs. However, sulfate and chloride based acid solutions were also tried but not found suitable. Initially, dismantled PCBs were depopulated, crushed, and beneficiated to generate mix metallic concentrate. After getting concentrate, experiments were conducted for the optimization of various process parameters such as selection of acid, effect of acid concentration, time, and temperature to dissolve lead and copper separately leaving tin in the residue part. The following conclusions can be drawn based on results of experimental studies of lead and copper dissolution.

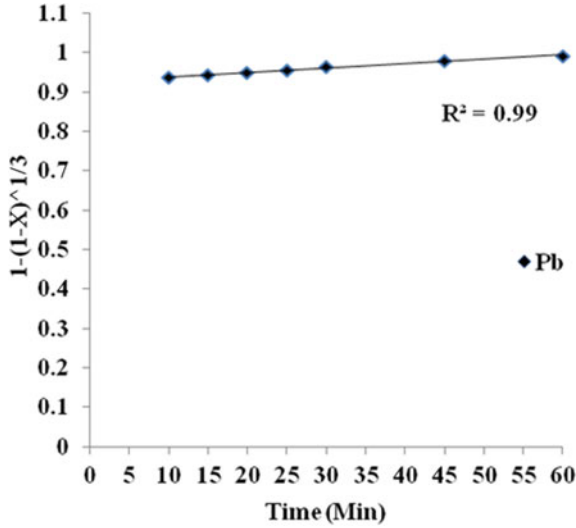
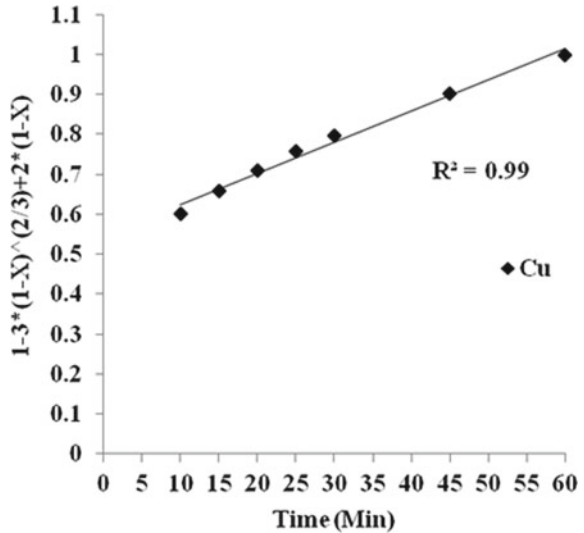


Fig. 8 Leaching kinetics of lead [0.1 M nitric acid, Pulp density: 100 g/L; Temp: 90 °C]

Fig. 9 Leaching kinetics of copper [5 M nitric acid, Pulp density: 100 g/L; Temp: 90 °C]



Nitric acid is effective for the dissolution of lead and copper leaving tin as residue. The maximum dissolution of lead was achieved 99.99% using 0.1 M nitric acid at 90 °C maintaining 100 g/L of pulp density in 75 min. However, very little dissolution of copper 0.54% was also occurred on this condition but a very large quantity of copper gets lead free. Further 99.99% copper dissolution was achieved from lead free concentrate obtained as residue using 5 M nitric acid at 90 °C in 60 min. The results

obtained in both dissolution experiments were validated with standard equations and found well fitted Figs. 8 and 9. Tin present in the sample remained as residue in the form of  $\text{SnO}_2$  salt. Thus, study will be useful for the separation and recovery of lead, copper, and tin from such mix concentrate of depopulated PCBs of discarded hard disc drives.

**Acknowledgements** The authors are grateful to the Director, CSIR-National Metallurgical Laboratory Jamshedpur, India, for kind permission to publish the paper. The grant supported by CSIR, New Delhi, India, under Fast Track Commercialization (FTC) project (FTC-0014/MLP-3116) is highly acknowledged.

## References

1. Huang K, Guo J, Xu Z (2009) Recycling of waste printed circuit board: a review of current technologies and treatment status in China. *J Hazard Mater* 164:399–408
2. Li J, Lu H, Xu Z, Zhou Y (2008) Critical rotation speed model of the rotation roll electrode in corona electrostatic separation for recycling waste printed circuit board. *J Hazard Mater* 154:331–336
3. Zhou Y, Wu W, Qiu K (2010) Recovery of materials from waste printed circuit boards by vacuum pyrolysis and vacuum centrifugal separation. *Waste Manage* 30:2299–2304
4. Luyima A, Zhang L, KERS J, LAURMAA V (2012) Recovery of metallic materials from printed wiring board by green pyrolysis process *Materials Science (Medziagotyra)* 18(3):1392–1320.
5. Hester RE and Harrison RM (2009) *Electronic waste management: design analysis and application* royal society of chemistry Cambridge UK 49–95
6. Sohaili J, Muniyandi SK, Mohamad SS (2012) A review on printed circuit boards waste recycling technologies and reuse of recovered nonmetallic materials. *Int J Sci Eng Res* 3(2):2229–5518
7. Lee CH, Chang CT, Fan KS (2004) An overview of recycling and treatment of scrap computers. *J Hazard Mater B* 114:93–100
8. Ludwig C, Hellweg S, Stucki S (2003) *Municipal solid waste management, pp 320–322. Strategies and Technology for Sustainable Solution* Springer Berlin
9. Zhou G, Luo Z, Zhai X (2007) Experimental study on metal recycling from waste PCB. In: *Proceeding of the international conference on sustainable solid management*, pp 155–162, 5–7 Sept 2007 Chennai India
10. Yoo JM, Jeong J, Yoo K, Lee J, Kim W (2009) Enrichment of the metallic components from waste printed circuit boards by a mechanical separation process using a stamp mill. *Waste Manage* 29:1132–1137
11. Kumar V, Lee Jc, Jeong J, Jha MK, Kim Bs (2014) Recycling of printed circuit boards (PCBs) to generate enriched rare metal concentrate. *J Indus Eng Chem* 21:805–813
12. Arshadi A, Yaghmaei S, Mousavi SM (2018) Content evaluation of different waste PCBs to enhance basic metals recycling. *Resour Conserv Recycl* 139:298–306
13. Lu Y, Song Q, Xu Z (2017) Integrated technology for recovering Au from waste memory module by chlorination process selective leaching extraction and distillation. *J Clean Prod* 161:30–39
14. Dutta D, Panda R, Kumari A, Goel S, Jha MK (2018) Sustainable recycling process for metals recovery from used printed circuit boards sustainable. *Mater Technol* 17:e00066
15. Gamez S, Garces K, de la Torre E, Guevara A (2019) Precious metals recovery from waste printed circuit boards using thiosulfate leaching and ion exchange resin. *Hydrometallurgy* 186:1–11

16. Segura-Bailon B and Gretchen T Lapidus (2021) Selective recovery of copper contained in waste PCBs from cellphones with impurity inhibition in the citrate-phosphate system. *Hydrometallurgy* 203:105699
17. Isildar A, Vossenber Jvd, Rene ER, Hullebusch EDv, Lens PNL (2015) Two-step bioleaching of copper and gold from discarded printed circuit boards (PCB). *Waste Manage* 57:149–157
18. Fujita T, Ono H, Dodbiba G, Yamaguchi K (2014) Evaluation of a recycling process for printed circuit board by physical separation and heat treatment. *Waste Manage* 34(7):1264–1273
19. Peiro LT, Giron AC, Durany XG (2019) Examining the feasibility of the urban mining of hard discs drives. *J Clean Prod* 248:119216
20. Tanvar H, Barnwal A, Dhawan N (2019) Characterization and evaluation of discarded hard disc drives for recovery of copper and rare earth values. *J Clean Prod* 249:119377



# Extraction of Tungsten, Yttrium, and Uranium from Tantalum–Niobium Ore from Muchinga Province in Zambia



Mazwi Douglas Musowoya, Yotamu Rainford Stephen Hara, Fredrick Chileshe, Janet Mundundu, and Stephen Parirenyatwa

**Abstract** A clean method of extracting tungsten, yttrium, and uranium from tantalum–niobium ore located in the Muchinga province of Zambia has been developed. Tungsten is selectively extracted by roasting with alkaline at 700 and 750 °C followed by leaching in water to solubilize alkaline tungstate. The alkaline leach residue is cured with sulphuric acid to sulphate uranium and yttrium which are then leached out in acidic media. The effects of sulphation temperature, time, and particle size were studied. Yttrium was recovered from leach solution via precipitation with oxalic acid in which yttrium oxalate with purity of more than 99 wt% was obtained. Uranium was recovered from the leach solution through precipitation with sodium hydroxide. Extraction of tungsten, yttrium, and uranium from the material concentrated tantalum oxide by two times. A process flowsheet was developed based on optimised test works.

**Keywords** Tungsten · Yttrium · Uranium · Rare earth · Zambia

## Introduction

Yttrium oxide has high temperature stability, and hence, it is used in glass, optic, and ceramic applications [1]. On the other hand, tungsten oxide is the major source of tungsten metal, the latter has wider applications in areas where heat resistance, wear resistance, and hardness are required [2]. By comparison, tantalum and niobium are both used in special alloys and production of electronic components [3].

The common ore for tantalum and niobium is columbite ((Fe,Mn)(Nb,Ta)<sub>2</sub>O<sub>6</sub>), Tantalite ((Fe,Mn)(Ta,Nb)<sub>2</sub>O<sub>6</sub>), Euxenite ((Y,Ca,Ce,U,Th)(Nb,Ti,Ta)<sub>2</sub>O<sub>6</sub>), etc. [4]. In Muchinga province of Zambia, tantalum–niobium bearing mineral contains tungsten, yttrium, and uranium in significant amounts. The presence of uranium makes

---

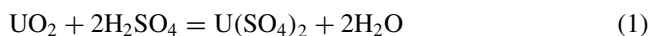
M. D. Musowoya · Y. R. S. Hara (✉) · F. Chileshe  
School of Mines and Mineral Sciences, The Copperbelt University, Kitwe, Zambia  
e-mail: [yotamuhara@gmail.com](mailto:yotamuhara@gmail.com)

J. Mundundu · S. Parirenyatwa  
YCS Sustainable Solutions Limited, Kitwe, Zambia

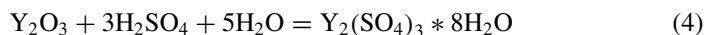
Muchinga tantalum–niobium ore not easily saleable due to challenges in transportation. This study focuses on extraction of tungsten, yttrium, and uranium from tantalum–niobium ore with the aim of upgrading tantalum and niobium.

## Thermodynamic Consideration

Uranium is soluble in acidic ( $\text{pH} < 6$ ) and alkaline ( $\text{pH} > 10$ ) media [5, 6]. At lower pH, uranium oxide may be dissolved in sulphuric acid media to yield uranium sulphate [5, 7] as shown in Eq. 1 while the alkaline dissolution of uranium oxide may be presented by Eqs. 2 and 3.



There is limited thermodynamic data regarding the dissolution of yttrium in acidic and alkaline media. However, yttrium may react with sulphuric acid according to Eq. 4. Note, the Gibbs free energy change for Eq. 4 is negative [8, 9], indicating the reaction is thermodynamically feasible.



In contrast, tungsten is only soluble in less acidic ( $\text{pH} > 4$ ) [10] or alkaline media.

The solubility of niobium and tantalite has been extensively studied by Makanyire et al. [11]. It was found that niobium is soluble at pH of less than 0.5. Therefore, the extraction of tungsten, yttrium, and uranium from Muchinga ore may consequently lead to production of niobium and tantalum pentoxides.

## Experimental

### Materials

Chemical analysis of the Muchinga ore is shown in Table 1 from which it can be observed that the ore contains a number of valuable minerals such as tantalum, niobium, tungsten, yttrium, and uranium oxides. The gangue impurities are iron oxide, silica, calcium oxide, titanium oxide, and manganese oxide.

**Table 1** Chemical analysis of the Muchinga ore in weight %

Ta <sub>2</sub> O <sub>5</sub>	Nb <sub>2</sub> O <sub>5</sub>	UO <sub>2</sub>	WO <sub>2</sub>	Y <sub>2</sub> O <sub>3</sub>	Fe <sub>2</sub> O <sub>3</sub>	CaO	SiO <sub>2</sub>	Al <sub>2</sub> O <sub>3</sub>	TiO <sub>2</sub>	MnO <sub>2</sub>
6.99	50.15	14.76	6.45	7.99	7.01	2.49	5.06	0.37	0.51	0.60

### *Metallurgical Test Work*

The sample was crushed and milled down to a particle size of less than 106 microns. The milled sample was mixed with sulphuric acid in the ratio of ore: weight of 1:1 and cured for 2 h at 250 °C. During the curing process, the sample agglomerated requiring it to be ground with a mortar and pestle. The ground cured sample was leached in acidic media (pH of 1.8) to dissolve the soluble sulphates formed during curing. The leach residue was filtered to separate the solids from leach solution. The leach residue was dried in an oven at 105 °C.

### *Roasting with Potassium Hydroxide*

Ground ore was thoroughly mixed with 20 weight % potassium hydroxide or sodium, transferred into a clay crucible, and roasted for 1.5 h at 700 and 750 °C to form soluble potassium tungstate. The roast calcine was leached in alkaline media for 1 h, and the resulting leach residues were dried in an oven and analyzed.

### *Chemical Analysis*

The as-received ore and all samples from the experiments were analyzed by Rigaku X-ray fluorescence machine using a pressed pellet method. Each sample was milled down to particle size of less than 63 microns to make it homogeneous.

## **Results and Discussion**

### *Acid Curing of the As-Received Ground Material*

The results for the sample cured with sulphuric acid are shown in Table 2, and it can be observed that nearly all yttrium oxide was leached out. In comparison, 50% of uranium and iron oxides were extracted. On the other hand, the grades of uranium, tungsten, and iron have decreased slightly and this is due to partial dissolution. By comparison, the grades of tantalum oxide, niobium oxide, and silica have all increased

**Table 2** Chemical analysis (weight %) of the as-received ore before and after acid curing

Fraction	Ta <sub>2</sub> O <sub>5</sub>	Nb <sub>2</sub> O <sub>5</sub>	UO <sub>2</sub>	WO <sub>2</sub>	Y <sub>2</sub> O <sub>3</sub>	Fe <sub>2</sub> O <sub>3</sub>	CaO	SiO <sub>2</sub>	Al <sub>2</sub> O <sub>3</sub>	TiO <sub>2</sub>	MnO <sub>2</sub>
Feed	6.99	50.15	14.76	6.45	7.99	7.01	2.49	5.06	0.37	0.51	0.60
Residue	8.87	63.34	7.54	5.21	0.10	3.54	0.26	6.99	0.77	0.61	0.63

in the leach residue as a result of decrease in the mass of the material due to elements being leached out.

The Gibbs free energy change for the sulphation of yttrium is more negative than that of uranium and could explain the partial dissolution of the latter while the former was nearly all dissolved. Calcium is generally not soluble in sulphuric acid media but it was mostly dissolved during leaching. This unexpected dissolution of calcium might be due to the presence of yttrium ions in leach solution.

### *Alkaline Roasting of the Samples*

Chemical analysis results for the sample that was roasted with 20 weight % potassium hydroxide at 700 and 750 °C and leached in alkaline media are presented in Table 3. Mass balance showed that 98% of tungsten was extracted during leaching process. Even though uranium is soluble in alkaline media, it did not dissolve during the leaching process.

The grade of the other elements in the residue did not change significantly from the feed, and this is because tungsten was replaced by potassium. Results from the analysis of the leach solution are shown in Table 4 from which it can be observed the major elements in the solution are tungsten, potassium, silicon, sodium, and phosphorous in the decreasing order. Based on this, it can be concluded that alkaline roast—leach is very selective in extracting tungsten among the valuable elements in Muchinga ore. The formation of potassium tungstate proceeds according to Eq. 5.

**Table 3** Chemical analysis for the residue that was obtained after roasting ore with 20 weight % potassium hydroxide

Sample ID	Ta <sub>2</sub> O <sub>5</sub>	Nb <sub>2</sub> O <sub>5</sub>	UO <sub>2</sub>	WO <sub>2</sub>	Y <sub>2</sub> O <sub>3</sub>	Fe <sub>2</sub> O <sub>3</sub>	CaO	SiO <sub>2</sub>	Al <sub>2</sub> O <sub>3</sub>	TiO <sub>2</sub>	MnO <sub>2</sub>	K <sub>2</sub> O
Feed	6.99	50.15	14.76	6.45	7.99	7.01	2.49	5.06	0.37	0.51	0.60	
700 °C residue	6.21	51.09	11.75	0.45	7.42	5.84	0.71	4.79	0.21	0.37	0.35	8.11
750 °C residue	6.47	50.90	11.36	0.35	7.44	5.90	1.56	5.69	0.16	0.18	1.14	7.83

**Table 4** Chemical analysis in weight % of the leach alkaline solution. The ore was roasted with KOH at 750 °C and water leached

W	K	Si	P	Na	S	Al	Mn
15.00	31.59	4.38	0.94	1.13	0.36	0.4	0.56

### *Acid Curing of the Alkaline Roast—Leach Residue*

The alkaline roast—leach residue was cured with sulphuric acid, and chemical analysis for the acid curing—leach residue is shown in Table 5. It is evident from the results in Table 5 that both yttrium and uranium were completely dissolved during leaching and hence extracted. The dissolution of uranium and yttrium leads to upgrading of tantalum and niobium to 10.6 and 67.04 weight %, respectively.

### *Recovery of Valuable Metals from Leach Solution*

#### **Precipitation of Tungsten**

Tungsten oxide was recovered from the alkaline roast—leach solution via precipitation with sulphuric acid by following the stoichiometric in Eq. 6. Chemical analysis of the precipitate from the alkaline roast—leach solution is shown in Table 6. It can be observed that the dried precipitate has 93.63 weight %  $\text{WO}_3$ . The impurities in the precipitate in the decreasing order are  $\text{K}_2\text{O}$ ,  $\text{Al}_2\text{O}_3$ , Cl, S, CaO, and  $\text{Fe}_2\text{O}_3$ . It is possible that thorough washing of the precipitate may further decrease the grades of  $\text{K}_2\text{O}$  and S. Uranium was not detected in the precipitate as shown from the results in Table 6, and measurement using a Geiger counter showed no radiation.



#### **Precipitation of Yttrium**

Oxalic acid ( $\text{C}_2\text{H}_2\text{O}_4$ ) was utilized to selectively precipitate out yttrium as an oxalate according to Eq. 7, where it can be noted that the precipitation of yttrium oxalate generates sulphuric acid and hence the solution becomes acidic. The reaction between yttrium sulphate and oxalic acid was very rapid, reaching completion within 5 min. Yttrium oxalate was then heated in air to decompose it to yttrium oxide as shown in Eq. 8. It can be observed (Table 7) that the precipitate has 99.01 weight %  $\text{Y}_2\text{O}_3$ .

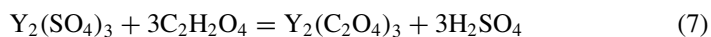


**Table 5** Chemical analysis (weight %) of the leach residue. The alkaline leach residues were cured with sulphuric acid and leached in acidic media

Sample ID	Ta <sub>2</sub> O <sub>5</sub>	Nb <sub>2</sub> O <sub>5</sub>	UO <sub>2</sub>	WO <sub>2</sub>	Y <sub>2</sub> O <sub>3</sub>	Fe <sub>2</sub> O <sub>3</sub>	CaO	SiO <sub>2</sub>	Al <sub>2</sub> O <sub>3</sub>	TiO <sub>2</sub>	Na <sub>2</sub> O	MnO <sub>2</sub>	K <sub>2</sub> O
Roasted at 700 °C	9.69	67.78	0.00	0.00	0.00	3.03	0.00	15.28	0.09	0.27	1.75	0.10	0.24
Roasted at 750 °C	10.61	67.04	0.00	0.00	0.00	3.46	0.00	13.91	1.15	0.50	1.88	0.06	0.31

**Table 6** Chemical analysis (weight %) results for the precipitate from the alkaline roast—leach solution

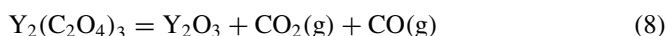
WO <sub>3</sub>	K <sub>2</sub> O	S	Al <sub>2</sub> O <sub>3</sub>	CaO	Cl	SiO <sub>2</sub>	UO <sub>2</sub>	Nb <sub>2</sub> O <sub>5</sub>	Ta <sub>2</sub> O <sub>5</sub>	Fe <sub>2</sub> O <sub>3</sub>
93.63	3.23	0.46	0.89	0.43	0.85	< 0.01	ND	ND	ND	0.13

**Table 7** Chemical analysis (weight%) for the precipitated yttrium oxide

Ta <sub>2</sub> O <sub>5</sub>	Nb <sub>2</sub> O <sub>5</sub>	UO <sub>2</sub>	WO <sub>2</sub>	Y <sub>2</sub> O <sub>3</sub>	Fe <sub>2</sub> O <sub>3</sub>	CaO	Al <sub>2</sub> O <sub>3</sub>	MgO	Na <sub>2</sub> O	Ni	Co
0.00	0.00	0.00	0.18	99.01	0.16	0.20	0.10	0.06	0.02	0.08	0.17

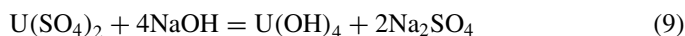
**Table 8** Chemical analysis in % weight for the precipitated uranium oxide

Ta <sub>2</sub> O <sub>5</sub>	Nb <sub>2</sub> O <sub>5</sub>	UO <sub>2</sub>	WO <sub>2</sub>	Y <sub>2</sub> O <sub>3</sub>	Fe <sub>2</sub> O <sub>3</sub>	CaO	SiO <sub>2</sub>	Al <sub>2</sub> O <sub>3</sub>	MgO	Na <sub>2</sub> O	MnO <sub>2</sub>
< 0.01	< 0.01	71.85	< 0.01	0.00	0.48	16.93	0.31	0.52	0.72	6.76	< 0.01



### Precipitation of Uranium

Solubility of uranium in solution is pH dependent, as is the formation of uranium hydroxide due to the solubility of uranium hydroxide at a lower pH (Eq. 9).



Uranium was precipitated from the solution at a pH of 9.3 by using sodium hydroxide. Chemical analysis of the precipitated yellow or uranium cake is shown in Table 8, where it is evident that the yellow cake has 71.85 weight % uranium oxide. The main impurities in the cake are calcium and sodium oxides.

### General Discussion

The results obtained from the laboratory test works have clearly shown that tungsten, yttrium, and uranium may be extracted from tantalum–niobium ore from Muchinga province of Zambia. The extraction of tungsten, yttrium, and uranium upgrades tantalum and niobium in the leach residue which may be processed further to produce separate oxides of tantalum and niobium. The developed process flowsheet from the test works is shown in Fig. 1.

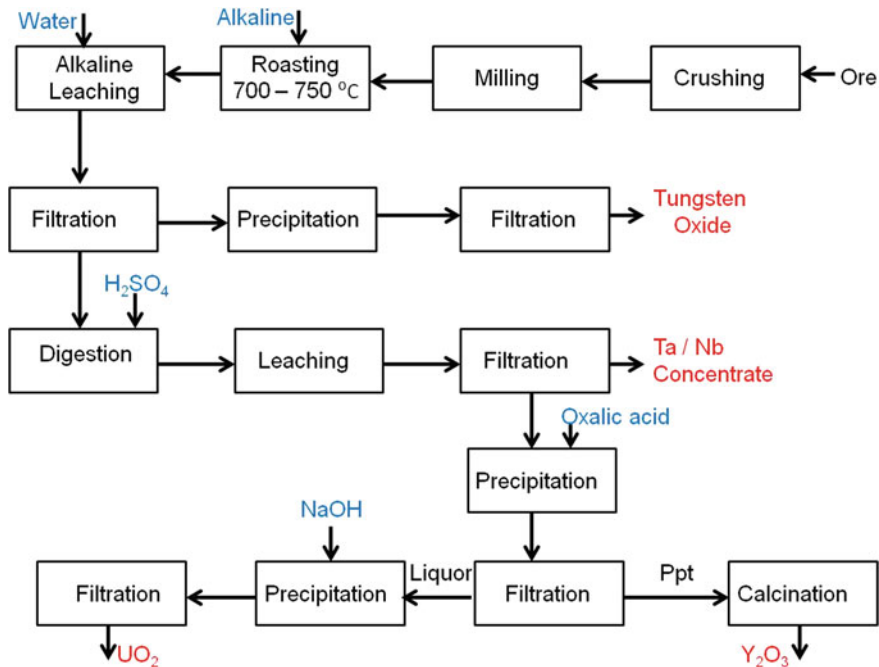


Fig. 1 Proposed process flowsheet based on optimized test works

## Conclusions

From the test works carried out, the following conclusions were made:

1. Curing of the material with sulphuric acid at 250 °C followed by leaching in acidic media gives leach efficiency of 98.6% for yttrium. On the other hand, the leach efficiencies for iron and uranium are less than 50%.
2. Tungsten was selectively extracted among the valuable elements in the material via alkaline roast—leach process. The leached tungsten was precipitated with sulphuric acid at a pH of 1.8. Chemical analysis of the precipitate gave 93.63 weight % tungsten oxide.
3. Yttrium and uranium were both dissolved when the alkaline roast—leach residues were cured with sulphuric acid at 250 °C.
4. Yttrium was recovered from solution via precipitation with oxalic acid. The precipitate had about 99.01 weight %  $Y_2O_3$ .
5. Uranium was recovered from leach solution using sodium hydroxide and the precipitate had 71.85 weight %  $UO_2$ . The main impurities in precipitate were calcium oxide.



## References

1. Rajakumar G et al (2021) Yttrium oxide nanoparticle synthesis: an overview of methods of preparation and biomedical applications. *Appl Sci* 11(5):2172
2. Han Z, Golev A, Edraki M (2021) A review of tungsten resources and potential extraction from mine waste. *Minerals* 11(7):701
3. Buckman R (2000) New applications for tantalum and tantalum alloys. *Jom* 52(3):40–41
4. Linnen R, Trueman DL, Burt R (2014) Tantalum and niobium. *Critical metals handbook*, pp 361–384
5. Habashi F (1969) *Principles of extractive metallurgy*. Gordon and Breach, London, pp 194–196
6. Habashi F (1999) *Kinetics of metallurgical processes*. Quebec: Metallurgie Extractive
7. Sato T (1962) The extraction of uranium (VI) from sulphuric acid solutions by di-(2-ethylhexyl)-phosphoric acid. *J Inorg Nucl Chem* 33:1081–1087
8. Bale CW et al (2002) FactSage thermochemical software and databases. *Calphad: Comput Coupling Phase Diagrams Thermochem* 26(2):89–228
9. Roine A (2002) *HSC Chemistry 5.1*. Outokumpu Research Oy, Finland
10. Martins JI (2003) Leaching of synthetic scheelite by nitric acid without the formation of tungstic acid. *Indus Eng Chem Res* 42(21)
11. Makanyire T, Jha A, Sutcliffe S (2016) Kinetics of hydrochloric acid leaching of niobium from TiO<sub>2</sub> residues. *Int J Miner Process* 157:1–6

# Production of High-Purity Mg Metal from Various MgO Resources Through a Novel Electrolytic Process Using a Cu Cathode and Vacuum Distillation



Hyeong-Jun Jeoung, Tae-Hyuk Lee, Youngjae Kim, Jin-Young Lee, Young Min Kim, Toru H. Okabe, Kyung-Woo Yi, and Jungshin Kang

**Abstract** Recently, a new eco-friendly electrolytic process using a metal cathode followed by vacuum distillation was developed to produce high-purity Mg metal from MgO. In this study, the viability of this novel Mg metal production process using primary and secondary resources containing MgO as a feedstock was examined. In the electrolysis experiments, an average current of 1.44 A was applied to the electrolysis cell at 1043 K for 12.5 h using Cu cathode and graphite anode in an Ar gas atmosphere. The electrolysis yielded Mg–Cu alloys of 14.0–14.4 mass% Mg with an average cell potential of 2.43–2.67 V and current efficiency of 89.6–92.4%. Vacuum distillation of the Mg alloys, obtained after the electrolysis, at 1300 K for 10 h yielded Mg metals with a purity of 99.994–99.999%. Therefore, this study demonstrated that the production of high-purity Mg metal from various resources that contain MgO through the novel Mg metal production process is feasible.

**Keywords** Magnesium metal · Magnesium oxide resources · Molten salt electrolysis · Copper cathode · Vacuum distillation

---

H.-J. Jeoung · T.-H. Lee · Y. Kim · J.-Y. Lee · J. Kang (✉)

Korea Institute of Geoscience and Mineral Resources, 124 Gwahak-Ro Yuseong-Gu, Daejeon 34132, Korea  
e-mail: [jkang@pusan.ac.kr](mailto:jkang@pusan.ac.kr)

H.-J. Jeoung · K.-W. Yi

Department of Materials Science and Engineering, Seoul National University, 1 Gwanak-Ro, Gwanak-Gu, Seoul 08826, Korea

Y. M. Kim

Korea Institute of Materials Science, 797 Changwondae-Ro, Seongsan-Gu, Changwon, Gyeongnam 51508, Korea

T. H. Okabe

Institute of Industrial Science, The University of Tokyo, 4-6-1 Komaba, Meguro-Ku, Tokyo 153-8505, Japan

J. Kang

School of Materials Science and Engineering, Pusan National University, 2 Busandaehak-Ro, Geumjeong-Gu, Busan 46241, Korea

## Introduction

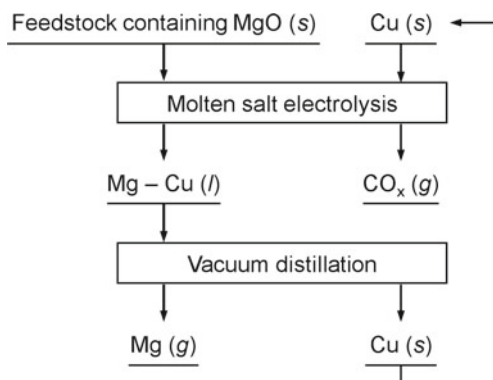
Magnesium (Mg) metal is gaining significant attention in various applications owing to its superior properties, such as lightweight and high specific strength [1]. For the production of Mg metal, the Pidgeon and electrolytic processes are currently used [2]. In the Pidgeon process, Mg metal is produced through thermal reduction of calcined dolomite ( $\text{CaO}\cdot\text{MgO}$ ) using ferrosilicon (Fe-Si) at 1373–1473 K under vacuum [2, 3]. In the electrolytic processes, Mg metal is produced through electroreduction of anhydrous magnesium chloride ( $\text{MgCl}_2$ ) at 928–993 K [2].

However, there are several disadvantages in the commercial Mg metal production processes [2]. The Pidgeon process is a high energy-consuming process. In addition, it generates large amounts of carbon oxide ( $\text{CO}_x$ ) and sulfur oxide ( $\text{SO}_x$ ) gases during Mg production. The electrolytic processes require energy-intensive procedures for anhydrous  $\text{MgCl}_2$  preparation. In addition, it generates toxic chlorine ( $\text{Cl}_2$ ) gas during electrolysis.

Under these circumstances, several research efforts have been made to develop a process with environmental friendliness and effectiveness [4–10]. Among the processes, molten salt electrolysis of magnesium oxide (MgO) using a high-density metal cathode, such as copper (Cu), silver (Ag), or tin (Sn), followed by vacuum distillation is promising when the generation of oxygen ( $\text{O}_2$ ) gas using an inert anode and high current efficiency of electrolysis are considered [6–9]. In this process, MgO dissolved in a magnesium fluoride ( $\text{MgF}_2$ )–lithium fluoride (LiF) molten salt at 1053–1083 K is electroreduced to a high-density Mg alloy at the bottom of the electrolysis cell, thereby hindering the loss of Mg metal due to the recombination reaction with reactive gases, such as  $\text{O}_2$  generated at the anode. The obtained Mg alloy is recovered as high-purity Mg metal with a purity of 99.999% through vacuum distillation at 1200–1300 K.

In this study, we investigated the feasibility of producing Mg metal from MgO-containing primary and secondary resources through molten salt electrolysis using a Cu cathode, followed by vacuum distillation, as shown in Fig. 1. This is because the utilization of these resources has various advantages. For example, the primary resource has high MgO content and a large amount of reserves [11]. When secondary resources are used, processing required to produce MgO from primary resources is not necessary or reduced, and waste generation is reduced [10]. Therefore, the competitiveness and environmental friendliness of the process will be enhanced especially when secondary resources are used as a feedstock.

**Fig. 1** Flowchart of novel Mg metal production process used in this study for producing high-purity Mg metal from MgO-containing resource



## Experimental

### *Feedstock Preparation*

Before being used as a feedstock, pretreatment was conducted on the primary and secondary MgO resources used in this study. In case of the magnesite from North Korea and seawater MgO clinker, both of which are the primary MgO resources, calcination at 1073 K and drying at 383 K were conducted, respectively. The secondary MgO resource from MgO–C refractory brick was oxidized at 1073 K.

### *Molten Salt Electrolysis*

Before electrolysis,  $\text{MgF}_2$ ,  $\text{LiF}$ , and potassium chloride (KCl) were dried under vacuum at 453 K for more than 72 h to remove water. Further, pre-electrolysis was conducted on a mixture of  $\text{MgF}_2$ – $\text{LiF}$ – $\text{KCl}$  salt to remove impurities by applying a current of 0.15 A for more than 1 h. Afterward, the pre-electrolyzed  $\text{MgF}_2$ – $\text{LiF}$ – $\text{KCl}$  salt was charged in a graphite crucible, as shown in Fig. 2a. The graphite crucible was connected to a nickel (Ni) wire as the current lead. In addition, in the graphite crucible, a Cu cathode assembly was positioned, in advance. Subsequently, the graphite crucible was placed inside a vertical stainless steel reactor. Afterward, the reactor was assembled with a top flange plugged with a viton plug, and the interior gas of the reactor was changed to argon (Ar) gas. During electrolysis, Ar gas was continuously flowed to maintain the internal pressure of the reactor at 1 atm. After the installation of the reactor in a vertical electric furnace, the temperature was increased to 1043 K, and electrolysis was performed using a galvanostat by applying an average current of 1.44 A for 12.5 h. After the completion of electrolysis, the reactor was cooled to room temperature, and the Mg alloy was recovered.

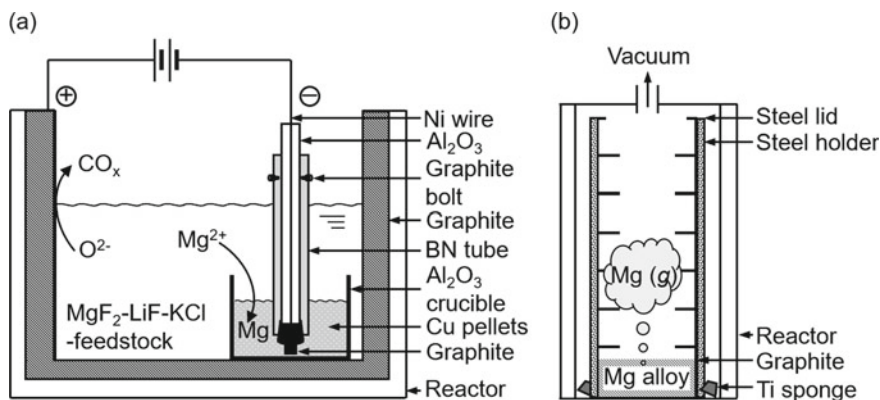


Fig. 2 Schematic of **a** molten salt electrolysis and **b** vacuum distillation experimental apparatus

### Vacuum Distillation

For vacuum distillation, the Mg alloy obtained after electrolysis was charged at the bottom of the graphite crucibles stack, as shown in Fig. 2b. The graphite crucibles stack was then placed inside a vertical steel reactor. The reactor was plugged with a viton plug and then evacuated. Subsequently, the reactor was set in a vertical electric furnace that was preheated to 1300 K. After vacuum distillation was conducted for 10 h, the reactor was removed from the electric furnace. When the reactor was cooled to room temperature, Mg metal and residue were recovered.

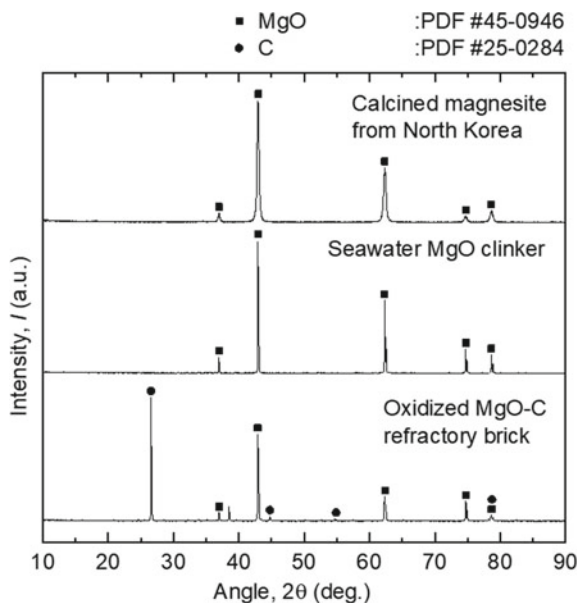
## Results and Discussion

### Feedstock for Molten Salt Electrolysis

Figure 3 shows the results of the XRD analysis of the feedstocks used for molten salt electrolysis. As shown in Fig. 3, the main crystalline phase identified in the resources was MgO. The only difference observed in the XRD results was that C was identified in the oxidized MgO–C refractory brick owing to the insufficient oxidization.

Meanwhile, Table 1 shows that the purities of MgO in the calcined magnesite from North Korea, seawater MgO clinker, and oxidized MgO–C refractory brick were 97.4%, 98.3%, and 87.2%, respectively. Therefore, the primary and secondary resources containing MgO used in this study are suitable feedstocks for the novel Mg metal production process using MgO as a feedstock.

**Fig. 3** XRD results of feedstocks used in this study



### *Molten Salt Electrolysis*

As shown in Table 2, the average cell potential measured was 2.43–2.67 V when the electrolysis of primary and secondary MgO resources was conducted in the  $\text{MgF}_2\text{-LiF-KCl}$  molten salt at 1043 K by applying an average current of 1.44 A for 12.5 h. The average cell potential measured is 0.81–1.05 V lower than the theoretical decomposition voltage of KCl, the supporting electrolyte component with the lowest theoretical decomposition voltage at 1043 K under standard state [12]. In addition, the theoretical decomposition voltage of MgO obtained using a graphite anode is 1.47–1.50 V at 1043 K [12], and the estimated decomposition voltage of MgO obtained using a graphite anode is 1.76 V at 1083 K [9]. Therefore, regardless of the type of feedstock, the electrolysis of MgO proceeded without the generation of  $\text{Cl}_2$  gas or fluorine ( $\text{F}_2$ ) gas by the decomposition of the supporting electrolyte during the electrolysis.

Figure 4 shows the current efficiencies obtained after the electrolysis of the MgO-containing resources used in this study. The current efficiency was calculated using Eq. (1) [6–10].

$$\begin{aligned} &\text{Current efficiency, } \eta(\%) \\ &= \left( \frac{\text{Actual weight of Mg obtained}}{\text{Theoretical weight of Mg obtained using Faraday's law}} \right) \times 100 \quad (1) \end{aligned}$$

**Table 1** Compositions of primary and secondary MgO resources used in this study

Species	Concentration of element $i$ , $C_i$ (mass%) <sup>a</sup>										
	MgO <sup>b</sup>	Al <sub>2</sub> O <sub>3</sub>	SiO <sub>2</sub>	Li <sub>2</sub> O	Fe <sub>2</sub> O <sub>3</sub>	Na <sub>2</sub> O	K <sub>2</sub> O	CaO	Cr <sub>2</sub> O <sub>3</sub>	MnO	
Calcined magnesite from North Korea	97.4	0.19	0.38	N.D	0.19	0.03	0.02	1.75	N.D	0.01	
Seawater MgO clinker	98.3	0.25	0.79	N.D	0.22	0.01	N.D	0.42	0.01	0.05	
Oxidized MgO–C refractory brick	87.2	8.22	2.59	N.D	0.64	0.03	0.08	1.03	0.18	0.04	

<sup>a</sup> Determined by ICP-OES and ICP-MS analysis; N.D: Not Detected (< 0.0001–0.0050 mass%).

<sup>b</sup> The purity of MgO (%) was calculated as follows: 100 – (sum of concentrations of metal oxides except MgO).

**Table 2** Experimental conditions and results for the electrolysis of MgO-containing resources using a Cu cathode in MgF<sub>2</sub>-LiF-KCl molten salt at 1043 K

Exp. no. <sup>a</sup>	Feed	Feed weight, $w_{\text{feed}}/\text{g}$	Avg. potential, $E/\text{V}$	Conc. of element $i$ , $C_i$ (mass%) <sup>b</sup>				
				Mg	Li	Al	Si	Cu
210224	Calcined magnesite from North Korea	30.00	2.43	14.0	0.09	0.05	0.04	Bal.
210318	Seawater MgO clinker	30.00	2.67	14.4	0.03	0.06	0.02	Bal.
210228	Oxidized MgO-C refractory brick	40.00	2.48	14.3	0.10	0.08	0.03	Bal.

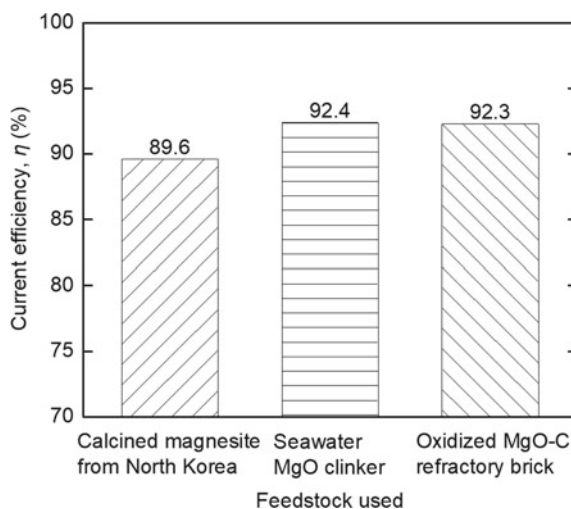
<sup>a</sup> Experimental conditions;

(1) Weight of MgF<sub>2</sub> = 256.0 g, weight of LiF = 219.0 g, and weight of KCl = 25.0 g

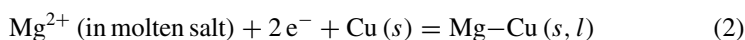
(2) Weight of Cu pellets used for the cathode = 45.0 g

(3) Reaction time,  $t$  = 12.5 h, applied average current,  $i$  = 1.44 A

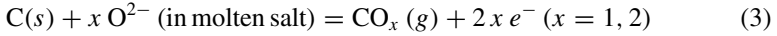
<sup>b</sup> Determined by ICP-OES analysis

**Fig. 4** Current efficiencies obtained after the electrolysis of MgO-containing resources used in this study

As shown in Fig. 4, the current efficiency of 89.6–92.4% was obtained when the Mg alloy of 14.0–14.4 mass% Mg was produced after the electrolysis of the calcined magnesite from North Korea, seawater MgO clinker, and oxidized MgO-C refractory brick. Therefore, when the values of the high current efficiency and average cell potential are considered, the reduction of Mg<sup>2+</sup> ions by Eq. (2) and the oxidation of O<sup>2-</sup> ions by Eq. (3) were the reactions that mainly occurred at Cu cathode and graphite anode, respectively, during the electrolysis.







However, the experimental results showed that the current efficiency of electrolysis did not reach 100%. In the molten salt electrolytic process using a high-density metal cathode, the occurrence of side reactions and evaporation of Mg from Mg alloy can affect the current efficiency of electrolysis. Meanwhile, it is shown in Table 2 that the Mg alloys obtained after the electrolysis contain total impurities with a concentration of 0.11–0.21 mass%. Therefore, the occurrence of side reactions such as the reaction between aluminium oxide (Al<sub>2</sub>O<sub>3</sub>) and reduced Mg was one of the reasons for the decrease in the current efficiency [6, 9].

Meanwhile, Fig. 5 shows that the vapor pressure of Mg in the Mg alloy increases to  $9.21 \times 10^{-4}$  atm as the Mg concentration in the Mg–Cu alloy approaches 15 mass% at 1043 K [13]. Although Mg evaporates actively from the Mg alloy when its vapor pressure in Mg alloy becomes larger than 0.01 atm [14], the vapor pressure of  $9.21 \times 10^{-4}$  atm is sufficient for the evaporation of a certain amount of Mg from Mg alloys. Therefore, the evaporation of Mg is also thought to contribute to the reduction in current efficiency during the electrolytic production of 15 mass% Mg–Cu alloy at 1043 K.

Interestingly, the concentration of impurities analyzed in the Mg alloys obtained after the electrolysis was low, although the feedstock contained a large amount of corresponding oxides. In the case of the oxidized MgO–C refractory brick feed, it contained 8.22 mass% Al<sub>2</sub>O<sub>3</sub> as the impurity. However, only trace amounts of

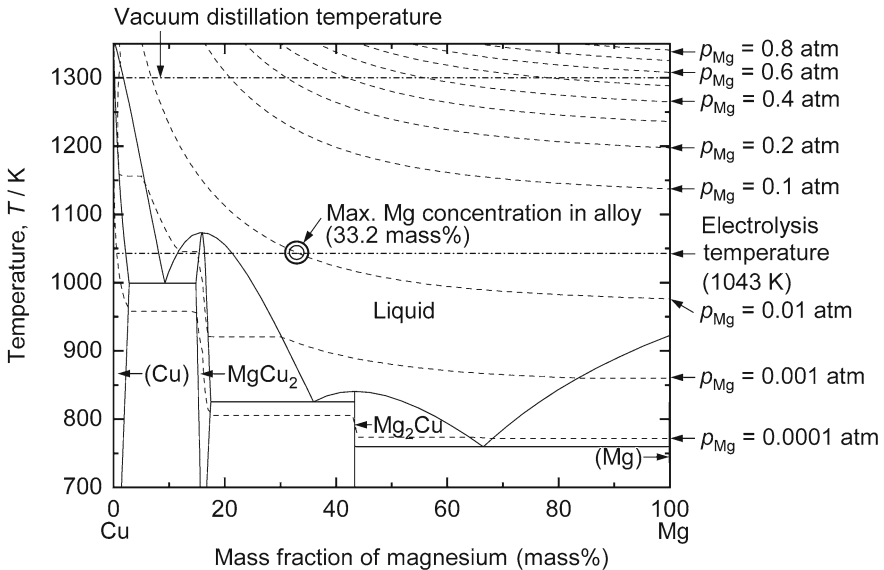
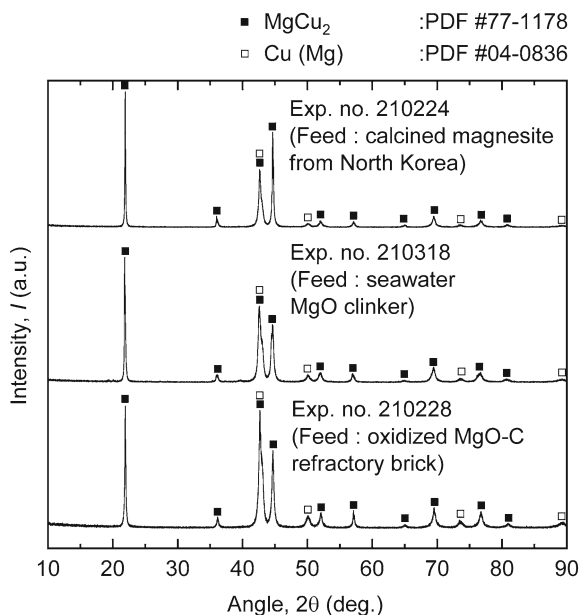


**Fig. 5** Phase diagram of the Mg–Cu binary system with the isobaric line of vapor pressure of Mg as a function of the temperature and Mg concentration

**Fig. 6** XRD results of Mg alloys obtained after the electrolysis of MgO-containing feedstock used in this study



aluminium (Al) were identified in the Mg alloy obtained after the electrolysis. Therefore, this result indicates that the electroreduction of  $\text{Al}_2\text{O}_3$  dissolved in the  $\text{MgF}_2$ – $\text{LiF}$ – $\text{KCl}$  at 1043 K, which can affect the electroreduction of MgO in the feedstock, was limited during the electrolysis.

Figure 6 shows the results of the XRD analysis of the Mg alloys obtained after the electrolysis. As expected from Fig. 5, the Mg alloy containing 14.0–14.4 mass% Mg had a mixture of  $\text{MgCu}_2$  and Cu (Mg) phases.

### *Vacuum Distillation of Obtained Mg Alloy*

As presented in Table 3, when the Mg alloys obtained after the electrolysis of primary and secondary MgO resources were vacuum distilled at 1300 K for 10 h, Mg metals with a purity more than 99.994% were produced.

Meanwhile, Table 3 shows the decrease in the concentrations of lithium (Li) in the alloys after vacuum distillation. Because Li has a vapor pressure of 0.07 atm at 1300 K [12], it is expected that Li would evaporate from the Mg alloys during vacuum distillation. However, when the concentration of Li in the Mg metal, < 0.001 ppm, is taken into account, Li is expected to be deposited in a region different from that where Mg is present.

**Table 3** Experimental conditions and analytical results of vacuum distillation of Mg alloy obtained after the electrolysis

Exp. no. <sup>a</sup>	Feed alloy	Concentration of element $i$ , $C_i$ (mass%)					
		Mg metal produced	Residue at bottom of reactor <sup>c</sup>				
		Mg <sup>b</sup>	Mg	Li	Al	Si	Cu
Alloy obtained using calcined magnesite from North Korea			14.0	0.09	0.05	0.04	Bal.
Alloy obtained using seawater MgO clinker			14.4	0.03	0.06	0.02	Bal.
Alloy obtained using oxidized MgO–C refractory brick			14.3	0.10	0.08	0.03	Bal.
210405	Alloy from Exp. no. 210224	99.994	1.40	N.D	0.05	0.05	Bal.
210408	Alloy from Exp. no. 210318	99.999	1.41	N.D	0.07	0.03	Bal.
210406	Alloy from Exp. no. 210228	99.994	1.51	N.D	0.10	0.04	Bal.

<sup>a</sup> Experimental conditions;

(1) Reaction temp.  $T = 1300$  K, reaction time,  $t = 10$  h, and feed alloy weight,  $w_{\text{feed}} = 30$  g

(2) Titanium sponge was used in Exp. no. 210408

<sup>b</sup> Determined by GD-MS analysis; The purity of Mg was calculated by subtracting the sum of all impurities except gaseous species, Detection limit of the GD-MS was  $< 0.001 - 0.144$  ppm

<sup>c</sup> Determined by ICP-OES analysis; N.D: Not Detected ( $< 0.0025 - 0.0060$  mass%)

## Conclusions

A feasibility of the novel Mg metal production process for producing Mg metal from various MgO resources was investigated. The electrolysis of the calcined magnesite from North Korea, seawater MgO clinker, and oxidized MgO–C refractory brick yielded Mg–Cu alloys of 14.0–14.4 mass% Mg when an average current of 1.44 A was applied at 1043 K for 12.5 h. The current efficiencies of 89.6–92.4% were obtained after the electrolysis of the primary MgO resources, such as calcined magnesite from North Korea and seawater MgO clinker. The current efficiency of 92.3% was obtained after the electrolysis of the secondary MgO resource, oxidized MgO–C refractory brick, owing to the high MgO purity. When vacuum distillation of the Mg alloy was conducted at 1300 K for 10 h, high-purity Mg metal with a purity of 99.994–99.999% was produced, regardless of the type of feedstock. Thus, high-purity Mg metal production from various MgO resources is feasible through the novel electrolytic process using a Cu cathode, followed by vacuum distillation.

## References

1. Zhong C, Liu F, Wu Y, Le J, Liu L, He M, Zhu J, Hu W (2012) Protective diffusion coatings on magnesium alloys: a review of recent developments. *J Alloys Compd* 520:11–21
2. Friedrich HE, Mordike BL (eds) (2006) *Magnesium technology: metallurgy, design data, applications*. Springer, Berlin
3. Pidgeon LM, Alexander WA (1944) Thermal production of magnesium-pilot plant studies on the retort ferrosilicon process. *Trans Am Inst Min Mater Eng* 159:315–352
4. Krishnan A, Lu XG, Pal UB (2005) Solid oxide membrane process for magnesium production directly from magnesium oxide. *Metall Mater Trans B* 36:463–473
5. Guan X, Pal UB, Powell AC (2014) Energy-efficient and environmentally friendly solid oxide membrane electrolysis process for magnesium oxide reduction: experiment and modeling. *Metall Mater Trans E* 1:132–144
6. Lee TH, Okabe TH, Lee JY, Kim YM, Kang J (2020) Molten salt electrolysis of magnesium oxide using a liquid-metal cathode for the production of magnesium Metal. *Metall Mater Trans B* 51:2993–3006
7. Lee TH, Okabe TH, Lee JY, Kim YM, Kang J (2021) Development of a novel electrolytic process for producing high-purity magnesium metal from magnesium oxide using a liquid tin cathode. *J Magnes Alloy* 9:1644–1655
8. Lee DH, Jeoung HJ, Lee TH, Yi KW, Lee JY, Kim YM, Okabe TH, Kang J (2021) Scale-up study of molten salt electrolysis using Cu or Ag cathode and vacuum distillation for the production of high-purity Mg metal from MgO. *J Sustain Metall* 7:883–897
9. Jeoung HJ, Kim Y, Lee TH, Lee JY, Kim YM, Yi KW, Kang J (2022) A novel electrolytic process using a Cu cathode for the production of Mg metal from MgO. *J Appl Electrochem* 52:1535–1549
10. Jeoung HJ, Lee TH, Kim Y, Lee JY, Kim YM, Okabe TH, Yi KW, Kang J (2022) Use of various MgO resources for high-purity Mg metal production through molten salt electrolysis and vacuum distillation. *J Magnes Alloy*. <https://doi.org/10.1016/j.jma.2022.07.009>
11. Bray EL (2017) Magnesium [Advance release]. In: U.S. geological survey minerals yearbook 2017-metals and minerals. U.S. Geological Survey
12. Barin I (1995) *Thermochemical data of pure substances*. VCH Verlagsgesellschaft mbH, Weinheim
13. Bale CW, Belisle E, Chartrand P, Deckerov SA, Eriksson G, Gheribi AE, Hack K, Jung IH, Kang YB, Melancon J, Pelton AD, Petersen S, Robelin C, Sangster J, Spencer P, Van Ende MA (2016) FactSage thermochemical software and databases, 2010–2016. *Calphad* 54:35–53
14. Kang J, Okabe TH (2014) Thermodynamic consideration of the removal of iron from titanium ore by selective chlorination. *Metall Mater Trans B* 45:1260–1271

# Recovery of Copper Metal from Discarded Printed Circuit Boards (PCBs) by Hydrometallurgical and Electrometallurgical Processes



Om Shankar Dinkar, Rukshana Parween, Rekha Panda, Pankaj K. Choubey, Balram Ambade, and Manis Kumar Jha

**Abstract** Limited metal resources and significant environmental hazards have urged researchers to find sustainable technology for recycling of waste printed circuit boards (PCBs) to recover metals. Therefore, the present paper is focused on the recovery of copper (Cu) from waste PCBs using mechanical pre-treatment followed by hydrometallurgical processing. Initially, depopulated PCBs were pre-treated to get enrich copper in metallic concentrate. Further, experiments were carried out with varying different process parameters, i.e. acid concentration, oxidant concentration, time, etc., to obtain optimized condition for efficient Cu leaching from metallic concentrate. It was found that 99.9% Cu was leached using 20% H<sub>2</sub>SO<sub>4</sub> at 75 °C in the presence of 20% H<sub>2</sub>O<sub>2</sub> within 120 min maintaining 100 g/L pulp density. The obtained leach liquor could be used for electro-winning to recover pure copper metal.

**Keywords** Waste printed circuit boards · Pre-treatment · Froth flotation · Hydrometallurgy processes

## Introduction

Due to rapid economic growth and continuous replacement of old electrical and electronic devices with advanced one resulted in the generation of massive amount of discarded e-waste such as personal computer, printer, and mobile phone. These e-wastes essentially contain printed circuit boards (PCBs) as a key component which is made up of glass reinforced resin and copper metal sheet including valuable metals (silver, gold, platinum, etc.) and hazardous metals. It has been reported that 52 million metric tons (Mt) e-waste were generated in 2021. But, only 10–20% e-waste are recycled by formal sector while others remain unaccounted or treated by informal sector

---

O. S. Dinkar · R. Parween · R. Panda · P. K. Choubey · M. K. Jha (✉)  
Metal Extraction and Recycling Division, CSIR-National Metallurgical Laboratory,  
Jamshedpur 831007, India  
e-mail: [mkjha@nmlindia.org](mailto:mkjha@nmlindia.org)

O. S. Dinkar · B. Ambade  
Department of Chemistry, National Institute of Technology, Jamshedpur 831014, India

which may cause environmental pollution as well as loss of valuables. Hence, it has been necessary to develop sustainable process for recovery of metals from e-waste in an eco-friendly way. Various processes have been reported for the recovery of metals from PCBs using pyrometallurgical and hydrometallurgical processes. During the pyrometallurgical process, poisonous fumes were evolved. Therefore, hydrometallurgical process consisting of pre-treatment, leaching, and solvent extraction has been considered adequate for metal recovery from PCBs [1–4].

As a result, the hydrometallurgical approach, which includes pre-treatment, leaching, solvent extraction, evaporation, and electro-winning procedures, is determined to be the best for recycling valuable metals with high commercial grade. As a result, there have been earnest attempts made globally to develop a process that uses mechanical pre-treatment in conjunction with hydrometallurgical technology [5].

The development of a revolutionary recycling method for PCBs, which involves releasing the metals from the PCBs through organic swelling and then treating the resin to get rid of or recover the hazardous soldering elements, has been the subject of several investigations. Lead, a dangerous metallic component, must be recovered from the resin's freed resin. Fresh solder that contained 63.9% Pb and the remainder Sn was used for leaching investigations. According to experimental findings under various circumstances, lead dissolved with 6 M  $\text{HNO}_3$  at a solid-to-liquid (S/L) ratio of 1:10 (g/mL) in 75 min [6]. Sulfuric acid and hydrogen peroxide leaching are optimized, and the amount of chemicals used at each stage is estimated. With 75 g/L pulp density and 3.5 mol/L sulfuric acid and 6% hydrogen peroxide, two optimum conditions for the leaching of copper were discovered and experimentally verified. These conditions differed in leaching temperature and time (186 min, at 60 °C, at 20 °C versus 60 min). Using electro-winning, copper was extracted directly from the leachate with a recovery rate of over 92% and a product purity of over 99.9%. Hydrogen peroxide and strong sulfuric acid were added during five consecutive recirculation cycles, and recovery rates were high [7].

From the extensive literature review made, it can be concluded that there is still lack of feasible and indigenous technology for complete recovery of valuables from waste PCBs in view of its feasibility and environmental concern. Due to significant conflict between availability of natural resources and lack of viable technology, laboratory scale Know-How has been developed by scientists at CSIR-NML to recover Cu from metallic friction of waste PCBs using hydrometallurgical route. The developed process is feasible and economical and will be helpful to fulfill the future demands of this metal.

## Experimental

### *Materials*

Scrap personal computers (PCs) were collected from local market and used for experimental purpose. Initially, PCs were disassembled to separate the PCBs and other components. Thereafter, PCBs were mechanically pre-treated using crushing, grinding, and gravity separation process to enrich the metallic values in concentrate. The typical analysis of metal values in metallic concentrate is presented in Table 2. Different leaching agents like sulfuric acid and hydrogen peroxide were supplied by Merck, India, used for experimental purpose to leach the metals whereas deionized water was used for dilution of sample.

### *Methodology*

#### **Pre-treatment of the Waste PCBs**

PCBs were dismantled and depopulated using hot air gun (DeWalt D26414). Naked PCBs were used for mechanical pre-treatment. Then, reduced size naked PCBs were pulverized into fine powder using pulverizer. Pulverized product comprised metallic concentrate, mix-metallic fractions, and epoxy resins. Further, the pulverized product was sieved in sieve shaker using mesh size of 150 ( $\mu$ ) microns which separates over-sized materials and fine particles of pulverized PCBs. The sieved metallic concentrate contains copper, nickel, lead, tin, aluminum, and iron. Thereafter, gravity separation technique was followed up using spiral concentrator or by thoroughly mixing the concentrate in water using mixer rod.

Heavier metallic concentrate was settled at the bottom, and epoxy resins are floated at the top of the slurry system which were skimmed off from the system and collected separately. Ceramics consisting of water and metallic concentrate containing pure copper with some impurities were collected separately. The copper containing concentrate is washed and dried in vacuum oven at temperature of 120 °C for 3 h whereas undersized ceramics is filtered and dried, and water is recycled for further processing. The process scheme developed for the recovery of copper concentrate from PCBs is shown in Fig. 1.

The samples are very heterogeneous in nature and mainly depend on the quality and type of PCBs used for various applications. Data collected by few sets of experiments based on 1 kg waste PCBs after every step of pre-treatment are shown in Table 1. The typical composition of metals in the PCBs samples is shown in Table 2.

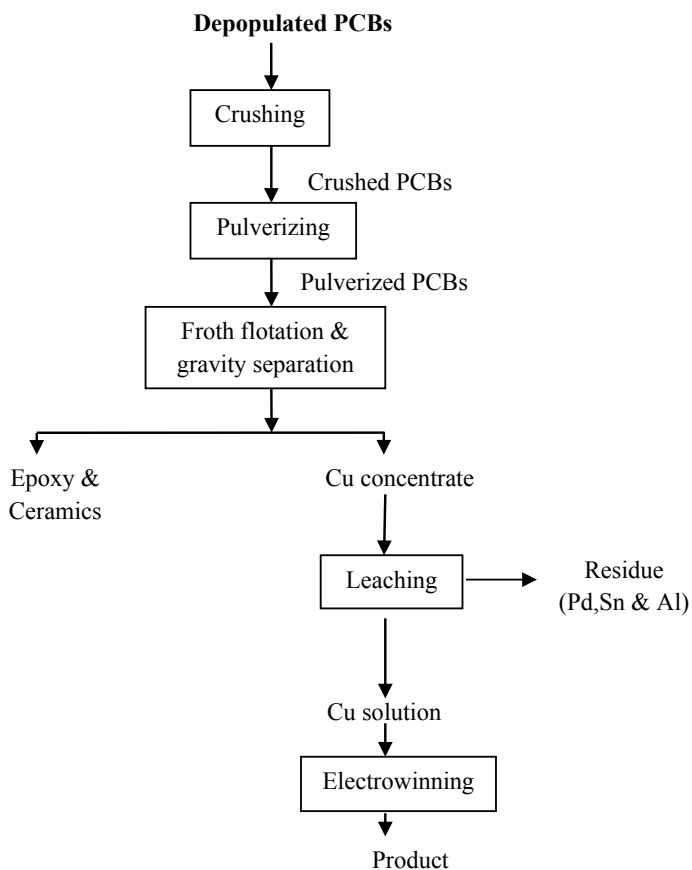


**Fig. 1** Proposed flow-sheet for the processing of waste PCBs

**Table 1** Data collected based on 1 kg waste PCBs

Wt. after cutting (g)	Total wt. after pulverize-1 and 2 + Sieve (g)	Wt. of mix-metals (g)	Wt. of epoxy and ceramics (g)	Wt. of metallic concentrate (g)
900	790	60	589	213
994	859	59	565	255
994	831	78	509	244

**Table 2** Composition of metals in metallic concentrate

Elements	Cu	Ni	Pb	Sn	Al	Fe
Wt. (%)	94.39	0.05	1.74	1.51	1.5	0.8



## Leaching Studies

The leaching experiment was carried out in 2 L three necked round-bottomed leaching reactor fitted with condenser and temperature control sensor with continuous stirring at fixed rpm, which was placed on hot plate to control temperature and stirring speed. Various process parameters were, viz. effect of leachate concentration; time, temperature, pulp density, and stirring speed were optimized. Further, a fixed amount of metallic concentrate is precisely weighted and then sulfuric acid ( $\text{H}_2\text{SO}_4$ ) and hydrogen peroxide ( $\text{H}_2\text{O}_2$ ) is used as leaching agents. When the solution temperature reaches up to desired temperature, then sample was added slowly with continuous stirring at fixed rpm. The Cu metal and other impurities present in the concentrate were leached using 20%  $\text{H}_2\text{SO}_4$  and 20%  $\text{H}_2\text{O}_2$  at 75 °C for 2 h to maintain pulp density of 100 g/L for maximum dissolution of metals. Leach liquor was filtered, and the residue obtained was washed (Pd, Sn & Al), dried in vacuum oven, and further treated for electro-winning. The chemical reactions occurring in  $\text{H}_2\text{SO}_4$  and  $\text{H}_2\text{O}_2$  media are presented Eq. 1 [8].



## Analytical Procedure

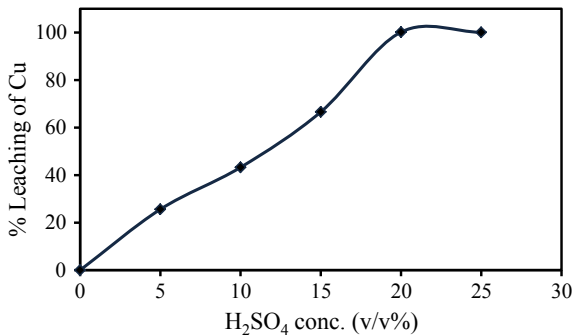
Atomic absorption spectrometer (AAS, VARIAN AA240 + VGA77) was used for analysis of metals in the leach liquor generated during leaching studies. pH meter (Model: 797 Basic Titrimo; Make: Metrohm, Switzerland) with an electrode and automated temperature correction was used to measure the pH of the solution.

## Results and Discussion

### *Effect of Leachate Concentration*

Leaching experiments were carried out by varying the sulphuric acid from 5 to 25% (v/v) at 75 °C for 120 min in the presence of an oxidant ( $\text{H}_2\text{O}_2$ ) to leach the copper from metallic concentrate of PCBs. Figure 2 shows that 25.60% Cu was leached with 5%  $\text{H}_2\text{SO}_4$  at 75 °C in 120 maintaining pulp density 100 g/L, while 99.9% Cu was leached in 20%  $\text{H}_2\text{SO}_4$  while other parameters were kept constant. The enhancement in leaching efficiency was observed with increase in acid concentration due to increase in the flow of  $\text{H}^+$  ions across the particle boundaries of metallic concentrate [9]. Further, increase in acid concentration above 20%  $\text{H}_2\text{SO}_4$  had no effect on the leaching efficiency of copper. Therefore, 20%  $\text{H}_2\text{SO}_4$  has been considered as

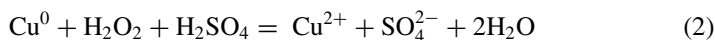
**Fig. 2** Effect of H<sub>2</sub>SO<sub>4</sub> Conc. (v/v%) [Acid—20% H<sub>2</sub>O<sub>2</sub> Time - 120 min, Temperature - 75 °C, and Pulp density - 100 g/L]



optimum sulphuric acid concentration for copper leaching from metallic fraction of PCBs.

### *Effect of H<sub>2</sub>O<sub>2</sub> Concentration*

To determine the effect of oxidant (H<sub>2</sub>O<sub>2</sub>) concentration on the leaching of Cu from the metallic concentrate of waste PCBs, the experiment was performed using a pulp density of 100 g/L, time of 120 min, temperature of 75 °C, and 20% sulphuric acid. It was observed that the leaching percentage of copper increased with an increase in oxidant concentration (H<sub>2</sub>O<sub>2</sub>) as shown in Fig. 3. The leaching percentage of copper was increased from 28 to 99.9% with an increase in the concentration of H<sub>2</sub>O<sub>2</sub> from 5 to 20% (v/v). When H<sub>2</sub>O<sub>2</sub> breaks down, oxygen is produced. This oxygen combines with copper to form cupric oxide, which then reacts with H<sub>2</sub>SO<sub>4</sub> to form cupric sulphate [10, 11]. Equation (2) shows the leaching reaction, in which sulphuric acid and hydrogen peroxide act together actively as reactants [10].



### *Effect of Time*

Experiments were conducted by varying time range from 5 to 150 min by maintaining pulp density of 100 g/L at 75 °C to optimize the equilibration time for the leaching of Cu from metallic fraction. The results (Fig. 4) show that leaching reaction of copper increases with increase in mixing time. 36.22% copper dissolved in 5 min, whereas 99.9% copper dissolved was found in 120. Additionally, increasing the reaction time has no effect on effectively dissolving the copper. It shows that the reaction has

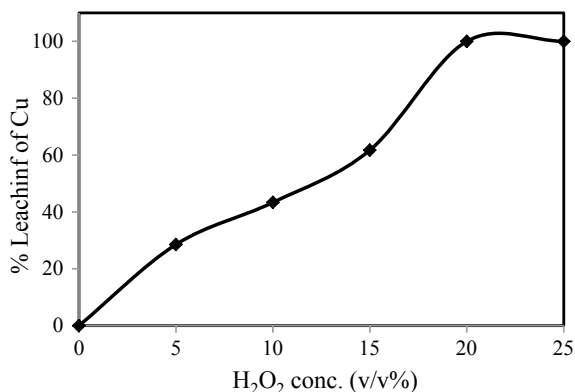


**Fig. 3** Effect of H<sub>2</sub>O<sub>2</sub> Conc.(v/v%) [Acid—20% H<sub>2</sub>SO<sub>4</sub>, Time - 120 min, Temperature - 75 °C, and Pulp density - 100 g/L]

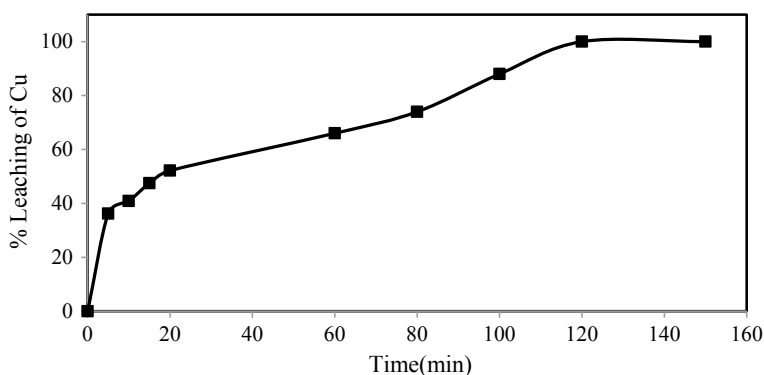


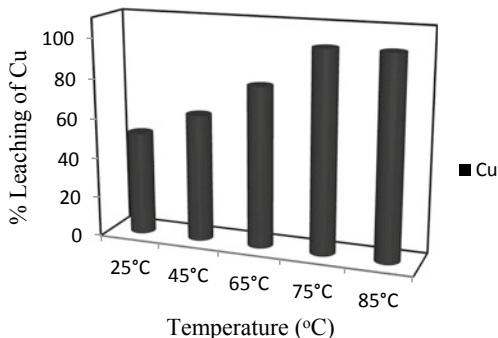
**Fig. 4** Effect of time [Acid—20% H<sub>2</sub>SO<sub>4</sub> + 20% H<sub>2</sub>O<sub>2</sub> (v/v), Pulp density - 100 g/L, and Temperature - 75 °C]

reached equilibrium in 120 min, so 120 min is chosen as the optimized reaction time for the dissolution of copper from metallic friction.

### *Effect of Temperature*

To see the role of temperature on copper leaching from metallic concentrate of PCBs, experiments were carried in a range of temperature varying from 25 to 85 °C in 20% H<sub>2</sub>SO<sub>4</sub> and 20% H<sub>2</sub>O<sub>2</sub> (v/v) for 20 min at pulp density of 100 g/L. It was found that leaching of copper increased from 51.7 to 99.99%, with increase in temperature from 25 to 75 °C (Fig. 5) due to increase in the rate of reaction. It was observed that

**Fig. 5** Effect of temperature [Acid—20% H<sub>2</sub>SO<sub>4</sub> + 20% H<sub>2</sub>O<sub>2</sub>, Pulp density - 100 g/L, and Time-120 min]



reaction attained the equilibrium at 75 °C and further temperature had no significant effect on copper leaching. Therefore, 75 °C has been chosen as optimum temperature for copper dissolution.

### Kinetic Studies

The leaching data obtained at different times (5–120 min) and temperatures (25–75 °C) were fitted with kinetics models/equations to determine the leaching mechanism of copper [12]. In all these equations for copper, this equation was selected  $(1-(1-X)^{1/2}K_c t)$ , where  $K_c$  is the reaction rate constant ( $\text{min}^{-1}$ ),  $t$  = time (min), and  $x$  = value and reaction the basis of metal fraction (% extraction/100) is shown in Fig. 6. The highest value of  $R^2$  is considered to be the basis for selecting the equation for one of the models, i.e. the regression coefficient obtained in the case of mixed samples and constants. The complete process flow-sheet developed for the recovery of Cu from metallic friction from waste PCBs is presented in Fig. 7.

*Film diffusion control dense constant size small particles in all geometries (Eq. 3)*

**Fig. 6** Kinetics of Cu dissolution [Acid: 20% H<sub>2</sub>SO<sub>4</sub> + 20% H<sub>2</sub>O<sub>2</sub> (v/v) and Pulp density: 100 g/L]

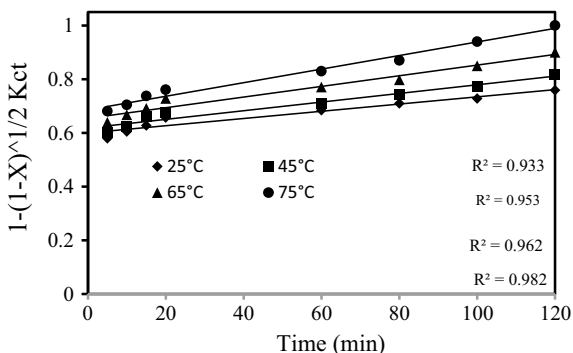
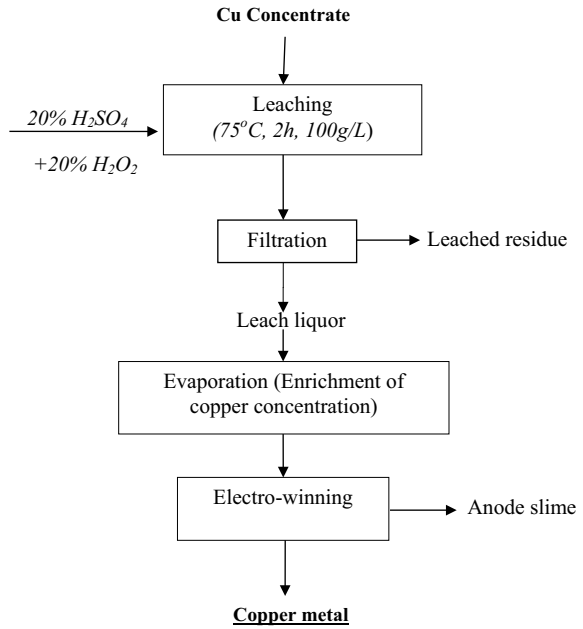


**Fig. 7** Developed process flow-sheet to recover Cu from copper concentrate of discarded PCBs



$$X K ct \tag{3}$$

*Film diffusion control dense shrinking spheres (Eq. 4)*

$$1 - (1 - X)^{2/3} K ct \tag{4}$$

*Chemical reaction control dense constant size cylindrical particles (Eq. 5)*

$$1 - (1 - X)^{1/2} K ct \tag{5}$$

*Chemical reaction control dense constant size or shrinking spheres (Eq. 6)*

$$1 - (1 - X)^{1/3} K ct \tag{6}$$

*Ash diffusion control dense constant size spherical particles (Eq. 7)*

$$1 - 3(1 - X)^{2/3} + 2(1 - X) K ct \tag{7}$$

## Treatment of Residues, Effluent, and Gases Evolved During Metal Recovery

After the metal was dissolved, the leached residue was primarily subjected to TCLP testing before being used or disposed of in the environment. The residue was safe for use as disposal because the presence of metals was below the allowed limit, according to the TCLP results. The gases produced during the leaching process were condensed back because the leaching was done in a reactor with a condenser. After extraction, the effluent was collected and taken to effluent treatment facility for neutralization, where the pH was measured and kept at 7 before being disposed of otherwise we can reuse after treating.

## Conclusions

In this study, a feasible process to recover Cu from waste printed circuit boards (PCBs) using the hydrometallurgical route is developed. The following steps are involved to achieve the above objective:

- More than 94% metallic concentrate was observed by the mechanical froth flotation and gravity separation processes.
- It was found that 99.9% Cu leached with 20% sulfuric acid and 20% H<sub>2</sub>O<sub>2</sub> (v/v) at 75 °C, 100 g/L, and time 120 min.
- Copper leaching followed the shrinking core model in this Eq.  $1-(1-X)^{1/2}Kct$ .

**Acknowledgements** The authors are grateful to the Director, CSIR-National Metallurgical Laboratory, Jamshedpur, India, for kind cooperation.

## References

1. Rajahalm J, Peramaki S, Budhathoki R, Vaisanen A (2021) Effective recovery process of copper from waste printed circuit boards utilizing recycling of leachate. *Adv Manuf* 4:73
2. Babu BR, Parande AK, Basaha CA (2007) Electrical and electronic waste a global environmental problem. *J Waste Manag* 25:307–318
3. Choubey PK, Panda R, Jha MK, Lee JC, Pathak DD (2015) Recovery of copper and recycling of acid from the leach liquor of discarded printed circuit boards (PCBs) *Sep. Purif Technol* 156:269–275
4. Jha MK, Choubey PK, Kumar A, Kumar R, Kumar V, Lee JC (2011) Recycling of electronic waste. II Proceedings of the second symposium
5. Lee JC, Kim DJ (2004) Product recovery and impurity control i: pure products from clean processing. Proceedings of hydrometallurgy conference
6. Zhang Y, Xie S, Zeng X, Li J (2012) Current status on leaching precious metals from waste printed circuit boards. *Procedia Environ Sci* 16:560–568

7. Sawahbkeh RA (2010) Hydrometallurgical extraction of zinc from Jordanian electric arc furnace dust. *Hydrometallurgy* 104:61–65
8. Birloaga I, Michelis ID, Ferella F, Buzatu M, Veglio F (2013) Study on the influence of various factors in the hydrometallurgical processing of waste printed circuit boards for copper and gold recovery. *J. Waste Manag* 33:935–941
9. Flores-campos R, Estrada-ruiz RH, Velarde-sánchez EJ (2017) Study of the physico chemical effects on the separation of the non-metallic fraction from printed circuit boards by inverse flotation. *J Waste Manag* 69:400–406
10. Wang JC, Wang H, Wang CQ, Zhang LL, Wang ZL (2017) A novel process for separation of hazardous poly (vinyl chloride) from mixed plastic wastes by froth flotation. *J. Waste Manag.* 69:59–65
11. Jha MK, Kumar V, Maharaj L, Singh RJ (2004) Studies on leaching and recycling of zinc from rayon waste sludge. *Ind Eng Chem Res* 43:1284–1295
12. Lee J, Kim S, Kim B, Lee JC (2018) Effect of mechanical activation on the kinetics of copper leaching from copper sulfide (CuS). *Metals* 8:150–158

**Part III**  
**New Extractant and Biometallurgical**  
**Processing**



# New Insights on Titanium(IV) Speciation to Improve the Purification of Concentrated Phosphoric Acid



Alexandre Chagnes, Lucas Mangold, Hubert Halleux, and Gérard Cote

**Abstract** The first step of phosphoric acid production consists of leaching phosphate-containing material (mainly from primary resources) with sulfuric acid. During this step, a wide range of metallic elements are also leached, leading to high concentrations of impurities in phosphoric acid. Solvent extraction is the suitable technology to reach a high extraction efficiency of phosphoric acid while minimizing impurity co-extraction. In the case of an extraction solvent containing a mixture of *n*-tributyl phosphate (TBP) and di-*iso*-propyl ether (DiPE), titanium(IV) is co-extracted with phosphoric acid. In order to reduce titanium(IV) co-extraction, it is of great interest to understand the mechanisms involved at the liquid–liquid interface, which is controlled by the speciation. This paper gives an overview on the speciation of titanium(IV) in non-complexing media in order to get relevant information to investigate the titanium(IV) speciation in concentrated phosphoric acid.

**Keywords** Titanium(IV) · Speciation · Non-complexing media · Phosphoric acid

## Introduction

The production of phosphates is crucial since phosphates are used for many industrial applications in large quantities, including the production of fertilizers. Phosphorite and phosphorus have also been on the list of the 30 critical raw materials defined by the European Union since 2014 [1]. Worldwide, it is estimated that around 227

---

A. Chagnes (✉) · L. Mangold  
Université de Lorraine, CNRS, GeoRessources, 54000 Nancy, France  
e-mail: [alexandre.chagnes@univ-lorraine.fr](mailto:alexandre.chagnes@univ-lorraine.fr)

L. Mangold  
e-mail: [lucas.mangold@univ-lorraine.fr](mailto:lucas.mangold@univ-lorraine.fr)

L. Mangold · H. Halleux  
Prayon, Rue Joseph Wauters 144 À, B-4480 Engis, Belgium

G. Cote  
Institut de Recherche de Chimie Paris, PSL Research University, Chimie ParisTech – CNRS, 11  
Rue Pierre Et Marie Curie, 75005 Paris, France

million tonnes of marketable phosphates ( $P_2O_5$  content > 30% after ore beneficiation [2]) were produced in 2019 and 223 million in 2020 [3]. In 2020, the global demand in phosphate for fertilizers reached 47.1 million tons  $P_2O_5$  equivalent with a projected growth of 3% of additional demand each year [4].

The production of phosphoric acid from phosphate rocks relies on pyrometallurgy and hydrometallurgy. The pyrometallurgical route makes it possible to obtain a high purity phosphoric acid whose concentration is between 75 and 85% (m/m  $H_3PO_4$ ). However, this route is very marginal (approximately 5% in 2007) due to its high energy cost and its environmental impact. This route consists of a high-temperature reduction of the phosphates to phosphorus in an electric furnace in the presence of silica or coke [5]. The phosphorus thus produced is then recovered by condensation, and then it is oxidized and then hydrolyzed into phosphoric acid [6]. The majority of phosphate rock produced in the world is treated by a hydrometallurgical process, called “wet process”. It consists of a digestion of the phosphate rocks by using sulfuric acid. The phosphate, in the form of apatite (hydroxo, fluoro, or chlorapatite, formula  $XCa_5(PO_4)_3$  with  $X = Cl, F, OH$ ), is then converted into phosphoric acid while the calcium present in the apatite reacts with sulfates in solution to form gypsum  $CaSO_4$  (phosphogypsum). The phosphoric acid solution contains many impurities [7] including non-metallic inorganic anions such as fluoride, sulfate, or chloride. It also contains metallic impurities such as iron or titanium which can reach levels greater than 10 and 1  $g.kg^{-1}$ , respectively, or heavy metals such as arsenic or cadmium, both present at levels of several tens of  $mg.L^{-1}$  [8–10]. In order to obtain an acid with the required specifications for the desired application (fertilizer, food additives, the pharmaceutical industry, or electronics), various purification processes can be implemented. In general, these processes exploit liquid–liquid partitioning [11, 12], chelation [13, 14], precipitation [15], or adsorption of metals [16–20], sometimes with the goal to recover certain impurities such as rare earths [12, 20–23] or uranium [24, 25].

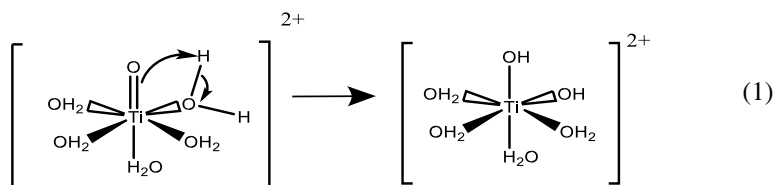
The technique most used to date to purify phosphoric acid remains liquid–liquid extraction. In all cases, during this stage, the leachate obtained by the wet process is put into contact with an organic extraction solvent, but this operation can have two different objectives: (i) selectively extracting the phosphoric acid by leaving the impurities in the raffinate as much as possible [26] and (ii) extracting the impurities (at least the most troublesome) so as to leave a purified phosphoric acid in the raffinate. This last option has been the subject of many developments, in particular to recover uranium from concentrated phosphoric acid [23, 25, 27–29]. However, most of the liquid–liquid extraction processes currently implemented at the industrial scale aim to selectively extract phosphoric acid while limiting the co-extraction of impurities. Regarding the selective extraction of phosphoric acid, different extraction systems have been proposed such as aliphatic alcohols [30, 31], Cyanex®923 (mixture of organophosphinic oxides) [32], methyl isobutyl ketone (MIBK) [7] tri-*n*-butylphosphate (TBP) [33], or mixtures of MIBK and TBP [32, 34]. After several stages of mineral processing such as concentration by gravimetric separation or by flotation, the phosphate rocks are leached with sulfuric acid. Several pre-treatments

to eliminate arsenic and sulphate are carried out before extracting the phosphoric acid by liquid–liquid extraction.

For example, the Prayon process is based on the liquid–liquid extraction of phosphoric acid using a mixture of TBP and di-iso-propyl ether (DiPE). This solvent makes it possible to obtain a phosphoric acid free of most of the initial impurities such as magnesium, iron, or aluminum. Nevertheless, it may happen that certain elements such as titanium are still present at high concentration in phosphoric acid after the liquid–liquid extraction stage. Additional operations must therefore be implemented to remove titanium. These additional operations thus increase the complexity and therefore the overall cost of the process for producing purified phosphoric acid. To date, the co-extraction mechanism of titanium in the organic phase during the purification process is unknown. To better understand the phenomena responsible for titanium(IV) co-extraction, it is necessary to know the speciation of this metal in concentrated phosphoric acid. In this paper, we will present the state of the art of titanium(IV) in non-complexing medium and the recent advances on this subject. The knowledge of titanium(IV) speciation in non-complexing aqueous media is indeed a prerequisite before investigating the speciation of titanium(IV) in complex media such as concentrated phosphoric acid.

## Titanium(IV) Chemistry

Titanium(IV) in solution undergoes spontaneous hydrolysis [35] leading to the formation of the titanyl ion  $\text{TiO}^{2+}$  (represented in its hydrated form on the left side of Eq. 1) [36]. However, other studies [35–38] consider the following reaction leading to the formation of  $[\text{Ti}(\text{OH})_2]^{2+}$  instead of  $\text{TiO}^{2+}$ :

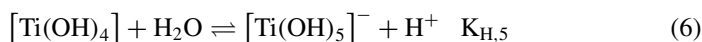
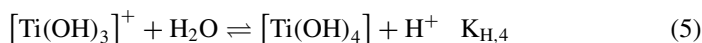
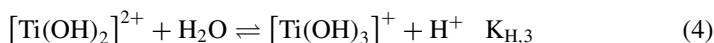
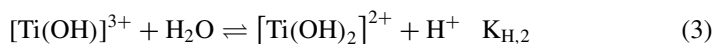
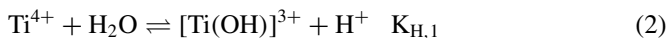


Actually, these two species may exist in solution [35]. Although the majority of authors who have studied the distribution of mononuclear titanium(IV) species have concluded that the  $\text{Ti} = \text{O}$  bond is stabilized only in the presence of complexing agents (such as in the presence of dimethylsulfoxide [39]), other authors like Grätzel et al. [40] gave evidence for the presence of  $\text{Ti} = \text{O}$  bonds in free titanium(IV) species in acidic solution. In this study, the Raman spectra of perchloric acid (ca.  $2 \text{ mol.L}^{-1}$ ) and hydrochloric acid (ca.  $2 \text{ mol.L}^{-1}$ ) containing titanium(IV) (ca.  $0.08 \text{ mol.L}^{-1}$ ) were recorded. A peak in the spectrum of titanium(IV)-hydrochloric acid system and a shoulder in the spectrum of the titanium(IV)-perchloric acid system at  $975 \text{ cm}^{-1}$

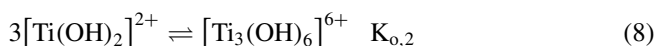
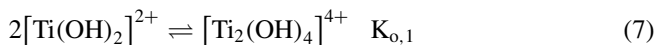
were observed and associated with the presence of the Ti = O bond within the titanium(IV) species present in solution. The peak detected by Raman spectroscopy at  $975\text{ cm}^{-1}$  could thus correspond to the vibration of a TiO bond within a polynuclear titanium(IV) species since this wavelength was also observed in other systems containing polyoxometalates between  $900$  and  $1100\text{ cm}^{-1}$  depending on the metal [41, 42]. In these studies, the vibration frequencies were attributed to the M–O bonds where M is a metal and O an oxygen engaged in an M–O–M bridge in polynuclear species.

However, the following two forms of the divalent cation of titanium(IV) were reported in solution:  $[\text{Ti}(\text{OH})_2]^{2+}$  or  $\text{TiO}^{2+}$ . Likewise, for higher degrees of hydrolysis, the species  $[\text{Ti}(\text{OH})_5]^-$  is sometimes referred to in the literature as  $\text{HTiO}_3^-$ . Generally, for titanium as for other metals, the speciation of more or less hydrolyzed free titanium(IV) is studied in perchloric acid. Since the perchlorate ion ( $\text{ClO}_4^-$ ) is not very complexing [43], it is possible to change the pH without modifying titanium(IV) speciation. Several studies have been conducted to determine the equilibrium constants of the different species of titanium(IV) in non-complexing medium [37, 38, 44–47]. Although the publications more or less agree on the fact that the most stable titanium(IV) species in acidic aqueous medium ( $\text{pH} < 3$ ) is the divalent cation  $[\text{Ti}(\text{OH})_2]^{2+}$ , the protonation constants of this species vary from one publication to another and the authors disagree on the predominant species in neutral solution and slightly alkaline solution.

Usually, the following equilibria are considered [38, 44]:



However,  $[\text{Ti}(\text{OH})]^{3+}$  is usually the more acidic form of titanium(IV) considered in the literature. In some cases, the following oligomerization equilibria are also considered [48]:



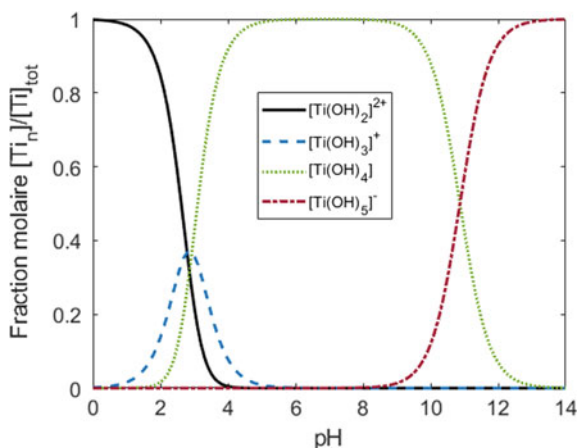
The speciation of mononuclear titanium(IV) species in solution was studied by different techniques. Liberti et al. [44] determined the equilibrium constants by using the liquid–liquid extraction method, i.e. by contacting an aqueous phase containing titanium(IV) and perchloric acid with an organic phase composed of 8-hydroxyquinoline diluted in chloroform or 2-thenoyltrifluoroacetone (TTA) diluted in benzene. The influence of pH from 0 to 4 at constant ionic strength ( $0.1 \text{ mol.L}^{-1} \text{ ClO}_4^-$ ) on the distribution ratio of titanium(IV) was studied. This method led to the conclusion that  $\text{Ti}(\text{OH})^{3+}$  is the main species for pH values between 0 and 1.7 while  $\text{Ti}(\text{OH})_2^{2+}$  is predominant between pH 1.7 and 2.2, and  $\text{Ti}(\text{OH})_4$  exists at pH greater than 2.2.

Other methods were used to study the hydrolysis of free titanium(IV) in perchloric acid [49, 31]. For example, Sugimoto et al. [49] recorded the UV–Vis spectra of solutions prepared by dissolving a precipitate of titanium(IV) hydroxide in perchloric acid (so as to reach a total titanium(IV) concentration of  $1.25 \cdot 10^{-4} \text{ mol.L}^{-1}$ ). The pH of the solution was adjusted between 0.8 and 9.31 using sodium hydroxide and perchloric acid (ionic strength of  $0.1 \text{ mol.L}^{-1}$ ). These authors were thus able to notice the appearance of an increasingly intense peak around 250 nm when the pH increases from 0.8 to 3.3. They considered that among the species likely to exist in solution, i.e. titanium hydroxides  $\text{Ti}(\text{OH})_n^{(4-n)+}$  with  $n = 2, 3$  or 4, only  $\text{Ti}(\text{OH})_2^{2+}$  may exist as long as the pH is below 1.2. Finally, they were able to plot the speciation diagram of the species considered in Eqs. 4 and 5.

Shkol'nikov et al. [31] showed the solubilities of titanium(IV) oxides are equal to  $2.1 \cdot 10^{-2} \text{ mol.L}^{-1}$  for  $\text{TiO}_2$  (particle size of approximately 8–19 nm) and  $1.4 \text{ mol.L}^{-1}$  for hydrated amorphous  $\text{TiO}_2$  (particle size approximately 1.6 nm) in  $1.0 \text{ mol.L}^{-1}$  perchloric acid. This shows that the use of this method is only reliable if the solid phases are well defined since the solubility measurement strongly depends on the crystallinity, the morphology, and the size of the particles. This has been shown in particular by Schmidt et al. [38] who calculated equilibrium parameters by measuring solubility of titanium(IV) dioxide with different crystallinities. Despite different results, they calculated the average of the constants of equilibria reported in Eqs. (4) and (5). Figure 1 shows the titanium(IV) speciation diagram in an aqueous medium for pH values between 0 and 14 at a total titanium concentration of  $1 \text{ mol.L}^{-1}$  calculated using the set of constants determined by Schmidt et al. [38].

The calculated values are close to those mentioned by Liberti et al. [44]. It is interesting to underline that these authors considered that the chloride ions do not complex titanium(IV). Unlike Liberti et al. [44], the speciation diagram deduced from the data of Schmidt et al. [38] does not include a region where the monohydroxylated  $\text{Ti}(\text{OH})^{3+}$  can be found. Solubility measurements of rutile at different temperatures reported by Ziemniak et al. [30] made it possible to determine the Gibbs energy of formation of the species involved in the equilibria (2) to (6). By combining these Gibbs energies of formation with the data reported by Vasil'ev et al. [45] and by Baes et al. [46], it is then possible to plot the speciation diagram displayed in Fig. 2. This speciation diagram is similar to that determined by Schmidt et al. [38] (Fig. 1). In their study, Ziemniak et al. were able to calculate the Gibbs energy of formation for different values of pH ranging from 9.3 to 11.2 in the presence of phosphate and

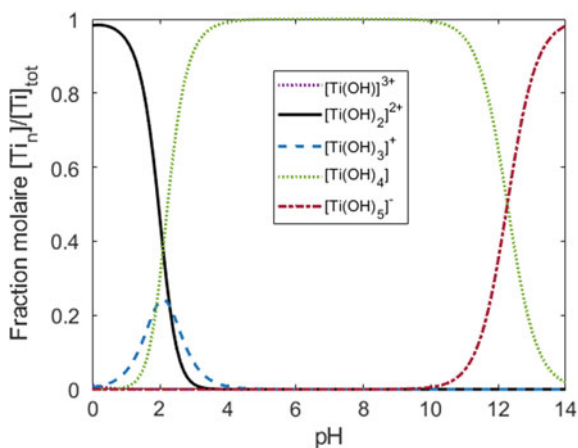
**Fig. 1** Speciation diagram of mononuclear titanium(IV) species at 25 °C as a function of pH determined by using equilibrium constants 3–6 (corrected for activity effects by a Davies model and calculated by Schmidt et al. at zero ionic strength [38]). Diagram plotted for a total titanium(IV) concentration  $[\text{Ti}]_{\text{tot}} = 1 \text{ mmol.L}^{-1}$



sodium hydroxide as well as ammonium hydroxide. They considered the acid–base equilibria (2) to (6) but also the equilibria involved in the formation of titanium(IV) hydroxophosphate complexes. Then, the Gibbs energies of formation were calculated by using a chemical equilibrium model and solubility data at different temperatures and different pH values. To plot this speciation diagram, only the mononuclear species were taken into account as the latter were ignored.

Similar work was published by Knauss et al. [50]. The solubility of rutile in nitric/nitrate medium at  $\text{pH} = 1\text{--}13$  was measured at high temperatures (100–300 °C). The authors were able to carry out regressions of their data in order to determine the equilibrium constants (5) and (6). The extrapolated Helgeson model [51] was used to take into account the water activities and the presence of ions in solution. Nevertheless, the calculations only work providing that  $\text{Ti}(\text{OH})_2^{2+}$  was removed from the model. Calculations with the model including reactions (5) and (6) led to

**Fig. 2** Speciation diagram of mononuclear titanium(IV) species for a total titanium concentration of  $[\text{Ti}]_{\text{tot}} = 1 \text{ mmol.L}^{-1}$  as a function of the pH (the speciation diagram was determined by using the Gibbs energies of formation reported by Ziemniak et al. [30])



the conclusion that  $\log(K_{H,4})$  and  $\log(K_{H,5})$  (in molarity scale) vary from  $2.28 \pm 0.15$  to  $-3.31 \pm 1.1$  and from  $-10.11 \pm 0.16$  to  $-7.43 \pm 1.11$ , respectively, when the temperature goes from 100 to 300 °C. These values should be compared with those mentioned by Pichavant et al. [37] and gathered in Table 1. This work by Knauss et al. [50] also led to the conclusion of the possible presence of Na-titanate species at high pH values.

More recently, Chagnes et al. [56] reinvestigated the speciation of titanium(IV) in non-complexing acidic solutions by combining UV–visible spectroscopy and molecular modeling techniques. It was necessary to add other titanium(IV) species than mononuclear species such as titanyl ion or titanium dihydroxide to simulate UV–visible spectra by DFT calculations.

Conversely, accounting for the presence of polytitanate clusters such as the dimer or the trimer reported in Fig. 3 allows for a satisfactory agreement between the experimental UV–Vis spectra and the UV–Vis spectra calculated by DFT.

However, in spite of such a good fitting, the determination of the exact nature of the observed polytitanates (i.e. size and hydrolysis state) was not possible due to the multiplicity and similarity of corresponding structures. UV–visible spectroscopy coupled with chemometric analyses and  $^{31}\text{P}$  NMR spectroscopy were also successfully used to qualitatively investigate the speciation of titanium(IV) in a large range of phosphoric acid concentrations (i.e. 0.1 to 11.6 mol L $^{-1}$ ). Thus, it is concluded that titanium(IV) is present as mononuclear ( $\mu = 1$ ) or polynuclear ( $\mu > 1$ ) free cation(s),  $[(\text{TiO})_\mu]^{2\mu}$ , in diluted  $\text{H}_3\text{PO}_4$  solutions (typically < 0.1 mol L $^{-1}$ ) and then progressively forms orthophosphate complexes as the concentration of phosphoric acid is increased, namely  $[(\text{TiO})_\mu(\text{H}_{3-m}\text{PO}_4)_\gamma]^{2\mu-\gamma m}$  and  $[(\text{TiO})_\mu(\text{H}_{3-m}\text{PO}_4)_\gamma(\text{H}_{3-n}\text{PO}_4)_\beta]^{2\mu-\gamma m-\beta n}$  in moderate (typically > 1 mol L $^{-1}$ ) and concentrated (typically > 6 mol L $^{-1}$ )  $\text{H}_3\text{PO}_4$  solutions, respectively.

## Conclusion

Thus, the divalent ion (dihydroxylated or titanyl) is considered in most cases as the predominant species at very acidic pH. For pH values close to the neutrality, the hydroxide species  $\text{Ti}(\text{OH})^{3+}$  and  $\text{Ti}(\text{OH})_4$  coexist but can be in equilibrium with polynuclear forms (octamers, dimers, or tetramers). A more recent study has called into question the speciation of titanium(IV) in non-complexing medium reported in the literature by suggesting the formation of small clusters of dimeric or trimeric polytitanate in addition to the formation of mononuclear species such as the titanyl ion or the titanium(IV) dihydroxide.

**Table 1** Logarithm of the equilibrium constants for the hydrolysis reactions of titanium(IV) in acidic solutions [37]

Hydrolysis	Liberti [44]	Nabivanets [51]	Lobanov[52]	Nazarenko [53]	Zienmiak [30]	Schmidt [38]	JANAF database [54, 55]
$\text{Ti}^{4+}(\text{aq.}) + \text{H}_2\text{O} \rightleftharpoons$	ND	2.79	-0.16	0.097	ND	ND	3.75
$\text{Ti}(\text{OH})^{3+}(\text{aq.}) + \text{H}^+$							
$\text{Ti}(\text{OH})_2^{2+}(\text{aq.}) + \text{H}_2\text{O} \rightleftharpoons$	-1.8	2.35	-0.59	-0.31	ND	ND	3.26
$\text{Ti}(\text{OH})_2^{2+}(\text{aq.}) + \text{H}^+$							
$\text{Ti}(\text{OH})_2^{2+}(\text{aq.}) + \text{H}_2\text{O} \rightleftharpoons$	-2.4	-2.1	-0.92	-0.64	-2.28	-1.85	-1.71
$\text{Ti}(\text{OH})_3^+(\text{aq.}) + \text{H}^+$							
$\text{Ti}(\text{OH})_3^+(\text{aq.}) + \text{H}_2\text{O} \rightleftharpoons$	-2.1	-3.37	1.05	-0.96	-1.9	-2.95	-3.07
$\text{Ti}(\text{OH})_4(\text{aq.}) + \text{H}^+$							



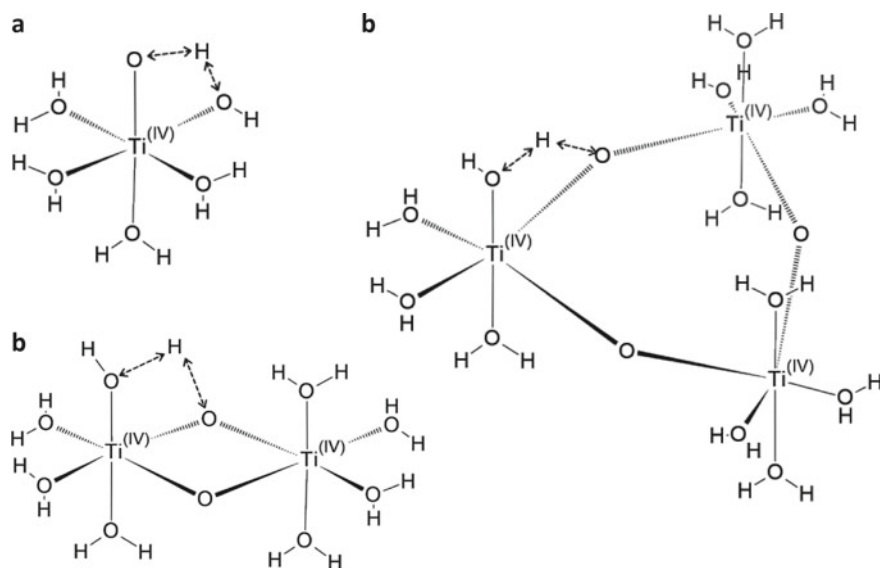


**Fig. 3** Schematic structures suggested for the free form of titanium  $[\text{TiO}]_{\mu}^{12\mu}$  considering various sizes, i.e. monomeric (a,  $\mu = 1$ ), dimeric (b,  $\mu = 2$ ), and trimeric (c,  $\mu = 3$ ). Eventual intramolecular proton exchanges are represented by dashed double arrows

## References

1. Commission Européenne, Résilience des matières premières critiques: la voie à suivre pour un renforcement de la sécurité et de la durabilité, <https://eur-lex.europa.eu/legal-content/FR/TXT/HTML/?uri=CELEX:52020DC0474&from=EN>. Accessed 19 Aug 2022
2. Watti A, Alnjjar M, Hammal A (2016) Arab J Chem 9:637–642
3. Phosphate Rock (2021) Mineral commodity summaries, U.S. Geological Survey
4. International Fertilizer Association (2020)
5. Klugh BG (1932) Ind Eng Chem 24:371–374
6. Pereira F (2003) Production d'acide phosphorique par attaque chlorhydrique de minerais phosphatés avec réduction des nuisances environnementales et récupération des terres rares en tant que sous-produits, Thèse, Ecole Nationale Supérieure des Mines de Saint-Etienne
7. Kijkowska R, Pawlowska-Kozinska D, Kowalski Z, Jodko M, Wzorek Z (2002) Sep Purif Technol 28:197–205
8. Assunção MC (2017) Etude physicochimique et formulation d'un nouveau solvant d'extraction pour la purification de l'acide phosphorique. Université Pierre et Marie Curie - Paris VI, Thèse
9. Kouzbour S, Gourich B, Gros F, Vial C, Allam F, Stiriba Y (2019) Hydrometallurgy 188:222–247
10. Hinojosa Reyes L, Saucedo Medina I, Navarro Mendoza R, Revilla Vázquez J, Avila Rodríguez R, Guibal E (2001) Ind Eng Chem Res 40:1422–1433
11. Hannachi A, Habaili D, Chtara C, Ratel A (2007) Sep Purif Technol 55:212–216
12. Lokshin EP, Tareeva OA, Elizarova IR (2013) Russ J Appl Chem 86:623–628
13. Xu D, Wan J, Xu D, Luo T, Zhong Y, Yang X, Yang L, Zhang Z, Wang X (2020) Can J Chem Eng 98:665–675
14. Bessiere J, Bruant M, Jdid EA, Blazy P (1986) Int J Miner Process 16:63–74
15. Zieliński J, Huculak-Mączka M, Kaniewski M, Nieweś D, Hoffmann K, Hoffmann J (2019) Hydrometallurgy 190:105157

16. Gad HMH, Awwad NS, El- A, Daifullah AAM, El- SA, Aly V (2010) Purification of industrial phosphoric acid using silica produced from rice husk (part 1). *Arab J Nucl Sci Appl* 43(1):65–74
17. Daifullah AAM, Awwad NS, El- SA (2004) *Chem Eng Process* 43:193–201
18. Amin MI (2020) *J Environ Anal Chem* 1–18
19. El- AA, Ali MM, Ahmed AM, Khalifa ME, Abdel- EM (2015) *Chem Tech Indian J* 10:210–219
20. Barrak H, Ahmedi R, Chevallier P, M'nif A, Laroche G, Hamzaoui AH (2019) *Sep Purif Technol* 222:145–151
21. Wu S, WangL ZL, Zhang P, El-Shall H, Moudgil B, Huang X, Zhang L (2018) *Chem Eng J* 335:774–800
22. Lokshin EP, Tareeva OA, Elizarova IR (2011) *Russ J Appl Chem* 84:773–781
23. Chagnes A, Cote G (2016) *Solvent Extr Ion Exch* 34:577–578
24. Beltrami D, Cote G, Mokhtari H, Courtaud B, Moyer BA, Chagnes A (2014) *Chem Rev* 114:12002–12023
25. Girgin S, Acarkan N, Sirkeci AA (2002) *J Radioanal Nucl Chem* 251:263–271
26. Assuncao MC, Cote G, Andre M, Halleux H, Chagnes A (2017) *RSC Adv* 7:6922–6930
27. Dartiguelongue A, Chagnes A, Provost E, Fürst W, Cote G (2016) *Hydrometallurgy* 165:57–63
28. Krea M, Khalaf H (2000) *Hydrometallurgy* 58:215–225
29. Hurst FJ, Crouse DJ (1974) *Ind Eng Chem Process Des Dev* 13:286–291
30. Ziemniak SE, Jones ME, Combs KES (1993) *J Solution Chem* 22:601–623
31. Shkol'nikov EV, Russ (2016) *J Phys Chem* 90:567–571
32. Ahmed IM, Ammanoeil RN, Saad EA, Daoud JA (2019) *Period Polytech Chem Eng* 63:122–129
33. Alibrahim M (2007) *Period Polytech Chem Eng* 51:39–42
34. Hamdi R, Hannachi A (2012) *J Chem Eng Process Technol* 3(2):1000134
35. Jolivet JP, Henry M (2012) *De la solution à l'oxyde—condensation des cations en solution aqueuse*. Chimie de surface des oxyde, EDP Sciences, Paris
36. Einaga HJ (1979) *Chem Soc, Dalton Trans* 1917–1919
37. Pichavant A, Provost E, Fürst W, Hochepeid JF (2019) *J Chem Thermodyn* 131:184–191
38. Schmidt J, Vogelsberger W (2009) *J Solution Chem* 38:1267–1282
39. Lundberg D, Persson I (2017) *J Solution Chem* 46:476–487
40. Graetzel M, Rotzinger FP (1985) *Inorg Chem* 24:2320–2321
41. Redkin AF, Bondarenko GV (2010) *J Solution Chem* 39:1549–1561
42. Aureliano M, Ohlin CA, Vieira MO, Marques MPM, Casey WH, De Carvalho LAEB (2016) *Dalton Trans* 45:7391–7399
43. Szilágyi I, Königsberger E, May PM (2009) *Dalton Trans*. 7717–7724
44. Liberti A, Chiantella V, Corigliano F (1963) *J Inorg Nucl Chem* 25:415–427
45. Vasil'ev VP, Vorob'ev PN, Khodakovskii IL (1974) *Russ J Inorg Chem* 19:1481
46. Baes CF, Mesmer RE (1976) *The hydrolysis of cations*. Wiley-Interscience, New York
47. Brown PM, Ekberg C (2016) *Hydrolysis of metal ions*. Wiley, 433–498.
48. Comba P, Merbach A (1987) *Inorg Chem* 26:1315–1323
49. Sugimoto T, Zhou X, Muramatsu A (2002) *J Colloid Interface Sci* 252:339–346
50. Knauss KG, Dibley MJ, Bourcier WL, Shaw HF (2001) *Appl. Geochemistry* 16:1115–1128
51. Helgeson HC (1969) *Am J Sci* 267:729–804
52. Lobanov FI, Savostina VM, Serzhenko IV, Peshkova VM (1969) *Russ J Inorg Chem* 14:562
53. Nazarenko VA, Antonovich VP, Nevskaya EM (1968) *Russ J Inorg Chem* 71(16):530
54. Chase MW, Curnutt JL, Prophet H, McDonald RA, Syverud AN (1975) *J Phys Chem Ref Data* 4:1–176
55. Testino A, Bellobono IR, Buscaglia V, Canevali C, D'Arienzo M, Polizzi S, Scotti R, Morazzoni F (2007) *J Am Chem Soc* 129:3564–3575
56. Mangold L, Halleux H, Leclerc S, Moncomble A, Cote G, Chagnes A (2021) *RSC Adv* 11:27059–27073

# Di-Phenols Functionalized Chitosan as Selective Adsorbents for Extraction of Germanium



Madhav Patel and Athanasios K. Karamalidis

**Abstract** In the current study, catechol functionalized chitosan, C-Cat, was investigated for selective solid-phase extraction of germanium. Germanium is one of the critical elements because of its growing demand, supply risk, and inefficient production. The current Ge production processes, such as chlorination-distillation and solvent extraction, suffer from high energy requirements, high chemical consumptions, impurities co-extractions, and waste stream generations. The adsorbent was synthesized via Schiff's base reaction. The adsorbent morphology was different from the chitosan due to surface modification. C-Cat adsorbed Ge selectively in the presence of competitive ions with  $K_d$  values of 10,832.0 mL/g at pH 3 and 7417.6 mL/g at pH 4. The selectivity for Ge was also observed in Ge-spiked coal fly ash leachate. The distribution coefficients were correlated with metal hydrolysis constants, and linear free-energy relationships were developed for C-Cat. These LFERs can be used to predict the selectivity of C-Cat using the metal hydrolysis constants.

**Keywords** Solid-phase extraction · Critical element · Germanium · Chitosan · Catechol · Linear free-energy relationship

## Introduction

Germanium (Ge) is one of the critical elements due to its applications in infrared systems, optical fibers, semiconductors, solar panels, and polymer catalysis. It lacks substitutes in these applications and has potential supply risk. The demand for germanium has been growing steadily and is expected to grow more due to the growth of 5G network and the potential terrestrial use of multi-junctional solar cells [1, 2]. Germanium minerals rarely form in economically sustainable quantities; but only 3–5% of Ge is recovered primarily from secondary sources, such as Zn refinery residue and coal fly ash, worldwide [2, 3], mostly due to a lack of efficient and profitable processes that can recover the element from dilute sources.

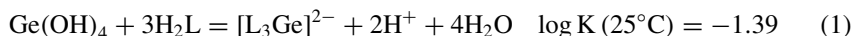
---

M. Patel · A. K. Karamalidis (✉)

Department of Energy and Mineral Engineering, Pennsylvania State University, University Park, Pennsylvania, PA 16802, USA  
e-mail: [akk5742@psu.edu](mailto:akk5742@psu.edu)

Solid-phase extraction with ligand functionalized solid support can solve the issue of efficient and economic separation with its advantages such as efficient extraction in dilute solutions, lower energy input, high reusability of the adsorbent, high selectivity and capacity, and elimination of environmentally harmful chemicals [4–6]. Chitosan has been functionalized with different ligands for the adsorption of critical elements such as rare-earth elements [7–11], Ge [12], Pd, and Pt [13].

Germanium occurs in oxidation states of +2 and +4, with the +4 state being more stable and the most common in natural systems. In an aqueous solution, Ge(IV) is the dominant species within the water stability region of the Eh–pH diagram [14]. The solubility constants for  $\text{GeO}_2$  (major Ge(IV) solid) are available in literature [2, 14–16]. The different aqueous species of Ge(IV) at different pH are shown in Fig. 1a.  $\text{Ge(OH)}_4$  is the dominant species at  $\text{pH} < 9.32$  [2, 14–16]. For germanium separation, complexing ligand catechol has been used in solvent extraction [17–21], complexation followed by ion exchange [17, 22–26], as well as solid-phase extraction [27]. Ge(IV) has a high affinity for catechol and can complex with catechol in an aqueous solution as per the following reaction [2]:



In this study, we investigated catechol functionalized chitosan for selective separation of Ge in synthetic multi-ion solutions and spiked coal fly ash leachate solutions. Synthesis of catechol functionalized chitosan and its performance can be found in Patel and Karamalidis 2022 (in review). The competitive-ion adsorption is studied using a linear correlation between free-energies of metal hydrolysis and the adsorption distribution coefficient.

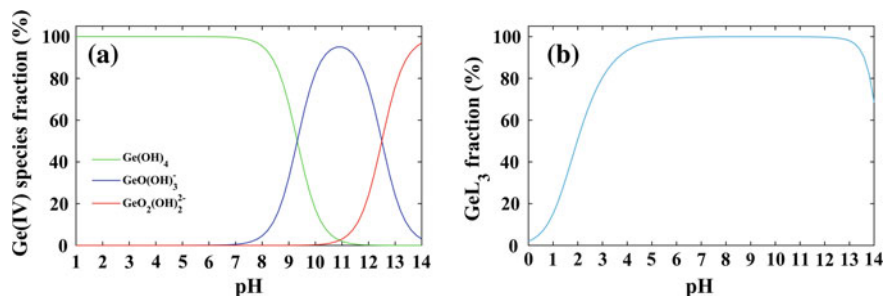


**Fig. 1** a Different Ge-species as a function of pH Source [2]; b The fraction of Ge-catechol complex as a function of pH based on reaction 1

## Experimental Studies

### *Materials*

Chitosan (High molecular weight 310,000–375,000 Da, Sigma Aldrich), two polystyrene-divinylbenzene based spherical beads with amine-functional groups (Purolite), and an amino-methacrylate bead (LifeTech) were used as solid supports. 3,4-dihydroxybenzaldehyde (> 98%, TCI), glacial acetic acid (> 99.7% ACS grade, Thermo Scientific), NaBH<sub>4</sub> (99%, Sigma Aldrich), ethanol (> 99.5% ACS grade, Supelco), and anhydrous methanol (HPLC grade, Fisher Scientific) were used for the functionalization.

Ge oxide (GeO<sub>2</sub> 99.9999% metal basis, Alfa Aesar), HCl (trace metal grade, BDH Aristar Plus), H<sub>2</sub>SO<sub>4</sub> (trace metal grade, BDH Aristar Plus), and NaOH pellets (99–100% ACS grade, Millipore Sigma) were used to prepare Ge stock solution with different pH. Single-element ICP stock solutions (Inorganic Venture) were used to prepare mixed elements solutions for competitive-ion adsorption.

### *Functionalization of Solid Supports*

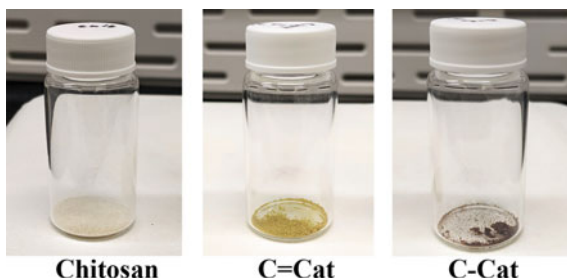
The beads were functionalized via Schiff's base reaction following the procedure in the literature [28, 29]. Briefly, 0.5 g (dry weight) of bead was taken in 100 ml ethanol solution, and 1.5 g 3,4-dihydroxybenzaldehyde was added to the mix. The mix was refluxed for 24 h. After 24 h, the beads were filtered and washed with ethanol and dried overnight in an oven at 60 °C for 24 h.

The catechol can oxidize to quinone in an alkaline medium and can self-polymerize [30–33], which could result in the loss of capacity. Hence, a different protocol was used for the functionalization of chitosan. The chitosan functionalization process is reported in Patel and Karamalidis (2022, in review). Briefly, chitosan and 3,4-dihydroxybenzaldehyde were refluxed for 24 h in acetic acid–methanol media. The solids (C=Cat) were then washed and dried, followed by reduction of C=N using NaBH<sub>4</sub> to produce the catechol functionalized adsorbent (C-Cat). The functionalized chitosan at different stages of the reaction is shown in Fig. 2.

### *Characterization and Adsorption Studies*

The characterization processes and adsorption experiments are reported in detail in Patel and Karamalidis (2022, in review). In the current study, adsorption studies at different pH were conducted for C=Cat. The adsorbent dose was 10 mg/10 ml with end-to-end mixing at 30 rpm for 24 h. No background electrolyte was added to fix

**Fig. 2** Picture of chitosan, C = Cat, and C-Cat



ionic strength. Competitive-ion adsorptions were done in the presence of competitive ions commonly present along with Ge in Zn refinery residue and coal fly ash. Additionally, Ge-spiked coal fly ash leachate was used. Coal fly ash was leached using 1 M HCl at a dose of 1 g/50 ml. The leachate from fly ash did not contain Ge; thus, the leachate was spiked with 20 mg/L Ge.

The adsorption parameters such as the equilibrium adsorption capacity ( $q_e$ ) (Eq. 2), the % adsorption (Eq. 3), solid-liquid distribution (partitioning) coefficient ( $K_d$ ) (Eq. 4), and selectivity factor (Eq. 5) were calculated as:

$$q_e \left( \frac{\text{mg}}{\text{g}} \right) = (C_0 - C_e) * \frac{V}{m} \quad (2)$$

$$\text{Adsorption (\%)} = \frac{(C_0 - C_e)}{C_0} * 100 \quad (3)$$

$$K_d (\text{L/g}) = \frac{C_0 - C_e}{C_e} \frac{V}{m} = \frac{q_e}{C_e} \quad (4)$$

$$\text{SF}(\text{Ge}/M^{n+}) = \frac{K_{d\text{Ge}}}{K_{dM^{n+}}} \quad (5)$$

where  $C_o$  and  $C_e$  are initial and equilibrium concentrations of the adsorbate in the solution in batch adsorption (mg/L),  $m$  is the mass of the adsorbent used (g), and  $V$  is the total volume of the solution (L).

## Results and Discussions

The functionalized beads showed low adsorption capacity (2.5–5 mg Ge/g adsorbent); in contrast, the functionalized chitosan showed almost tenfold higher capacity (maximum of 48.5 mg Ge/g C = Cat) (Table 1). The capacity of C = Cat is higher than C-Cat due to incomplete reduction of C = N and loss of catechol during reduction steps. Still, C-Cat shows higher capacity than the functionalized beads. The unfunctionalized chitosan did not adsorb Ge in preliminary experiments.

**Table 1** The adsorption capacities of different adsorbents synthesized

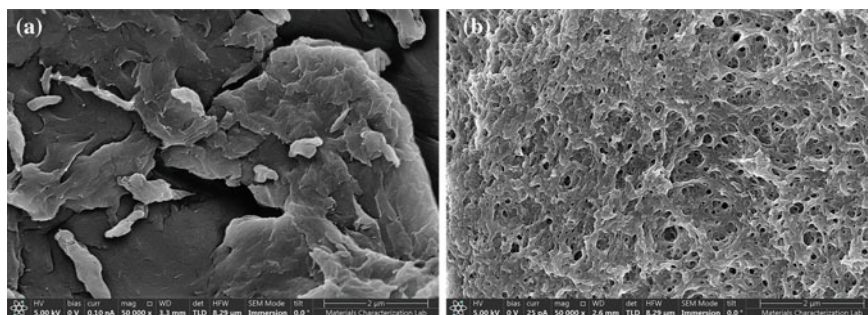
Adsorbent	Ge adsorption Capacity	
	(mg/g)	( $\mu\text{mol/g}$ )
P <sub>1</sub> =Cat	2.5	34.8
P <sub>2</sub> =Cat	3.7	51.5
M=Cat	5.1	70.4
C=Cat	48.5	673.5
C-Cat	22.6	313.3

P<sub>1</sub> and P<sub>2</sub> are aminated-polystyrene beads, M is aminated-methacrylate bead, and C is chitosan

The BET surface area of C-Cat (391.1 m<sup>2</sup>/kg) was lower than chitosan (457.5 m<sup>2</sup>/kg), with smaller average pore width (Patel and Karamalidis 2022, in review). The chitosan had pores with plate slit structure, crack, and wedge structure, while C-Cat had complex pores (Patel and Karamalidis 2022, in review), also visible in the SEM analysis (Fig. 3). The EDS elemental mapping of C-Cat after Ge adsorption shows that the C, O, N, and Ge are uniformly distributed (Fig. 4); hence, the adsorption sites are uniformly distributed on the adsorbent and not concentrated in a particular region. The EDS spectrum revealed peaks of C, O, and N present in chitosan and the peak for the adsorbed Ge.

The adsorption increased with an increase in pH for C=Cat, while for C-Cat, it reached the maximum at pH 3 and then decreased slightly at higher pH (Fig. 5). The adsorption vs. pH curve follows a similar trend as the Ge-catechol complexation in the solution shown in Fig. 1b. The adsorption at pH 1 and 2 are almost the same for both C=Cat and C-Cat despite having different ligand densities.

Adsorbent C-Cat adsorbed Ge almost entirely (> 99.5%) in the presence of competitive ions Cu(II), Zn(II), Cd(II), and Pb(II) present at different levels of concentrations (Fig. 6). However, the C-Cat also adsorbed other elements after complete adsorption of Ge since empty sites were available in the adsorbent.

**Fig. 3** SEM image (50,000  $\times$  magnification) of **a** chitosan and **b** C-Cat

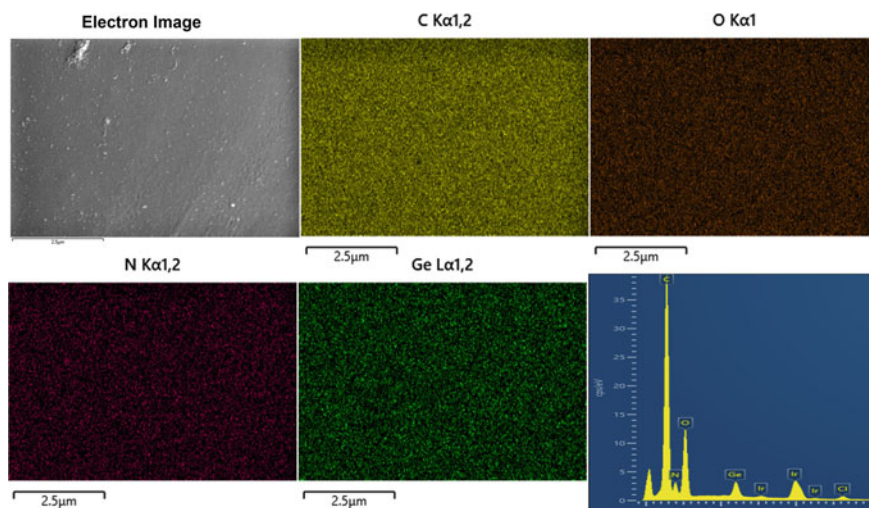


**Fig. 4** EDS elemental mapping of C-Cat after the adsorption of germanium

**Fig. 5** Adsorption of Ge onto C=Cat and C-Cat at different pH with 40 mg/L and 75 mg/L Ge, respectively (pH adjusted with HCl and NaOH). The data for C-Cat has been reported in Patel and Karamalidis (2022, in review)

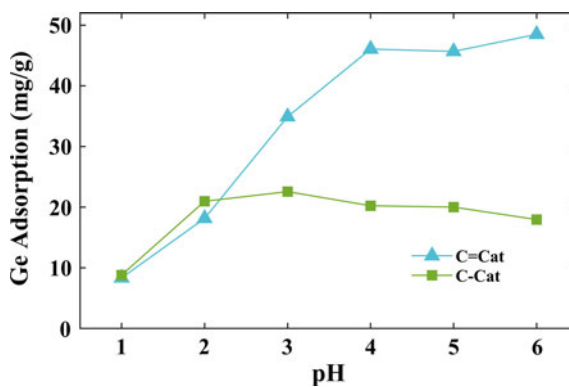
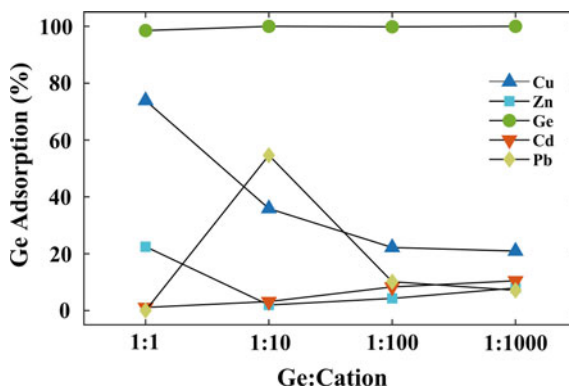


**Fig. 6** Ge adsorption onto C-Cat with different concentration of competitive ions (1 mg/L:1 mg/L, 1 mg/L:10 mg/L, 1 mg/L:100 mg/L, and 0.1 mg/L:100 mg/L) at pH 3





The competitive-ion adsorption was studied in terms of solid–liquid distribution coefficients ( $K_d$ ) and is shown in Fig. 7. The distribution coefficient ( $K_d$ ) is the ratio of the amount adsorbed to the amount remaining in the solution and depends on aqueous chemical conditions (e.g., pH, adsorbate concentration, solution/electrolyte matrix, temperature) [34]. C-Cat showed higher  $K_d$  for Ge at both pH 3 ( $K_d = 10,832.0$  mL/g) and pH 4 ( $K_d = 7417.6$  mL/g) compared to other elements. The  $K_d$  for competitive ions increased with pH. The equilibrium pH after adsorption in the case of the pH 4 experiment was 6.25. The change in pH may have resulted in the removal of some elements via precipitation. The equilibrium pH in the pH 3 experiment was 4.51. The selectivity factor for Ge over other ions ranged from 8.7 against Fe to 816.7 against Cd at pH 3 and 1.5 against Fe to 25.1 against Cd at pH 4 (Table 2).

The logarithms of equilibrium constants of one series of reactions can be linearly correlated with logarithms of equilibrium constants of related series of reactions and are known as linear free-energy relationships (LFERs) [35]. In the case of negatively charged O-donor atom ligands such as catechol, the ligand–metal stability constants ( $\log K_{aq}$ ) in the solution are linearly correlated with the metal hydrolysis constants [2, 36–39]. In the current study, the distribution coefficients were assumed to represent the adsorption equilibrium in multi-ion adsorption; hence, they were considered for LFER. Therefore, a linear correlation between  $\log K_d$  for the functionalized adsorbent

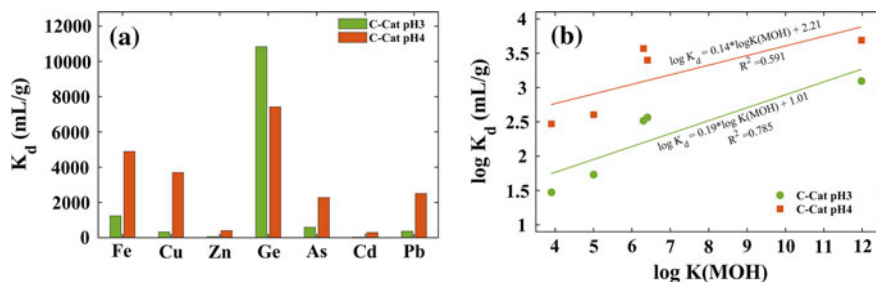
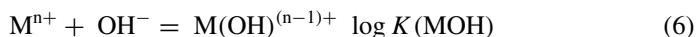


**Fig. 7** **a** The distribution coefficients of various elements in competitive-ion adsorption with C-Cat at pH 3 and pH 4, 20 mg/L concentration of each ion **b** Linear correlations between the  $\log K_d$  for the C-Cat and the first hydrolysis constant of the metal cations

**Table 2** The Ge selectivity factors (SF; Eq. 5) for C-Cat at different pH

Element	Selectivity factor (SF)	
	pH 3	pH 4
Fe(III)	8.7	1.5
Cu(II)	29.7	2.0
Zn(II)	201.1	18.4
As(V)	18.3	3.3
Cd(II)	816.7	25.1
Pb(II)	15.4	3.0

and the first hydrolysis constant of the metal cations is investigated (Fig. 7b). Ge and As were not considered since they lack experimental hydrolysis constants. The first hydrolysis constant is for the following form of reaction:



The linear fit for C-Cat-pH 3 was better than C-Cat-pH 4 based on  $R^2$ . The competitive-ion adsorption at pH 4 had an equilibrium pH of 6.25, that could have resulted in precipitation of ions; hence, the removal mechanism in pH 4 experiment could be a combination of complexation with surface catechol and precipitation/co-precipitation due to changes in solution condition during adsorption. Therefore, the LFER for pH 4 experiment has lower  $R^2$  than pH 3 experiment as the LFER can only account for the surface complexation. The distribution coefficient is dependent on the solution composition and pH; thus, the LFER of  $\log K_d$  is a function of aqueous chemical conditions. Even so, the LFER can be used to predict selectivity for ions not included in the multi-ion adsorption experiment.

The fly ash was leached with 1 M HCl. Elements present in leachate with concentrations higher than 5 mg/L are shown in Table 3. The pH of the Ge-spiked leached solution was adjusted to pH 3. The equilibrium pH after adsorption with C-Cat was 3.47. The adsorbent C-Cat was selective for Ge against other elements except for Fe, Si, and Te. C-Cat has shown selectivity for Ge over Fe in synthetic solution (Fig. 7a). The aqueous  $Si(OH)_4$ -Catechol complex has lower stability constant ( $\log K = -12.0$ ) than  $Ge(OH)_4$ -catechol complex ( $\log K = -1.39$ , same form of reaction as for  $Ge(OH)_4$ ) [40]. Ti has a higher affinity for hydroxide than Fe ( $\log K_{TiOH} = 14.01$  versus  $\log K_{FeOH} = 11.6$ ) [41] but a lower affinity compared to Ge and Si, whose

**Table 3** The aqueous ion composition of fly ash leachate, distribution coefficient ( $K_d$ ), and Ge selectivity factor (SF; Eq. 5)

Element	Concentration (mg/L)	$K_d$ (mL/g)	SF (Ge/other)
Na	44,742.4	60.9	16.1
Ca	2981.5	57.4	17.1
Al	316.0	85.5	11.5
Mg	158.5	61.6	15.9
W	126.2	0.0	n. ads
Fe	120.7	2099.5	0.5
Si	114.1	2529.4	0.4
K	61.7	83.6	11.7
Ge	21.7	980.8	1.0
Ti	8.7	6261.6	0.2
Zn	6.1	100.1	9.8
B	5.1	0.0	n. ads
Sr	5.0	21.5	45.5

n.ads.: No adsorption of the ion

hydrolysis constants are unknown due to the formation of Ge and Si hydroxide in even highly acidic medium. Hence, the non-selectivity of C-Cat for Ge against Fe, Si, and Te may have been a result of precipitation/co-precipitation of these ions due to a change in pH during adsorption. The precipitation of Fe, Si, and Ti during adsorption can be avoided by using a pre-adsorption step involving an increase of solution pH to pH 4–6 to remove Fe, Si, and Ti. The solution pH can then be reduced to pH 3, and C-Cat can be used to selectively adsorb Ge. Alternatively, the pH of the leachate can be adjusted to pH 2. At pH 2, C-Cat has shown higher selectivity for Ge than pH 3 in synthetic solution (Patel and Karamalidis 2022, in review). With initial pH of 2, the precipitation of Fe, Si, and Ti during adsorption can be avoided, and Ge can be extracted selectively.

## Conclusions

The catechol-functionalized chitosan adsorbent, C-Cat, was investigated for selective separation of germanium. The capacity of C-Cat was 22.6 mg/g at pH 3, whereas the non-reduced adsorbent C=Cat showed a capacity of 48.5 mg/g. Incomplete reduction of imine bridge of C=Cat and loss of surface functional groups during reduction led to lower capacity of C-Cat compared to C=Cat. C-Cat adsorbent showed > 99.5% adsorption of Ge in the presence of competitive ions at different levels of concentration and was selective for Ge at both pH 3 and pH 4 with selectivity factor in the range of 1.5 against Fe at pH 4 to 816.7 against Cd at pH 3. The distribution coefficients ( $\log K_d$ ) of different elements were correlated with the first hydrolysis constant of the element. The correlation can be used to predict the selectivity of the adsorbent. In the case of Ge-spiked fly ash leachate, the Ge adsorption was not selective against Fe, Si, and Ti, due to the precipitation/co-precipitations of these ions. In the presence of these ions in the solution, the catechol-functionalized chitosan adsorbent C-Cat can be used for selective separation of Ge after a pre-adsorption precipitation step for removing Fe, Ti, and Si.

## References

1. Nguyen TH, Lee MS (2020) A review on germanium resources and its extraction by hydrometallurgical method. *Miner Process Extr Metall Rev* 00:1–21. <https://doi.org/10.1080/08827508.2020.1756795>
2. Patel M, Karamalidis AK (2021) Germanium: a review of its US demand, uses, resources, chemistry, and separation technologies. *Sep Purif Technol* 275:118981. <https://doi.org/10.1016/j.seppur.2021.118981>
3. Licht C, Peiró LT, Villalba G (2015) Global substance flow analysis of gallium, germanium, and indium: quantification of extraction, uses, and dissipative losses within their anthropogenic cycles. *J Ind Ecol* 19:890–903. <https://doi.org/10.1111/jiec.12287>

4. Hidayah NN, Abidin SZ (2017) The evolution of mineral processing in extraction of rare earth elements using solid-liquid extraction over liquid-liquid extraction: a review. *Miner Eng* 112:103–113. <https://doi.org/10.1016/j.mineng.2017.07.014>
5. Florek J, Giret S, Juère E, Larivière D, Kleitz F (2016) Functionalization of mesoporous materials for lanthanide and actinide extraction. *Dalton Trans* 45:14832–14854. <https://doi.org/10.1039/C6DT00474A>
6. Perreault LL, Giret S, Gagnon M, Florek J, Larivière D, Kleitz F (2017) Functionalization of mesoporous carbon materials for selective separation of lanthanides under acidic conditions. *ACS Appl Mater Interfaces* 9:12003–12012. <https://doi.org/10.1021/acsami.6b16650>
7. Roosen J, Spooren J, Binnemans K (2014) Adsorption performance of functionalized chitosan–silica hybrid materials toward rare earths. *J Mater Chem A* 2:19415–19426. <https://doi.org/10.1039/C4TA04518A>
8. Roosen J, Binnemans K (2014) Adsorption and chromatographic separation of rare earths with EDTA- and DTPA-functionalized chitosan biopolymers. *J Mater Chem A Mater.* 2:1530–1540. <https://doi.org/10.1039/c3ta14622g>
9. Galhoum AA, Mafhouz MG, Abdel-Rehem ST, Gomaa NA, Atia AA, Vincent T, Guibal E (2015) Cysteine-Functionalized chitosan magnetic nano-based particles for the recovery of light and heavy rare earth metals: uptake kinetics and sorption isotherms. *Nanomaterials* 5:154–179. <https://doi.org/10.3390/nano5010154>
10. Ramasamy DL, Wojtuś A, Repo E, Kalliola S, Srivastava V, Sillanpää M (2017) Ligand immobilized novel hybrid adsorbents for rare earth elements (REE) removal from waste water: Assessing the feasibility of using APTES functionalized silica in the hybridization process with chitosan. *Chem Eng J* 330:1370–1379. <https://doi.org/10.1016/j.cej.2017.08.098>
11. Ramasamy DL, Puhakka V, Iftekhar S, Wojtuś A, Repo E, Hammouda SB, Iakovleva E, Sillanpää M (2018) N- and O- ligand doped mesoporous silica-chitosan hybrid beads for the efficient, sustainable and selective recovery of rare earth elements (REE) from acid mine drainage (AMD): understanding the significance of physical modification and conditioning of th. *J Hazard Mater* 348:84–91. <https://doi.org/10.1016/j.jhazmat.2018.01.030>
12. Song X, Chen H, Gong L, Cui J, Wang Y, Wen S, Xing Z, Xiong Y (2022) Synthesis of novel diol modified chitosan and their enhanced selective adsorption behavior for germanium(IV). *J Environ Chem Eng* 10:107082. <https://doi.org/10.1016/J.JECE.2021.107082>
13. Kong D, Foley SR, Wilson LD (2022) An overview of modified chitosan adsorbents for the removal of precious metals species from aqueous media. *Molecules* 27. <https://doi.org/10.3390/MOLECULES27030978>
14. Marcel (1966) Pourbaix, Atlas of electrochemical equilibria in aqueous solutions, Pergamon Press, Oxford, New York
15. Rosenberg E (2009) Germanium: Environmental occurrence, importance and speciation. *Rev Environ Sci Biotechnol* 8:29–57. <https://doi.org/10.1007/s11157-008-9143-x>
16. Wood SA, Samson IM (2006) The aqueous geochemistry of gallium, germanium, indium and scandium. *Ore Geol Rev* 28:57–102. <https://doi.org/10.1016/j.oregeorev.2003.06.002>
17. Kuroiwa K, Ohura SI, Morisada S, Ohto K, Kawakita H, Matsuo Y, Fukuda D (2014) Recovery of germanium from waste solar panels using ion-exchange membrane and solvent extraction. *Miner Eng* 55:181–185. <https://doi.org/10.1016/j.mineng.2013.10.002>
18. Arroyo F, Fernández-Pereira C (2008) Hydrometallurgical recovery of Germanium from coal gasification fly ash. Solvent extraction method. *Ind Eng Chem Res* 47:3186–3191. <https://doi.org/10.1021/ie7016948>
19. Arroyo F, Fernández-Pereira C, Olivares J, Coca P (2009) Hydrometallurgical recovery of germanium from coal gasification fly ash: pilot plant scale evaluation. *Ind Eng Chem Res* 48:3573–3579. <https://doi.org/10.1021/ie800730h>
20. Arroyo F, Fernández-Pereira C, Oroz PB, Olivares J (2011) Industrial equipment design for the recovery of germanium from coal fly ash leachates by solvent extraction. *World of Coal Ash Conference*, pp 1–11
21. Kamran Haghighi H, Irannajad M, Fortuny A, Sastre AM (2018) Recovery of germanium from leach solutions of fly ash using solvent extraction with various extractants. *Hydrometallurgy* 175:164–169. <https://doi.org/10.1016/j.hydromet.2017.11.006>

22. Takemura H, Morisada S, Ohto K, Kawakita H, Matsuo Y, Fukuda D (2013) Germanium recovery by catechol complexation and subsequent flow through membrane and bead-packed bed column. *J Chem Technol Biotechnol* 88:1468–1472. <https://doi.org/10.1002/jctb.3985>
23. Torralvo FA, Fernández-Pereira C (2011) Recovery of germanium from real fly ash leachates by ion-exchange extraction. *Miner Eng* 24:35–41. <https://doi.org/10.1016/j.mineng.2010.09.004>
24. van Roosendaal S, Roosen J, Banerjee D, Binnemans K (2019) Selective recovery of germanium from iron-rich solutions using a supported ionic liquid phase (SILP). *Sep Purif Technol* 221:83–92. <https://doi.org/10.1016/j.seppur.2019.03.068>
25. Marco-Lozar JP, Cazorla-Amorós D, Linares-Solano A (2007) A new strategy for germanium adsorption on activated carbon by complex formation. *Carbon N Y*. 45:2519–2528. <https://doi.org/10.1016/j.carbon.2007.08.020>
26. Marco-Lozar JP, Linares-Solano A, Cazorla-Amorós D (2011) Effect of the porous texture and surface chemistry of activated carbons on the adsorption of a germanium complex from dilute aqueous solutions. *Carbon N Y*. 49:3325–3331. <https://doi.org/10.1016/j.carbon.2011.04.017>
27. Cruz CA, Marie S, Arrachart G, Pellet-Rostaing S, Arrambide Cruz C, Marie S, Arrachart G, Pellet-Rostaing S (2018) Selective extraction and separation of germanium by catechol based resins. *Sep Purif Technol* 193:214–219. <https://doi.org/10.1016/j.seppur.2017.11.013>
28. Cui W, Wang S, Peng J, Zhang L, Zhang G (2016) Catechol-functionalized nanosilica for adsorption of germanium ions from aqueous media. *J Solgel Sci Technol*. 77:666–674. <https://doi.org/10.1007/s10971-015-3898-7>
29. Bernard J, Branger C, Nguyen TLA, Denoyel R, Margailan A (2008) Synthesis and characterization of a polystyrenic resin functionalized by catechol: application to retention of metal ions. *React Funct Polym* 68:1362–1370
30. Wang H, Wang L, Zhang S, Zhang W, Li J, Han Y (2021) Mussel-inspired polymer materials derived from nonphytogenic and phytogenic catechol derivatives and their applications. *Polym Int* 70:1209–1224. <https://doi.org/10.1002/PI.6230>
31. Duan L, Yuan Q, Xiang H, Yang X, Liu L, Li J (2018) Fabrication and characterization of a novel collagen-catechol hydrogel. *J Biomater Appl* 32:862–870. <https://doi.org/10.1177/0885328217747125>
32. Pinnataip R, Lee BP (2021) Oxidation chemistry of catechol utilized in designing stimuli-responsive adhesives and antipathogenic biomaterials. *ACS Omega* 6:5113–5118. [https://doi.org/10.1021/ACSOMEGA.1C00006/ASSET/IMAGES/LARGE/AO1C00006\\_0004.JPEG](https://doi.org/10.1021/ACSOMEGA.1C00006/ASSET/IMAGES/LARGE/AO1C00006_0004.JPEG)
33. Yang J, Stuart MAC, Kamperman M (2014) Jack of all trades: versatile catechol crosslinking mechanisms. *Chem Soc Rev* 43:8271–8298. <https://doi.org/10.1039/C4CS00185K>
34. EPA (1999) O. of Radiation, I. Air, understanding variation in partition coefficient, K<sub>d</sub>, VALUES Volume I: the K<sub>d</sub> model, methods of measurement, and application of chemical reaction codes. <https://www.epa.gov/sites/default/files/2015-05/documents/402-r-99-004a.pdf>. Accessed 28 Aug 2022
35. IUPAC (2008) linear free-energy relation, in: IUPAC compendium of chemical terminology. IUPAC, Research Triangle Park, NC. <https://doi.org/10.1351/goldbook.i03551>
36. Ashurst KG, Hancock RD (1977) Characterization of inner- and outer-sphere complexes by thermodynamics and absorption spectra. Part 1. Sulphato-complexes of the first-row transition elements. *J Chem Soc Dalton Trans.*, 1701–1707. <https://doi.org/10.1039/DT9770001701>
37. Martell AE, Hancock RD (1996) Metal complexes in aqueous solutions. Springer, US. <https://doi.org/10.1007/978-1-4899-1486-6>
38. Carbonaro RF, Atalay YB, Di Toro DM (2011) Linear free energy relationships for metal-ligand complexation: Bidentate binding to negatively-charged oxygen donor atoms. *Geochim Cosmochim Acta* 75:2499–2511. <https://doi.org/10.1016/j.gca.2011.02.027>
39. Nakani BS, Hancock RD (1984) the effect of non-coordinated charged groups on the stability of complexes in aqueous solution. The stability of complexes of 2,3-dihydroxynaphthalene-6-sulfonic acid. *J Coord Chem* 13:143–151. <https://doi.org/10.1080/00958978408079766>
40. Pokrovski GS, Schott J (1998) Experimental study of the complexation of silicon and germanium with aqueous organic species: implications for germanium and silicon transport and Ge/Si ratio in natural waters. *Geochim Cosmochim Acta* 62:3413–3428. [https://doi.org/10.1016/S0016-7037\(98\)00249-X](https://doi.org/10.1016/S0016-7037(98)00249-X)

41. Saxena M, Loza-Rosas SA, Gaur K, Sharma S, Pérez Otero SC, Tinoco AD (2018) Exploring titanium(IV) chemical proximity to iron(III) to elucidate a function for Ti(IV) in the human body. *Coord Chem Rev* 363:109–125. <https://doi.org/10.1016/j.ccr.2018.03.006>

# Recycling of Copper and Gold from Waste Printed Circuit Boards by Leaching Followed by Solvent Extraction



Kamalesh Kumar Singh and Mudila Dhanunjaya Rao

**Abstract** This article presents a two-stage, eco-friendly hydrometallurgical route for the recovery of gold from the delaminated metallic layers of waste mobile phone Printed Circuit Boards (PCBs). The downsized PCBs were treated with an organic solvent dimethylacetamide (DMA) for the separation of metallic fraction from non-metallic glass fibre. The liberated metallic sheets are used for the selective dissolution of copper in an aqueous leaching reagent. Influence of various parameters such as type of leaching reagent, the concentration of the solution, temperature, time, and pulp density is optimized for the effective leaching (almost 100%) of copper. Results show that 3 M nitric acid is a suitable reagent for copper leaching but gold remained in solid residue. In the second stage, the separated residue is used for the recovery of gold by sulphuric acid with a combination of halide salt. Results have shown that almost 92% of gold is recovered at the optimized parameters. Solvent extraction with 0.1M tertiary amide revealed the selective and quantitative recovery of gold from gold leach solution.

**Keywords** Recycling · Secondary recovery · Hydrometallurgy · Extraction

## Introduction

The rapid change in technology and the electronic gadgets are becoming obsolete at faster rate [1]. In turn, the quantity of electronic waste is growing at faster rate. In year 2019, the global e-waste generation crossed 53.6 million tonnes [2]. The lower recycling rate in developing countries makes the situation alarming [3–7]. The 100% recycling is still a distant dream to be achieved. The lower recycling rate is not only burdening the environmental load through toxic elements but also

---

K. K. Singh (✉) · M. D. Rao  
Department of Metallurgical Engineering, Indian Institute of Technology (Banaras Hindu University), Varanasi 221005, India  
e-mail: [kksingh.met@iitbhu.ac.in](mailto:kksingh.met@iitbhu.ac.in)

M. D. Rao  
CSIR—National Metallurgical Laboratory, Jamshedpur 831007, India

losing many valuable and scarce metals [8]. The printed circuit boards are most valuable component of any electronic gadget because it hosts as many as 60 elements including precious metals like gold, silver, platinum, and palladium and valuable metals like copper, tin, nickel, aluminium, and iron [9, 10]. The metallic content may be as high as 40% of the total weight of PCBs [10]. In the present paper, two-stage leaching and subsequent solvent extraction have opted for recovery of most valuable gold and abundantly present copper from WPCBs. Nitric acid dissolves the base metals present, and it becomes easier to extract those metals successfully by application of highly selective metal extractant [11]. In addition, for the dissolution of gold, halide leaching reagents at acidic conditions are more significant than the traditional processes [12–16]. Here, for copper extraction from leached solution hydroxyl oximes [17] are used whereas amides are used to recover gold [18].

## Methodology

The printed circuit boards of mobile phones were collected from local vendors. The attached components and wires were removed from the circuit boards at a temperature below 200 °C by application of heat gun. The bare PCBs were cut into smaller pieces of the size 1 cm × 1 cm approximately with the help of shear cutter. These pieces were soaked into the solution of organic solvent N, N-dimethylacetamide (DMA) for 10 h to dissolve the resin of printed circuit boards to liberate the metallic components and the fibreglass present. The bare metallic fractions are subjected to hydrometallurgical extraction processes comprising acid leaching, solvent extraction, and stripping to recover gold and copper as shown in Fig. 1.

## Results and Discussion

### *Chemical Analysis and Two-Stage Leaching*

The metallic and non-metallic components were estimated through complete dissolution of the delaminated metallic components in *aqua regia*. One gram of sample was dissolved in 20 ml of *aqua regia* for 3 h at 50 °C at 500 rpm in a glass reactor fitted with stirring and heating facility. The solution was analysed through AAS/ICP-OES, and the obtained results are shown in Table 1.

It is clear that the major portion (84%) of the metallic values are copper followed by small quantities of nickel, zinc, tin, cadmium, aluminium, and lead and trace quantities of gold, silver, and palladium. The non-metallic plastics and glass fiber are separated manually from the metallic sheets.

Further, in next step, i.e. in stage-1 leaching, the metallic sheets of waste printed circuit boards are leached with 3 M nitric acid. However, some non-metallic fraction



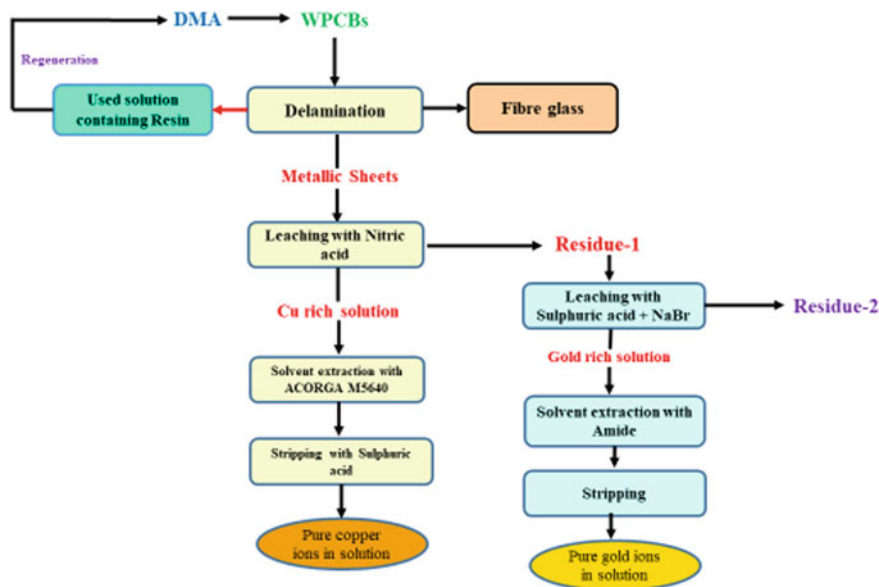


Fig. 1 Flow sheet of proposed process to recover copper and gold from WPCBs

Table 1 Chemical analysis of the sheared WPCB sample

Element	Wt%
Cu	84
Au	0.05
Ag	0.03
Sn	0.4
Pd	0.007
Ni	2.3
Zn	0.4
Pb	0.1
Cd	0.3
Al	0.2
Plastic and glass fiber	12.2

(12 wt%) is also still available with the metallic fraction. The leaching conditions are optimised and carried out at the temperature 30 °C for 2 h with the pulp density 50 g/L. The stirring speed was maintained at 500 rpm. AAS/ICP-OES analysis data are given below in Table 2, which shows that precious metals gold, silver, and palladium have not entered the solution whereas other metals except copper also leached in very small quantity. This stage of leaching is able to extract more than 97% of copper.

**Table 2** Chemical analysis of the first stage leached solution

Element	Wt%
Cu	97.3
Au	0
Ag	0
Sn	0.4
Pd	0
Ni	0.8
Zn	0.6
Pb	0.5
Cd	0.4
Al	0

**Table 3** Chemical analysis of the second stage leached solution

Element	Wt%
Cu	0.2
Au	7
Ag	3
Sn	89

**Table 4** Extraction of copper and gold after leaching from 5 g initial WPCB sample

Metal	Extracted wt	Extraction (%)
Copper	4.99 g	99.96%
Gold	0.0025 g	95.28%

Precious metals such as gold and silver have been observed in the residue of stage-1 leaching along with a non-metal fraction.

The residue with non-metallic fraction obtained after the first stage of leaching is subjected to second stage of leaching with sodium bromide in presence of sulphuric acid. The optimised conditions are maintained at 3M sulphuric acid with 3M sodium bromide at the temperature of 70 °C for 1 h and at the same stirring speed of 500 rpm. AAS/ICP-OES analysis of stage-2 leached samples is given in Table 3. The collected residue after stage-2 leaching consists of non-metallic fraction in a minor quantity.

After completion of two-stage leaching from 5 g initial PCB sample, stage-1 and stage-2 leachates comprise 4.99 g copper and 0.0025 g gold individually as shown in Table 4. Further purification process is required for stage-2 leach solution to separate gold from silver and tin. For that, solvent extraction process is used with an amide as an extractant.

## Solvent Extraction of Gold

The recovery of Au(III) was observed using solvent extraction with an organic amide diluted in toluene as an extractant by leaving other elements in the raffinate. The protonation of an amide plays a crucial role in the selective extraction of Au(III) into the organic phase. Combination of the protonated and neutral amide with  $[\text{AuBr}_4]^-$  through hydrogen bonding and electrostatic interactions creates a neutral assembly and transport into the organic phase. The process of Au(III) extraction with primary amide as an extractant diluted in toluene is shown in Fig. 2.

From the analysis of the organic phase, it is evident that the amount of gold extracted into the organic phase increased from  $\text{L}^1$  (80%) to  $\text{L}^2$  (98%) and  $\text{L}^3$  (99%). In addition to gold, a proportion of tin (16–20%) is also extracted by all amides as shown in Table 5. However, no silver and copper are seen. Therefore, tertiary amide has been chosen for the maximum extraction of gold.

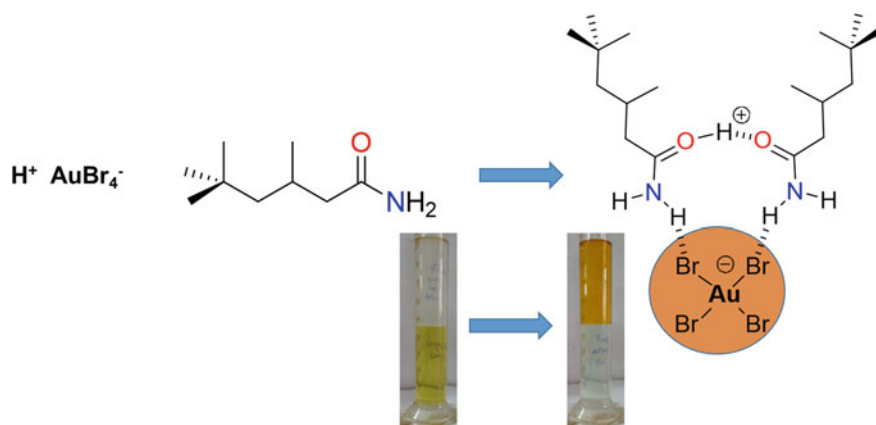


**Fig. 2** Summary of the process involved in the extraction of Au(III) from an aqueous leach solution into an organic phase containing primary amide

**Table 5** Transport of gold from the stage-2 leach liquor into a toluene solution of 0.1 M primary ( $\text{L}^1$ ), secondary ( $\text{L}^2$ ), or tertiary amide ( $\text{L}^3$ ) [Conditions: o/a 1:1; 1 h; 20 °C]

Amide	Au (% recovery)	Sn (% recovery)
$\text{L}^1$	80	20
$\text{L}^2$	98	18
$\text{L}^3$	99	16

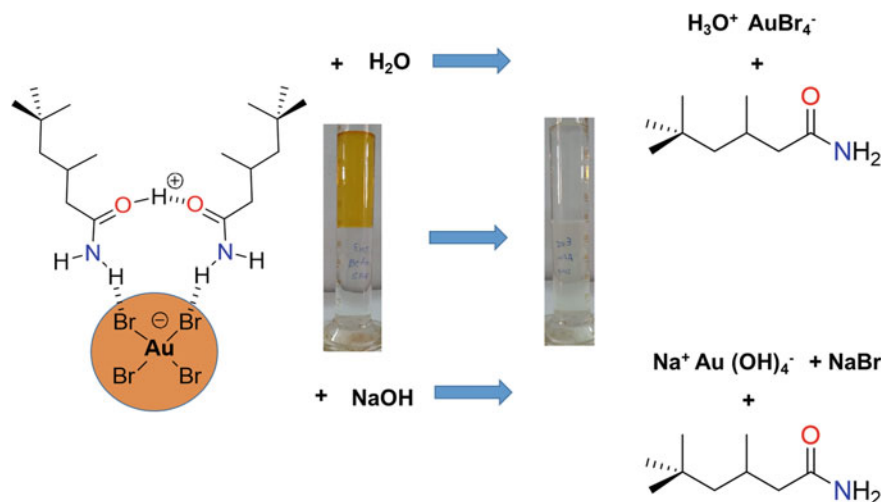


**Fig. 3** Summary of the process involved in the back extraction of Au(III) from primary amide complex into an aqueous (water or sodium hydroxide) solution

## Stripping

Back extraction of  $[\text{AuBr}_4]^-$  from the amide neutral complex into an aqueous phase is also essential for the generation of pure gold solution and the re-generation of free extractant for another extraction cycle. The process of back extraction or stripping with either water or sodium hydroxide is also shown in Fig. 3

From ICP-OES analysis, it is observed that no gold is stripped into water from extraction solutions of **L**<sup>1</sup> and **L**<sup>2</sup>, and 10% of gold is stripped with water from metal-loaded toluene solutions of **L**<sup>3</sup>. Using 0.1 M NaOH solution as the stripping reagent, gold stripping increased from **L**<sup>1</sup> (40%), **L**<sup>2</sup> (78%) to **L**<sup>3</sup> (82.6%). In contrast, when 1 M NaOH is used as the stripping reagent, almost all gold recovery is achieved from all amide extractions as shown in Table 6. Therefore, 1 M sodium hydroxide was chosen for the back extraction of gold from either secondary or tertiary amides.

In addition to gold stripping, tin is also stripped from the organic solutions to some extent and gradually decreases from **L**<sup>1</sup> to **L**<sup>3</sup> with water and sodium hydroxide as

**Table 6** Effect of reagent on stripping of gold from the organic phase, using 0.1 M **L**<sup>1-3</sup> in toluene as the extracting agent [Conditions: o/a 1:1; 1 h; 20 °C]

Amide	% recovery of gold with water stripping	% recovery of gold with 0.1 m NaOH stripping	% recovery of gold with 1 m NaOH stripping
<b>L</b> <sup>1</sup>	0	40	95
<b>L</b> <sup>2</sup>	1	70	98
<b>L</b> <sup>3</sup>	10	80	99

**Table 7** Effect of reagent on stripping of tin from the organic phase, using 0.1 M  $L^{1-3}$  in toluene as the extracting agent [Conditions: o/a 1:1; 1 h; 20 °C]

Amide	% recovery of tin with water stripping	% recovery of tin with 0.1 m NaOH stripping	% recovery of tin with 1 m NaOH stripping
$L^1$	10	40	60
$L^2$	8	35	22
$L^3$	5	17	9

shown in Table 7. It shows that traces of tin (9%) were only found with 1 M sodium hydroxide as a stripping reagent from tertiary amide. The repetition of extraction cycles can reduce tin contamination. After completion of solvent extraction from 5 g initial PCB sample, strip solution comprises 0.0024 g gold. The strip solution consists of 480 ppm of gold.

## Conclusions

The two-stage metal leaching process selectively dissolves copper from delaminated WPCBs in stage-1 leaching to leave a gold-rich solid residue for the subsequent extraction of gold in stage-2 leaching. Selective leaching of copper was achieved when using 3 M nitric acid at 30 °C, over a 2 h resident time, for 50 g/L pulp density, and 500 rpm agitation speed. Importantly, no gold was dissolved using these conditions. In the stage-2 leaching, selective extraction of gold is observed with bromide leaching with 3 M sulfuric acid with 3 M sodium bromide at 70 °C, over a 1 h time and 500 rpm agitation speed. The use of 0.1 M tertiary ( $L^3$ ) amide is efficient for the transportation of Au(III) into toluene solution. In addition, fraction of tin was also co-extracted. The extracted Au(III) was stripped from the toluene solution, with 99% recovered, with 1 M NaOH as stripping reagent.

**Acknowledgements** Authors are thankful to the head, department of metallurgical engineering, Indian Institute of Technology (Banaras Hindu University), Varanasi, for providing the experimentation and analysis facilities.

## References

1. Rao MD, Singh KK, Morrison CA, Love JB (2020) Challenges and opportunities in the recovery of gold from electronic waste. *RSC Adv* 10:4300–4309. <https://doi.org/10.1039/C9RA07607G>
2. Forti V, Baldé CP, Kuehr R, Bel G (2020) The Global e-waste monitor 2020: quantities, flows and the circular economy potential. United Nations University (UNU), International telecommunication union (ITU) and international solid waste association (ISWA), Geneva, Bonn, Rotterdam

3. Rocchetti L, Vegliò F, Kopacek B, Beolchini F (2013) Environmental impact assessment of hydrometallurgical processes for metal recovery from WEEE residues using a portable prototype plant. *Environ Sci Technol* 47(3):1581–1588. <https://doi.org/10.1021/es302192t>
4. Jadhav U, Hocheng H (2015) Hydrometallurgical recovery of metals from large printed circuit board pieces. *Sci Rep* 5(101):1–10. <https://doi.org/10.1038/srep14574>
5. Moltó J et al (2013) Thermogravimetric study of the decomposition of printed circuit boards from mobile phones. *J Anal Appl Pyrolysis* 103:189–200. <https://doi.org/10.1016/j.jaap.2012.12.020>
6. Jha R, Rao MD, Meshram A, Verma HR, Singh KK (2020) Potential of polymer inclusion membrane process for selective recovery of metal values from waste printed circuit boards: a review. *J Clean Prod* 265:121621. <https://doi.org/10.1016/j.jclepro.2020.121621>
7. Tsydenova O, Bengtsson M (2011) Chemical hazards associated with treatment of waste electrical and electronic equipment. *Waste Manag* 31:45–58. <https://doi.org/10.1016/j.wasman.2010.08.014>
8. Chaurasia A, Singh KK, Mankhand TR (2013) Extraction of tin and copper by acid leaching of PCBs. *Int J Metall Eng* 2(2):243–248. <https://doi.org/10.5923/j.ijmee.20130202.17>
9. Greenfield A, Graedel TE (2013) The omnivorous diet of modern technology. *Resour Conserv Recycl* 74:1–7. <https://doi.org/10.1016/j.resconrec.2013.02.010>
10. Cui J, Forssberg E (2003) Mechanical recycling of waste electric and electronic equipment: a review. *J Hazard Mater* 99:243–263. [https://doi.org/10.1016/S0304-3894\(03\)00061-X](https://doi.org/10.1016/S0304-3894(03)00061-X)
11. Cui H, Anderson CG (2016) Literature review of hydrometallurgical recycling of printed circuit boards (PCBs). *J Adv Chem Eng* 6(1):1–11. <https://doi.org/10.4172/2090-4568.1000142>
12. Melashvili M, Fleming C, Dymov I, Manimaran M, O’Day J (2014) Study of gold leaching with bromine and bromide and the influence of sulphide minerals on this reaction. *Conf Metall Proc*
13. Li C, Li H, Yang X, Wang S, Zhang L (2015) Gold leaching from a refractory gold concentrate by the method of liquid chlorination. In: *Rare metal technology 2015*, pp 71–77. [https://doi.org/10.1007/978-3-319-48188-3\\_9](https://doi.org/10.1007/978-3-319-48188-3_9)
14. Harjanto S, Pratama FW, Lazuardiyani A, Taris M, Salam MY (2019) Additional of NaCl on chloride leaching of gold ore from Indonesian Artisanal mining. *IOP Conf Ser Mater Sci Eng* 515. <https://doi.org/10.1088/1757-899X/515/1/012032>
15. Groenewald T (1977) Potential application of thiourea in the processing of gold. *J. South African Inst. Min. Metall.* 77(4):217–223
16. Oraby EA, Li H, Eksteen JJ (2020) An alkaline glycine-based leach process of base and precious metals from powdered waste printed circuit boards. *Waste Biomass Valorization* 11(8):3897–3909. <https://doi.org/10.1007/s12649-019-00780-0>
17. Rao MD, Singh KK, Morrison CA, Love JB (2021) Recycling copper and gold from e-waste by a two-stage leaching and solvent extraction process. *Sep Purif Technol* 263(January):118400. <https://doi.org/10.1016/j.seppur.2021.118400>
18. Doidge ED, Carson I, Tasker PA, Ellis RJ, Morrison CA, Love JB (2016) A simple primary amide for the selective recovery of gold from secondary resources. *Angew Chemie Int Ed* 55(40):12436–12439. <https://doi.org/10.1002/anie.201606113>

# Hydrometallurgical Extraction of Molybdenum and Rhenium from Molybdenite Flue Dust



Sadia Ilyas, Rajiv Ranjan Srivastava, Hyunjung Kim, Humma Akram Cheema, and Ijaz Ahmad Bhatti

**Abstract** Herein, the leaching of molybdenum and rhenium from the molybdenite roasting flue dust in  $\text{H}_2\text{SO}_4$  was studied. The parametric studies showed that leaching performed at a pulp density, 10 wt./vol.%;  $\text{H}_2\text{SO}_4$  concentration, 1.0 M; temperature, 90 °C; and time, 90 min was sufficient to yield 96% molybdenum and 93% rhenium. The leaching process significantly improved by raising the temperature from 30 °C to 90 °C, indicating an exothermic dissolution of refractory metals. Whereas the leaching kinetics indicated that the reaction mechanism changed from diffusion-controlled to chemically controlled, which was further confirmed by the apparent activation energy evaluated to be  $E_a(\text{Mo})$ , 35.5 kJ/mol, and  $E_a(\text{Re})$ , 21.5 kJ/mol.

**Keywords** Hydrometallurgy · Molybdenites flue dust · Refractory metals

## Introduction

Molybdenum and rhenium are the refractory metals critically applied in metal (as superalloys) and chemical (as active catalytic elements) industries [1–3]. Both metals primarily co-occur in their sulphidic forms like molybdenites, reniite, and copper porphyry ores [4]. Due to their increasing demands in the respective application industries, their efficient metallurgy is very important [5, 6].

In the conventional processing, molybdenites are usually roasted at 600 °C to convert the sulfide ores to their easy-to-leach oxidized form [3–5]. It results in a

---

S. Ilyas (✉) · H. Kim

Department of Earth Resources & Environmental Engineering, Hanyang University, Seongdong-Gu, Seoul 04763, Republic of Korea  
e-mail: [Ilyas.sadia24@gmail.com](mailto:Ilyas.sadia24@gmail.com)

R. R. Srivastava

Center for Advanced Chemistry, Institute of Research and Development, Duy Tan University, Da Nang 550000, Vietnam

Faculty of Natural Sciences, Duy Tan University, Da Nang 550000, Vietnam

H. A. Cheema · I. A. Bhatti

Department of Chemistry, University of Agriculture, Faisalabad 38040, Pakistan

significant loss of molybdenum in flue dust along with the major portion of volatilized rhenium oxide in the outgoing dust of the roasting furnace [5–7]. It has been determined that such flue dust usually contains 50% of molybdenum with a significant amount of rhenium therein [7]. A second time blending the dust in the roasting process with a fresh charge creates a problem due to the fine particle size ( $< 37 \mu\text{m}$ ) [8]. Therefore, the effective extraction of molybdenum from the flue dust is equally important to the metallurgy of both refractory metals. Except for a few studies, molybdenum extraction has been given less importance than rhenium through the processing of flue dust, and molybdenum is accounted as an impurity for rhenium extraction. However, a limited literature review is available on the leaching of both metals from Mo-bearing sources [9, 10] that provides no clues on the effect of important leaching parameters. It has been reported that  $\sim 40\%$  rhenium was leached in deionized water at  $80^\circ\text{C}$  [11], whereas  $80\%$  leaching efficiency was achieved in  $1.0 \text{ mol/L H}_2\text{SO}_4$  solution [1].

The present study, therefore, evaluated the role of agitation speed, acid ( $\text{H}_2\text{SO}_4$ ) concentration, temperature, and time on simultaneous leaching of both molybdenum and rhenium along with the metal impurities from the molybdenite roasting flue dust that was received from Shanxi (China). Moreover, the leaching kinetics and mechanism of molybdenum and rhenium leaching have been emphasized in this study.

## Experimental

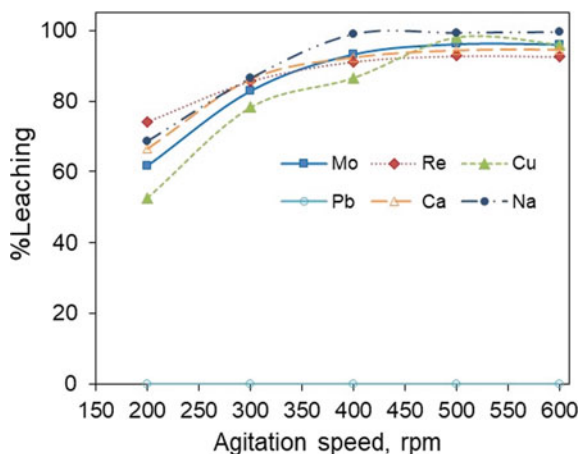
A 5 kg of flue dust sample was supplied by a molybdenite roasting process carried out in the Shanxi City of China. The homogenized sample was digested in aqua regia ( $\text{HCl} + \text{HNO}_3$ ) solution and analyzed by an Inductively Coupled Plasma Spectrometer (ICP, Burker model Varian 820-MS, California, USA). The metal composition was found to be  $12.6\%$  Mo,  $0.26\%$  Re,  $0.46\%$  Cu,  $0.54\%$  Pb,  $0.05\%$  Ca,  $0.006\%$  K, and  $0.68\%$  Na in the sample. For the leaching studies, a known quantity of flue dust was placed in a glass beaker of 500 mL capacity that contains a predetermined concentration of sulfuric acid to prepare the slurry of a fixed pulp density. When required, the acid solution was pre-heated on the magnetic hot plate *cum* stirrer (Robus-RTH-340, UK) at a particular temperature and the sample was always charged under the stirring condition. After leaching time, the slurry was filtered using the Whatman-40 filter paper and Buckner funnel. The filtrate was collected after a proper washing with 20 mL of hot water twice and analyzed using ICP for knowing the leaching efficiency as follows:

$$\% \text{Leaching} = \left( \frac{M_{\text{LL}}}{M_{\text{IS}}} \right) \times 100 \quad (1)$$

where  $M_{\text{IS}}$  and  $M_{\text{LL}}$  are metals' input from sample and output in leach liquor (on an absolute basis in gram), respectively.



**Fig. 1** Effect of agitation speed on leaching efficiency of metals at the conditions of pulp density, 5 wt./vol.%; H<sub>2</sub>SO<sub>4</sub> concentration, 1.0 mol/L; temperature, 90 °C; and time, 90 min



## Results and Discussion

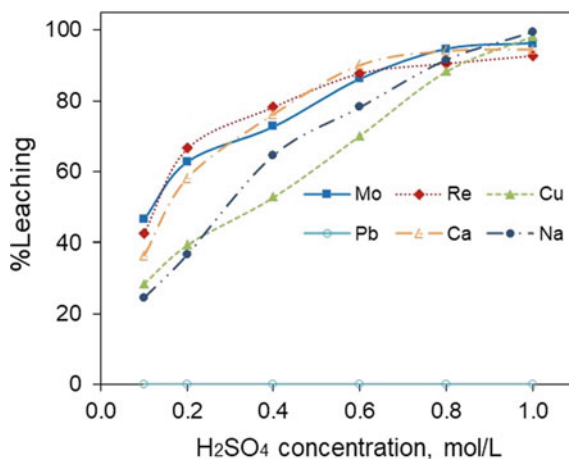
### *Effect of Agitation Speed*

The effect of agitation speed was studied in the range of 200–600 rpm, while keeping pulp density (5 wt./vol.%), H<sub>2</sub>SO<sub>4</sub> concentration (1.0 mol/L), temperature (90 °C), and time (90 min) constant. Figure 1 shows that the degree of leaching significantly improved (Mo 61.6% to > 93%; Re 74% to > 92%; Cu 52.6% to 87%; Ca 66% to 92%; and Na 68.6% to 99%) by increasing the agitation speed from 200 to 400 rpm. This can be corroborated by the increased contacts between metal compounds and lixiviant molecules that improve reaction rate [12]. Then after, leaching did not improve and reached the plateau region. The maximum leaching obtained at 500 rpm was optimized to maintain throughout the experimental sets.

### *Effect of H<sub>2</sub>SO<sub>4</sub> Concentration*

The effect of acid concentration was studied in the range of 0.1 – 1.0 mol/L H<sub>2</sub>SO<sub>4</sub> while keeping the pulp density (5 wt./vol.%), temperature (90 °C), time (90 min), and agitation speed (500 rpm) constant. Figure 2 shows that metals' leaching significantly improved with increasing acid concentration. As can be seen, the leaching was significantly improved (Mo 6.6% to 96%; Re 42.6% to ~ 93%; Cu 28.6% to ~ 98%; Ca 36.4% to > 94%; and Na 25% to ~ 99%) by increasing the acid concentration from 0.1 mol/L to 1.0 mol/L H<sub>2</sub>SO<sub>4</sub>. It indicates that a slow leaching at a lower acid concentration via the diffusion rate could supersede the rate of chemical reactions at

**Fig. 2** Effect of acid concentration on leaching efficiency of metals at the conditions of pulp density, 5 wt./vol.%; agitation speed, 500 rpm; temperature, 90 °C; and time, 90 min



a higher acid concentration [12–14]. No dissolution of lead at any acid concentration can be corroborated by the formation of insoluble lead sulfate in sulfuric acid solutions.

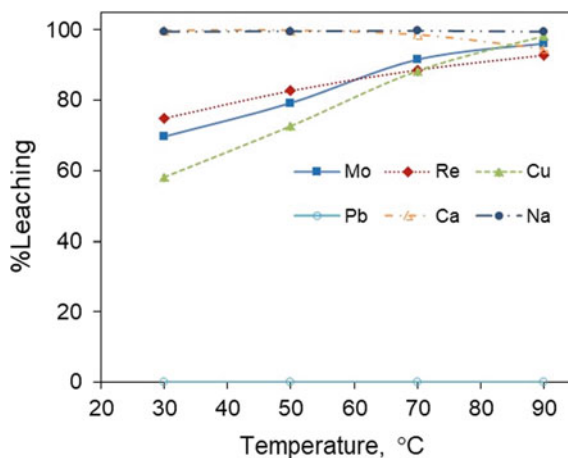
### *Effect of Temperature*

The effect of temperature on metals leaching was studied in the range of 30 °C to 90 °C at constant parameters of pulp density (5 wt./vol.%), acid concentration (1.0 mol/L H<sub>2</sub>SO<sub>4</sub>), time (90 min), and agitation speed (500 rpm). Figure 3 shows that the leaching efficiency increased by raising the temperature from 30 °C to 90 °C, certainly due to the change in the reaction rate [12, 15]. As can be seen, the leaching efficiency of Mo (69–96%), Re (75–93%), and Cu (58–98%) increased by raising the temperature from 30 °C to 90 °C. Interestingly, leaching of Ca declined from 99.8% to <95% with increasing temperature, possibly due to the low solubility of CaSO<sub>4</sub> at a high temperature. On the other hand, the leaching of Na was unchanged (> 99%) regardless of temperature.

### *Effect of Time*

The effect of time on metals' leaching was studied for up to 90 min while other parameters were kept unchanged as optimized above. Figure 4 shows that the leaching rate was rapid mainly in the early duration of the process, where about 48% Mo, 39% Re, 36% Cu, 24% Ca, and 35% Na were leached within 5 min of contact. Leaching was remarkably increased in 30 min and finally reached 96% Mo, 93% Re, 98% Cu,

**Fig. 3** Effect of temperature on leaching efficiency of metals at the conditions of pulp density, 5 wt./vol.%; H<sub>2</sub>SO<sub>4</sub> concentration, 1.0 mol/L; agitation speed, 500 rpm; and time, 90 min



92% Ca, and 99% Na after 90 min of leaching. The residual sulfide minerals of Mo can describe the reason for incomplete dissolution as the prominent peak of MoS<sub>2</sub> was observed by XRD analysis of the leached residue (refer to Fig. 5b), which was initially showing the patterns of MoO<sub>3</sub> and MoO<sub>2</sub> in the flue dust (refer to Fig. 5a). Also, the formation of insoluble PbSO<sub>4</sub> was observed in the XRD pattern of leached residue along with the co-existing mineral phase of crystalline Fe<sub>2</sub>O<sub>3</sub>.

**Fig. 4** Effect of leaching time on metals dissolution at the conditions of pulp density, 5 wt./vol.%; H<sub>2</sub>SO<sub>4</sub> concentration, 1.0 mol/L; temperature, 90 °C; and time, 90 min

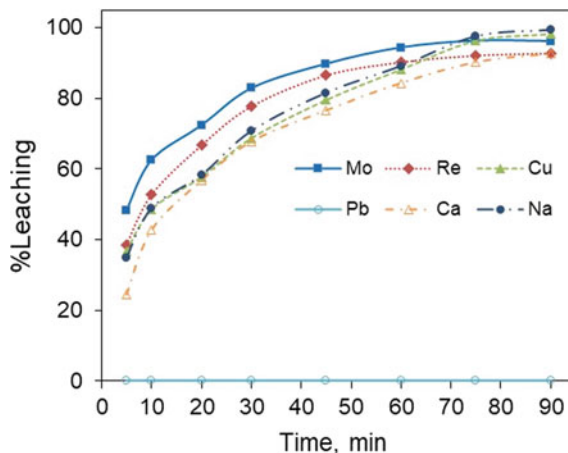
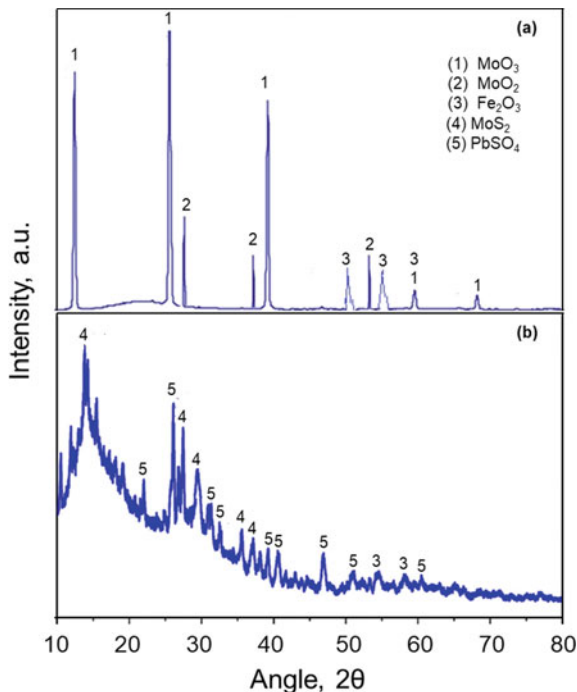


**Fig. 5** XRD patterns of molybdenite flue dust (a) and leached residue (b)



### *Leaching Kinetics and Mechanism*

The experimental data was further used to evaluate the leaching kinetics and mechanism of the main targeted metals (i.e., Mo and Re) in the flue dust. The common models fitting for the heterogeneous reactions, viz. shrinking core model involving small particles, were analyzed using the following equations [12, 15]:

$$1 - (1 - x)^{1/3} = k_c * t \quad (2)$$

$$1 - (1 - x)^{2/3} = k_d * t \quad (3)$$

where  $x$  = solid–liquid mass transfer rate of metal,  $t$  = time fraction in min, and  $k_c$  and  $k_d$  = the rate constant for chemically controlled and diffusion-controlled reactions, respectively.

When evaluating the dissolution data with Eqs. (2) and (3), the model did not fit well; hence, an empirical model following the logarithmic rate law was investigated next by using the following equation [12, 14]:

$$\{-\ln(1 - x)\}^2 = k_{\text{emp}} * t \quad (4)$$

where  $k_{\text{emp}}$  = the specific rate constant.

The plots of  $\{-\ln(1-x)\}^2$  vs.  $t$  for both molybdenum and rhenium yielded straight lines with values of regression coefficients ( $R^2$ ) more than 0.99 at all the studied temperatures showing the best model fits.  $k_{emp}$  for both metals at each temperature was determined from the slope values of the straight lines. As can be seen, the rate of metal dissolution significantly increased with temperature elevation.

Furthermore, the obtained  $k_{emp}$  (slope) values were expressed in the Arrhenius equation to determine the apparent activation energy ( $E_a$ ) of both metals using the following equation [15, 16]:

$$k_{emp} = Ae^{\left(\frac{-E_a}{RT}\right)} \quad (5)$$

where  $A$  = the Arrhenius constant,  $R$  = the Universal gas constant (8.314 kJ/mol), and  $T$  = the temperature (in Kelvin).

Thus, plotted  $\ln k_{emp}$  versus  $1/T$  for both molybdenum and rhenium are shown in Fig. 6. The slope values from the straight lines of the plots were used to determine the apparent activation energy values for molybdenum and rhenium dissolution in sulfuric acid solution, which were found to be  $E_{a(Mo)}$ , 35.5 kJ/mol, and  $E_{a(Re)}$ , 21.5 kJ/mol. The value of apparent activation energy in the range of 4 kJ/mol to 12 kJ/mol indicates that a reaction is controlled by surface diffusion, while a greater value ( $> 41.8$  kJ/mol) indicates that the dissolution is driven by the chemically controlled reaction. In this study, the  $E_a$  obtained using Eq. (5) lies between 12.0 kJ/mol and 41.8 kJ/mol, which indicates that the dissolution process is governed by an intermediate-controlled mechanism [15, 16]. This confirmed the assumption that the rapid dissolution of metals during the initial time was limited by the diffusion-controlled mechanism, which shifted towards the chemically controlled mechanism with a prolonged duration of dissolution.

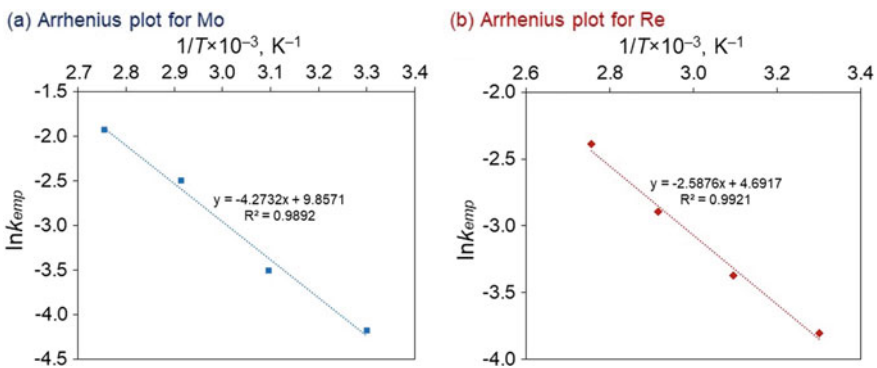


Fig. 6 Arrhenius plots of  $\ln k_{emp}$  versus  $t$  for molybdenum (a) and rhenium (b)

## Conclusions

The present study demonstrated the leaching strategy for the extraction of Mo and Re from molybdenite roasting flue dust leached in sulfuric acid solution. The effect of influential parameters like agitation speed, acid concentration, temperature, and time on metals' dissolution was examined. The leaching significantly improved by changing H<sub>2</sub>SO<sub>4</sub> concentration and yielded 96% Mo, 93% Re, 98% Cu, 94% Ca, and 99% Na in the leach liquor using 1.0 mol/L H<sub>2</sub>SO<sub>4</sub>. The variation in leaching temperature showed the exothermic nature of the leaching process and exhibited the change in reaction mechanism from diffusion-controlled to chemically controlled process. The apparent activation energy of Mo = 35.5 kJ/mol and Re = 21.5 kJ/mol indicated that the leaching process was driven by an intermediate-controlled mechanism. The present study reported the details of impurities profile as well, which can be useful in the practical exploitation of critical metals (molybdenum and rhenium) from the roasting flue dust.

**Acknowledgements** This work was supported by the Brain Pool Program through the National Research Foundation of Korea (NRF) funded by the Ministry of Science and ICT (Grant No. 2021H1D3A2A01100016) and the Basic Science Research Program through the National Research Foundation of Korea (NRF) funded by the Ministry of Education (Project no. 2020R1I1A1A01074249), and grant funded by the Korea Government (MSIT) (No. 2022R1A5A1032539).

### Conflicts of Interest

There are no conflicts to declare.

## References

1. Cheema HA, Ilyas S, Masud S, Muhsan MA, Mahmood I, Lee JC (2018) Sep Purif Technol 191:116
2. Srivastava RR (2017) Hydrometallurgical recovery of rhenium from engine reverted turbine-blade superalloy. Ph.D. Dissertation, University of Science and Technology, South Korea
3. Ilyas S, Kim H, Bhatti IA, Cheema HA, Srivastava RR (2022). In: Ouchi T et al (eds) Rare metal technology 2022, The minerals, metals and materials series. Springer, Cham., pp 135–145
4. Srivastava RR, Lee JC, Kim MS (2015) J Chem Technol Biotechnol 90:1752
5. Helbig T, Gilbricht S, Lehmann F, Daus B, Kelly N, Haseneder R, Scharf C (2018) Miner Eng 128:168
6. Habashi F (2010) Invest Appl Innov 4:121
7. Cheema HA, Bhatti IA, Srivastava RR, Jahan N, Zia MA (2022) Chem Pap 76:4049
8. Alamdari EK (2017) Trans Indian Inst Met 70:1995–1999
9. Hong D, Meng X, Han KN (1998) Min Metall Explor 15(1):8
10. Ma H, Wang Y, Lan X, He M (2005) J Rare Earths 23:96
11. Vosough M, Shahtahmasebi N, Behdani M (2016) Int J Refract Met Hard Mater 60:125
12. Munir H, Srivastava RR, Kim H, Ilyas S, Khosa MK, Yameen B (2020) J Chem Technol Biotechnol 95:2286

13. Ilyas S, Kim H, Srivastava RR (2021) JOM 73:19
14. Ilyas S, Srivastava RR, Kim H, Ilyas N, Sattar R (2020) Sep Purif Technol 232:115971
15. Habashi F (1969) Principles of extractive metallurgy, vol I. Gordon and Breach, New York
16. Levenspiel O (1999) Chemical reaction engineering, 3rd edn. Wiley, New York

# Recovery and Separation of Vanadium and Tungsten from Spent SCR Catalyst by Hydrometallurgical/Hybrid Routes



Rajesh Kumar Jyothi, Ana Belen Cueva Sola, Jong Hyuk Jeon,  
and Jin-Young Lee

**Abstract** One of the most harmful air contaminants is nitrogen oxides ( $\text{NO}_x$ ) produced usually in combustion processes. To reduce the effluents, the most effective technology to date is selective catalytic reduction (SCR) where nitrogen oxides are reduced into nitrogen to be released freely. Due to the increasingly strict environmental regulations, the demand for SCR catalysts has increased, and inevitably, the necessity of disposal of those spent catalysts has increased accordingly. Most catalysts for stationary applications contain around 0.5–1.5% wt  $\text{V}_2\text{O}_5$  and 7–10% wt of  $\text{WO}_3$  in a  $\text{TiO}_2$  glass fiber matrix, and due to the environmental burden of disposal and the necessity of finding secondary sources for vanadium (V) and tungsten (W), the recycling of spent SCR catalyst becomes a pressing issue for current research. During this investigation, different tertiary amines were used and compared to observe the effectiveness in the extraction of vanadium and tungsten from spent SCR catalyst, the enrichment process was optimized and the loaded organic (9 times concentration) went through a crowding process where vanadium was replaced by tungsten to obtain highly pure tungsten loaded organic. The crowding parameters such as crowding agent, concentration, and pH were optimized.

**Keywords** SCR catalyst · Vanadium · Tungsten · Crowding · Purification

---

R. K. Jyothi · A. B. C. Sola · J. H. Jeon · J.-Y. Lee (✉)  
Mineral Resources Division, Resources Recovery Center, Korea Institute of Geoscience and Mineral Resources (KIGAM), Daejeon 34132, Korea  
e-mail: [jinlee@kigam.re.kr](mailto:jinlee@kigam.re.kr)

R. K. Jyothi  
e-mail: [rkumarphd@kigam.re.kr](mailto:rkumarphd@kigam.re.kr)

R. K. Jyothi · A. B. C. Sola · J.-Y. Lee  
Department of Resources Engineering, Korea University of Science and Technology (UST), Daejeon 34113, Korea



## Introduction

Lately, secondary wastes such as electronics, scraps, sludge, and spent catalysts among others have been extensively studied to help alleviate the demand for different valuable metals contained in these wastes. Depletion of the primary sources alongside the environmental concerns of the current waste generation globally has led to that boom [1–3]. In particular, Selective Catalytic Reduction (SCR) W-V/TiO<sub>2</sub> catalyst is considered the most prominent technology to treat the noxious nitrogen oxides generated during combustion processes, especially in power plants [4]. SCR catalyst has a great lifespan, great regeneration capability, and excellent conversion of NO<sub>x</sub> into N<sub>2</sub> [5, 6]; however, eventually it deactivates and has to be landfilled posing a great environmental issue, not only due to the lack of landfill areas but also due to the toxicity of the materials in the catalyst. This waste contains a considerable amount of valuable metals such as vanadium (0.5–1.5%), tungsten (7–10%), and titanium (70–80%); however, the presence of vanadium and tungsten leads to difficulty in the separation of those due to their identical speciation properties while titanium can be easily separated in an initial step [7]. The investigation of our research group [7–10] has focused on the selective recovery of titanium, followed by a leaching process of vanadium and tungsten from a soda-roasted spent SCR catalyst. Thus, the issue to research further is the separation of either metal to obtain a pure product.

Several hydrometallurgical routes have been employed for the extraction and recovery of those metals; however, liquid–liquid extraction has shown a promising field to separate vanadium and tungsten. Several commercial extractants such as D2EHPA [11–16], PC88A [15], Cyanex 272, LIX series reagents [13, 17], and TBP [11, 12, 16] have shown excellent extraction properties towards vanadium and tungsten; however, amine-based reagents have shown a greater ability to extract the metals from the aqueous phase. The main shortcoming up to date has been the difficulty in the separation of vanadium and tungsten in the extraction or stripping process. Therefore, in this study different tertiary amines are compared for the extraction and enrichment of vanadium and tungsten from spent SCR catalyst leach liquor to obtain a highly concentrated in both metals loaded organic. The loaded organic will go through a crowding process, using a solution rich in tungsten to replace vanadium in the organic phase and yield highly concentrated tungsten loaded organic as shown in Fig. 1.

## Experimental

### *Apparatus and Reagents*

To obtain the concentrations of vanadium and tungsten in the aqueous solutions at different stages of the process, ICP-OES Spectrometer (iCAP 6000 Thermo Scientific) was employed. The pH of the solutions was determined using a Thermo

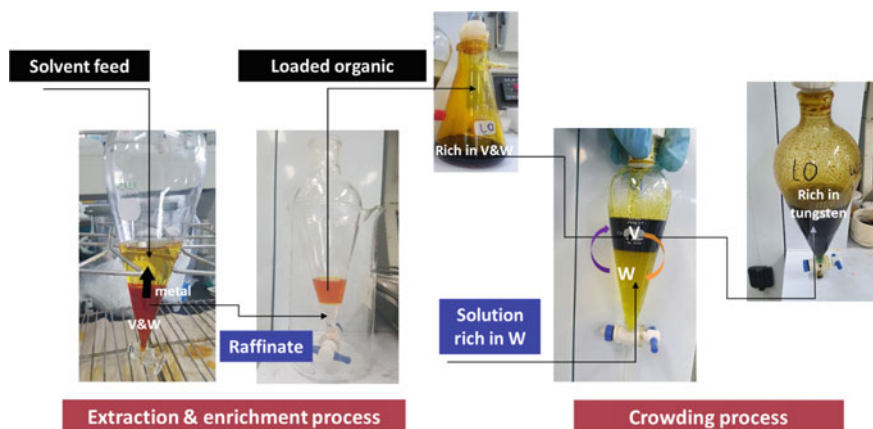


**Fig. 1** Schematic of the experimental proposal

Scientific pH meter. The extractant used for this research is the commercial grade commonly known as Alamine 336 (tri-*n*-octylamine) acquired from Thermo Scientific, while Exxsol™ D80 was used as a solvent. Sodium Tungstate (Junsei Chemical Co., Ltd., Japan) of analytical grade was used as it is for the crowding experiments. To prepare the leach liquor used in the investigation, the process developed in previous studies in the same research group was used [8, 18, 19] and Fig. 1 presents the extraction, enrichment, and crowding process studied.

### ***Solvent Extraction Method***

A 30 mL of the aqueous phase, containing V and W from spent SCR catalyst, and the organic phase were placed in separation funnels and mixed for 30 min in separation funnels in a shaking incubator at 250 rpm and ambient temperature (25 °C). After phase disengagement, the raffinate (aqueous) was analyzed by ICP-OES to determine vanadium and tungsten concentration. The content of the metals in the loaded organic was obtained using mass balance.

The  $D$  value was obtained as follows:

$$D = \text{Metal concentration organic} / \text{Metal concentration aqueous} \quad (1)$$

Metal concentrations were taken after extraction

$$\% \text{ Extraction} = D \times 100 / (D + 1) \quad (2)$$

where  $D$  = distribution ratio, 1 represents the phase ratio (Aqueous (A)/Organic (O)) = 1

## Results

### *Comparison Between Alamine 336 and Alamine 308*

To determine the efficiency of Alamine 336 and Alamine 308 for the extraction of vanadium and tungsten from a spent SCR catalyst leach liquor, the pH before extraction was varied from 0.5 to 7 while other parameters such as temperature (25 °C), concentration of extractant (0.5 mol/L), and time (30 min) were maintained as constant.

Figure 2 shows that on the acid side of the spectrum, when equilibrium pH increases the extraction of the V and W also increases; however, it reaches a maximum at equilibrium pH (4.65) corresponding to 2.01 initial pH. The phenomena can be explained due to the different speciation of vanadium and tungsten ions at different pH. In a highly acidic pH condition, vanadium is mostly present as oxo-anionic moieties such as  $V_{10}O_{26}(OH)^{2-}$  [13], while tungsten forms derives of  $WO_4^{2-}$  in the structure of  $W_{12}O_{41-2n}^{(10-4n)-}$  ( $n = 0,1$ ) [20]. Due to the slight difference in the extraction efficiency of Alamine 336 and Alamine 308 for vanadium and tungsten extraction, Alamine 336 is taken as the optimum extractant for further enrichment of the metals.

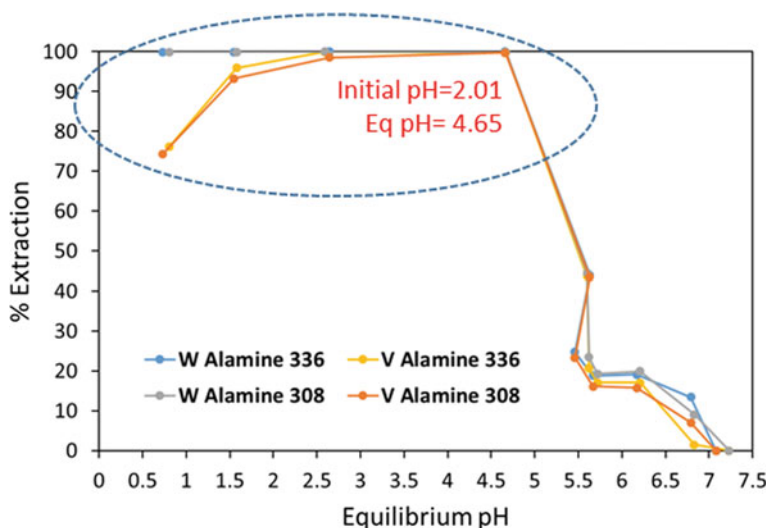


**Fig. 2** Extraction efficiency of V and W at different pH for different extractants

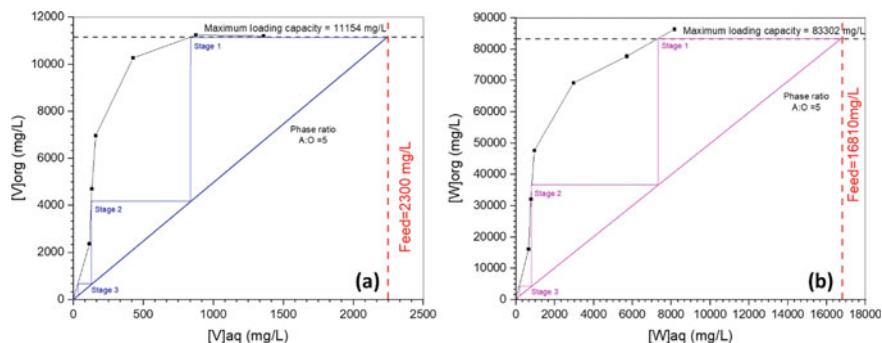


Fig. 3 Extraction isotherms for **a** vanadium and **b** tungsten

### ***McCabe Thiele Plot for Vanadium and Tungsten and Counter-Current Simulations (CCS)***

To further understand the enrichment potential of Alamine 336 for vanadium and tungsten, the extraction isotherm for both metals was constructed. The leach liquor containing 2300 mg/L and 16,800 mg/L of vanadium and tungsten, respectively, was contacted for 30 min with Alamine 336 (0.5 mol/L) varying the phase ratio from 1:1 (A:O) to 10:1 (A:O) while initial pH of the aqueous solution was kept constant at 2.01. Figure 3 shows that at the conditions set, there can be a five-fold enrichment of both metals by employing three extraction stages for a quantitative extraction. The organic phase can bear a loading capacity of 11.15 g/L of vanadium and 83.3 g/L of tungsten.

To support the results obtained by the McCabe Thiele simulation, counter-current extraction in three stages was performed for several cycles, and the percentage of extraction averages 98.72% for vanadium and 99.99% for tungsten yielding a loaded organic with an average concentration of 21 g/L of vanadium and 134 g/L of tungsten.

### ***Crowding Process for Vanadium and Tungsten Separation***

Due to the unique speciation and extraction behavior of both tungsten and vanadium with Alamine 336 at the initial pH of 2.01, more than 99% of extraction for both metals was confirmed; however, there was no significant separation of V and W from the enriched solution. Thus, a crowding process was implemented to attain a loaded organic rich in tungsten and low or negligible in vanadium. For this process, a concentrated solution of  $\text{Na}_2\text{WO}_4$  was contacted at different pH with the loaded organic rich in vanadium and tungsten with the aim to replace the vanadium moieties in the loaded organic with tungsten. Figure 4 shows the influence of pH in the crowding solution containing 30 g/L of tungsten in the amount of vanadium replaced.

It can be observed that when pH is higher than 7, the crowding effect reaches a plateau having a 57% replacement of vanadium in the loaded organic.

In addition, to further elucidate the crowding process, the concentration of tungsten in the crowding solution was modified from 10 g/L to 50 g/L while keeping the temperature (25 °C) and pH (8.53) constant. Figure 5 shows that increasing the concentration of tungsten increases the amount of vanadium replaced in the loaded organic up to 76%, yielding a loaded organic rich in tungsten (106 g/L) and with 4 g/L of vanadium.

**Fig. 4** Effect of crowding solution pH in the vanadium replacement in the loaded organic

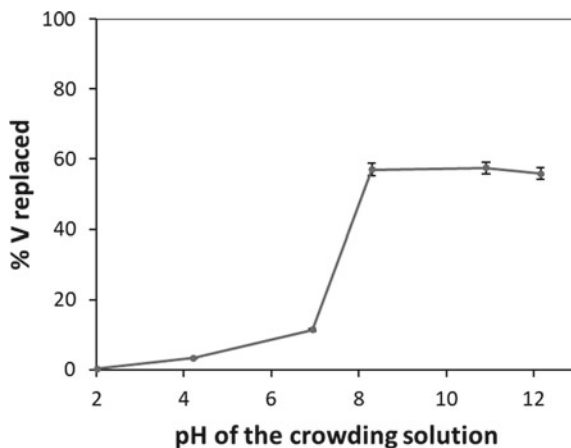
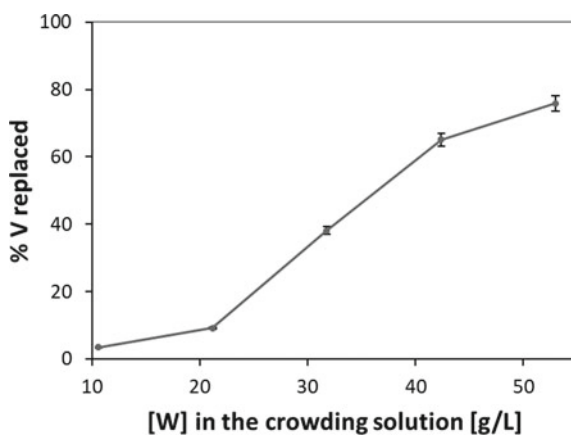


**Fig. 5** Effect of tungsten concentration in the crowding solution in the vanadium replacement



## Conclusion

The experimental study shown above focuses on the comparison of different amine-based commercial extractants for the extraction and enrichment of vanadium and tungsten from spent SCR catalysts. By using Alamine 336, a 99% extraction of vanadium and tungsten can be obtained with a ninefold enrichment of both metals. Due to the similar speciation of the metals, the separation of them has been of interest to several researchers; thus, the crowding process has been used to replace vanadium from the enriched loaded organic with tungsten and obtain a solely tungsten enriched solution. By using a 50 g/L crowding solution from  $\text{Na}_2\text{WO}_4$  at a pH of 8.53, 76% of vanadium was replaced yielding an enriched tungsten solution containing 106 g/L.

**Acknowledgements** This research was supported by the Basic Research Project (22-3803) of the Korea Institute of Geoscience and Mineral Resources (KIGAM) funded by the Ministry of Science and ICT of Korea.

## References

1. Mossali E, Picone N, Gentilini L et al (2020) Lithium-ion batteries towards circular economy: a literature review of opportunities and issues of recycling treatments. *J Environ Manage* 264:110500. <https://doi.org/10.1016/j.jenvman.2020.110500>
2. Wagner TP, Raymond T (2015) Landfill mining: case study of a successful metals recovery project. *Waste Manag* 45:448–457. <https://doi.org/10.1016/j.wasman.2015.06.034>
3. Dutta T, Kim KH, Uchimiya M et al (2016) Global demand for rare earth resources and strategies for green mining. *Environ Res* 150:182–190. <https://doi.org/10.1016/j.envres.2016.05.052>
4. Choi IH (2018) Study on the Recovery of Vanadium and Tungsten from Spent V2O5-WO3/TiO2 Catalyst. University of Science and Technology (UST)
5. Ferella F (2020) A review on management and recycling of spent selective catalytic reduction catalysts. *J Clean Prod* 246:118990. <https://doi.org/10.1016/j.jclepro.2019.118990>
6. Li J, Zhang P, Chen L et al (2020) Regeneration of selective catalyst reduction catalysts deactivated by Pb, As, and alkali metals. *ACS Omega* 5:13886–13893. <https://doi.org/10.1021/acs.omega.0c01283>
7. Jyothi RK, Moon G, Kim H-R et al (2017) Spent V2O5-WO3/TiO2 catalyst processing for valuable metals by soda roasting-water leaching. *Hydrometallurgy* 175:292–299. <https://doi.org/10.1016/j.hydromet.2017.12.010>
8. Choi IH, Moon G, Lee JY, Jyothi RK (2018) Extraction of tungsten and vanadium from spent selective catalytic reduction catalyst for stationary application by pressure leaching process. *J Clean Prod* 197:163–169. <https://doi.org/10.1016/j.jclepro.2018.06.196>
9. Kim HL, Moon G, Choi IH et al (2018) Hydrometallurgical process development for the extraction, separation and recovery of vanadium from spent desulfurization catalyst bio-leach liquors. *J Clean Prod* 187:449–458. <https://doi.org/10.1016/j.jclepro.2018.03.247>
10. Choi IH, Moon G, Lee JY, Jyothi RK (2018) Hydrometallurgical processing of spent selective catalytic reduction (SCR) catalyst for recovery of tungsten. *Hydrometallurgy* 178:137–145. <https://doi.org/10.1016/j.hydromet.2018.04.011>
11. Cheraghi A, Ardakani MS, Keshavarz Alamdari E et al (2015) Thermodynamics of vanadium (V) solvent extraction by mixture of D2EHPA and TBP. *Int J Miner Process* 138:49–54. <https://doi.org/10.1016/j.minpro.2015.03.011>

12. Li X, Deng Z, Wei C et al (2015) Solvent extraction of vanadium from a stone coal acidic leach solution using D2EHPA/TBP: continuous testing. *Hydrometallurgy* 154:40–46. <https://doi.org/10.1016/j.hydromet.2014.11.008>
13. Nguyen TH, Lee MS (2016) A review on the separation of molybdenum, tungsten, and vanadium from leach liquors of diverse resources by solvent extraction. *Geosystem Eng* 19:247–259. <https://doi.org/10.1080/12269328.2016.1186577>
14. Shakib B, Torab-Mostaedi M, Outokesh M, Asadollahzadeh M (2019) Mass transfer coefficients of extracting Mo (VI) and W (VI) in a stirred tank by solvent extraction using mixture of Cyanex272 and D 2 EHPA. *Sep Sci Technol* 00:1–11. <https://doi.org/10.1080/01496395.2019.1672741>
15. Shi Q, Zhang Y, Huang J et al (2017) Synergistic solvent extraction of vanadium from leaching solution of stone coal using D2EHPA and PC88A. *Sep Purif Technol* 181:1–7. <https://doi.org/10.1016/j.seppur.2017.03.010>
16. Zheng R, Bao S, Zhang Y, Chen B (2018) Synthesis of Di-(2-ethylhexyl) phosphoric acid (D2EHPA)-tributyl phosphate (TBP) impregnated resin and application in adsorption of vanadium(IV). *Minerals* 8:1–12. <https://doi.org/10.3390/min8050206>
17. Zeng L, Yong Cheng C (2009) A literature review of the recovery of molybdenum and vanadium from spent hydrodesulphurisation catalysts Part II: separation and purification. *Hydrometallurgy* 98:10–20. <https://doi.org/10.1016/j.hydromet.2009.03.012>
18. Choi IH, Moon G, Lee JY, Jyothi RK (2019) Alkali fusion using sodium carbonate for extraction of vanadium and tungsten for the preparation of synthetic sodium titanate from spent SCR catalyst. *Sci Rep* 9:1–8. <https://doi.org/10.1038/s41598-019-48767-0>
19. Jeon JH, Cueva Sola AB, Lee J-Y, Jyothi RK (2021) Hydrometallurgical process development to recycle valuable metals from spent SCR deNOX catalyst. *Sci Rep* 11:22131. <https://doi.org/10.1038/s41598-021-01726-0>
20. Nekovář P, Schrötterová D (2000) Extraction of V(V), Mo(VI) and W(VI) polynuclear species by primene JMT. *Chem Eng J* 79:229–233. [https://doi.org/10.1016/S1385-8947\(00\)00207-2](https://doi.org/10.1016/S1385-8947(00)00207-2)

# Removal of Selenium from Chloride Media Using Bioadsorbent



Mohamed Abdallah and Shafiq Alam

**Abstract** Selenium is an important mineral for plants and living organisms. Trace amounts of selenium are needed for our everyday functions; however, when large amounts are consumed, it becomes really dangerous with adverse health effects; as a result of this, its removal has been the focus of many studies over the past decades. The mining and refining industries release the most amounts of selenium which are present in their wastewater in most cases. This paper will discuss the removal of selenium from chloride media by adsorption using biobased materials. Data analysis revealed that the adsorption rate of selenium on lignin progressed via the pseudo-second-order rate model. Adsorption isotherm model studies indicate that the adsorption of selenium by lignin followed the Freundlich adsorption isotherm. Other thermodynamic data were calculated to examine the nature and efficiency of selenium removal from chloride media.

**Keywords** Mining · Mineral processing · Selenium · Biosorption · Biomass · Lignin · Chloride · Modeling

## Introduction

Selenium (Se) and its oxyanions have become a major health and environmental concern in recent years. Environmental contamination by selenium can occur due to various sources like metal ores, mine drainage, water drainage, industrial effluents, and fossil fuel residues. Various studies have focused on selenium removal from water using different techniques [1]. In the periodic table, Se belongs to the chalcogen group and is mostly present in minerals containing sulfur [2]. Selenium, the essential trace mineral, is vital to human health. Selenium deficiency may have detrimental impacts on the resistance to diseases and overall health maintenance. Several studies show that selenium deficiency affects the immune system, viral infection, cardiovascular disorders, and thyroid function [3]. Another disease associated with selenium

---

M. Abdallah · S. Alam (✉)

Department of Chemical and Biological Engineering, University of Saskatchewan, 57 Campus Drive, Saskatoon, SK S7N 5A9, Canada  
e-mail: [shafiq.alam@usask.ca](mailto:shafiq.alam@usask.ca)



deficiency is clinical Se deficiency also known as white muscle disease, which can cause nutritional myodegeneration, which is a disease that occurs mostly in farm animals like sheep and cows [4]. The only micronutrient regulated by the food and drug administration (FDA) as a feed additive is selenium and that is due to its toxicity. In 1974, the environmental protection agency (EPA), under the safe drinking water act, determined the maximum contaminant level goal (MCLG) of selenium to be 0.05 mg/L (ppm) or 50 ppb, so selenium removal from surface and ground waters is necessary to meet drinking water standards. The selenium concentration in contaminated wastewater must also be reduced to minimize its impact on natural water resources or to be reused [5]. Electronics, glass, ceramics, glass coloring, steel, pigment manufacturing, and rubber production are only a few of the industries that use selenium. Selenium is used in antidandruff shampoos and as a dietary supplement in medicine [6]. The presence of selenate and selenite, the low discharge limits, and the generation of huge amounts of wastewater made the removal of selenium from the aqueous medium complex and expensive [7]. The principal aqueous forms of selenium are selenite ( $\text{Se}^{4+}$ ) and selenate ( $\text{Se}^{6+}$ ); selenate is harder to treat and remove than selenite. Selenate is present in the oxidizing state as  $\text{SeO}_4^{2-}$  and selenite is present in the reducing state as  $\text{SeO}_3^{2-}$  or  $\text{HSeO}_3^-$  [8]. In the pH range of 6 to 8 only elemental selenium [Se, (0)], selenate, selenite, and bi-selenite ion ( $\text{HSeO}_3^-$ ) exist in water.

Selenium contamination is a global problem and is related to various human activities [9]. One of the key contributors to the release of selenium into the atmosphere is the mining industry. Active mining used to reach coal, phosphate, or ore body produces lots of waste rocks. As a result, runoff and other releases produced from tailings and piles of waste rock can release huge amounts of selenium, which can end up in aquatic ecosystems if they are not controlled or mishandled [10] as shown in Fig. 1.

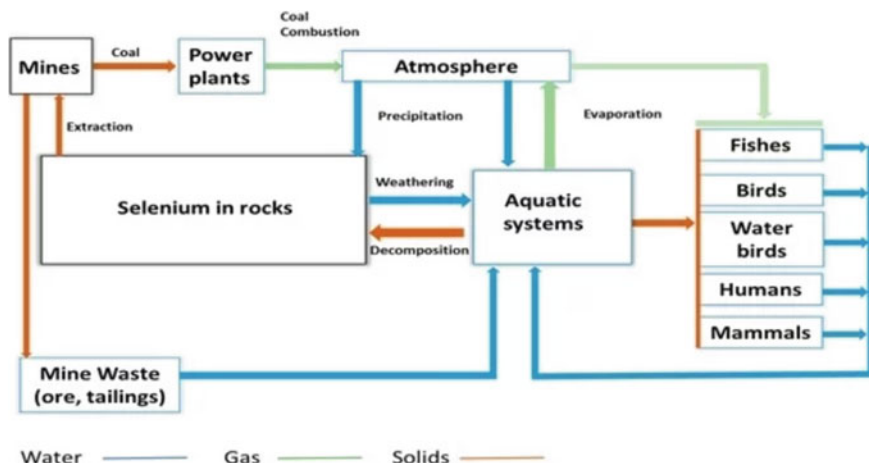


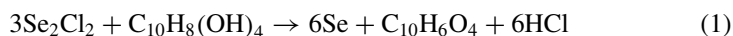
Fig. 1 Cycle of selenium in the environment during mining [7]

Different recovery or treatment processes like (biological) oxidation/reduction, phytoremediation, membrane separation technologies, coagulation or flocculation, and adsorption have been studied and used by researchers to recover selenium. Although industries might receive economic gain from recovering selenium with these processes, excessive operation costs and obeying environmental regulations may make selenium recovery less likely to be adopted on a massive scale. Researchers have favored biosorption because it produces almost no waste; it is more economical compared to other processes. Finally, it is practical in the sense that each country could use the abundant biomass it has to recover selenium. Roberts et al. [1] used *Gracilaria* waste biomass as a bioresource for selenium biosorption, where the *Gracilaria* waste was treated with iron (Fe) and observed that almost 99% of selenium was removed. In our research, following an experiment work, a METSIM model has been developed to separate selenium from chloride media using bioadsorbents prepared from wood lignin, which is described below.

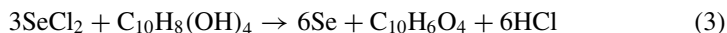
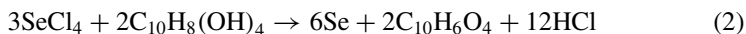
## Modeling of Selenium Recovery

METSIM is a simulator used for metallurgical processes because of its ability to deal with heterogeneous solutions (containing solids and liquids) and modify thermodynamic properties. In this research, selenium monochloride ( $\text{Se}_2\text{Cl}_2$ ) was used in the model since it is one of the most soluble crystalline structures in water, so it is very probable that it would be available in metallurgical solutions or industrial waste effluents. The components needed in this model were  $\text{Se}_2\text{Cl}_2$ , hydrochloric acid (HCl), water, and lignin. The main purpose of HCl and water is to control the pH of the solution entering the reactor tank where a chemical reaction is specified. As in the case of any simulation model, some assumptions must be made for the model to work properly. One of these assumptions was the rate of reaction. For the model to run in METSIM, the reaction rate was entered as a function of temperature and time such as “ $1-xRT/t$ ”, where  $x$  is the initial rate of reaction (e.g. 0.4),  $R$  is the gas constant,  $T$  is temperature, in K and  $t$  is time in minutes. This helps study the effect of residence time on the rate of reaction. Another assumption made in this simulation was the room temperature, according to different researchers, the room temperature in the laboratory was between 20 °C and 25 °C, so a room temperature of 25 °C was assumed in this model. The final assumption made in this simulation was the revolutions per minute (rpm) in the reactor; most researchers were stirring their solution at 200 to 300 rpms; therefore, a 300 rpm agitation was used for this simulation.

The reaction entered in METSIM model is an adsorption reaction where  $\text{Se}_2\text{Cl}_2$  reacts with lignin ( $\text{C}_{10}\text{H}_8(\text{OH})_4$ ) to produce selenium, hydrochloric acid, and product lignin ( $\text{C}_{10}\text{H}_6\text{O}_4$ ) as shown in Eq. 1.



Reactions for both selenium dichloride ( $\text{SeCl}_2$ ) and selenium tetrachloride ( $\text{SeCl}_4$ ) were entered as shown in Eqs. 2–3.



Selenium monochloride was the chloride form of choice because chlorine ions compete with the adsorption of other anions such as selenate and selenite, especially when present at higher concentrations; therefore, choosing a chloride form that has equal number of selenium and chloride ions would be more beneficial than  $\text{SeCl}_2$  and  $\text{SeCl}_4$  as the chlorine concentration would be much higher in these species which would lead to less percent recovery [11]. Elemental selenium [ $\text{Se}(0)$ ] is the selenium species present in both  $\text{Se}_2\text{Cl}_2$  and  $\text{SeCl}_2$ . On the other hand, selenite ( $\text{Se}^{4+}$ ) is present in  $\text{SeCl}_4$ .

A mixer, a heat exchanger, and an agitated reactor tank were the three-unit operation utilized in this simulation. The main purpose of the mixer is to adjust the flow rates and concentrations of  $\text{HCl}$  and  $\text{Se}_2\text{Cl}_2$ , which in turn controls the theoretical pH of the solution entering the heat exchanger which heats the solution to a set temperature before entering the reactor where the main reaction takes place. The process flow diagram is shown in Fig. 2, and Table 1 shows the details of the components present in each stream.

The obtained results from the kinetic studies performed on lignin for selenium adsorption are presented in Fig. 3.

It is clearly indicated that at 25 °C, the adsorption reaction is very good, where 99% of (100 mg/L) selenium available in selenium monochloride solution is adsorbed in 12 h.

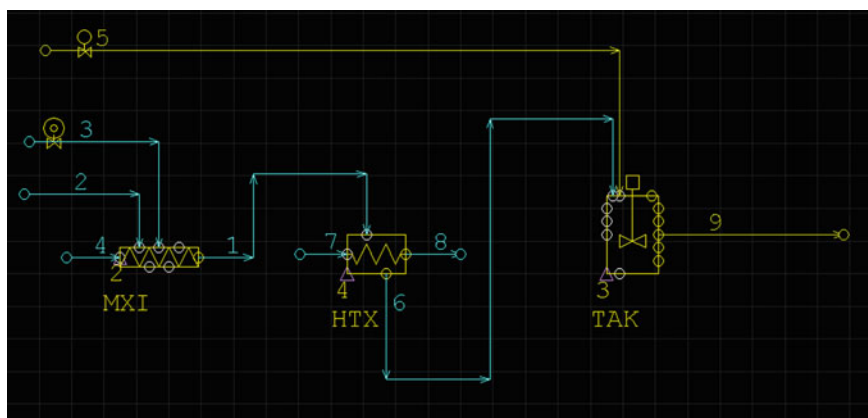


Fig. 2 METSIM model developed with all components and unit operations needed

**Table 1** Components present in each stream

Stream No.	Component(s)
1	Heat exchanger feed ( $\text{Se}_2\text{Cl}_2$ , HCl and $\text{H}_2\text{O}$ )
2	HCl
3	$\text{H}_2\text{O}$
4	$\text{Se}_2\text{Cl}_2$
5	Lignin
6	Hot feed into reactor ( $\text{Se}_2\text{Cl}_2$ , HCl and $\text{H}_2\text{O}$ )
7	Cold water in
8	Hot water out
9	Reactor outlet (Se, product lignin, and HCl)

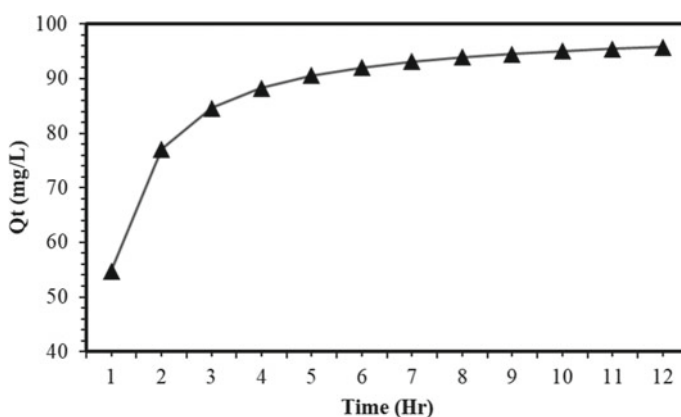
**Fig. 3** Plotting of uptake versus time at Se starting concentration of 100 mg/L

Table 2 shows the selenium uptake capacity at equilibrium ( $q_e$ ) in Langmuir and Freundlich adsorption models, where it was found that the adsorption of selenium by lignin followed the Freundlich adsorption isotherm.

Pseudo-first-order and pseudo-second-order models were fitted and calculated on the results for selenium biosorption on lignin. Table 3 shows the rate constants of pseudo-first order and second order as  $K_1$  and  $K_2$ , respectively. It can be concluded that the methods used to fit obtained experimental data to the pseudo-second-order model are reliable. The activation energy was calculated to be 9.49 kJ/mol and the adsorption process is chemisorption.

**Table 2** Summary of Langmuir and Freundlich adsorption model

Temp. (K)	Langmuir adsorption model		Freundlich adsorption model	
	$q_e$	$R^2$	$q_e$	$R^2$
298	98.4	0.9169	99	0.998

**Table 3** Summary of pseudo-first-order and pseudo-second-order kinetic parameters

Temp. (K)	Pseudo-first-order model		Pseudo-second-order model	
	$K_1$ ( $\text{h}^{-1}$ )	$R^2$	$K_2$ ( $\text{mg ppm}^{-1} \text{h}^{-1}$ ) $\times 10^4$	$R^2$
298	0.2229	0.9169	0.0217	0.998

## Conclusion

A METSIM model has been developed for the adsorption of selenium from chloride media using bioadsorbents prepared from woody biomass, where 99% selenium was recovered from the solution. The model showed that the adsorption process followed the Freundlich adsorption isotherm and the pseudo-second-order kinetic model, and the process is chemisorption.

## References

1. Roberts DA, Paul NA, Dworjanyan SA, Hu Y, Bird MI, Denys R (2015) Gracilaria waste biomass (sampah rumput laut) as a bioresource for selenium biosorption. *J Appl Phycol* 27(1):611–620. <https://doi.org/10.1007/s10811-014-0346-y>
2. Etteieb S, Magdouli S, Zolfaghari M, Brar S (2020) Monitoring and analysis of selenium as an emerging contaminant in mining industry: a critical review. *Sci Total Environ* 698:134339. <https://doi.org/10.1016/j.scitotenv.2019.134339>
3. Plano D, Lizarraga E, Font M, Palop JA, Sanmartín C (2009) Thermal stability and decomposition of sulphur and selenium compounds. *J Therm Anal Calorim* 98(2):559–566. <https://doi.org/10.1007/s10973-009-0291-1>
4. Brummer FA, Gow-Hogge L, Mueller C, Pirelli G, Bobe G (2019) Short Communication: Mineral assessment of rangeland-managed beef cows in the high desert region of oregon. *Appl Animal Sci* 35(6):577–585. <https://doi.org/10.15232/aas.2019-01871>
5. Santos S, Ungureanu G, Boaventura R, Botelho C (2015) Selenium contaminated waters: an overview of analytical methods, treatment options and recent advances in sorption methods. *Sci Total Environ* 521–522:246–260. <https://doi.org/10.1016/j.scitotenv.2015.03.107>
6. Gad SC, Pham T (2014) Selenium. In: Encyclopedia of toxicology, Elsevier, pp 232–235. <https://doi.org/10.1016/B978-0-12-386454-3.00926-X>
7. Stefaniak J, Dutta A, Verbinnen B, Shakya M, Rene ER (2018) Selenium removal from mining and process wastewater: a systematic review of available technologies. *J Water Supply Res Technol Aqua* 67(8):903–918. <https://doi.org/10.2166/aqua.2018.109>
8. Reinsel M (2016) Selenium removal technologies: a review. Available at: <https://www.wateronline.com/doc/industrial-water-treatment-for-inorganic-contaminants-emerging-technologies-0001>
9. Lemly AD (2004) Aquatic selenium pollution is a global environmental safety issue. *Ecotoxicol Environ Saf* 59(1):44–56. [https://doi.org/10.1016/S0147-6513\(03\)00095-2](https://doi.org/10.1016/S0147-6513(03)00095-2)
10. North American Metals Council (2010) Review of available technologies for the removal of selenium from water. <https://www.namec.org/docs/00062756>
11. Schulthess CP, Hu Z (2001) Impact of chloride anions on proton and selenium adsorption by an aluminum oxide. *Soil Sci Soc Am J* 65(3):710–718. <https://doi.org/10.2136/sssaj2001.653710x>

# Biosorption as a Vital Tool for Metal Recovery in Effluent Treatment: A Review



Shilpa Kalamani Bawkar, Pramod K. Singh, Pankaj K. Choubey, Rekha Panda, Jhumki Hait, and Manis K. Jha

**Abstract** The present paper is focused on the application of environment-friendly processes on metals adsorption using bioadsorbent. A huge amount of effluents is generated in electronic manufacturing/ recycling industries containing various metals such as Cu, Cr, Pb, Zn, and Ni. An exhaustive review has been made based on varieties of adsorbents, targeted metals, and medium. The objective of this review is to find out low-cost, easily available, potential adsorbent for metal reclamation. The present paper is engrossed in 'Bioadsorption' as a vital tool for metal recovery. It includes various classified bioadsorbent with their mode of action, adsorption capacities, and feasibility. It gives an overview to researchers and industrialists to find out potential bioadsorbents for further research in effluent treatment and metal recovery. Based on the salient features of developed processes, recommendation for suitable processes has also been made.

**Keywords** Bioadsorbent · Heavy metals · Industrial effluents · Effluent treatment

## Introduction

Metals have larger applications in many processes-based industries like electroplating, surface coating, chemical, and mechanical polishing industries, etc. They have unique properties like conductivity for heat and electricity, ductility, and lustrous effect. Hence, it is showing tremendous market value. These get utilized into different equipment like electronics, vehicles, and construction-based equipment, which we use in day-to-day life. Due to rapid industrialization and globalization, dependency

---

S. K. Bawkar · P. K. Choubey · R. Panda · J. Hait · M. K. Jha (✉)  
Metal Extraction and Recycling Division, CSIR-National Metallurgical Laboratory,  
Jamshedpur 831007, India  
e-mail: [mkjha@nmlindia.org](mailto:mkjha@nmlindia.org)

S. K. Bawkar · P. K. Singh  
Netaji Subhas University, Pokhari, Jamshedpur 831012, India

on these equipment is increasing rapidly. Further, the limited life span of these equipment produces a larger amount of electronic waste, which are non-biodegradable. It creates a large amount of environmental pollution and loss of these valuable metals.

The effluent generated from the industries has large metal values, which get discharged into water bodies without recovering it. Some of the metals from the effluent discharge are harmful to the environment and living organisms. Heavy metals released into the water, enter into the food chain of living organisms, and ultimately can produce problems like bioaccumulation and toxicity effects. All heavy metals are toxic in nature and show many hazardous effects on the human being if get consumed above the recommended level of WHO (Table 1).

There are different techniques of effluent treatment through which these metals get reclaimed from the water bodies to reduce pollution and utilize for betterment. Techniques like coagulation, floatation, membrane filtration, flocculation, magnetic separation, ion-exchange, and adsorption are used for effluent treatment. But all of them have some challenges like process and maintenance costs, harmful side product generation, etc. Amongst all, adsorption is one of the effective techniques showing faster kinetics and higher capacity for metal recovery [1]. The adsorption technique was utilized by many researchers and industrialists for the removal of dyes, different pollutants, heavy metals, etc., using different types of adsorbents like chemical and biological adsorbents from polluted water [2]. Bioadsorbent is an adsorbent prepared by different biodegradable materials like plants, animals, micro-organisms, and waste produced from it. These are easily available, low-cost, eco-friendly, and potential adsorbent for metal recovery from effluent [3].

The present paper reviewed various bioadsorbents, which indicated that bioadsorption is one of the vital tools for metal recovery. This paper gives an overall idea about their preparation and adsorption capacity for different metals along with their advantages and disadvantages. Enlisted information about these classified bioadsorbent will help researchers, and industrialists utilize the information related to their adsorption potential for metal reclamation and effluent treatment.

## **Adsorption of Metal Ions Using Various Bioadsorbent**

The adsorption process is one of the surface interactions between adsorbate and adsorbent. It produces monolayer or multilayer on homo or heterogeneous adsorbent surfaces. Figure 1 explains different surface interactions including the adsorption mechanism.

Many conventional methods are costly and inefficient in heavy metal recovery from effluent having low metal concentration. Many studies have shown the potentiality of different biological materials for metal recovery from wastewater. Bioadsorption is cost-effective, easily available, simple operation, high surface area, and has fewer side effects (no production of hazardous material). It is a beneficial technique for metal recovery, improving the quality of water, and also effective biowaste

**Table 1** Bioadsorbents used for the different heavy metal adsorption

Metal	Hazardous effect and its recommended level (R.L.) in human body	Bioadsorbent	Experimental Condition			Adsorption capacity (mg/g)	References
			Adsorbent dose (g/L)	time (min)	pH		
Cu	Gastrointestinal disease, haemolysis, hepatotoxic effects, nephrotoxic effects R.L.: 2 ppm	1. Sunflower stalk	4	60	4.2	142.8	[5]
		2. Banana peel	5	60	6.5	20.37	[6]
		3. Neem leaf powder	0.01	240	–	185.58	[7]
		4. Chitosan beads	1	1440	5.3	43.13	[8]
		5. Horn core	4	30	–	99.98	[9]
Pb	Anemia, encephalopathy, and hepatitis. Saturates in bones, brain, kidney and affect badly to reproductive system R.L.: 0.01 ppm	1. Maize comb and husk	20	10	7.5	456.7	[10]
		2. Maize leaf	10	30	3	37.31	[11]
		3. Saffron flower waste	2	9	6	45.62	[12]
		4. Cocoa shells	15	1440	2	52.96	[13]
		5. Orange peel	100	20	5	46.61	[14]
		6. Goat hoof	0.1	5	5	27	[15]
Zn	Nausea, skin irritation, vomiting, anaemia R.L.: 5 ppm	1. <i>Azadirachta indica</i> bark	16.6	45	6	33.49	[16]
		2. Palm tree leaves	2	10	5.5	14.7	[17]
		3. Maize comb and husk	20	10	7.5	495.9	[10]
		4. Rice husk ash	10	180	5	14.3	[18]
		5. Chicken feathers	5	10	–	3.06	[19]
Cr	Carcinogenic and mutagenic effect, damage liver, kidney, blood capillaries, cause gastrointestinal irritation R.L.: 0.05 ppm	1. <i>Datura stramonium</i> fruit	0.2	60	2	138.07	[20]
		2. Durian shell waste	1–10	60	2.5	117	[21]
		3. Peanut shell	10	20	5	27.86	[1]
		4. Human Hair	1	50	1	9.853	[22]

(continued)



**Table 1** (continued)

Metal	Hazardous effect and its recommended level (R.L.) in human body	Bioadsorbent	Experimental Condition			Adsorption capacity (mg/g)	References
			Adsorbent dose (g/L)	time (min)	pH		
		5. Waste egg shell	20	10	1.75	92.8	[23]
Cd	Kidney damage, renal disorder, human carcinogen R.L.: 0.003 ppm	1. Neem leaf powder	0.01	240	–	154.5	[7]
		2. <i>Datura innoxia</i> , a medicinal plant leaves	0.1	240	5	12.5	[24]
		3. Modified sugarcane bagasse	1	30	6.5–7.5	196	[25]
		4. Calcinated egg shell	25	10	1.75	92.8	[23]
		5. Maize comb and husk	20	10	7.5	493.7	[10]
Ni	Detrimental and carcinogenic effect, lung and kidney related issues, dermatitis R.L.: 0.07 ppm	1. Tea waste	10	240	4	18.47	[26]
		2. Coir pith	1	40	4	4.17	[27]
		3. Peanut shell	0.3	60	7	2	[28]
		4. Neem leaf powder	0.01	240	–	120.6	[7]
		5. Agro-industrial wastes: plantain (PSR) production and yam starch	0.677 1.19	1440 1440	2 2	47.6 64.5	[29]

use [4]. This review has classified bioadsorbent based on different target metal adsorption. Some of the heavy metals, their hazardous effect, and bioadsorbent used for their adsorption process are summarized in Table 1. The present review gives an idea about efficient bioadsorbent for specific metals with its optimized adsorption mechanism along with its kinetics and suitable isotherm model. Equations utilized for calculating the adsorption efficiency of bioadsorbent are mentioned in Table 2.

### ***Copper (Cu) Adsorption Using Bioadsorbents***

The use of biowaste for copper adsorption is one of the interesting topics in waste water treatment. Sunflower stalk had been proved as one of the efficient copper adsorbents. A 4 g/L sunflower stalk biomass was kept in shaking condition at 120 rpm

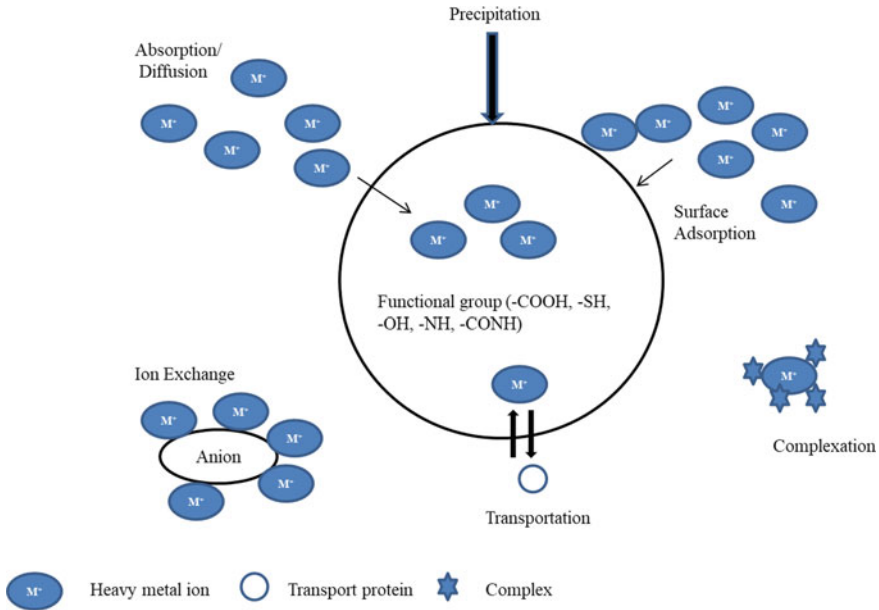


**Fig. 1** Different interaction between adsorbent surface and metal ions (Adopted and modified from [2])

speed with 100 ppm Cu solution for 60 min, 25 °C temperature at pH: 4.2 gave 70–80% copper adsorption. It had shown 142.8 mg/g adsorption capacity. Both Langmuir–Freundlich models gave the best fitting for these experimental results. Further, column studies are performed to validate batch copper adsorption results in continuous mode. The result indicates that modification of the sunflower stalks by nitric acid enhances the adsorption capacity to some extent [5].

Patel and the group studied copper adsorption using activated charcoal produced via neem leaf powder. 0.01 g/L of adsorbent dose was kept in contact with 100 ppm copper-containing aqueous feed solution for 240 min, 41.85 °C temperature, and 200 rpm speed. It showed an adsorption capacity of 185.8 mg/g for Cu. Adsorption reaction follows pseudo-second order kinetic model and Langmuir adsorption isotherm model had shown more suitable for batch and column adsorption experimental data as compared to other adsorption models. This adsorbent had shown seven times regeneration efficiency by treating with 0.1 M HCl indicating reversible and chemical adsorption mechanism of Neem leaf [7].

Recently, Karimi (2022) studied magnetic chitosan beads (developed by EDTA functionalization) for the adsorption of copper. Experiments were carried out using 1 g/L of modified chitosan beads kept in contact with 10 ppm Cu containing aqueous feed solution for 1440 min at pH: 5.3. Results indicated that 93.69% of Cu adsorbed on EDTA modified chitosan beads with 43.19 mg/g adsorption capacity. It obeyed pseudo-second order equation and the Langmuir isotherm. It proved that EDTA

**Table 2** Equations for adsorption process

	Equation	Description	References
% Adsorption	$[(C_o - C_e)/C_o] \times 100$	C <sub>o</sub> : Initial copper concentration in feed solution (mg/L) C <sub>e</sub> : Equilibrium copper concentration in the raffinate (mg/L) m: Mass of adsorbent (gm) V: Volume of adsorbate (L) C <sub>f</sub> : Equilibrium copper concentration in elutant (mg/L)	[24]
Adsorption capacity (mg/g)	$[(C_o - C_e)/m] \times V$		
% Elution	$[C_f / (C_o - C_e)] \times 100$		
<b>Adsorption isotherm</b>			
(i) Langmuir adsorption isotherm	$1/q = [(1/k_1 \cdot q_m) (1/C_e) + (1/q_m)]$	q: Amount of metal adsorbed at equilibrium k <sub>1</sub> : Langmuir constant/ Constant related to the affinity of binding sites for the copper q <sub>m</sub> : The adsorbent capacity (Maximum adsorption of copper metal on adsorbent in mg per unit mass of adsorbent in grams) C <sub>e</sub> : Equilibrium copper concentration in the raffinate (mg/L)	[4]
(ii) Freundlich adsorption isotherm	$q = k_f \times (C_e)^{1/n}$	k <sub>f</sub> : Freundlich constant/ Constant related to the affinity of binding sites for the copper n: Freundlich exponent	
<b>Adsorption kinetics</b>			
(i) Pseudo-first order	$dq/dt = K_1 (q_e - q)$	q <sub>e</sub> : Copper adsorbed on the adsorbent at equilibrium (mg/g) q: Copper adsorbed on the adsorbent at time t (mg/g) k <sub>1</sub> : Rate constant of pseudo-first order reaction (g/mg min)	[7]
(ii) Pseudo-second order	$dq/dt = K_2 (q_e - q)^2$	k <sub>2</sub> : Rate constant of pseudo-second order reaction (g/mg min)	

enhances the adsorption process so it was having great potential in wastewater treatment [8].

### ***Lead (Pb) Adsorption Using Bioadsorbents***

Different biodegradable wastes have been utilized by many researchers for lead adsorption from aqueous solutions. Amongst studied literature, Maize comb and husk indicated maximum adsorption efficiency. It is used for adsorption of lead from the effluent containing 1000 ppm Lead. Experiments were performed using 20 g/L of Maize comb was kept in contact for 10 min at pH: 7.5. Results show that 456.7 mg lead was adsorbed per gram of Maize comb. Further, the surface of Maize comb and husk were modified by the carboxymethylation process to enhance the adsorption efficiency of lead but carboxymethylation have an adverse effect on the lead adsorption resulting in the decrease in adsorption efficiency of Maize comb for lead recovery [10].

Further, saffron flower waste was also utilized for efficient lead adsorption from wastewater. 2 g/L saffron flower waste were kept in contact for 9 min with 30 ppm lead solution with 200 rpm shaking speed at pH: 6 for maximum adsorption. The result indicates that batch experimental data fitted well in the Langmuir adsorption isotherm and follow the second order rate equation. The maximum adsorption capacities were 36.97 mg/g and 45.62 mg/g for the ultrasonic and shaking process, respectively. Results indicated that shaking was a more efficient way for adsorption than the sonication method [12].

Another household waste like cocoa shells was studied by Meunier and his coworkers for lead adsorption from acidic wastewater. Batch studies were performed using 15 g/L of Cocoa shells contacted with 4.5 ppm Pb containing aqueous feed solution for 1440 min at 150 rpm speed, the 22–24 °C temperature at pH: 2. Results had shown that 94.21% Pb adsorbed without other salt interference with 52.96 mg/g adsorption capacity. The importance of this research was to study the effect of different parameters like different salt concentrations, pH, initial feed concentration of metal, etc. It indicated that lead removal from the acidic wastewater in the presence of high Ca and Mg concentrations were reduced. However, it was unaffected in the presence of high K and Na concentrations. Studies had been revealed that the carboxyl and amino functional group was involved in the adsorption process of lead by cocoa shells [13].

### ***Zinc (Zn) Adsorption Using Bioadsorbents***

Different bioadsorbent were reviewed for zinc adsorption and it was found that maize comb and husk had shown a maximum adsorption capacity of 495.9 mg/g. Experimental conditions for maize comb as an adsorbent were similar to those used for

lead adsorption [10]. King and team studied Zn adsorption using 16.6 g/L *Azadiracta indica* bark powder where adsorbent was contacted with 20 ppm zinc solution for 45 min, 30 °C temperature, and 100 rpm shaking speed at pH: 6. Adsorption capacity of neem bark was 33.49 mg/g with 96% adsorption. Isothermal data were well fitted in the Langmuir model and pseudo-second order kinetic model. Neem plant is effective bioadsorbent of Zn, but bioadsorption process was affected due to intraparticle diffusion of metal through the adsorbent surface [16].

Slaughter house waste like chicken feathers was utilized as a bioadsorbent for zinc recovery from wastewater. Al-Ashesh and group studied changes in the adsorption pattern of chicken feathers with or without chemical treatment. Experiments were carried out by taking 5 g/L of adsorbent soaked in 100 ppm concentration of Zn containing aqueous for 10 min. Results indicated that 2.52 and 3.06 mg/g of zinc was adsorbed on adsorbent after treatment with 0.6% dodecyl sulfate and 0.2 N NaOH, respectively, while non-activated chicken feather shows only 1.8 mg/g of adsorption. They proved pretreatment of 0.2 N NaOH and 0.6% dodecyl sulfate (anionic surfactant) separately was best for the sorption process because it improves porosity in keratin for easy sorption of metal in it. Data were well fitted in Freundlich isotherm indicating a multilayer adsorption process [19].

### ***Chromium (Cr) Adsorption Using Bioadsorbents***

Various bioadsorbents had been investigated for chromium adsorption in which *Datura stramonium* fruit had shown a maximum adsorption capacity of 138.07 mg/g amongst all reviewed literature. Experiments were carried out by using 0.2 g/L of fruit sample kept in contact with 100 ppm chromium containing aqueous solution for 60 min contact time, 60 °C temperature with 100 rpm shaking speed at pH: 2. Result indicates that phosphoric acid treated *Datura stramonium* (PDSF) had shown maximum adsorption capacity 138.07 mg/g as compared to raw fruit powder showing 84 mg/g adsorption. Experimental data fitted well in Langmuir isotherm and pseudo-second order kinetic equation. In this literature, chemical modification using phosphoric acid treated *Datura stramonium* fruit was checked for chromium adsorption. Energy dispersive X-ray (EDX) studies of the sample revealed that phosphoric acid treated *Datura stramonium* (PDSF) had different sizes and shapes of pores and fibers compared to raw fruit powder. It indicated that the adsorption process was governed by the physisorption mechanism. It was proved as an economical and efficient alternative to bioadsorbent [20].

One more biodegradable waste like durian shell waste was used for chromium adsorption from industrial waste effluents. Batch experiments were performed using 1–10 g/L Durian shell waste retained in 200 ppm Cr metal containing effluents for 60 min contact time, 60 °C temperature, 100 rpm shaking speed at pH: 2.5. Result indicates that adsorption capacity of durian shell was 117 mg/g. Further, kinetic data showed that pseudo-first order data fit well as compared to pseudo-second order rate reaction. It followed both Langmuir and Freundlich isotherm model. Chromium

adsorption by durian shell adsorbent was spontaneous, independent, and endothermic reaction proved to be a potent bioadsorbent [21].

### ***Cadmium (Cd) Adsorption Using Bioadsorbents***

Cadmium adsorption was one of the important topics to review due to its highly carcinogenic property. Many bioadsorbents were reviewed for cadmium adsorption and showed that maize comb husk had shown maximum adsorption capacity (493.7 mg/g). Details about experimental conditions for cadmium adsorption using maize comb husk have been already discussed in the lead adsorption section [10].

One of the animal wastes like poultry eggshell was used as bioadsorbent for cadmium adsorption from acidic wastewater. Experiments were carried out by using 20 g/L of calcinated waste egg shell kept in contact with 3 ppm Cd metal solution in shaking condition at 200 rpm for 10 min contact time, the 23–25 °C temperature at pH: 1.75. Results had shown 100% removal of cadmium from wastewater through the adsorption process with 92.8 mg/g adsorption capacity. It was obtained through modification of eggshell by burning it up to 800 °C at a heating speed of 40 °C/min. Calcination of eggshell began at 650 °C by the formation of pure CaCO<sub>3</sub> and converted to CaO, resulting in a phase change in the sample. Calcination of eggshells transformed it into lime (CaO) and pore enlargement, which enhances the adsorption process. It strongly recommends the use of calcinated eggshells in the treatment of wastewater for metal recovery [23].

Junior and the team used modified sugarcane bagasse for Cd adsorption. Experiments were performed by taking 1 g/L of modified sugarcane bagasse kept in contact for 30 min with an aqueous solution containing 200 ppm cadmium at pH: 6.5–7.5. It had shown maximum cadmium adsorption with an adsorption capacity of 196 mg/g with its chemical modification. Sugarcane bagasse was chemically modified with succinic anhydride for better results. Adsorption data fitted well in both Freundlich and Langmuir isotherm models. It had been proved that the metal adsorption efficiency of the prepared adsorbent was directly related to the number of amine groups present on its surface. Therefore, it was proved to be one of the effective, cheap methodologies for cadmium adsorption [25].

### ***Nickel (Ni) Adsorption Using Bioadsorbents***

Various biological adsorbents were reviewed for nickel adsorption from wastewater indicating that neem leaf powder had shown a maximum adsorption capacity of 120.6 mg/g of adsorbent, experimental conditions for this research were discussed along with the copper adsorption section [7]. Although, tea leaves waste from factories is used as a bioadsorbent for nickel adsorption from an aqueous solution, maximum adsorption was achieved by 10 g/L adsorbent kept in contact with 200 ppm

Ni solution for 240 min, 60 °C temperature, and 360 rpm shaking speed at pH: 4. It was analyzed that maximum adsorption capacity of tea waste was 18.42 mg/g. A thermodynamic investigation was also done in this study, which indicates that the adsorption reaction was spontaneous, slightly endothermic, and irreversible. Adsorption data fitted well in the Langmuir isotherm model. The breakthrough curve for Ni was studied by column experiments. Factory waste tea leaf powder had shown enormous potential for Ni adsorption from industrial wastewater [26].

Further, agro-industrial waste like yam starch (YSR) was used for nickel adsorption. Experiments were carried out by using 1.19 g/L yam starch as an adsorbent was kept in contact with 31.82 ppm Ni initial metal concentration for 1440 min, 70 °C temperature, and 200 rpm shaking speed at pH: 2 for maximum adsorption. Results indicated that yam starch had 64.5 mg/g adsorption capacity for nickel. It followed pseudo-second order equation and data fitted well in the Freundlich model. Column studies were performed for large-scale applications. This was proved to be one of the low-cost, efficient, easily available biomaterial, which was rich in cellulose, lignin, and hemicelluloses [29].

Maximum adsorption capacities of different bioadsorbent for specific metals give indication about their potentiality as an adsorbent. Still, work related to contact with multi-metal solution systems, adsorption in continuous mode, desorption, and scale-up studies need to be investigated before its commercialization. A generalized flow sheet for the overall adsorption mechanism has been included in Fig. 2.

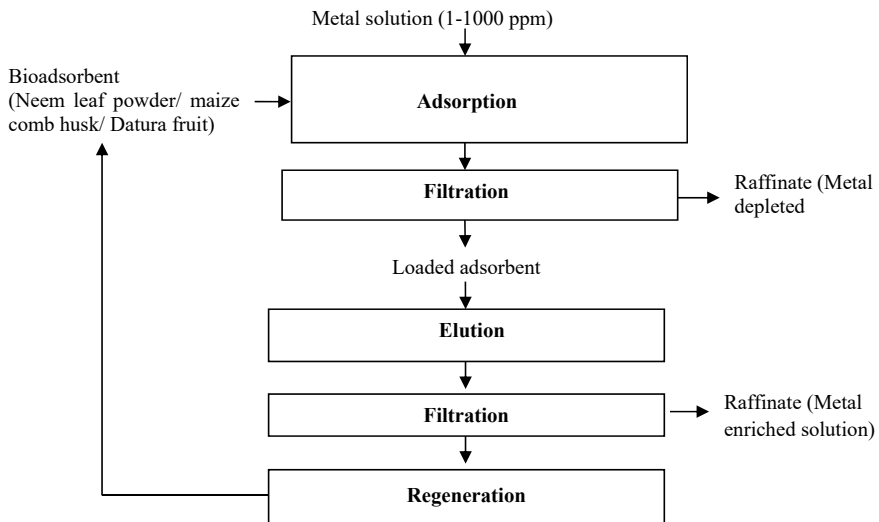


Fig. 2 Generalized flow sheet for overall adsorption mechanism

## Conclusions

In the extension of finding new separation and purification techniques for metals, bioadsorption is one of the indispensable techniques in metal recovery from effluent. Reviewed bioadsorbents had shown high adsorption capacity, simple operation, easy handling, cost-effectiveness, and abundance in nature. Bioadsorbents enlisted in this paper give an overall idea about its potentiality for specific metal. The present review concludes that

- Neem leaf powder is a good adsorbent for copper (Capacity: 185.8 mg/g) and nickel (Capacity: 120.6 mg/g) metal from the aqueous solution.
- Maize comb husk as an adsorbent is found to be efficient for cadmium (Capacity: 493.7 mg/g), lead (Capacity: 456.7 mg/g), and zinc (Capacity: 495.9 mg/g) metal adsorption from the effluent.
- *Datura (Datura stramonium)* fruit powder (Capacity: 138.07 mg/g) was efficiently used amongst all for chromium adsorption from wastewater.

This review offers wide perspectives on the use of various bioadsorbents, but that are applied to a laboratory scale. Further research is essential to validate the results and scale up to industrial wastewater treatment.

**Acknowledgements** One of the authors—Mrs. Shilpa Kalamani Bawkar—would like to extend gratitude towards CSIR-NML, Jamshedpur for providing a research facility (Grant FTC-0014/MLP-3116) to carry out this research work.

## References

1. Witek-Krowiak A, Szafran RG, Modelski S (2011) Biosorption of heavy metals from aqueous solutions onto peanut shell as a low-cost biosorbent. *Desalination* 265:126–134
2. Mathew BB, Jaishankar M, Biju V, Beeregowda KN (2016) Role of bioadsorbents in reducing toxic metals. *J Toxicol* 12:1–13
3. Gautam RK, Mudhoo A, Lofrano G, Chattopadhyaya MC (2014) Biomass-derived biosorbents for metal ions sequestration: adsorbent modification and activation methods and adsorbent regeneration. *J Environ Chem Eng* 244:1–21
4. Abas SNA, Ismail MHS, Kamal ML, Izhar S (2013) Adsorption process of heavy metals by low-cost adsorbent: a review. *World Appl Sci J* 28(11):1518–1530
5. Hussein BI (2010) Removal of copper ion from waste water by adsorption with modified and unmodified sunflower stalk. *J Eng* 16(3):5411–5421
6. Hossain MA, Ngo HH, Guo WS, Nguyen TV (2012) Biosorption of Cu (II) from water by banana peel based biosorbent: experiments and models of adsorption and desorption. *J Water Sustain* 2(1):87–104
7. Patel H (2020) Batch and continuous fixed bed adsorption of heavy metals removal using activated charcoal from neem (*Azadirachta indica*) leaf powder. *Sci Rep* 10:16895
8. Karimi F, Ayati A, Tanhaei B, Sanati AL, Afshar S, Kardan A, Dabirifar Z, Karaman C (2022) Removal of metal ions using a new magnetic chitosan nano-bio-adsorbent; A powerful approach in water treatment. *Environ Res* 203:111753



9. Ngueagni PT, Woumfo ED, Kumar PS, Siewe M, Vieillard J, Brun N, Nkuigwe PF (2019) Adsorption of Cu(II) ions by modified horn core: effect of temperature on adsorbent preparation and extended application in river water. *J Mol Liq* 298(1):112023
10. Igwe JC, Ogunewe DN, Abia AA (2005) Competitive adsorption of Zn (II), Cd (II) and Pb (II) ions from aqueous and non- aqueous solution by maize cob and husk. *Afr J Biotech* 4(10):1113–1116
11. Babarinde NAA, Babalola JO, Sanni RA (2006) Biosorption of lead ions from aqueous solution by maize leaf. *Int J Phys Sci* 1(1):023–026
12. Khoshsang H, Ghaffarinejad A (2018) Rapid removal of lead (II) ions from aqueous solutions by saffron flower waste as a green biosorbent. *J Environ Chem Eng* 6(5):6021–6027
13. Meunier N, Laroulandie J, Blais JF, Tyagi RD (2003) Lead removal from acidic solutions by sorption on cocoa shells: effect of some parameters. *J Environ Eng* 129:693–698
14. Lugo-Lugo V, Hernandez- S, Barrera- C, Urena-Nunezb F, Bilyeu B (2009) A comparative study of natural, formaldehyde-treated and copolymer-grafted orange peel for Pb(II) adsorption under batch and continuous mode. *J Hazard Mater* 161:1255–1264
15. Gayathri NS, Andal NM, Anuradha J (2017) An investigation approach on the sequestration of divalent metal ions employing animal waste. *Orient J Chem* 33(3):1406–1413
16. King P, Anuradha K, Lahari SB, Kumar YP, Prasad VSRK (2008) Biosorption of zinc from aqueous solution using *Azadirachta indica* bark: equilibrium and kinetic studies. *J Hazard Mater* 152:324–329
17. Abu FA, Al-Rub. (2006) Biosorption of zinc on palm tree leaves: equilibrium, kinetics, and thermodynamics studies. *Sep Sci Technol* 41:3499–3515
18. Bhattacharya AK, Mondal SN, Das SK (2006) Adsorption of Zn(II) from aqueous solution by using different adsorbents. *Chem Eng J* 123(1–2):43–51
19. Asheh SA, Banat F, Rousan DA (2003) Beneficial reuse of chicken feathers in removal of heavy metals from wastewater. *J Clean Prod* 11:321–326
20. Kumar S, Shahnaz T, Selvaraju N, Rajaraman PV (2020) Kinetic and thermodynamic studies on biosorption of Cr(VI) on raw and chemically modified *Datura stramonium* fruit. *Environ Monitoring Assess* 192(248):1–24
21. Kurniawan A, Sisnandya VOA, Trilestari K, Sunarso J, Indraswatia N, Ismadjia S (2011) Performance of durian shell waste as high capacity biosorbent for Cr(VI) removal from synthetic wastewater. *Ecol Eng* 37:940–947
22. Mondal NK, Basu S (2019) Potentiality of waste human hair towards removal of chromium(VI) from solution: kinetic and equilibrium studies. *Appl Water Sci* 9(49):1–8
23. Jai PH, Wook JS, Kyu YJ, Gil KB, Mok LS (2007) Removal of heavy metals using waste eggshell. *J Environ Sci* 19:1436–1441
24. Begum S, Yadamari T, Yakkala K, Gurijala RN (2015) Adsorption and Equilibrium Studies of Cadmium(II), Chromium (VI) and Lead (II) Ions using Ecofriendly Biosorbent. *Int J Eng Res Technol (IJERT)* 4(5):696–702
25. Junior OK, Gurgel LVA, Melo JCP, Botaro VR, Melo TMS, Gil RPF, Gil LF (2007) Adsorption of heavy metal ion from aqueous single metal solution by chemically modified sugarcane bagasse. *Biores Technol* 98(6):1291–1297
26. Malkoc E, Nuhoglu Y (2005) Investigations of Nickel (II) removal from aqueous solutions using tea factory waste. *J Hazard Mater* 127:120–128
27. Swarnalatha K, Ayoob S (2016) Adsorption studies on coir pith for heavy metal removal. *Int J Sustain Eng* 9(4):259–265
28. Yildiz S (2018) Artificial neural network approach for modeling of Ni(ii) adsorption from aqueous solution by peanut shell. *Ecol Chem Eng S* 25(4):581–604
29. Tejada-Tovar C, Villabona-Ortiz A, Ortega-Toro R (2021) Batch and packed bed column study for the removal of Cr (VI) and Ni (II) using agro-industrial wastes. *Appl Sci* 11:9355

**Part IV**  
**Process Development and Optimization**

# Formation of Different Zinc Oxide Crystal Morphologies Using Cellulose as Nucleation Agent in the Waste Valorization and Recycling of Zn-Ion Batteries



Billy W. Hoogendoorn, Xiong Xiao, Veerababu Poliseti, Fritjof Nilsson, Kåre Tjus, Kerstin Forsberg, and Richard T. Olsson

**Abstract** The formation of zinc oxide particles of different hierarchical morphologies was investigated. By performing elemental analysis on samples extracted from the supernatant solution during precipitations yielding two distinctly different morphologies, the consumption of zinc ions was used to follow the liquid-to-solid phase formation. While a rapid Zn-ion consumption was synonymous with the formation of predominantly oxygen terminated flower-shaped ZnO-particles, with half of the zinc ions being precipitated during the first minute, less than 10% of the zinc ions were converted to sea urchin-shaped ZnO-particles (with mixed terminations) after 1 min of the reaction. The unique ZnO-particle morphologies may therefore be related to the precipitation rates, which can be further explored as a tool for understanding how ZnO-particles with differently faceted surfaces form. Interestingly, the different formation rates remained with identical patterns when 0.5 g/L cellulose (0.005 wt%) was added to the reactions as nucleating agent for improved yields. The controlled formation of specific functional ZnO-particle surfaces is an important method for recycling inexpensive zinc waste from batteries to high value materials useful in a variety of catalytic applications.

**Keywords** ZnO-particle synthesis · Hydrometallurgy · Precipitation · Cellulose · Battery recycling

---

B. W. Hoogendoorn · X. Xiao · V. Poliseti · F. Nilsson · R. T. Olsson (✉)  
Department of Fiber and Polymer Technology, KTH Royal Institute of Technology, Teknikringen 56, 11428 Stockholm, Sweden  
e-mail: [rols@kth.se](mailto:rols@kth.se)

K. Forsberg (✉)  
Department of Chemical Engineering, KTH Royal Institute of Technology, Teknikringen 42, 11428 Stockholm, Sweden  
e-mail: [kerstino@kth.se](mailto:kerstino@kth.se)

K. Tjus  
IVL Swedish Environmental Research Institute, Stockholm, Sweden

## Introduction

Metal oxide particles are a group of materials that are attributed with significant value in research as well as in industrial applications. While inorganic materials such as tin and indium oxide are seeing an increased use in photovoltaics, [1] titanium dioxide and zinc oxide (ZnO) have been seen as a viable material choice in sunscreens as well as novel energy storage systems of zinc ion batteries [2–4]. However, a fundamental aspect when it comes to using these materials in high value applications is related to taking advantage of the morphologies of the inorganic particles. Due to the anisotropic behavior of the different crystal facets of ZnO-particles, shapes and sizes have a significant impact on the properties of the materials, in particular when it comes to properties useful in reactions or interactions taking place on the particle surfaces [5, 6]. While empirically refined synthesis protocols to obtain specific metal oxide-morphologies are common in the scientific literature [5, 7–10], studies focusing on the particle formation rates (kinetics) as related to the development of the final morphologies are scarce, and pinpointing the exact underlying mechanisms leading to the formation of different morphologies is challenging. Experiments providing insight into the reaction kinetics may contribute to an understanding of the formation of specific ZnO-particle shapes and sizes, which in turn can be used to adjust the reaction conditions and tune the morphologies during synthesis towards preferred ZnO-particle shapes. This will allow for designing protocols that generate particle shapes and surfaces in anisotropic ZnO-particles with a favorable reactive nature (catalytic, optical, etc.) from inexpensive recycled zinc waste material, e.g. from the emerging zinc battery industry [4, 11–13]. The use of tailormade faceted and anisotropic ZnO-particles with optimized atomic surface compositions in sunscreens may allow for either use of smaller amounts of ZnO content in the sunscreen, or better performance for the same quantity of ZnO in terms of UV screening capability. The catalytic activity of ZnO has also been shown to be strongly related to the nature of the lattice terminations of the ZnO-particles, providing more than 100% improved photocatalytic performance for oxygen terminated surfaces [4]. Overall, the possibility to control the particle morphologies during the synthesis is relevant for the applied use of the particles, and within recycling efforts since it may allow for immediate waste valorization of readily abundant and inexpensive zinc, while minimizing waste accumulation in landfills. ZnO photocatalytic particles presently retail for \$2000 per kg whereas the zinc metal as raw material is sold at \$3 per kg, demonstrating the economic value of developing efficient waste valorization streams [14, 15].

In this study, the reaction progressions during the precipitations (de-supersaturation) resulting in different ZnO-morphologies were investigated. The conversion from zinc ions to ZnO-particles was studied for two reactions yielding two different particle morphologies, flower- and sea urchin-shaped particles. These morphologies are synonymous with specific surface properties and atomic representation in the outer layers of the particles, providing very different reactive nature of the materials. The conversion of zinc ions to solid zinc oxide was monitored by

following the zinc ions concentration in the solution used to precipitate the solid ZnO-particles. The results revealed that the growth patterns (formation) were significantly different for the two particle morphologies. The presence of 0.005 wt.% cellulose nanofibers as a nucleating agent was also evaluated for the two reactions to establish if the cellulose also had an impact on the growth patterns of the ZnO-particles.

## Materials and Methods

### *Materials*

Zinc nitrate hexahydrate ( $\text{Zn}(\text{NO}_3)_2 \cdot 6\text{H}_2\text{O}$ , 98%, Fischer Scientific), sodium hydroxide (NaOH, > 98%, Sigma-Aldrich), sulfuric acid ( $\text{H}_2\text{SO}_4$ , 95–97%, Sigma-Aldrich), and milliQ water (MQw, 18.2 M $\Omega$ , pH = 7) were used as obtained. Cellulose nanofibers were extracted and isolated from ultra clean and highly crystalline bacterial cellulose (BC) using sulphuric acid at 30% (aq) concentration. The BC was purchased in the form of cubes with an approximate volume of 1 cm<sup>3</sup> from Monstra LLB (dba, Pacific Rim). The detailed protocol for the isolation of the fibers is available in Liu et al. 2015 and Hoogendoorn et al. 2022, although more environmentally friendly protocols have also been reported by Rovera et al. 2018 [16–18].

### *Synthesis of Zinc Oxide Particles*

Zinc oxide particles were prepared according to protocols previously developed by Hoogendoorn et al. [17] 750 ml of an aqueous 0.15 M solution of zinc nitrate hexahydrate was prepared and mixed over night at room temperature before being heated in a cylindrical plastic container under mechanical stirring to a temperature specified in Table. 1 (40 or 60 °C). The synthesis was initiated by quickly (< 5 s) adding 250 ml of an aqueous NaOH-solution (see Table 1; 3 or 4.5 M), heated to the same temperature as the zinc-salt solution. The concentration of zinc species in the mixed solution was 0.1125 M. The reaction was allowed to progress for 1 h before being quenched with 0.7 L of cold MQw. The reaction mixture was centrifuged 4 × 10 min with an intermediate exchange of MQw between each cycle. For each ZnO-synthesis, 4 ml aliquots were taken at 1, 15, 30, 45 and 60 min after the initiation of the reactions. The aliquots were centrifuged for 2 min at 12 100 × g to concentrate and isolate the solid phase. The supernatant containing the unreacted zinc ionic species was immediately mixed with 10 ml of a 5 vol.%  $\text{HNO}_3$ -solution. When performing the ZnO-reactions in the presence of bacterial CNF, a volume of the CNF-dispersion corresponding to 0.05 g of solid CNF was dispersed into the Zn-salt solution prior to mixing it overnight.

**Table 1** Concentrations of the NaOH-solutions ( $C_{\text{NaOH}}$ ), and temperatures used for the synthesis reactions yielding flower-shaped or sea urchin-shaped particles, respectively.\*

Sample specification	$C_{\text{NaOH}}$ [M]	T (°C)
ZnO-flowers	3	40
ZnO-sea urchins	4.5	60

\* A Zn-salt concentration of 0.15 M (prior to adding the NaOH-solution) was used in both reactions, resulting in a 0.1125 M concentration after mixing. When incorporating CNF, a CNF-concentration of 0.05 g/L after mixing was used

## Characterization

**Microscopy:** Scanning electron microscopy (SEM) was performed on the ZnO-particles using a Hitachi S-4800 field emission scanning electron microscope. The dried samples were attached to the sample holder using carbon tape before being sputtered with a Pt/Pd-coating for 40 s. The acceleration voltage used for the imaging was 5 kV and the emission current was 10  $\mu\text{A}$ .

**Crystallographic analysis:** X-ray diffraction was performed on the samples using a PANalytical X'Pert PRO X-ray diffractometer. The measurements were performed at a start and stop angle of 5 and 80 degrees, respectively, at 45 kV and 40 mA (using a Cu  $K\alpha$ ) as a source for X-ray generation. The measurements were performed at a step size of 0.06 degrees at a wavelength of 0.154 nm.

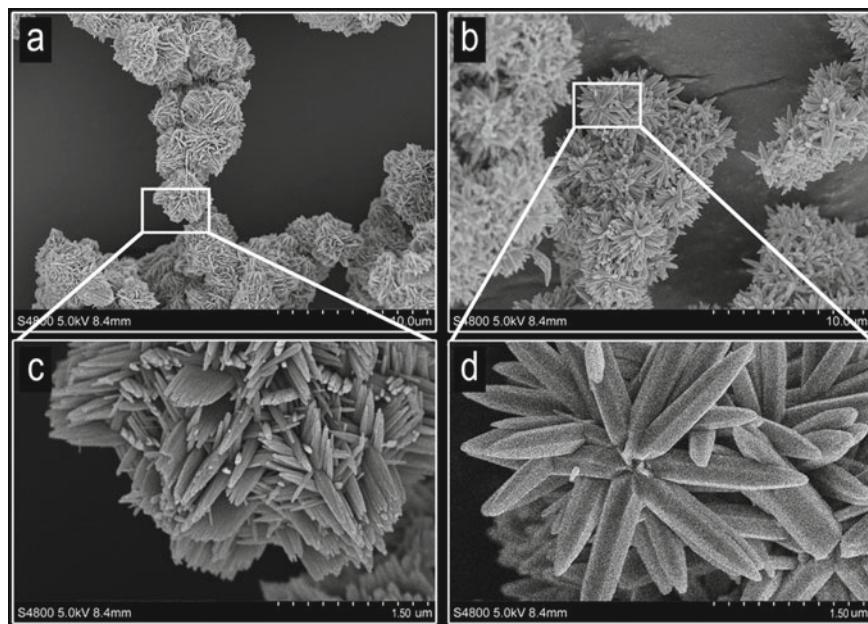
**Elemental analysis:** Inductively coupled plasma-optical emission spectroscopy (ICP-OES, Thermo Fisher iCAP 7400, USA) was performed on the supernatant samples (where the solid phase had been removed). The supernatant was exposed to nitric acid (see section regarding the synthesis of ZnO-particles) for maintaining unreacted zinc ionic species in solution. The samples were diluted to concentrations suitable for the ICP-OES measurements (< 100 mg/L) using 5 vol.%  $\text{HNO}_3$  (aq).

## Results and Discussion

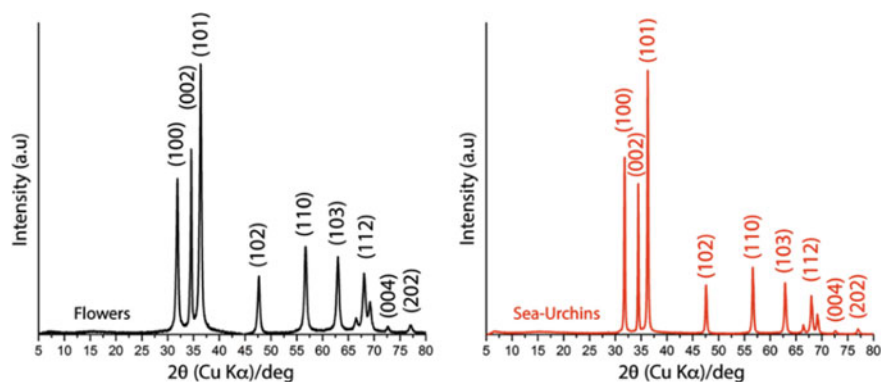
### Development of ZnO-Particles with Time

Figure 1 shows the particles for the two different synthesis protocols. The micrographs confirm that the conditions resulted in two morphologies with distinctively different features. The reaction taking place at 40 °C at a lower alkalinity (see Table. 1) resulted in the formation of 3–4  $\mu\text{m}$  spherical particles (referred to as flower-shaped structures, Fig. 1a) consisting of a mix of significantly smaller sheet and rod-like structures (Fig. 1c), whereas the reaction taking place at 60 °C and at a higher alkalinity resulted in the formation of faceted rod-structures assembled into 3–4  $\mu\text{m}$  sea urchin particles (Fig. 1b). These sea urchin-shaped particles had an underlying structure dominated by 300–500 nm thick and clearly visible hexagonal

rods (Fig. 1d). The XRD-measurements, seen in Fig. 2, confirmed that both reactions resulted in the formation of the hexagonal Wurtzite structure associated with ZnO (ICSD PDF 075–0576).



**Fig. 1** Micrographs of flower-shaped (a, c) and sea urchin-shaped (b, d) particles. The consumption of zinc ions during the formation of the particles was followed by sequential supernatant extractions and ICP concentration measurements, allowing for determining that the flower-shaped particles (a, c) grew into their final morphology significantly faster than the sea urchin-shaped particles (b, d)



**Fig. 2** X-ray diffractograms of flower-shaped ZnO-particles (left) and sea urchin-shaped ZnO-particles (right)

Earlier research consists of an extensive record of studies investigating how the conditions of ZnO-synthesis reactions can be altered to promote different morphologies. The studies have revealed that a high  $\text{OH}^-/\text{Zn}^{2+}$ -ratio promotes the formation of rod-like structures, while a lower  $\text{OH}^-/\text{Zn}^{2+}$ -ratio shifts the reaction to favor the formation of sheet-like morphologies [7, 10]. However, since the studies mostly follow an empirical approach to determine the crucial conditions for reaching certain morphologies at the end of the reactions, the underlying growth patterns and formation rates for the different morphologies remain largely unknown.

Previously, Hoogendoorn et al. demonstrated that the formation of flower-like structures, partially built up by sheets, is accompanied by higher yields as compared to rod-based sea urchin-structures [17]. The yield values in this current study were obtained by drying and weighing the products and revealed that the flower-shaped particle was formed at an ultimate yield of 83%, whereas the sea urchin particles showed a yield of 57%. However, whereas the extracted solid phase allowed for following the phase formation and the morphological changes of the particles (how the shape of the particles developed over time), the overall progression of the reactions in terms of consumed and precipitated zinc ion species was challenging to establish from the weighted samples. Therefore, instead of estimating the progression of the reactions from morphological changes over time, and weighing the formed ZnO to determine the amount of zinc ions that had been converted to solid phase, measuring the concentration of Zn-ions remaining in the solution allowed for a more accurate and quantitative analysis of the formation rates of ZnO, see Fig. 3.

Figure 3 shows the yield of ZnO as a function of time for the two reactions. The yield was indirectly obtained from the ICP-data of the remaining Zn-ions in the solution as the solid phase formed. The graph confirms that the two morphologies stem from growths' having significantly different Zn-ion consumption rates during the formation of the solid phases. The precipitation of the flower-shaped ZnO-particles

**Fig. 3** Graph showing the consumption of Zn-ions with time for the synthesis protocols resulting in flower-shaped (black) and sea urchin-shaped (red) particles. Measurements were made from the supernatant of un-precipitated zinc ions to allow for accurate monitoring of the reaction progressions

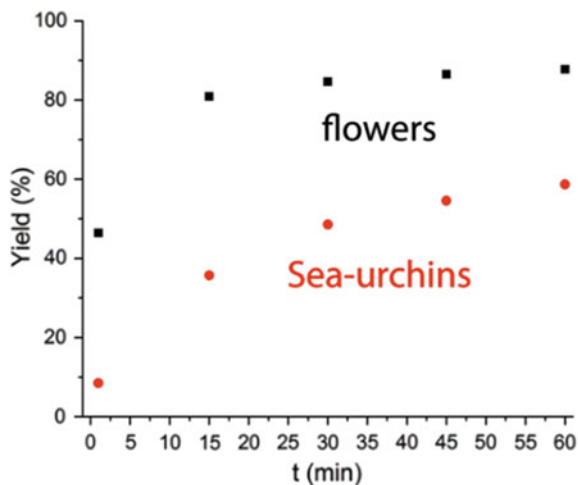




(Fig. 1a, c) was revealed to be initiated by a fast consumption of Zn-ions within the first minute of the reaction, resulting in almost half of the Zn-ions, ca. 46%, being consumed within 1 min. After 15 min, the total consumption reached 80% of the total amount of zinc ions present at the start of the reaction. At this point, the consumption of Zn-ions reached a plateau, leading to a total yield of solid phase stagnating at 87%, according to the ICP-measurements. This consumption pattern was in contrast to the sea urchin-shaped particles, which was characterized by a slow consumption during the first minute of the reaction, with less than 10% being consumed (ca. 7.6%) at the point when the system generating flower-shaped particles had consumed 46% of the Zn-ions. The difference in initial consumption of Zn-ions within the first minute corresponds to a difference of ca. 600% when comparing the amount of precipitated ZnO for the flower-shaped and the sea urchin-shaped particles. The consumption of ions for the sea urchin particles was thereafter more gradually being consumed throughout the reaction, ending up at 58% yield after 60 min. Further analysis showed that the time to reach 50% absorption of the dissolved zinc ion species was at ca. 2 min for the flower-shaped particles and ca. 40 min for the sea urchins, indicating that the former process was about 20 times faster than the latter. In sorption experiments with flat samples, the diffusivity is proportional to the squared sample thickness divided with the time to reach 50% sorption [19]. In analogy with those diffusion calculations, it can be concluded that the faster consumption for the flower-shaped particles was either due to thinner crystals with a higher specific surface area and/or a higher chemical reaction rate. The specific surface area (SSA) at the full reaction time (60 min) for the flower- and sea urchin-shaped particles was 5.45 m<sup>2</sup>/g and 1.98 m<sup>2</sup>/g, [17] respectively, although the SSA at any given time during the reaction was unknown. The relatively small difference in SSA as compared to the marked higher reaction rates associated with the underlying flat thinner crystals of the flower-shaped particles suggests that the higher growth rate was still uniquely associated with the formation of oxygen terminated sheets. The higher calculated yields for both reactions, as compared to the established yields by weighing the precipitated materials, were suggested to be caused by small mass losses during the purification of the product (centrifugation and removal of counter ions).

### ***Zinc Species Reaction Consumptions Rate Associated with the Formation of Facetted Surfaces with Different Theoretical Atomic Compositions***

Figure 4 shows the atomic terminations associated with different four exposed lattice planes for the ZnO crystals surfaces, which may form with the precipitations of anisotropic ZnO Wurtzite (Fig. 4a, b).

The illustrated sheet-like morphologies associated with the flower-shaped particles were previously reported as oxygen rich in their outer terminating (2 $\bar{1}0$ ) atomic layers (Fig. 4a) [20]. This surface is not only oxygen rich in its nature but also highly

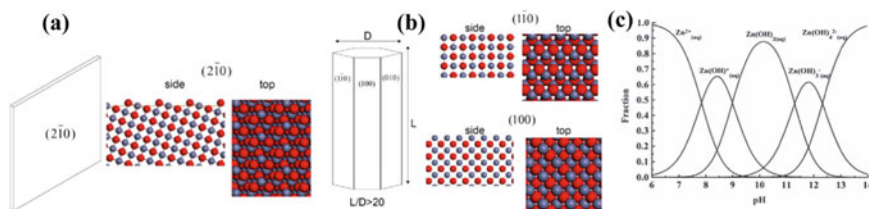


**Fig. 4** **a** and **b** Graphic illustrations of the formed ZnO planes associated with the formation of flower-shaped and sea urchin-shaped particles containing faceted surfaces with different atomic representation. Modelled lattice planes of the ZnO adopted from [20] **c** Zn (II) ions species existing as  $Zn^{2+}$  (aq),  $Zn(OH)^+$  (aq),  $Zn(OH)_2$  (aq),  $Zn(OH)_3^-$  (aq) and  $Zn(OH)_4^{2-}$  (aq) over a range of pH at 25 °C, plot adopted from [21]

polar and very reactive (electrostatically unstable) and always stabilized by hydroxyl groups [22]. In contrast, Fig. 4b shows the sides of the spiky rods contained in the sea urchins (Fig. 1b and d), which are either polar as terminated by the Zn-ions in its outer layers (100), or non-polar as mixed terminated ZnO represented by  $(1\bar{1}0)$  or  $(010)$ . The reactivities shown in Fig. 3 consequently are in agreement with a more rapid consumption of Zn-ion species when the flower-shaped particles form by deposition of zinc species on oxygen rich surfaces, whereas the rods form more slowly when yielding surfaces that are less reactive as zinc terminated or mixed terminated surfaces. Figure 4c shows the predominance diagram for the different zinc species at  $pH > 13.5$ , where the typical fraction vs pH curve indicates the presence of highly negatively charged  $Zn(OH)_4^{2-}$  (aq) [21]. This suggests that the colloidal state of the zinc species prior to precipitation, although indicated from the predominance diagram as the same, generates completely different ZnO-morphologies forming at significantly different reaction rates.

## Cellulose as Nucleation Agent During the Initial Nucleation and Progressing Growth of the Anisotropic ZnO Crystals

Figure 5 shows the results of carrying out the same reactions with the only difference that 0.005 wt.% crystalline cellulose nanofibers were added to the zinc ion solution.

The consumption rates of zinc ions during the reactions were only shifted upwards (increased, see Fig. 5) with the addition of cellulose. This indicated that the adsorption and condensation reaction mechanisms in the solid phase formations of the ZnO were proceeding in a similar fashion when cellulose was not present, compare Fig. 3. The micrographs in Fig. 5c, d show the sea urchin particles synthesized in the presence of CNF, which was the system that was most affected by the presence of CNF, i.e. in terms of zinc ion consumption rate. The major differences concerned the size of the particles (see Fig. 5c, d), which decreased by *ca.* 50%, [17] which was related to a larger number of nuclei forming [17].

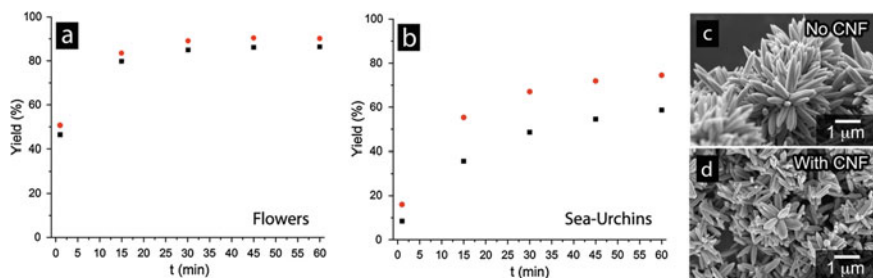


**Fig. 5** Shows the effect of 0.005 wt.% crystalline cellulose on the formation patterns and yield values for the synthesis of **a** flower-shaped and **b** sea urchin-shaped ZnO. Red spherical dots represent the cellulose containing reactions, whereas the black squares are the same reactions as presented in Fig. 3 where no cellulose was present. The micrographs show the appearance of the sea urchin-shaped particles synthesized without (c) the presence of CNF and in the presence of 0.005 wt.% CNF (d), after thermal treatment at 400 °C

## Conclusion

This study shows that:

- Sequential measurements of the zinc ion concentration during the precipitation of ZnO-particles is a useful method for accurately following the consumption rates of zinc ionic species as related to the development of different ZnO-particle morphologies.
- ZnO-particles were prepared from two previously reported protocols, resulting in predominantly oxygen terminated flower-shaped particles built up by a mix of sheets and rods, or mixed zinc and oxygen terminated sea urchin-shaped particles built up by rods. However, although both reactions were carried out at conditions with a dominant presence of  $\text{Zn}(\text{OH})_4^{2-}$  (aq) ion species (according to predominance diagrams, Fig. 4c), the formation of the two ZnO-morphologies followed significantly different patterns in consumption of zinc ions during the reactions (Fig. 3).
- The flower-shaped particles with more polar oxygen-terminations formed much faster compared to sea urchin-shaped particles built up by faceted rod-structures with higher presence of zinc.
- The Zn-ion consumption profiles were the same when 0.005 wt.% cellulose was added as a nucleation agent, although the amounts of consumed Zn-ions during the precipitation increased.
- The observations show that cellulose can be used as an effective and inexpensive additive to enhance the nucleation and yields of the ZnO precipitations reactions.

The aqueous precipitation of ZnO in alkaline conditions is one of the most common ways to consolidate zinc ions into a solid form. However, the amount of precipitated ZnO and the morphology of the formed particles has in this work been shown to be heavily affected by subtle changes in the reaction conditions. The ability

to control shapes and sizes of inorganic particles during metal recycling is particularly important since it allows for tuning the properties of the recycled inorganic material in ways that makes it more suitable towards specific applications. The knowledge of the prerequisites for specific morphologies thereby allows for an up-conversion (waste valorization) of the recycled metal where the zinc may find use in novel high end value materials, e.g. photocatalytic materials [5].

**Acknowledgements** This study was carried out within the Wallenberg Wood Science Center, KTH (WWSC), and the Knut and Alice Wallenberg foundation is acknowledged for their financial contribution.

## References

1. Barraud L, Holman Z, Badel N, Reiss P, Descoeurdes A, Battaglia C, De Wolf S, Ballif C (2013) *Sol Energ Mat Sol C* 115:151–156
2. Li F-T, Ran J, Jaroniec M, Qiao SZ (2015) *Nanoscale* 7:17590–17610
3. Dransfield GP (2000) *Radiat Prot Dosim* 91:271–273
4. Asiri AM, Boddula R (2020) *Zinc batteries: basics, developments, and applications*. Wiley
5. Pourrahimi AM, Liu D, Andersson RL, Ström V, Gedde UW, Olsson RT (2016) *Langmuir* 32:11002–11013
6. Talebian N, Amininezhad SM, Doudi M (2013) *J Photoch Photobio B* 120:66–73
7. Cho S, Jang JW, Lee JS, Lee KH (2010) *Langmuir* 26:14255–14262
8. Moghri Moazzen MA, Borghei SM, Taleshi F (2013) *Appl Nanosci* 3:295–302
9. Peng W, Qu S, Cong G, Wang Z (2006) *Cryst Growth Des* 6:1518–1522
10. An D, Tong X, Liu J, Wang Q, Zhou Q, Dong J, Li Y (2015) *Superlattices Microstruct* 77:1–11
11. Liu P, Chen X, Ouyang B, Fan X, Liu W, Li P, Peng J, Yan J, Liu K (2021) *Energy Fuels* 35:5352–5359
12. Molaei E, Doroodmand MM, Shaali R (2022) *Sci Rep* 12:1–9
13. Kar M, Winther-Jensen B, Forsyth M, MacFarlane DR (2014) *Phys Chem Chem Phys* 16:10816–10822
14. Aldrich S Sigma aldrich product-zinc oxide, <https://www.sigmaaldrich.com/SE/en/product/aldrich/544906>. Accessed 6 Oct 2022
15. Insider B Business insider, commodities, zinc price, <https://markets.businessinsider.com/commodities/zinc-price>. Accessed 6 Oct 2022
16. Liu D, Wu Q, Andersson RL, Hedenqvist MS, Farris S, Olsson RT (2015) *J Mater Chem A* 3:15745–15754
17. Hoogendoorn BW, Birdsong BK, Capezza AJ, Ström V, Li Y, Xiao X, Olsson RT (2022). *Langmuir*. <https://doi.org/10.1021/acs.langmuir.2c01713>
18. Rovera C, Ghaani M, Santo N, Trabattoni S, Olsson RT, Romano D, Farris S (2018) *ACS Sustain Chem Eng* 6:7725–7734
19. Crank J (1979) *The mathematics of diffusion*, Oxford University Press
20. Castro-Mayorga JL, Fabra MJ, Pourrahimi AM, Olsson RT, Lagaron JM (2017) *Food Bioprocess Process* 101:32–44
21. Reichle RA, McCurdy KG, Hepler LG (1975) *Can J Chem* 53:3841–3845
22. Wöll C (2007) *Prog Surf Sci* 82:55–120

# Production of Micro-sized Metallic Tungsten Particles from Natural Wolframite and Scheelite via Sulfide Chemistry



Charles Boury, Sierra R. Green, and Antoine Allanore

**Abstract** The development of sulfide-based chemistry and physical separation has opened the way for new industrial production methods. A new route for the production of micron sized metallic tungsten particles from natural wolframite  $(\text{Fe, Mn})\text{WO}_4$  and scheelite  $\text{CaWO}_4$  is presented. Sulfidation of mineral concentrates allows for the breaking of the tungstate crystal structure into a mix of sulfides containing tungsten disulfide  $\text{WS}_2$ . The thermal instability of  $\text{WS}_2$  at high temperature allows for its selective thermal reduction to metallic tungsten particles under inert atmosphere.

**Keywords** Tungsten · Sulfides chemistry · Metal

## Introduction

Tungsten has a set of unique properties among metals, such as a high melting point, low vapor pressure, high density, and mechanical resistance. It has specific applications in spatial, military, and heavy-duty industrial domains where the use of tungsten, in a metallic or carbide form, is irreplaceable. In 2020, the world mines production was around 84,000 metric tons of tungsten content, with more than 80% extracted in China [1]. Tungsten mines are usually of small size due to its dispersed concentration and low concentration in the ore [2]. Wolframite  $(\text{Fe, Mn})\text{WO}_4$  and scheelite  $\text{CaWO}_4$  are the main ores processed for tungsten production. After ore beneficiation, low purity sodium tungstate is produced by hydrometallurgy. Then a solid or liquid ion exchange process is applied to remove most of the impurities. Ammonium paratungstate (APT) is then formed by addition of ammonium-based solutions. The

---

C. Boury · S. R. Green · A. Allanore (✉)

Department of Materials Science and Engineering, Massachusetts Institute of Technology, 77  
Massachusetts Ave, Cambridge, MA 02139, USA

e-mail: [allanore@mit.edu](mailto:allanore@mit.edu)

C. Boury

e-mail: [boury@mit.edu](mailto:boury@mit.edu)

S. R. Green

e-mail: [sierragr@mit.edu](mailto:sierragr@mit.edu)

© The Minerals, Metals & Materials Society 2023

T. Ouchi et al. (eds.), *Rare Metal Technology 2023*, The Minerals, Metals  
& Materials Series, [https://doi.org/10.1007/978-3-031-22761-5\\_21](https://doi.org/10.1007/978-3-031-22761-5_21)

pyrolysis of APT has for main product tungsten trioxide  $\text{WO}_3$ . Lastly, metallic tungsten particles are obtained by hydrogen reduction. The obtained tungsten powder is used for powder metallurgy, metal injection molding, or other types of processes. The high temperature and pressure required in the powder metallurgy allows to further refine the tungsten. More information can be found in the work by Trasorras et al. [2] and Lassner et al. [3].

Sulfide chemistry presents a major opportunity in terms of ore treatment, refining and recycling. Demonstrations of its applications already cover a diverse range of chemistries and applications, from iron and copper production [4] to batteries recycling [5] and rare earth separation [6]. Amhad et al. demonstrated the application of selective sulfidation for chromite removal from ilmenite concentrates [7]. Yong et al. managed to treat low grade lead-zinc oxide with elemental sulfur for flotation separation [8]. Zhang et al. used the sulfide chemistry and HCl leaching to retrieve zinc from zinc-rich neutralization sludge [9]. Zinc was also selectively sulfidized in lead smelter slag by Zheng et al. [10, 11] and Han et al. [12].

A new route to produce tungsten metallic particles is presented herein. The initial materials are natural minerals of wolframite and scheelite. No chemical pretreatment was applied to remove impurities. The sulfidation of both tungstate crystal structures allowed for the formation of  $\text{WS}_2$  among other sulfides and remaining oxides. The sulfidation of wolframite showed a higher yield than the sulfidation of scheelite for the same experimental parameters. The thermodynamic of thermal reduction of tungsten sulfide to tungsten is presented as function of the partial pressure of sulfur and the temperature. Experimental results demonstrate the ease of the thermal reduction process and its high purity outcome. The obtention of W particles embedded in a mix of sulfides and oxides is the result. The physical separation post reduction was not attempted.

## Experimental

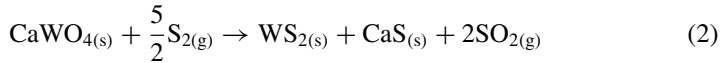
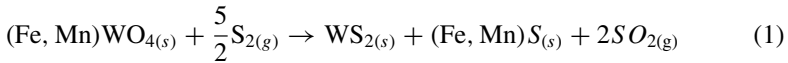
Natural mineral samples are processed herein. The natural wolframite (139g) is from the Hunan Province, China, while the natural scheelite (151g) is from Guttannen, Switzerland. Both samples have been ground and sorted to 230 mesh (63  $\mu\text{m}$  maximum particle size) using an agate mortar and pestle and a stainless-steel sieve. Both rocks demonstrated relatively high purity. The detailed composition of the natural rocks is presented in Table 1. Wolframite is primarily composed of tungsten, manganese, iron, and oxygen. Scheelite is primarily composed of tungsten, calcium, and oxygen. Impurities are present but always at a content lower than 0.5 wt%.

**Table 1** ICP-AES and LECO (for C, O, S) results, values are in wt%

Sample type	W	Fe	Mn	Ca	O	S	C	Sn	Al	Cr	K	Mg	Nb	Si	Ti	Zn
Natural wolframite	56.28	9.262	12.05	0.029	21.42	0.010	0.018	0.022	0.073	0.030	0.088	0.022	0.403	0.257	0.014	0.032
Sulfidized wolframite	47.71	11.46	11.77	0.040	0.133	27.96	0.078	<0.001	0.078	0.027	0.263	0.025	0.361	0.067	0.014	0.020
Natural scheelite	63.66	0.069	0.167	12.88	22.89	0.004	0.015	<0.001	<0.001	0.036	0.137	<0.001	0.024	0.088	0.002	0.027
Sulfidized scheelite	61.11	0.100	0.037	12.53	9.021	16.70	0.039	<0.001	<0.001	0.035	0.292	<0.001	0.019	0.090	0.003	0.025
Re-sulfidized scheelite	58.54	0.081	0.029	11.75	3.426	25.62	0.051	<0.001	<0.001	0.034	0.320	<0.001	0.019	0.098	0.003	0.024

## *Sulfidation*

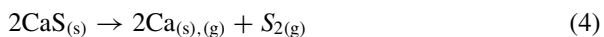
The sulfidation mechanism consists in breaking the tungstate structure into a mix of sulfides. The sulfidation reactions of wolframite and scheelite are presented in Reactions 1 and 2.



The sulfidation furnace used is similar in design to the one described in Stinn et al. [6]. EDM grade graphite trays (Graphite Store, Northbrook, IL 60062, USA) were custom-made. After machining, the crucibles were sonicated in acetone and dried in a vacuum oven for several hours. 100 g of sulfur powder (99.5 % sublimed, Acros organics, CAS 7704-34-9) were melted and cooled down in a quartz crucible, then loaded at the bottom of the furnace. Experiments were conducted under 400 sccm of ultra-high purity argon flow (UHP Ar, less than 10 ppm O<sub>2</sub>, AirGas). The reduction steps to form metallic tungsten particles were conducted on two sulfidized samples. The first one is denominated sulfidized wolframite with highest conversion yield, the second one sulfidized scheelite with highest conversion yield. The sulfidized wolframite has been obtained after 2 h at 1400 °C in a graphite crucible loaded in an alumina tube. The initial powder size was below 230 mesh, and the bed thickness was around 1 cm. For scheelite, two sulfide samples have been produced for analysis. One has been sulfidized once in the same conditions as wolframite above. The other sample has been sulfidized twice in the same conditions. Between the two sulfidation steps, the powder was re-crushed at 230 mesh in a glove box. The product from the second sulfidation step of scheelite is designated as the scheelite with highest conversion yield.

## *Thermodynamic Framework*

The powders obtained after sulfidation contained a high concentration of tungsten sulfide, calcium sulfide, iron sulfide, and manganese sulfide. The Reactions 3, 4, 5, and 6 represent the general thermal decomposition reactions of the pure sulfides to metal and elemental sulfur as investigated herein. All thermodynamic data have been obtained via FactSage 8.0 using the FactPS database (FactSage TM).





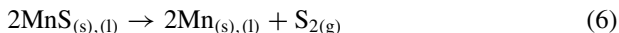
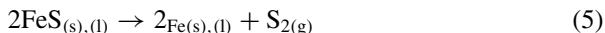


Figure 1 represents an Ellingham-like diagram for the Reactions 3, 4, 5, and 6 per mole of S<sub>2</sub> for different total or partial pressure of sulfur, considering the activities of solid, liquids, and gaseous calcium as unity and taking into account the reported phase transitions.

The diagram shows the anticipated strong effect of the partial pressure of sulfur depending on the temperature range, helping to define the most suitable process conditions for selective production of W, CaS and MnS (Reactions 4 and 6) demonstrate high stability even under very low partial pressure of sulfur. For both WS<sub>2</sub> and FeS (Reactions 3 and 5), their decomposition temperature can be close to 1000 °C for a very low partial pressure of sulfur (10<sup>-6</sup> bar). However, the thermal reduction selectivity range is increasing with the increase of partial pressure of sulfur. At a sulfur partial pressure of 10<sup>-2</sup> bar, pure WS<sub>2</sub> is expected to thermally decomposes into W and S<sub>2</sub> at 1475 °C while FeS is stable up to 1975 °C.

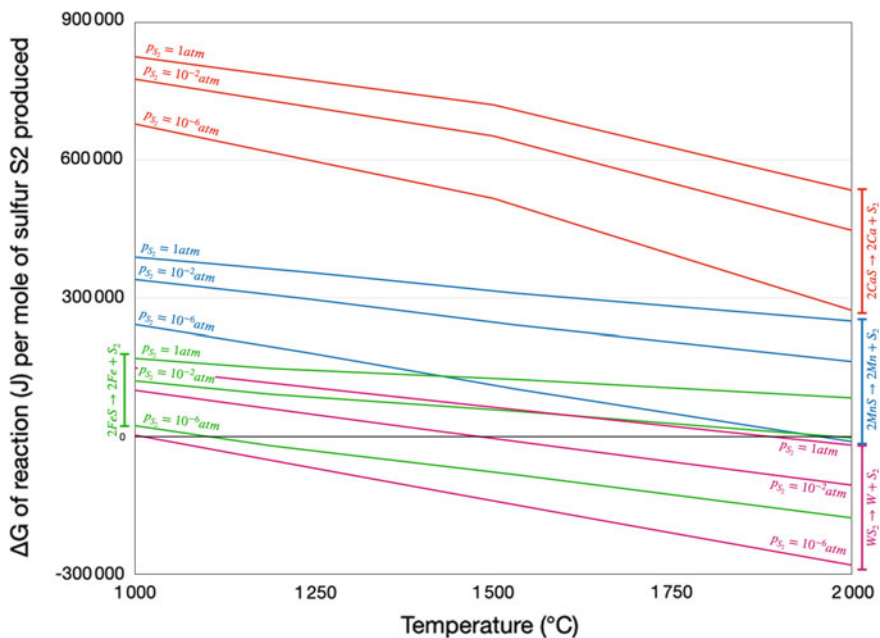


Fig. 1 Ellingham-like diagram for the Reactions 3, 4, 5, and 6 per mole of S<sub>2</sub> as a function of the total pressure of sulfur, considering the activities of solid, liquids and other gas as unity

## ***Metallic Tungsten Production***

A container-less thermal imaging furnace (High Temperature Xenon Lamp furnace, Model TX-12000-I) was employed to produce metallic tungsten. Samples were prepared in a similar fashion as the one presented in previous work [12]. The sulfidized sample powders were compacted as rods of about 0.25 in. in diameter. Each rod was held in the center of the furnace. The furnace tube was evacuated to a pressure of  $10^{-3}$  atm and re-purged with UHP argon three times, then 200 sccm of argon were flowed continuously. The hot zone of the furnace is around  $1\text{ cm}^3$  and the thermal gradient can reach several hundreds of degrees per centimeter. The sample could rotate at a speed of 6 rpm during a defined amount of time. The temperature could not be monitored due to the solid form of the sample. The oxygen concentration in the furnace, below 9 ppm, was monitored by an oxygen analyzer (Advanced Micro Instruments, Model 2001RS/RSP). Samples of respectively 5 and 3 grams of sulfidized wolframite and scheelite with highest conversion yield were used for the experiments.

## ***Physicochemical Analysis***

The natural wolframite, natural scheelite, and their sulfides with highest conversion yield have been analyzed by Induction Coupled Plasma—Atomic Emission Spectroscopy (ICP-AES, Applied Technical Services, 1049 Triad Court, Marietta, GA 30062), LECO combustion (Applied Technical Services, 1049 Triad Court, Marietta, GA 30062) and X-Ray Diffraction (XRD, PANalytical X'Pert Pro XRPD, MIT MRL facilities, MA, 02139). Samples containing metallic tungsten were analyzed by X-Ray Diffraction and elemental analysis was conducted with a scanning electron microscope (SEM, JEOL JSM 7900F Schottky FE-SEM, JEOL) equipped with Energy Dispersive Spectroscopy (EDS, Oxford Ultim Max EDS Detector; Oxford Instruments) and Wavelength Dispersive Spectroscopy microprobes (WDS, Oxford Wave WDS detector, Oxford Instruments). The samples have been polished to  $0.25\text{ }\mu\text{m}$  with kerosene (Sigma Aldrich, reagent grade, low odor, CAS number 8008-20-6).

## **Results**

### ***Sulfidation Results***

Table 1 presents the composition of the natural wolframite, the natural scheelite, the sulfidized wolframite, the single sulfidized scheelite, and the doubly-sulfidized scheelite with highest conversion yield obtained by ICP-AES and LECO. The amount of oxygen left in the doubly-sulfidized scheelite is 3.426 wt%, compared to 0.133 wt%

for the sulfidized wolframite. Among the other elements analyzed, the carbon content increases only slightly (0.018–0.078 wt% for wolframite and 0.015–0.051 wt% for scheelite). The graphite crucibles may contain small carbon powder ending up in the resulting sulfides mix. Tin is absent from the sulfidized wolframite, likely because it is expected to form tin sulfide SnS which boils at 1274 °C under one atmosphere of sulfur (FactPS, FactSage TM). The reliability of the ICP-AES results is questionable because of the difficulty of dissolving the tungstate minerals in hydrofluoric acid. Therefore, we do not consider variation of W, Fe, Mn, and Ca content from natural minerals to their respective sulfides quantitatively using this analytical method.

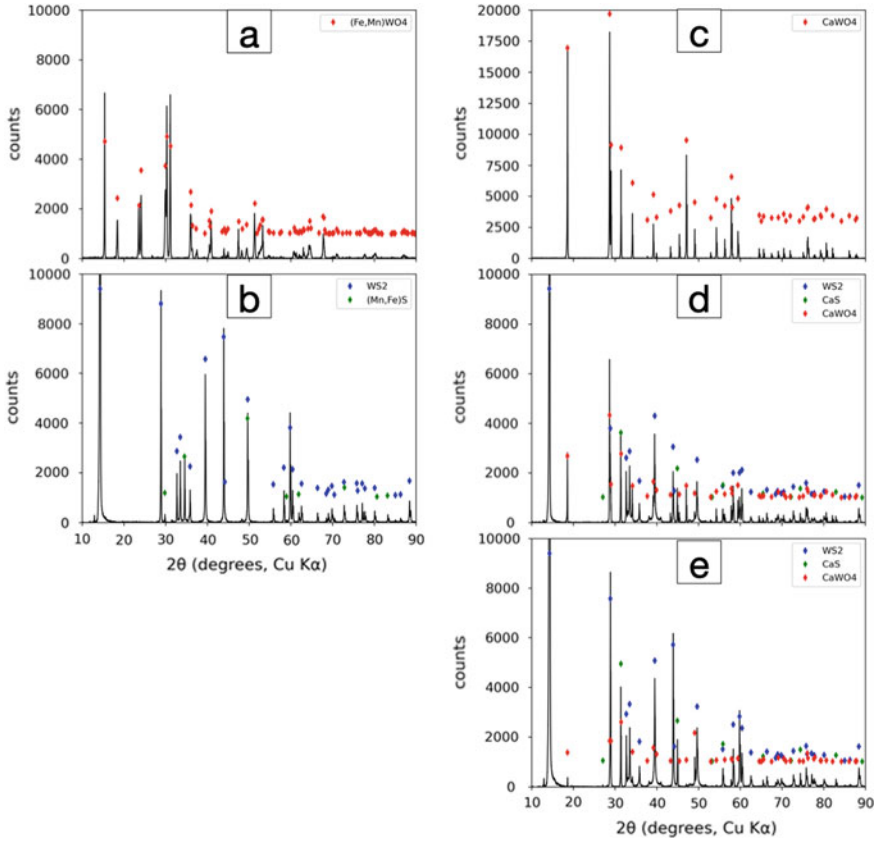
### ***Sulfidation Effects on the Tungstate Crystal Structure***

Figure 2a–e are the XRD results of the natural wolframite, sulfidized wolframite, natural scheelite, sulfidized scheelite, and doubly-sulfidized scheelite, respectively. The sulfidized wolframite sample, in Fig. 2b, contains a mixture of WS<sub>2</sub> and a solid solution of FeS and MnS. The initial wolframite crystal structure as observed in Fig. 2a is not present anymore, indicating the complete sulfidation of the wolframite sample. The residual oxygen noted in Table 1 is therefore diluted in the mix of sulfides since no oxides are observed by XRD or EDS. The sulfidation of scheelite is found to be incomplete. From Fig. 2c–e, it can be noticed that the initial calcium tungstate crystal structure is still found by XRD after the first (Fig. 2d) and second sulfidations (Fig. 2e). The two new sulfide phases found post sulfidation are WS<sub>2</sub> and CaS.

### ***Metallic Tungsten Production***

Figure 3a, b is example of a compacted sulfidized wolframite rod at the beginning and at the end of the thermal treatment inside the thermal imaging furnace. During the experiment with the sulfidized wolframite, a large amount of gas left the rod, and the sample was found to shrink with time. A shiny crust formed on the outside of the sample. After almost an hour at temperature, the experiment was stopped. A part of the recovered sample was crushed for XRD analysis, while another uncrushed part was casted in epoxy for SEM and EDS/WDS detailed analysis. The experiment on the doubly-sulfidized scheelite generated a lower amount of gas. Once the crust was formed on the outside, no more off-gas was visible.

Figure 4a, b shows the XRD pattern of the samples after their thermal decomposition. Metallic tungsten peaks are present for the wolframite samples, though the conversion to metal did not reach completion as revealed by the presence of peaks attributed to WS<sub>2</sub>. The solid solution of manganese and iron sulfide was not thermally decomposed. For the scheelite sample, the metallic tungsten pattern is visible but only to a small extent, suggesting a very limited advancement of the thermal decomposition. The CaS and CaWO<sub>4</sub> patterns are also still visible post thermal reduction. For



**Fig. 2** XRD scans of **a** the natural wolframite, **b** sulfidized wolframite, **c** natural scheelite, **d** sulfidized scheelite, and **e** doubly-sulfidized scheelite. The counts axes are scaled for clarity and not at the highest peak of the scans

both wolframite and scheelite, the FeS/MnS solid solution, CaS, and  $\text{CaWO}_4$  XRD patterns are unchanged post thermal reduction experiment.

Figure 4c, d is SEM image of the tungsten particles remaining in the samples from the reduction experiments of sulfidized wolframite and scheelite, respectively. In Fig. 4c, the light particles are the metallic tungsten particles, while the darker phase is a mix of tungsten sulfide and the solid solution of manganese and iron sulfide. For Fig. 4d, the light particles are metallic tungsten, the dark phase is the calcium sulfide, and the gray phase is a mix of calcium tungstate and tungsten sulfide. Table 2 presents the average concentration of the tungsten particles analyzed by EDS/WDS. The highest contaminant post reduction is the oxygen. Other elements are below 0.5 wt% on average.

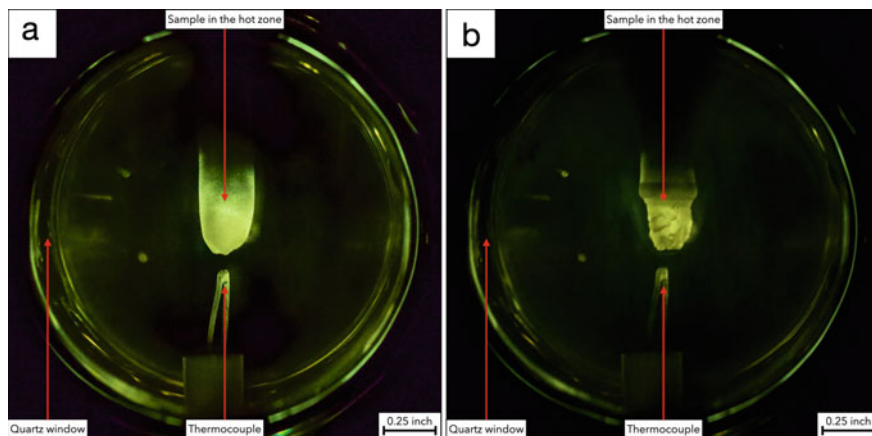


**Fig. 3** Pictures of compacted sulfidized wolframite rod at **a** the beginning and at **b** the end of the thermal treatment inside the thermal imaging furnace

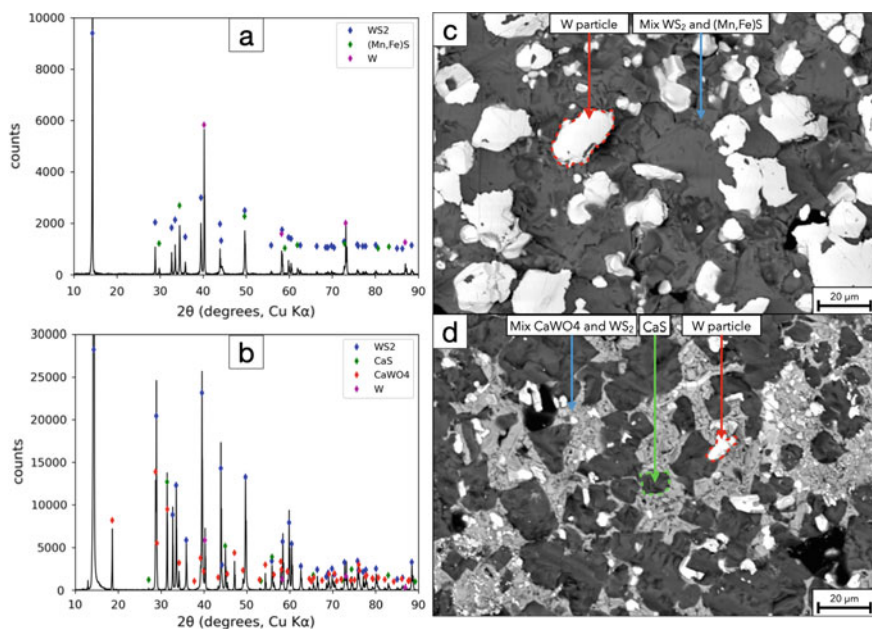


**Fig. 4** XRD scans of the **a** sulfidized wolframite and **b** doubly-sulfidized scheelite after their thermal treatment in the thermal imaging furnace. SEM images of the tungsten particles remaining in the samples from the **c** sulfidized wolframite and **d** doubly-sulfidized scheelite

**Table 2** Average composition of the analyzed metallic tungsten particles, values are in wt% and obtained via WDS except for O which values are obtained via EDS

Sample type	W	Fe	Mn	Ca	S	O
W from sulfidized wolframite	97.5011	0.2511	0.0004	–	0.2289	2.0185
W from doubly-sulfidized scheelite	97.6002	–	–	0.3022	0.3789	1.7188

## Conclusion and Future Work

The sulfidation of wolframite and scheelite formed a mix of sulfides containing  $WS_2$ . The tungsten sulfide selective reduction allowed for metallic tungsten particles production. However, much work is required to better understand this process. On the sulfidation step, limitations on the sulfidation of scheelite are observed, and oxygen is still present in both sulfidized powders with highest sulfidation yield, even to a low extent for wolframite. We note that the tungstate compound  $(WO_4)^{2-}$  exhibits a 6+ tungsten valence while  $WS_2$  involves a 4+ tungsten valence. Sulfide compounds may offer a unique method to alter cation valences vis-à-vis the other chalcogens. The actual experimental set-up for thermal reduction does not allow measurement of either the temperature or the partial pressure of sulfur. The determination of one or both parameters is required to be compared to the thermodynamic study. Oxygen contamination of the tungsten particles could be removed by hydrogen reduction following the current industrial process [2]. Physical separation and recovery of the particles by froth floatation is a possibility. Interesting results for the recovery of particles sized up to only few microns have been published [13, 14]. Other possible physical separation techniques can consist in sieving, centrifugal gravimetry [15], electromagnetic [16], or electrostatic separation.

## References

1. Shedd KB (2021) Tungsten. Technical report, U.S. Geological Survey
2. Trasorras JRL, Wolfe TA, Knabl W, Venezia C, Lemus R, Lassner E, Schubert W-D, Lu<sup>deritz</sup> E, Wolf H-U (2016) Tungsten, tungsten alloys, and tungsten compounds. In: Ullmann's Encyclopedia of industrial chemistry. Wiley-VCH Verlag GmbH & Co. KGaA, Weinheim, Germany, pp 1–53. <https://doi.org/10.1002/14356007.a27229.pub2>
3. Lassner E, Schubert W-D, Lu<sup>deritz</sup> E, Wolf HU (2000) Tungsten, tungsten alloys, and tungsten compounds. In: Ullmann's Encyclopedia of industrial chemistry. Wiley-VCH Verlag GmbH & Co. KGaA, Weinheim, Germany, pp 1–53. <https://doi.org/10.1002/14356007.a27229>
4. Daehn KE, Stinn C, Rush L, Benderly-Kremen E, Wagner ME, Boury C, Chmielowiec B, Gutierrez C, Allanore A (2022) Liquid copper and iron production from chalcopyrite, in the absence of oxygen. *Metals* 12(9):1440. <https://doi.org/10.3390/met12091440>
5. Stinn C, Allanore A (2021) Selective sulfidation and electrowinning of nickel and cobalt for lithium ion battery recycling. In: Ni-Co 2021: the 5th international symposium on nickel and cobalt. Springer, Cham, pp 99–110
6. Stinn C, Allanore A (2022) Selective sulfidation of metal compounds. *Nature* 602:78–83. <https://doi.org/10.1038/s41586-021-04321-5>

7. Ahmad S, Rhamdhani MA, Pownceby MI, Bruckard WJ (2014) Thermodynamic assessment and experimental study of sulphidation of ilmenite and chromite. *Miner Process Extr Metall* 123:165–177. <https://doi.org/10.1179/1743285514Y.0000000059>
8. Li Y, Wang J, Wei C, Liu CX, Jiang JB, Wang F (2010) Sulfidation roasting of low grade lead-zinc oxide ore with elemental sulfur. *Miner Eng* 23:563–566. <https://doi.org/10.1016/j.mineng.2010.01.004>
9. Zhang T, Liu W, Han J, Wu G, Jiao F, Qin W (2021) Selective separation of calcium from zinc-rich neutralization sludge by sulfidation roasting and HCl leaching. *Sep Purif Technol* 259:118064. <https://doi.org/10.1016/j.seppur.2020.118064>
10. Zheng Y-X, Liu W, Qin W-Q, Kong Y, Luo H-L, Han J-W (2014) Mineralogical reconstruction of lead smelter slag for zinc recovery. *Sep Sci Technol* 49:783–791. <https://doi.org/10.1080/01496395.2013.863342>
11. Zheng Y-X, Liu W, Qin W-Q, Han J-W, Yang K, Luo H-L, Wang D-W (2015) Improvement for sulphidation roasting and its application to treat lead smelter slag and zinc recovery. *Can Metall Q* 54:92–100. <https://doi.org/10.1179/1879139514Y.0000000155>
12. Han J, Liu W, Wang D, Jiao F, Qin W (2016) Selective Sulfidation of Lead Smelter Slag with Sulfur. *Metall and Mater Trans B* 47:344–354. <https://doi.org/10.1007/s11663-015-0526-4>
13. Boury C, Allanore A (2021) Liquid state properties and solidification features of the pseudo binary BaS-La<sub>2</sub>S<sub>3</sub>. *Sci Rep* 11:18189. <https://doi.org/10.1038/s41598-021-93576-z>
14. Pease JD, Curry DC, Young MF (2006) Designing flotation circuits for high fines recovery. *Miner Eng* 19:831–840. <https://doi.org/10.1016/j.mineng.2005.09.056>
15. Dehaine Q, Foucaud Y, Kroll-Rabotin J-S, Filippov LO (2019) Experimental investigation into the kinetics of Falcon UF concentration: implications for fluid dynamic-based modelling. *Sep Purif Technol* 215:590–601. <https://doi.org/10.1016/j.seppur.2019.01.048>
16. Pease JD, Young MF, Curry D, Johnson NW (2010) Improving fines recovery by grinding finer. *Miner Process Extr Metall* 119:216–222. <https://doi.org/10.1179/037195510X12816242170852>

# Purification of an Indigenous Barite Mineral for Sustainability of Operation in the Nigerian Oil and Gas Industries



Alafara A. Baba, Fausat T. Akanji, Rasheed A. Agava,  
Abdul Ganiyu F. Alabi, Abdullah S. Ibrahim, Kuranga I. Ayinla,  
Mustapha A. Raji, Seyi E. Adeboye, and Mohammed S. Haruna

**Abstract** The increasing demand for pure barite as a precursor in oil and gas drilling mud cannot be over-emphasized. Despite the abundance of this mineral in Nigeria, its exploration has been facing neglect because of the lower quality that could not meet the American Petroleum Institute (API) standards. Consequently, the treatment of a Nassarawa State barite mineral through acidic and alkaline leaching techniques was purified using a Denver flotation cell at pH 9. At optimal conditions, a leaching efficiency of 87.6% was achieved. In addition, the specific gravity of the purified barite product ( $\text{BaSO}_4$ ; 96-900-4486, *melting point* = 1465 °C) gave 4.42 g/cm<sup>3</sup> close to the API standard of 4.48 g/cm<sup>3</sup>. The product as characterized is therefore recommended for use as local drilling mud in the oil and gas industries to sustain the continuous operation in industries, thereby supporting human and capital development of Nigeria among others.

**Keywords** Barite ore · Nigeria · Leaching · Flotation · Drilling mud · Oil and gas industries

---

A. A. Baba (✉) · F. T. Akanji (✉) · A. S. Ibrahim · K. I. Ayinla · M. A. Raji  
Department of Industrial Chemistry, University of Ilorin, P.M.B. 1515, Ilorin 240003, Nigeria  
e-mail: [alafara@unilorin.edu.ng](mailto:alafara@unilorin.edu.ng)

F. T. Akanji  
Chemistry Advanced Research Centre, SHEDA Science and Technology Complex, P.M.B. 186,  
Garki, Abuja, Nigeria

R. A. Agava  
Department of Civil and Environmental Engineering, National Agency for Science and  
Engineering Infrastructure (NASENI), Abuja, Nigeria

A. G. F. Alabi  
Department of Material Science and Engineering, Kwara State University, P.M.B 1530, Malete,  
Nigeria

S. E. Adeboye  
National Biotechnology Development Agency, Abuja, Nigeria

M. S. Haruna  
Department of Engineering Infrastructure, National Agency for Science and Engineering  
Infrastructure, Abuja, Nigeria



## Introduction

Nigeria, a developing country, is one of the most abundant endowed countries across the globe richly blessed with varieties of mineral resources which are presently under-utilized. Thus, the importation of these mineral ores has become a major setback, especially in the Nigerian manufacturing sectors resulting in a rise in the cost of production among others. As the global oil and gas rig-wells appreciably rise, the continuous demand for pure barite and barium compounds of industrial grade cannot be over-emphasized. Due to the depletion of high-grade barite ores, the processing of low-grade ores to meet the industrial grade has been necessitated, not only to meet the demand, but also from environmental perspectives [1]. For example, about 85% of global barite produced is consumed in oil and gas industries as drilling mud due to its high specific gravity, inertness, and low solubility [2, 3]. Other industrial uses of barite are in rubber, paints, enamels, filler, wallpapers, leaded glass, and ceramic applications. However, drilling mud has a lot of distinct properties including cleaning, cooling, and lubricating [4, 5]. Some of the associated gangues with barite and its varieties include iron oxides, quartz, and carbonates, among others, are responsible for its diverse colouration such as tinted yellow, brown, grey, red green, and blue. The aforementioned gangues can be major sources of different drilling drawbacks such as hole invasion, specific gravity variation, etc. [6, 7]. Therefore, processing of the barite minerals by removing most of the associated matrixes becomes paramount to boost its quality and obtain a product acceptable for industrial utilizations.

The conventional purification routes of barite ore depend on the features of barite and matrixes. For instance, the magnetic separation is often employed if iron is the most dominant gangue present in the mineral [8]. Gravity separation including jigging, tabling, and spiral concentration is utilized for coarse ores with a higher specific gravity between barite and impurities phases [9]. However, flotation could be performed for enrichment when the barite is evolved in finely coarse fractions [10, 11]. Consequently, a lot of researchers have developed promising beneficiation routes including floatation, jigging, and magnetic separation, among others but have not been able to obtain the acceptable-*cum*-reliable grade as the aforementioned routes utilized are of high cost, complex, and as well gave rise to environmental pollution [12]. Thus, purification of barite ore in meeting the criteria for relevant industries most especially in oil and gas has been the focus of many researchers using the combinations of hydrometallurgical-*cum*-flotation processes which are assumed to be feasible, less toxic, and low-energy design [13, 14]. Therefore, the beneficiation of an indigenous barite ore for use as weighting agents in the oil and gas industries has been investigated in this study.

## Materials and Method

### *Material*

The barite ore used for this study was sourced from Azara (8° 32 20.22" N, 7° 42 29.56" E), Awe Local Government Area of Nassarawa State, Nigeria. The comminution of barite sample was carried out using a jaw crusher and roll crusher model *PE-150 \* 7500* and *2 PG 400 \* 400* respectively. Size reduction was further pulverized with *Yam 1100 Q4* model.

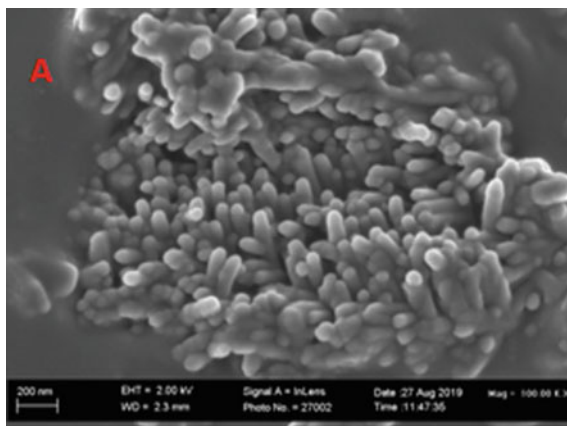
### *Leaching Test*

Dissolution experiments were executed in a 500 ml glass reactor furnished with a magnetic stirrer. A freshly prepared solution of 100 ml of HCl was agitated at 400 r/min when the temperature reached 55 °C. Further, a 1.0 g of barite ore was introduced and monitored at a different time interval (5–120 min). Subsequently, the fraction of barite dissolved (X) at different concentrations was recorded. The concentration which gave the highest percentage of dissolution was afterward used for the optimization of other parameters such as reaction temperature and particle size variation. The activation energy was evaluated from the Arrhenius plot, and the unleached product at optimal conditions was analyzed by XRD and SEM/EDX [15, 16].

### *Flotation Test*

A 2-L Denver mechanically agitated flotation machine was employed for the froth flotation experiment. About 250 g of the pulverized barite sample with particle size  $-140 + 63 \mu\text{m}$  was made to slurry using ceramic ball milling; pH was adjusted with NaOH and HCl. The system was running under the following conditions: 0.05 g of an acidified water glass as a depressant, pH 9, 0.2 cm<sup>3</sup> pine oil as a collector, and impeller speed of 150 rpm at 30 s, with a conditioning time of 10 min and a flotation period of 5 min. The floated (overflow) and tailing (underflow) particles were collected, filtered, and dried in an oven at 120 °C for 2 h [8, 11]. At optimal conditions, the concentration of pure barite (BaSO<sub>4</sub>) produced and other minor associated impurities were analyzed using SEM/EDX and XRD for material purity tests.

**Fig. 1** SEM micrograph of raw barite ore



## Results and Discussion

### *Ore Characterization*

The chemical analysis of the raw barite sample analyzed by EDXRF gave: 64.48 wt% BaO, 33.30 wt% SO<sub>3</sub>, 1.44 wt% SrO, 0.24 wt% SiO<sub>2</sub>, 0.03 wt% Fe<sub>2</sub>O<sub>3</sub>, and 0.045 wt% CuO. The XRD results affirmed that the barite mineral under investigation contained *barite* (BaSO<sub>4</sub>; 96-900-4486), *witherite* (Ba<sub>2</sub>C<sub>2</sub>O<sub>6</sub>; 96-900-6848), and *calcite* (CaCO<sub>3</sub>; 96-900-7287) as the dominant phases. However, the SEM micrograph of the raw barite was characterized by rough surfaces *cum* agglomerate particles associated with the ore body as summarized in Fig. 1.

### *Leaching Test*

The leaching tests affirmed that the barite ore upgrade in hydrochloric acid and sodium hydroxide solutions appreciably increases with increasing leachant concentration, reaction temperature, and decreasing particle fraction as summarized:

- (i) ***Influence of leachants concentration:*** HCl and NaOH concentrations varied between 0.1–2.5 mol/L at 50 °C within 5–120 min using the ore smallest particle size (–63 μm). Increasing the leachants concentration appreciably increases the ore upgrade up to 2.5 mol/L. Here, about 54.2% and 51.37% of the ore reacted within 120 min for HCl and NaOH leachants, respectively.
- (ii) ***Influence of reaction temperature:*** The influence of reaction temperature on the extent of ore upgrade was performed from 27–75 °C while keeping other parameters constant. Thus, increasing the reaction temperature from 27–70 °C

**Table 1** Established properties of the produced BaSO<sub>4</sub> at optimal conditions

Parameters	HCl	NaOH	Flotation	API
Density (g/cm <sup>3</sup> )	4.42	3.89	4.38	4.48
Viscosity (cp)	5.8	4.7	5.6	6.0
Melting point (°C)	1465	1398	1545	1580

appreciably increases the degree of ore dissolution yielding 87.6 and 79.5% for HCl and NaOH leachants, respectively, at optimal conditions.

### ***Purification Test***

At optimal conditions, the following data (Table 1) summarized the supporting properties of the prepared pure barite (BaSO<sub>4</sub>: 96-900-4486) in acidic, alkali, and flotation media as compared to the API standards [17].

### **Conclusion**

Barite, a vital industrial mineral finds a wide array of utilizations most especially as a weighting agent in the drilling mud (*specific gravity* 4.42 g/cm<sup>3</sup>). In this study, the purification of Azara (Nigeria) barite ore is eco-feasible and could by far place the nation among the global barite producers. Thus, the leaching and flotation routes were considered for enriching the indigenous barite ore for industrial value addition. At optimal conditions, the possibility of preparing high-grade barite (BaSO<sub>4</sub>: 96-900-4486; *melting point* = 1465 °C, *density* = 4.42 g/cm<sup>3</sup>) for use as a drillant in the oil and gas industries has been established in this study.

**Acknowledgements** The authors sincerely thank the Executive Vice Chairman/Chief Executive of the National Agency for Science and Engineering Infrastructure (NASENI), Engr. Prof. M. S. Haruna, *FAEng, FNSE, FIET* for the immeasurable support to attend and present this distinct research at the 152nd Annual Meeting & Exhibition of The Minerals, Metals & Materials Society (TMS 2023) held in San Diego, California, USA, between 19th and 23rd March 2023. Also, one of the authors (Prof. Alafara A. Baba) is grateful to the TMS EPD Council for their kind support to attend this meeting.

### **References**

1. Bhaskar Raju G, Ratchambigai S, Ananda Rao M, Vasumathi N, Vijaya Kumar TV, Prabhakar S, Subba Rao S (2015) Beneficiation of barite dumps by flotation column; lab-scale studies to commercial production. *Trans Indian Inst Met.* <https://doi.org/10.1007/s12666-015-0700-z>

2. Searls JP (2003) 'Barite', U.S. Geological Survey Minerals Yearbook, 9.1–9.8
3. Mgbemere HE, Obidiegwu EO, Obareki E (2008) Beneficiation of Azara barite ore using a combination of Jigging, froth flotation and leaching. *Niger J Technol (NIJOTECH)* 37(4):957–962
4. Seyedmohammadi J (2017) The effects of drilling fluids and environment protection from pollutants using some models. *Model Earth Syst Environ* 3:23
5. Ghalib HB, Almallah IAR (2017) Scaling simulation resulting from mixing predicted model between Mishrif formation water and different waters injection in Basrah oil field, southern Iraq. *Model Earth Syst Environ* 2(46):1–14
6. Al-Hitti AH, Al-Assaf SA, Ibrahim DS (2005) Reduction of formation damage due to drilling muds. *J Eng* 11:21–32
7. Molaei N, Razavi H, Chelgani SC (2018) Experimental modeling for upgrading of brown barite ore by different processing methods. *Model Earth Syst Environ*. <https://doi.org/10.1007/s40808-018-0429-x>
8. Wang H, Dai H, Yang W, Li T (2014) Research on the flotation experiment of low-grade barite ore in Myanmar. *Appl Mech Mater* 644–650:5277–5280
9. Ahmed MM, Ibrahim GA, Hassan MMA (2007) Improvement of Egyptian talc quality for industrial uses by flotation process and leaching. *Int J Miner Process* 83:132–145
10. Harris MJ (1988) New Mexico bureau of mines and mineral resources. Open File Report #336, Barite Flotation, El Cuervo Butte 1–17
11. Raju GB, Ratchambigai S, Rao MA, Vasumathii N, Vijaya Kumar TV, Prabhakar S, Rao SS (2016) Beneficiation of barite dumps by flotation column laboratory scale studies to commercial production. *Trans Indian Inst Met* 69(1):75–81
12. Zhao Y, Liu S, Li X, Li T, Hou K (2014) Recovery of low-grade barite ore by flotation in the southwest area of China. *Appl Mech Mater* 543–547:3865–3868
13. Raji MA, Baba AA, Bale RB, Alabi AGF, Ghosh MK (2020) Removal of Iron impurities from a Nigerian biotite-rich kaolinite ore by a sulphuric acid solution. *J Chem Technol Metall* 55(6):2128–2135
14. Baba AA, Kayode JO, Raji MA (2020) Low-energy feasibility for leaching an indigenous scheelite ore for industrial applications. *J Sustain Metall* 6:659–666
15. Baba AA, Swaroopa S, Ghosh MK, Adekola FA (2013) Mineralogical characterization and leaching amenability of Nigerian ilmenite ore. *Trans Non-ferrous Metals Soc China* 23:2743–2750
16. Xie K, Wang H, Wang S (2019) Direct leaching of molybdenum and lead from lean wulfenite raw ore. *Trans Nonferrous Metals Soc China* 29:2638–2645
17. Olasinde FT (2021) Comparative studies of the purification of some Nigerian barite ores using leaching and flotation processes, Ph.D. Dissertation, Department of Industrial Chemistry, University of Ilorin, Ilorin, Nigeria

# Pyrolysis of Waste Printed Circuit Boards: Optimization Using Response Surface Methodology and Characterization of Solid Product



Kurniawan Kurniawan, Sookyung Kim, and Jae-chun Lee

**Abstract** Recovery of precious and valuable metals from WPCBs faces challenges due to heterogeneous mixture of organic substrates and metal sheets. Pyrolysis is a promising and effective method for easing the separation of metals and organic substrates in WPCBs by transforming the organic substrates into high calorific products of oil and gases. In this study, the pyrolysis of WPCBs has been examined while investigating the effect of parameters, such as temperature, heating rate, and  $N_2$  flow rate. The pyrolysis process was optimized using response surface methodology with a central composite design (CCD). The results showed that a quadratic model explained adequately the nonlinear behavior of the modeled response with an  $R^2$  value of 0.98, showing that the model was adequately adjusted to the experimental data. The effect of each parameter and their interaction were discussed, and a variety of methodologies (metal analysis by ICP, XRD, SEM, and FTIR) were used to characterize the solid pyrolyzed WPCBs.

**Keywords** WPCBs · Recycling · Pyrolysis · Characterization · Response surface methodology

## Introduction

Electrical and electronic equipment has a shorter lifespan as a result of rapid technological progress and innovation, increased performance demands, and constant upgrades to related features. As a consequence, an enormous amount of electronic waste (e-waste) is produced. According to the “Global e-waste monitor 2020” report, 53.6 million metric tonnes of e-waste were produced globally in 2019, posing a significant concern for solid waste disposal and the emission of harmful chemicals from such wastes. Waste printed circuit boards (WPCBs) are one of the primary

---

K. Kurniawan · S. Kim (✉) · J. Lee  
Resource Recycling, University of Science and Technology, Daejeon 34113, Republic of Korea  
e-mail: [skkim@kigam.re.kr](mailto:skkim@kigam.re.kr)

Mineral Resources Research Division, Korea Institute of Geoscience and Mineral Resources (KIGAM), Daejeon 34132, Republic of Korea

components of e-waste, comprising 3–6 wt% of all e-waste generated [1]. WPCBs consist of a mixture of polymers (~40 wt%), glass and ceramics (~30%), and metals (~30 wt%), of which metals contained in WPCBs include base (e.g., Cu, Pb, Sn, Al, Fe) and precious metals (Au, Ag, Pt, Pd, etc.). These metals are significantly more concentrated in WPCBs than in their respective primary deposits. Therefore, there is significant potential in converting WPCBs into a metal resource. This can consequently result in economic and environmental benefits if effectively used.

WPCBs can be recycled utilizing a variety of techniques, including thermal, aqueous, and their combination [2]. Among these methods, the aqueous process by leaching is often preferred due to its simple control and environmentally benign methodology, coupled with the merits of lower capital cost, higher separation degree, total recyclability, and higher metal recovery rates. However, a pretreatment is necessary for liberating metals from chelated organic substrate before leaching process. The process of metal liberation has been accomplished by either mechano-physical or thermochemical methods [3]. The mechano-physical method combines disassembly, shredding, and size reduction, followed by a variety of physical separation techniques. However, the total flow process is complicated, energy- and time extensive, and frequently results in the loss of valuable metals. In addition, very fine particles are required to obtain an effective metal liberation degree. On the other hand, thermochemical method via pyrolysis has been regarded as the most promising method for liberating metals contained in WPCBs by transforming the organic substrate into high calorific value products such as oil and gas, thereby making subsequent processes for metal recycling simpler and more efficient [4]. In addition, the pyrolysis process has the benefits of no loss of important metals, decreased emissions, immobilization of heavy metals, a high degree of energy conversion, particularly the ability to recover energy, and rapid reaction kinetics.

Extensive research has been conducted on the pyrolysis of WPCBs, but the majority of studies only addressed the characterization of oil and gas products, bromine distribution, and pyrolysis kinetics, and frequently viewed pyrolysis as part of the procedures for treating non-metallic fraction (NMF) from WPCBs rather than as part of the metal recycling flow process [5–7]. Most of these research also employed a small amount of ground and single-type material in a small-scale furnace to gain the fundamental information and theoretical foundation for the pyrolysis stage. Hence, the objective of this study is to appropriately evaluate the pyrolysis of WPCBs under conditions comparable to those encountered in actual practice. The effect of key parameters, including temperature, heating rate, and N<sub>2</sub> flow rate on weight loss of WPCB sample was investigated using response surface methodology with a central composite design (CCD). In order to explain the pyrolysis result, solid char pyrolyzed WPCBs were analyzed using a variety of techniques, including wet analysis for metal concentration, proximate analysis, XRD, SEM–EDS, and FTIR.

## Experimental

### *Experimental Procedure*

Unpopulated WPCBs (electronic components, such as capacitors and metal blocks were first removed) with particle size +9.50 mm (after crushing) from a range of waste boards were used in the experiments. The pyrolysis experiments were performed by charging 20 g of WPCBs in a tubular furnace. Then, N<sub>2</sub> gas at a predetermined flow was passed into the furnace for 15 min to remove the oxygen inside the furnace. The WPCBs were then heated to a desired temperature at a certain heating rate and N<sub>2</sub> flow rate, and 10 min holding time at the final temperature. Once cooled, the solid char was weighed, and the weight loss was determined using Eq. (1). All the experimental runs were repeated in triplicates.

$$\text{Weight loss(\%)} = \frac{\text{Weight of char(g)}}{\text{Weight of initial sample(g)}} \times 100\% \quad (1)$$

### *Response Surface Methodology*

The parameters (temperature, heating rate, and N<sub>2</sub> flow rate) that influence the pyrolysis of WPCBs were investigated using a standard RSM based on central composite design (CCD). All parameters were utilized up to three levels, which are high (+1), center (0), and low (−1). The number of experiments was calculated as:  $N = 2^n + 2n + n_c$ , where  $n$  is the factor number and  $n_c$  is the repeated number of the center point. This study utilized temperatures of 400, 500, 600 °C; heating rates of 10, 20, 30 °C/min, and N<sub>2</sub> flow rates of 0.1, 0.3, 0.5 L/min, and the weight loss as the response value. There were a total of 20 experiments (14 unique runs and 6 center runs). Table 1 displays the complete design matrices of the conducted experiments as well as the weight loss during the experiments. The results were analyzed by using analysis of variance (ANOVA). Model terms were rejected or selected based on the  $p$ -values obtained with 95% confidence level.

### *Characterization*

WPCBs samples before and after pyrolysis were subjected to a series of characterization procedures. The metal compositions were determined by acid digestion and quantified using an inductively coupled plasma-optical emission spectroscopy (ICP-OES; iCAP6000 series, Thermo Scientific, USA). Proximate analysis was conducted using a thermogravimetric analyzer (TGA 701, Leco, Korea). Ultimate analysis was



**Table 1** Design and results of experiments

Observation	Std. order	Temperature (°C)	Heating rate (°C/min)	N <sub>2</sub> flow rate (L/min)	Weight loss (%)
1	16	500	20	0.3	25.73
2	5	400	10	0.5	21.58
3	15	500	20	0.3	25.96
4	4	600	30	0.1	27.43
5	10	600	20	0.3	26.88
6	18	500	20	0.3	25.68
7	20	500	20	0.3	25.63
8	14	500	20	0.5	26.23
9	3	400	30	0.1	23.05
10	1	400	10	0.1	21.58
11	11	500	10	0.3	24.11
12	19	500	20	0.3	25.49
13	13	500	20	0.1	24.71
14	9	400	20	0.3	22.15
15	2	600	10	0.1	26.52
16	6	600	10	0.5	26.91
17	12	500	30	0.3	26.51
18	7	400	30	0.5	23.21
19	17	500	20	0.3	25.81
20	8	600	30	0.5	28.40

performed by a CS elements analyzer (CS230, Leco, Korea). The calorific values of the solid samples were determined by a calorimeter (AC500, Leco, Korea). The mineralogical compositions, micro-morphology, and chemical functional groups of the two samples were analyzed by X-ray diffraction (XRD, D/MAX 2200, Rigaku Corp., Japan), scanning electron microscopy (SEM, Hitachi s4800, Hitachi, Japan), and Fourier transform infra-red spectroscopy (FTIR, Nicolet iS5, Thermo Scientific, USA), respectively.

## Results and Discussion

### *Statistical Analysis of Pyrolysis Model*

The statistical parameters derived from ANOVA for the developed regression model are presented in Table 2. The statistical significance of the designed experiments was established at a confidence level of 95%. According to the ANOVA, the model

**Table 2** Analysis of variance for the regression equation

Source	DF	Seq SS	Adj SS	Adj MS	F	<i>p</i>
Regression	9	71.2586	71.2589	7.9177	51.56	0.000
Linear	3	67.5730	67.5730	22.5243	146.67	0.000
Temperature	1	60.3587	60.3857	60.3857	393.22	0.000
Heating rate	1	6.2535	6.2535	6.2535	40.72	0.000
N <sub>2</sub> flow rate	1	0.9337	0.9337	0.9337	6.08	0.033
Square	3	3.3780	3.3780	1.1260	7.33	0.007
Temperature * temperature	1	3.3459	1.9868	1.9868	12.94	0.005
Heating rate * heating rate	1	0.0006	0.0080	0.0080	0.05	0.824
N <sub>2</sub> flow rate * N <sub>2</sub> flow rate	1	0.0315	0.0315	0.0315	0.21	0.660
Interaction	3	0.3079	0.3079	0.1026	0.67	0.591
Temperature * heating rate	1	0.0616	0.0616	0.0616	0.40	0.541
Temperature * N <sub>2</sub> flow rate	1	0.1777	0.1777	0.1777	1.16	0.307
Heating rate * N <sub>2</sub> flow rate	1	0.0686	0.0686	0.0686	0.45	0.519
Residual error	10	1.5357	1.5357	0.1536		
Lack-of-fit	5	1.4082	1.4082	0.2816	11.05	0.010
Pure error	5	0.1275	0.1275	0.0255		
Total	19	72.7946				

*F*-value and *p*-value are 51.56 and <0.001, respectively, indicating that the model is significant. The model developed for the predictive weight loss (%) of WPCBs during pyrolysis with actual values is presented through Eq. (2). Figure 1 depicts the weight loss predicted by Eq. (2) together with the experimental results. It has an *R*<sup>2</sup>-value and *R*<sup>2</sup> adjusted of 97.89% and 95.99%, respectively, exhibiting a very good or excellent fit of data to the model.

$$\begin{aligned}
 \text{Weight loss(\%)} = & -9.47 + 0.109 * A + 0.131B - 4.73C \\
 & - 8.5 \times 10^{-5} * A^2 - 5.381 \times 10^{-4} * B^2 \\
 & + 2.677 * C^2 - 8.78 \times 10^{-5} * A * B \\
 & + 0.0075 * A * C + 0.0463 * B * C \tag{2}
 \end{aligned}$$

where *A*, *B*, and *C* are the temperature (°C), heating rate (°C/min), and N<sub>2</sub> flow rate (L/min).

The *p*-value < 0.05 means the significant model terms; in the present case, the linear and quadratic terms are the significant model terms. Apparently, temperature (*A*) appears to be the most significant, and the order of significance is as follows: temperature (*A*) heating rate (*B*) > N<sub>2</sub> flow rate (*C*). In the quadratic term, only the quadratic temperature (*A*<sup>2</sup>) was significant, whereas other parameters had no

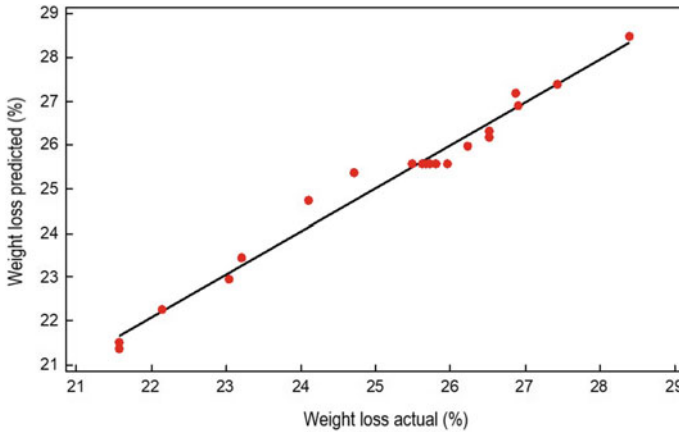


**Fig. 1** Comparison between actual and predicted weight loss of WPCBs

meaningful effect on weight loss. In addition, the effect of interaction between the parameters (temperature-heating rate ( $A * B$ ), temperature- $N_2$  flow rate ( $A * C$ ), and heating rate- $N_2$  flow rate ( $B * C$ )) had little or a minor impact on the weight loss of WPCBs.

## ***Effect of Operating Variables on the Weight Loss of WPCBs During Pyrolysis***

### **Single Parameters**

The influence of single parameters (temperature, heating rate, and  $N_2$  flow rate) on the weight loss of WPCBs is depicted in Fig. 2. Figure 2a depicts the weight loss of WPCBs as a function of temperature, illustrating the proportional rise in weight loss as the temperature increases. A similar pattern was observed in Fig. 2b, indicating that weight loss increased with increasing heating rate. However, the slope is significantly less than the effect of temperature, consistent with the ANOVA results. In contrast, the effect of  $N_2$  flow rate illustrated in Fig. 2c exhibited a small parabolic trend. The first rise in weight loss with increased  $N_2$  flow rate could be due to a sweeping effect of  $N_2$  to liberate the solid sample from condensed volatiles and other pyrolysis products [8]. Nonetheless, at extremely high  $N_2$  flow rates, this sweeping effect become severe, resulting in the quick removal of heat and products from the reaction media, hence lowering the possibility of secondary reactions [9].

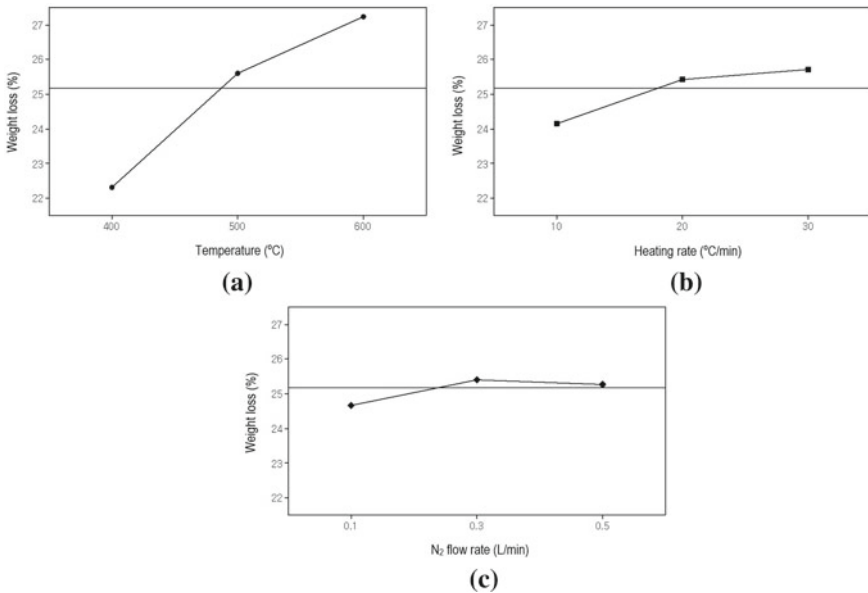


**Fig. 2** Effect of **a** temperature, **b** heating rate, and **c** N<sub>2</sub> flow rate on weight loss of WPCBs during pyrolysis after 10 min of attaining set temperature

### Interaction Between the Pyrolysis Parameters

Figure 3 presents the contour plots illustrating the interaction between the pyrolysis parameters. Similar to the previous observation, these plots likewise demonstrated the highest significance of temperature on the weight loss of WPCBs. As indicated in Fig. 3a, b, a maximum weight loss of >27% could be achieved at an operating temperature  $\geq 550$  °C while maintaining other parameters such as heating and N<sub>2</sub> flow rate at >15 °C/min and >0.2 L/min, respectively. The interactive effect of heating rate and N<sub>2</sub> flow rate (Fig. 3c) could only result in a weight loss of 26% even when both parameters were at their maximum and the temperature was maintained at 500 °C.

### Confirmation of Response Surface Modeling

The pyrolysis parameters considered in the present study were optimized. All the parameters were maintained within the range of the experimental conditions used, and the quadratic model (Eq. (2)) was used to predict the optimum parameters. Such optimum conditions should consider the energy consumption during the pyrolysis, and thus, the conditions were defined as 513 °C temperature, 22 °C/min heating rate, and 0.3 L/min N<sub>2</sub> flow rate, giving a weight loss of 25.93% with about 0.07% difference from the predicted value. The deviation between the experimental and

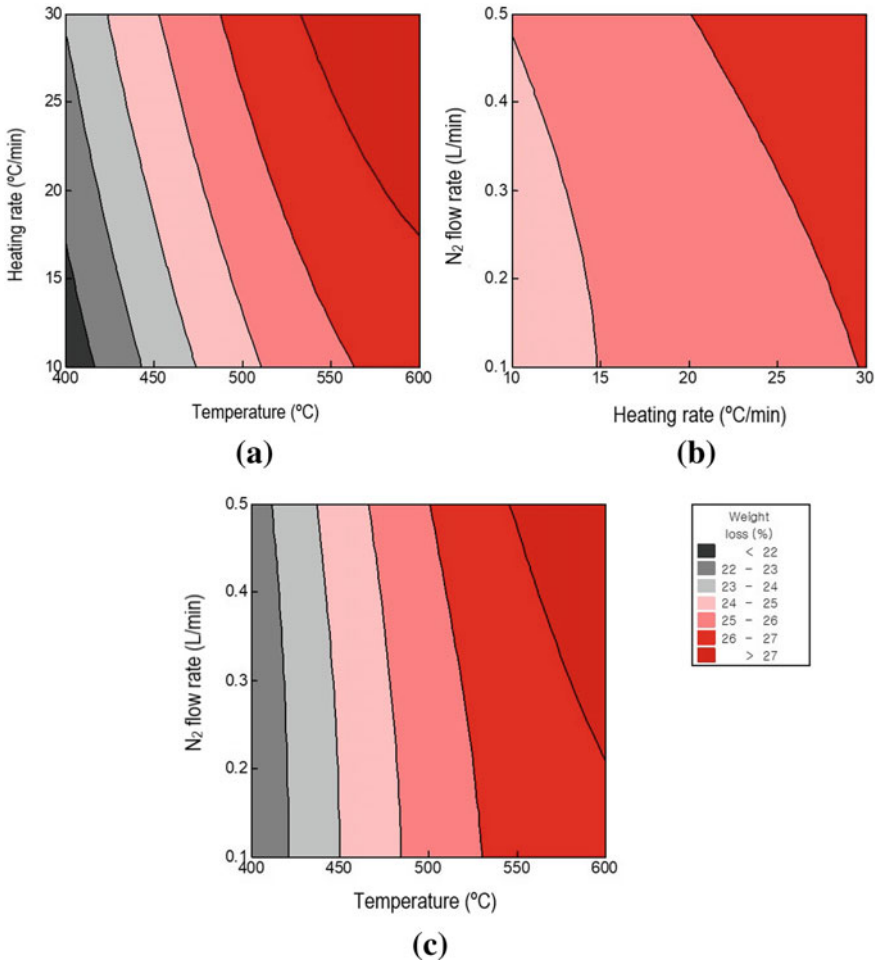


**Fig. 3** Contour plots between **a** temperature and heating rate, **b** heating rate and N<sub>2</sub> flow rate, and **c** temperature and N<sub>2</sub> flow rate

predicted results from the model is very low, suggesting the adequacy of the model for the pyrolysis of WPCBs.

### *Characterization of Pyrolyzed WPCBs*

Pyrolysis samples obtained at center point (500 °C, 20 °C/min, and 0.3 L/min N<sub>2</sub>) were used for the characterization purpose. The concentrations of main metals/elements (Cu, Pb, Sn, Al, Ag, Au, Pd, Rh, C) and proximate analysis of

WPCBs before and after pyrolysis are shown in Table 2. Apparently, ~100% of the metals were recovered in the char product. The metal concentrations and ash contents have accordingly increased after decomposition and volatilization of the organic substrate.

The cross-section of SEM images of WPCBs samples before and after pyrolysis is presented in Fig. 4. As can be seen from Fig. 4a, the glued multilayers of substrates and metal sheet are present in the raw WPCBs. The change of the multilayers on the WPCBs sample could be clearly seen after pyrolysis (Fig. 4b). Some holes and cracks were also formed, and the glued multilayers were completely destroyed.

The XRD patterns of WPCBs samples before and after pyrolysis are shown in Fig. 5. It clearly reflects the decrease in the degree of amorphousness along with the decomposition of the organic substrate during pyrolysis. The rising intensity of peaks at  $2\theta$  of  $43.35^\circ$ ,  $50.48^\circ$ , and  $74.16^\circ$  for Cu also confirmed the above results presented in Table 3.

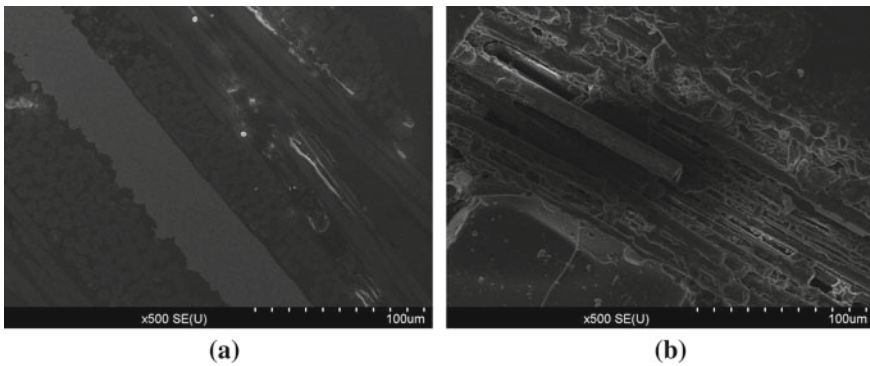
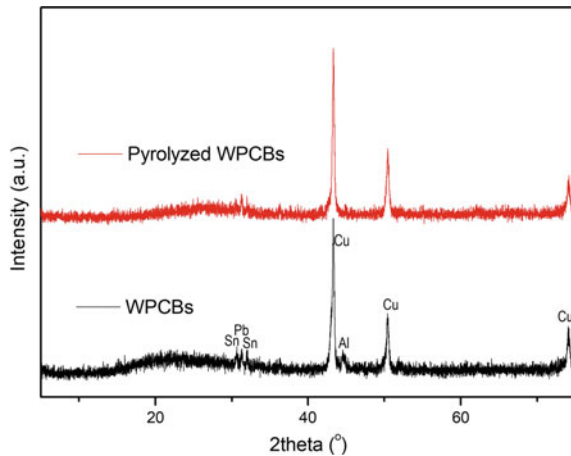


Fig. 4 Cross-sectional SEM images of WPCBs **a** before and **b** after pyrolysis at 500 °C

Fig. 5 XRD patterns of WPCBs before and after pyrolysis at 500 °C

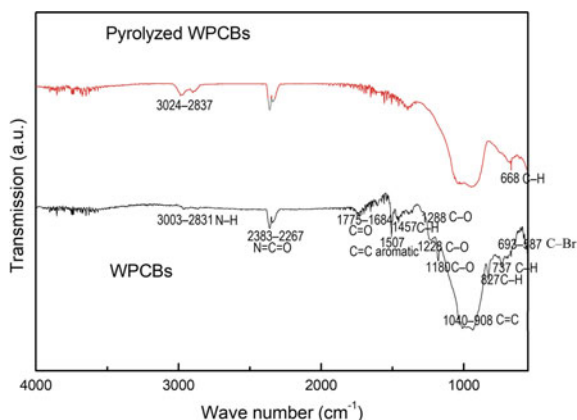


**Table 3** Metal/element compositions and proximate analysis of WPCBs before and after pyrolysis at 500 °C after 10 min holding time, 20 °C/min heating rate, and 0.3 L/min N<sub>2</sub> flow rate

Samples	Metal/element compositions (wt%)								Proximate analysis (wt%) <sup>b</sup>			
	Cu	Pb	Sn	Al	Ag	Au <sup>a</sup>	Pd <sup>a</sup>	Rh <sup>a</sup>	C	V <sub>d</sub>	Ash	FC
WPCBs	23.36	0.95	1.86	2.79	0.33	11.75	46.5	742.5	19.9	25.12	72.9	1.37
Pyrolyzed WPCBs	30.91	1.29	2.46	3.84	0.44	17.0	61.88	1032.3	8.51	6.85	92.51	0.64

<sup>a</sup> Au, Pd and Rh in g/ton

<sup>b</sup> V<sub>d</sub> = volatile content, FC = Fixed carbon

**Fig. 6** FTIR spectra of WPCBs before and after pyrolysis at 500 °C

The FTIR analysis of the raw WPCBs and pyrolyzed product is shown in Fig. 6. It can be seen that the raw WPCBs contained complex compound with main functional groups of C–Br, C–H, C=C, C–O, N=C=O, C–Br, and aromatic cycle [10]. The functional groups from C–H, C–Br, C–O, and aromatic cycle have disappeared after the pyrolysis process, as confirmed during the studies that the major compositions of gas and tar collected from the pyrolysis are from these groups, such as H<sub>2</sub>, CO<sub>2</sub>, CO, CH<sub>4</sub>, C<sub>2</sub>H<sub>4</sub>, C<sub>2</sub>H<sub>6</sub>, C<sub>2</sub>H<sub>5</sub>Br, alcohols, phenols [11].

## Recommendation of Metal Recycling Process

The organic substrate in WPCBs has been successfully degraded by the pyrolysis process, allowing for the separation of metal fraction with relative ease. No metal loss observed during the pyrolysis has also become advantageous for the recycling process. However, the metal layers were wrapped by the melted fiberboards. Thus, additional mechanical force, such as crushing for a brief period of time, may be

utilized. Sieving can be used to separate brittle coke (fine particles) and metal-rich fraction. Afterwards, well-known separation technologies based on magnetic-, electrostatic-, or gravity separation systems can be used to further separate metals from non-metallic black fiber. The resultant metal-rich concentration can be subjected to subsequent leaching-based metal recovery process.

## Conclusions

In the present study, the pyrolysis of WPCBs was examined using a series of experiments with CCD using response surface methodology (RSM). The effects of temperature, heating rate, and N<sub>2</sub> flow rate on the weight loss during pyrolysis were ranked as follows: temperature > heating rate > N<sub>2</sub> flow rate. A quadratic regression model was developed, and desired conditions of 513 °C temperature, 22 °C/min heating rate, and 0.3 L/min N<sub>2</sub> flow rate were selected based on the model. Under these conditions, a weight loss of 25.93% was observed, which was in good accordance with the predicted yield (26.0%). Metal analysis of pyrolyzed WPCBs revealed an increase in metal concentration with ~100% of metal recovery. SEM analysis clearly showed the change of morphological structure of the pyrolyzed WPCBs. XRD analysis corroborated the decrease in amorphousness in the pyrolyzed WPCBs, in accordance with the FTIR spectra demonstrating the disappearances of various organic peaks.

## References

1. Lee J-C, Song HT, Yoo JM (2007) Present status of the recycling of waste electrical and electronic equipment in Korea. *Resour Conserv Recycl* 50(4):380–397. <https://doi.org/10.1016/j.resconrec.2007.01.010>
2. Li H, Eksteen J, Oraby E (2018) Hydrometallurgical recovery of metals from waste printed circuit boards (WPCBs): current status and perspectives—A review. *Resour Conserv Recycl* 139:122–139. <https://doi.org/10.1016/j.resconrec.2018.08.007>
3. Hao J, Wang Y, Wu Y, Guo F (2020) Metal recovery from waste printed circuit boards: a review for current status and perspectives. *Resour Conserv Recycl* 157:104787. <https://doi.org/10.1016/j.resconrec.2020.104787>
4. Wang H, Zhang S, Li B, Pan DA, Wu Y, Zuo T (2017) Recovery of waste printed circuit boards through pyrometallurgical processing: a review. *Resour Conserv Recycl* 126:209–218. <https://doi.org/10.1016/j.resconrec.2017.08.001>
5. Gao R, Xu Z (2019) Pyrolysis and utilization of nonmetal materials in waste printed circuit boards: debromination pyrolysis, temperature-controlled condensation, and synthesis of oil-based resin. *J Hazard Mater* 364:1–10. <https://doi.org/10.1016/j.jhazmat.2018.09.096>
6. Gao R, Liu B, Zhan L, Guo J, Zhang J, Xu Z (2021) Catalytic effect and mechanism of coexisting copper on conversion of organics during pyrolysis of waste printed circuit boards. *J Hazard Mater* 403:123465. <https://doi.org/10.1016/j.jhazmat.2020.123465>
7. Liu J, Jiang Q, Wang H, Li J, Zhang W (2021) Catalytic effect and mechanism of in-situ metals on pyrolysis of FR4 printed circuit boards: insights from kinetics and products. *Chemosphere* 280:130804. <https://doi.org/10.1016/j.chemosphere.2021.130804>



8. Wulandari YR, Chen SS, Hermosa GC, Hossain MSA, Yamauchi Y, Ahamad T, Alshehri SM, Wu KC, Wu HS (2020) Effect of N<sub>2</sub> flow rate on kinetic investigation of lignin pyrolysis. *Environ Res* 190:109976. <https://doi.org/10.1016/j.envres.2020.109976>
9. Püttin E (2010) Catalytic pyrolysis of biomass: effects of pyrolysis temperature, sweeping gas flow rate and MgO catalyst. *Energy* 35(7):2761–2766. <https://doi.org/10.1016/j.energy.2010.02.024>
10. Zhao C, Zhang X, Shi L (2017) Catalytic pyrolysis characteristics of scrap printed circuit boards by TG-FTIR. *Waste Manage* 61:354–361. <https://doi.org/10.1016/j.wasman.2016.12.019>
11. Jadhao PR, Ahmad E, Pant KK, Nigam KDP (2020) Environmentally friendly approach for the recovery of metallic fraction from waste printed circuit boards using pyrolysis and ultrasonication. *Waste Manage* 118:150–160. <https://doi.org/10.1016/j.wasman.2020.08.028>

# Characterization and Beneficiation of Nigerian Lithium Ore: An Overview



Furqan Abdulfattah, Markus Daniel Bwala, Oladunni Oyelola Alabi,  
Musa Gafai Sayyadi, and Suleiman Bolaji Hassan

**Abstract** Lithium ore is one of the most sought after minerals of the twenty-first century due to its versatile application and specific application in sustainable energy. With the high development and increase in electronic equipment, small-scale power storage, and new energy industry, the consumption and demands for lithium are on a continuous rise. Nigeria is a country with abundant mineral resource deposits where lithium ore of several kinds have been identified to be deposited in not less than five states across the country. This paper gives an overview on characterization and beneficiation of Nigerian lithium ore reporting the work done so far and identifying the knowledge gap for advancement in the research of lithium ore in Nigeria.

**Keywords** Lithium · Beneficiation · Energy storage · Characterization · Pegmatite · Spodumene · Lapidolite · Recovery

## Introduction

The rapid growth of the world economy has greatly increased the requirement to exploit other natural resources to meet metal and energy demands for several industrial uses. Demand for lithium is rapidly increasing with a projected 10% annual consumption growth [1]. Due to the advancement in technological driven devices and new energy industry, the consumption and demands for lithium are on a rapid rise. Lithium is estimated to be the 25th most abundant element in the earth's crust [2]. The British Geological Survey risk level report (2013) stated that the crustal abundance was 16 ppm; thus, it is rated as a medium-risk on a global scale [3].

In appearance, lithium metal is silvery white; it is the lightest metal with an atomic number of 3 and density of 0.534 g/mL at room temperature [4]. Lithium is a highly reactive metal, when in contact with water, it reacts violently forming

---

F. Abdulfattah (✉) · M. D. Bwala · M. G. Sayyadi · S. B. Hassan  
Nigerian Institute of Mining and Geosciences, Jos, Plateau State, Nigeria  
e-mail: [furqanabdul1563@gmail.com](mailto:furqanabdul1563@gmail.com)

O. O. Alabi  
Federal University of Technology, Akure, Ondo State, Nigeria

lithium hydroxide, as a safety precaution, it is stored under liquid paraffin. Lithium is also the most electropositive of all the metals, it has a high standard electrode potential of 3.05 V when compared to other group 1 metals; 2.71 V for sodium and 2.92 V for potassium [5]. There are two major primary sources of lithium; Brines and Pegmatites of lithium-bearing minerals. The most important rock deposits of lithium are granitic pegmatites and greisens. It is estimated that the average grade of lithium in the earth's crust is around 1.6 ppm, whereas, in oceanic crust, it is 4.3 ppm, and the upper continental crust (rocks found on land) has an average of 20 ppm [6, 7].

Due to its reactivity, Li does not occur in elemental form in nature. However, there are more than 100 known minerals that may contain Li, although only a few of these are currently considered as economic sources. The majority of lithium minerals are found in lithium-cesium-tantalum pegmatites, which are coarsely crystalline granites due to slow cooling process of magma and are large intrusive igneous rocks, which included lithium. However, just some of them occur in magmatic crystalline rocks and have commercial/industrial potential—lepidolite, spodumene, petalite, amblygonite-montebrazite and zinnwaldite [8, 9].

Nigeria has in abundance up-to 35 industrial minerals which when exploited appropriately would improve the national income generation. Of such minerals is lithium ore deposited in several lithium-bearing pegmatites. The lithium-bearing mineral deposited in Nigeria include Spodumene, Lepidolite, Kunzite, Amblygonite, Petalite, and many more yet to be discovered [10].

In order to ascertain the potential deposit of lithium ore in Nigeria, appropriate characterization needs to be carried out, and the recovery of the lithium is necessary which is value addition process to the minerals which would increase the revenue from selling the concentrate for industrial use. This paper gives an overview on characterization and beneficiation of Nigerian lithium ore reporting the work done so far and identifying the knowledge gap for advancement in the research of lithium ore in Nigeria.

## **Lithium Ore Deposit and Mineralization in Nigeria**

Many African countries (most notably Zimbabwe, Namibia, Ghana, Democratic Republic of Congo, Mali, and others) have lithium ore deposit mostly found in low concentration in igneous rock nevertheless if appropriately exploited could be potential source for lithium concentrate [11].

Nigerian lithium ore is found in both the Northern and Southern parts of the country such as Kogi, Nasarawa, Kwara, Oyo, Plateau, Bauchi, Gombe, and Adamawa. The most common lithium ores in Nigeria is spodumene, petalite, amblygonite, kunzite, and lepidolite. These lithium ores are exported as mined without any value addition to it, which reduces the revenue generated by the country from mining and mineral industry [10] Table 1.

The pegmatitic belt and the orientation of the units within it appear to be related to rotational stresses created by the Benue Trough. From a more global perspective, this

**Table 1** Lithium ore deposits in Nigeria

Deposits	State	Associated minerals
Panda	Nasarawa	Pegmatite
Wamba	Nasarawa	Quartzite
Kabba	Kogi	Quartzite
Kushaka, Birnin Gwari	Niger	Pegmatite/Petalite
Isanlu Egbe	Kogi	Pegmatite
Ilesha	Osun	Pegmatite
Ijero Aramoko	Ekiti	Pegmatite
Arikyia Tsauni	Nasarawa	Pegmatite and Quartzite
Kafin Maiyarki	Nasarawa	Granite
Itakpe Area	Kogi	Quartzite and Pegmatite
Oke Ogun	Oyo	Quartzite
Ago Iwoye	Ogun	Pegmatite
Hong	Adamawa	Lepidolite/Kunzite
Zuru	Zamfara	Petalite
Kafanchan	Kaduna	Spodumene/Kunzite
Lere	Kaduna	Petalite
Jos- South	Plateau	Quartzite/Lapidolite
Ganjuwa	Bauchi	Lithium Oxide/Lithia
Gidan Boda, Baruten	Kwara	Spodumene
Keffi	Nasarawa	Lepidolite

Source MMSD, 2022; Azomite® Laboratory Report

trend is probably the northern extension of the Brazilian pegmatite belt, which runs from Rio Grande del Sul to Rio Grande del Norte. The pegmatite field of Nigerian lithium deposit is part of late Pan African, rare (specialty) metals granitic pegmatites [12, 13]. The primary mineralization of tantalum, niobium, tin, beryllium, and lithium is hosted in quartz-feldspar-muscovite pegmatites [14].

## Characterization and Beneficiation of Lithium Ore

Globally, research has been carried out in recent past on lithium ore due to development of its application in the energy storage industry. The need for reduction on usage of greenhouse gases has popularized the research on characterization and beneficiation of lithium ore as an alternative sustainable source of energy. Suspected lithium-bearing pegmatites could be characterized through several methods of characterization techniques such as; XRD, SEM-EDS, QEMSCAN, EDS-XRF, AAS, and any other kind of characterization.

Lithium can be recovered from lithium-bearing pegmatite ore using several beneficiation techniques such as magnetic separation, gravity concentration, electrostatic separation, leaching, and flotation [15]. In order to achieve a high-grade lithium concentrate, combination of the beneficiation procedure can be done.

Tassos et al. worked on the XRD and QEMSCAN mineralogical characterization of Zoro Lithium ore. The results show presence of spodumene (10.5%), quartz (29.3%), plagioclase (29.0%), K-feldspars (21.3%), micas (5.1%), tourmaline (2.9%), and Fe–Mn-phosphates (0.1%). While the electron probe micro-analyses and LA-ICP-MS showed that the average Li concentration is 3.7% in spodumene, 2196 ppm in micas, 1001 ppm in tourmaline, and 115 ppm in K-feldspars. The research also shows that Spodumene is the primary lithium mineral in the Zoro Pegmatite and accounts for 96% of the total lithium. From the research, beneficiation of the lithium ore deposit was achieved using heavy liquid separation (HLS) combined with magnetite separation; this indicates that it is possible to produce a high-grade (close to 6%  $\text{Li}_2\text{O}$ ) lithium concentrate after the rejection of iron silicate minerals [16].

Flotation is a widely adopted recovery technique of lithium from lithium-bearing pegmatite ores using reverse and direct flotation [17]. It is used to separate valuable minerals by taking advantage of the differences in surface characteristics between the two types of minerals from undesired gangue minerals [18, 19]. This process uses a mixture of chemicals, such as pH modifiers, collectors, frothers, and activators/depressants to separate minerals with different surface wettability either by attachment or detachment to bubbles [19–22].

Choi et al. worked the flotation of lepidolite utilizing stearyl trimethyl ammonium chloride (STAC) as a collector, one of the quaternary ammonium salts, without adding any depressant, and AF65 as a frother. The lepidolite, muscovite, quartz, calcite, and albite minerals form the majority of the ores obtained from the Boam mine in Uljin, South Korea. The zeta potentials of the minerals were measured by varying solution pH, and the results show that the values of isoelectric point (IEP) were determined to be about pH of 2.5, 2.3, and 9.7 for silica, albite, and calcite, respectively, and that of lepidolite was below 2. They performed three-stage flotation with the separation of calcite, albite, and quartz and recovered 76.3% of lepidolite with a concentrate grade of 3.8 times higher  $\text{Li}_2\text{O}$  than feed [23].

Also, Sousa et al. [24] obtained concentrate with a grade of 5.20%  $\text{Li}_2\text{O}$  and 4.58%  $\text{Li}_2\text{O}$  by flotation of spodumene-rich pegmatite from Långträsk (Finland) and Lepidolite-rich pegmatite from Gonçalo (Portugal) respectively. The lithium ores samples were characterized using optical microscopy, x-ray diffraction (XRD), scanning electron microscope-energy dispersive x-ray (SEM–EDX), and Raman spectra, and it was found that in the case of Långträsk, spodumene occurs with fine quartz intergrowths and is crosscut by fine albite and K-feldspar to some extent, whilst micro-inclusions of quartz and albite were found in the Gonçalo lepidolite [24].

Fosu et al. [25] researched on identifying and quantifying major minerals in Spodumene concentrate of the Pilbara region, Western Australia. The characterization was done using x-ray diffraction (XRD), scanning electron microscope-energy dispersive spectroscopy (SEM–EDS), XRF and ICP-OES, and Mineral Liberation

Analysis (MLA). The result of the elemental composition of the concentrate as oxides obtained from XRF and ICP-OES show the lithium concentration to be 2.14 wt%; consequently, the calculated lithium oxide and spodumene concentrations were 4.61 wt% and 57.39 wt% respectively, which is in close agreement with the 60.21 wt% spodumenes indicated by the MLA and 3 wt% Li content in spodumene. XRD spectra of the concentrate are show presence of Spodumene, mica (muscovite and biotite), quartz, feldspars (orthoclase, albite, anorthite), and the amphiboles are the predominant minerals identified which are typical minerals of spodumene ore of Pilbara [25].

In Nigeria, the Ministry of Mines and Steel Development conducted a preliminary study on lithium mining, processing, and extraction to ascertain the presence of lithium deposit in some suspected areas in the country. The result of the chemical characterization by the use of ED-XRF is shown in Table 2.

The elemental ED-XRF analysis shows the presence of lithium across the selected pegmatite ore deposit range 3.52–9.53% with Panda in Nasarawa State having the highest presence of lithium oxide in the lithium-bearing pegmatite [10]. Also, the beneficiation of the identified deposit was done using froth-flotation technique to achieve an improved lithium concentrate [10]. The ED-XRF of the ore shows a significant improvement in the lithium which ranges from 31.79–37.9%  $\text{Li}_2\text{O}$  and reduction in the silica as impurity from 54.21–66.00%  $\text{SiO}_2$  as shown in Table 3.

Akinola et al. researched on physico-chemical characteristics of thirty lepidolite samples were collected from Ijero-Aramoko pegmatite field, Southwestern Nigeria and analyzed them using the inductively coupled plasma-atomic emission spectrometry (ICP-AES). The results of the analysis indicate high presence of Li, Be, Cs, and Rb contents, the average Li values of 1859 ppm, 1778 ppm, and 1656 ppm were recorded for Oke-Asa, Oke-Igbo Aba, and Ijero Ekiti, respectively. The research established that Ijero-Aramoko pegmatite field could be a potential source of lithium ore in Nigeria [26].

**Table 2** Results of energy dispersive x-ray fluorescence spectrometer (ED–XRF) chemical analysis of sourced lithium ore at different deposits within Nigeria

Sample locations	$\text{SiO}_2$ wt%	$\text{Al}_2\text{O}_3$ wt%	$\text{Na}_2\text{O}$ wt%	$\text{K}_2\text{O}$ wt%	$\text{TiO}_2$ wt%	$\text{P}_2\text{O}_5$ wt%	$\text{MgO}$ wt%	$\text{Li}_2\text{O}$ wt%	$\text{MnO}$ wt%	$\text{CaO}$ wt%	$\text{Fe}_2\text{O}_3$ wt%	L.O.I wt%
Panda	73.8	3.21	2.14	0.12	2.14	1.04	0.26	9.53	0.06	2.36	4.31	0.01
Wamba	74.23	3.08	1.06	0.13	2.06	1.21	0.18	8.69	0.05	2.21	3.98	0.03
Kabba	82.86	2.14	1.05	2.10	0.06	0.03	0.50	8.69	0.01	0.16	2.07	0.01
Kushaka	94.08	0.06	0.03	0.12	0.18	0.002	0.05	3.51	0.01	0.14	2.04	0.01
Isanlu Egbe	78.4	2.63	2.01	0.25	3.14	0.001	0.05	9.336	0.37	1.05	1.29	0.02
Ilesha	85.51	1.01	2.01	3.62	0.21	0.002	0.43	4.379	0.089	0.96	1.93	0.01
Ijero Aramoko	87.21	1.86	1.05	0.34	0.069	0.006	0.061	6.102	0.42	1.71	1.16	0.03

Source MMSD, 2022

**Table 3** Results of ED—XRF chemical analysis of beneficiated lithium ores using froth flotation processing method

Sample locations	SiO <sub>2</sub> wt%	Al <sub>2</sub> O <sub>3</sub> wt%	Na <sub>2</sub> O wt%	K <sub>2</sub> O wt%	TiO <sub>2</sub> wt%	P <sub>2</sub> O <sub>5</sub> wt%	MgO wt%	Li <sub>2</sub> O wt%	MnO wt%	CaO wt%	Fe <sub>2</sub> O <sub>3</sub> wt%	L.O.I wt%
Panda	60.46	0.21	1.14	0.10	0.14	0.01	0.09	37.96	0.03	1.31	1.11	0.001
Wamba	58.21	3.08	0.68	0.13	0.96	0.11	0.08	36.86	0.05	0.21	1.78	0.001
Kabba	66.00	0.24	0.45	0.90	0.06	0.03	0.08	34.69	0.01	0.09	0.97	0.001
Kushaka	65.02	0.06	0.03	0.09	0.09	0.002	0.05	34.51	0.01	0.07	0.44	0.000
Isanlu Egbe	54.21	1.53	0.81	0.08	1.54	0.001	0.05	33.31	0.37	0.51	0.69	0.001
Ilesha	65.51	0.91	0.91	1.21	0.09	0.002	0.231	31.79	0.089	0.49	0.43	0.001
Ijero -Aramoko	63.72	0.76	0.85	0.14	0.05	0.006	0.061	32.11	0.42	0.64	0.66	0.001

Agaku et al. studied the qualitative analysis and hydrometallurgical extraction of lithium from polyolithionite ore obtained from Keffi pegmatite field, Nassarawa state, North-Central, Nigeria. The study therefore showed that the hydrometallurgical extraction of Li using chloride roasting additives (NaCl and CaCl<sub>2</sub>) is cost effective, less energy consuming, and efficient, since the chloride additives rationed in fractions (1:0.6:0.4 ore, NaCl, CaCl<sub>2</sub>) gave substantial optima lithium extraction efficiency of 89.90% at the optimized conditions. The chemical characterization using both energy dispersive x-ray fluorescence (ED-XRF) and flame atomic emission spectroscopy (FAES) composition of the lithium rich rock was show present of Li<sub>2</sub>O with Li content of 3.25 wt% [27].

## Conclusions and Recommendation

This work looks at several research works done on characterization and beneficiation of lithium ore. The research shows the advancement in research on characterization and beneficiation of lithium ore globally. Also, because spodumene seems to be the highest rich lithium-bearing pegmatite ore. It looks like little or no detailed studies are yet to be carried out on other lithium-bearing minerals such as lepidolite, petalite, kunzite, quartzite, and others.

Despite the presence of lithium deposit in Nigeria, it was observed that only very little research has been done on lithium characterization and beneficiation. There is a need to immensely exploit this visible knowledge gap for exploitation and processing of lithium in Nigeria.

Holistic research on characterization and beneficiation of lithium-bearing pegmatite ore in Nigeria is needed since minerals beneficiation complement key national development initiatives through the provision of mineral-based feedstock for a competitive manufacturing sector in an environmentally sustainable way.

## References

1. United States Geological Survey (2015) Mineral commodity summaries 2015. U.S. Geological Survey
2. Pratima Meshram BD, Pandey TR, Mankhand (2014) Extraction of lithium from primary and secondary sources by pre-treatment, leaching and separation: a comprehensive review. *Hydrometallurgy* 150:192–208. <https://doi.org/10.1016/j.hydromet.2014.10.012>
3. British Geological Survey (2016) Lithium profile, a series of Commodity Profiles. [www.MineralsUK.com](http://www.MineralsUK.com)
4. Hawkes JR, Harris PM, Dangerfield J, Strong GR, Davis AE, Nancarrow PHA, Francis AD, Smale CV (1987) The lithium potential of the St. Austell granite. *Br Geol Surv Rep* 19(4)
5. Garrett DE (2004) Handbook of lithium and natural calcium chloride, their deposits, processing, uses, and properties. Elsevier Academic Press, p 476
6. Bradley DC, Stillings LL, Jaskula BW, Munk L, McCauley AD (2017) Lithium, chap. K. In *Critical mineral resources of the United States—Economic and environmental geology and*



- prospects for future supply, Schulz KJ, DeYoungs Jr JH, Seal RRI, Bradley DC, K1–K21. Reston, VA: U.S. Geological Survey
7. McLennan SM (2001) Relationships between the trace element composition of sedimentary rocks and upper continental crust. *Geochem, Geophys, Geosyst* 2(4). <https://doi.org/10.1029/2000GC000109>
  8. Levich B (2009) A five-year strategic outlook for the lithium industry. In: *Metal Bulletin*, London
  9. Rudnick RL, Gao S (2014) Composition of the continental crust. *Treatise Geochem* 4:1–51
  10. Goodenough K, Deady E, Shaw R (2021) Lithium resources, and their potential to support battery supply chains, in Africa. *Br Geol Surv*
  11. MMSD (2022) Report on prospect of lithium mining, processing and extraction in Nigeria
  12. Jacobson R, Webb JS (1946) The Pegmatite of Central Nigeria. *Geol Surv Niger Bull* 17:61
  13. Wright JB (1976) Fracture systems in Nigeria and initiation of fracture zones in the South Atlantic. *Tectonophysics* 34:743–747
  14. Kinnaird JA (1984) Contrasting styles of Sn-Nb-Ta-Zn mineralisation in Nigeria. *J Afr Earth Sci* 2(2):81–90
  15. Sahoo SK, Tripathy SK, Nayak A, Hembrom KC, Dey S, Rath RK, Mohanta MK (2022) Beneficiation of lithium bearing pegmatite rock: a review. *Miner Process Extr Metall Rev*. <https://doi.org/10.1080/08827508.2022.2117172>
  16. Grammatikopoulos T, Aghamirian M, Fedikow M, Mayo T (2020) Mineralogical characterization and preliminary beneficiation of the Zoro Lithium Project, Manitoba, Canada. *Min, Metall Explor* <https://doi.org/10.1007/s42461-020-00299-2>
  17. Bhappu B, Fuerstenau MC (1964) Recovery of valuable minerals from pegmatite ores. *New Mex Bur Mines Miner Resour* 70:1–29
  18. Sahoo SK, Suresh N, Varma AK (2021) Performance evaluation of batch coal flotation from the petrologic point of view. *Int J Coal Prep Util* 41(3):159–176. <https://doi.org/10.1080/19392699.2018.1455668>
  19. Wills BA, Finch J (2015) *Wills' mineral processing technology: an Introduction to the practical aspects of ore treatment and mineral recovery*, 8th edn. Butterworth-Heinemann, Cambridge
  20. Sahoo SK, Suresh N, Varma AK (2019) Kinetic studies on petrographic components of coal in batch flotation operation. *Int J Coal Prep Util* 39(5):259–280. <https://doi.org/10.1080/19392699.2017.1314966>
  21. Sahoo SK, Suresh N, Varma AK (2020) Flotation production of vitrinite maceral concentrate and its optimization using response surface approach. *Int J Coal Prep Util* 40(3):155–174. <https://doi.org/10.1080/19392699.2017.1356827>
  22. Tabelin CB, Dallas J, Casanova S, Pelech T, Bournival G, Saydam S, Canbulat I (2021) Towards a low-carbon society: a review of lithium resource availability, challenges and innovations in mining, extraction and recycling, and future perspectives. *Miner Eng* 163:106743. <https://doi.org/10.1016/j.mineng.2020.106743>
  23. Choi J, Kim W, Chae W, Kim SB, Kim H (2012) Electrostatically controlled enrichment of lepidolite via flotation. *Mater Trans* 53(12):2191–2194. <https://doi.org/10.2320/matertrans.M2012235>
  24. Sousa R, Ramos V, Guedes A, de Sousa AB, Noronha F, Leite MM (2019) Flotation of lithium ores to obtain high-grade Li<sub>2</sub>O concentrates. Are there any mineralogical limitations? *Int J Min, Mater, Metall Eng* 5(1):7–18
  25. Fosu AY, Kanari N, Bartier D, Hodge H, Vaughan J, Chagnes A (2021) Physico-chemical characteristics of spodumene concentrate and its thermal transformations. *Materials (Basel)* 14(23):7423. <https://doi.org/10.3390/ma14237423>. PMID: 34885577; PMCID: PMC8658623
  26. Akinola OO, Okunlola OA, Obasi RA (2014) Physico-chemical characteristics and industrial potentials of Lepidolite from Ijero–Aramoko pegmatite field, south western Nigeria. *Int J Sci Technol Res* 3(3):278–283
  27. Agaku PI, Omoniyi KI, Nwokem NC, Dallatu YA (2020) Qualitative analysis and extraction of lithium from Keffi sourced polyolithionite ore by hydrometallurgical process. *Niger. Res. J. Chem. Sci.* 8(1) (ISSN: 2682-6054)

# Tantalum Recovery Technique for Recycling of Tantalum Coated Composite Materials



Akanksha Gupta and Brajendra Mishra

**Abstract** In recent years, tantalum is being increasingly researched as a replacement for coatings for high-temperature applications. Tantalum is a refractory metal with low recycling rate of less than 1% because most tantalum secondary recovery techniques are primarily meant for recovery of other elements. In this study, the objective is to review various potential methods for recycling of tantalum coated steel composite, either at its end of life or for coating refurbishment purposes when coating is damaged. Tantalum can be recovered by both pyrometallurgical and hydrometallurgical methods, or a combination of the two, and it usually involves a whole process development with multiple steps for separation and purification from other elements. The main factor for selecting the best recovery method is dependent on the materials which are mechanically or chemically bonded with tantalum. This review summarizes various methods to recover tantalum from different secondary sources like tantalum capacitors, tantalum mill products, and tantalum in chemical processing industry. Lastly, we comment on the best method to recover tantalum from tantalum coated scrap.

**Keywords** Tantalum recovery · Capacitor recovery · Bimetallic composite · Tantalum · Pyrometallurgy · Hydrometallurgy

## Introduction

Refractory metals like tantalum and tungsten are being extensively researched to replace traditional coatings in high-temperature applications. These metals offer properties of high melting point and superior resistance to extreme environments in high-temperature applications. Tantalum is a refractory metal with a high melting

---

A. Gupta · B. Mishra (✉)  
Department of Material Science and Engineering, Worcester Polytechnic Institute, Worcester,  
MA, USA  
e-mail: [bmishra@wpi.edu](mailto:bmishra@wpi.edu)

A. Gupta  
e-mail: [agupta7@wpi.edu](mailto:agupta7@wpi.edu)

point of 3017 °C. It is a very inert and heat resistant metal which finds applications in many fields including semiconductor industry in electronic capacitors for automotive, mobile phones and computers; alloying element for steels in aerospace and oil industries; in superalloys; as carbides for use in cutting tools; and as coatings for medical implants [1, 2]. Tantalum is also highly resistant to most acids or aggressive mediums, including HNO<sub>3</sub>, HCl and aqua regia below 150 °C, because of which it also finds applications in chemical reaction vessels. Tantalum supply is majorly from primary mining (artisanal and small-scale mining accounting for 48% and conventional mining 25%), tin slags (7%), secondary recycling (20%) and inventories and stockpiles, as reported in 2020 [3].

Tantalum belongs to the critical metal category with recycling rate of less than 1% [4]. In 2021, tantalum consumption in USA from secondary sources was reported to be nearly 30% [2]. Tantalum coated composites are a potential source for secondary tantalum recoveries. Moreover, tantalum coatings and coatings in general must be removed from substrate for a variety of reasons—replacement of damaged coating, inspection of substrate, recycling of coated composite or for cleaning of substrate. Traditional ways to recycle tantalum include both hydrometallurgical and pyrometallurgical route, with advantages and disadvantages for both. In the present review, the objective is review of various potential methods to recover tantalum from tantalum coated steel composites, with or without damage to the substrate. There is a lack of research for recovering tantalum from this specific form of tantalum coated steel composite in scientific journals. Therefore, we will carry out a broad review of extracting tantalum from different secondary sources with hopes of shedding light on potential route for recovering tantalum from tantalum coated steel composite.

## Pyrometallurgical Recovery

Pyrometallurgical processes are characterized by simple, high efficiency, energy intensive, high carbon footprint, and high-cost processing methods. There are various pyrometallurgy methods like high-temperature oxidation, chloride metallurgy, iodization, steam gasification, and pyrolysis, which have been reported to recover tantalum as its oxide or halogen compounds. For further separation and purification from other elements, hydrometallurgy like acid leaching, solvent extraction, or ion exchange may be used. To recover tantalum in metallic form, reduction using hydrogen gas or metallothermic reduction methods have been reported. The recovery rates are very high for tantalum using pyrometallurgy, but the purity rate solely depends on the secondary processes used to separate and purify the recovered tantalum. The various pyrometallurgical methods along with the complete process flow for recovering tantalum are summarized in Table 1.

**Table 1** Pyrometallurgical routes for recovering tantalum from different secondary sources

S. No. and Reference	Sample	Methodology (optimal conditions)	Recovery rate	Purity rate	Comments
1. [5]	Sintered tantalum electrode from tantalum capacitor: 50% Ta electrode with ~ 90% Ta by weight, and 10% Ni, Fe or Cu terminal	High-temperature oxidation with O <sub>2</sub> at 1150 K for 30 min to obtain Ta <sub>2</sub> O <sub>5</sub> powder without clumps, followed by mechanical (magnetic) and chemical purification (water and HNO <sub>3</sub> wash) of Ta <sub>2</sub> O <sub>5</sub> powder. Finally, reduction with Mg vapors to obtain Tantalum metal	90–92%	99%	Oxidation temperature must be optimized to effectively separate tantalum from other elements. Low temperature oxidation can cause collapse of tantalum electrode with the mold and high-temperature oxidation can oxidize other elements and contaminate tantalum and create a need for further treatment
2. [6]	Printed circuit boards from personal computers and household appliances	First, copper is recovered by carbonization in nitrogen and 2.5% oxygen environment at 873–1073 K. Next, nickel is recovered by carbonization at 873 K and magnetic separation. Finally, tantalum is recovered by oxidation at 873 K and separation from silica at 723 K	71%	Low purity	In printed circuit boards, recovery of tantalum requires recovery and separation from other elements. Tantalum recovery makes it economically favorable, but not energy and environmentally favorable; energy consumption increases by 50% with tantalum recovery
3. [7]	Sintered tantalum capacitor (same as above)	Steam gasification using NaOH at 530 °C for 5 min in a condenser to produce compact tantalum metal	Not reported	Not reported	Low temperature and pressure process; halogen gasses can be entrapped inside the reactor

(continued)

Table 1 (continued)

S. No. and Reference	Sample	Methodology (optimal conditions)	Recovery rate	Purity rate	Comments
4. [8]	Tantalum alloy scraps from two sources: 1. 99% pure tantalum from tantalum mill 2. Ta-2.5 W alloy from chemical processing industry	Secondary tantalum alloys are iodized using I <sub>2</sub> vapors to TaI <sub>5</sub> in step 1; followed by reduction to metallic tantalum nanopowder using H <sub>2</sub> /Ar gas at 2000–3500 °C	>99% (Step 1 and 2) 97.8% H <sub>2</sub> gas and 97% I <sub>2</sub> gas is recovered to be recycled again	Not reported	Ta is vaporized at high temperatures preventing complete reduction to Ta metal—Ta vaporization increases with increase in reduction temperature and increase in amount of H <sub>2</sub> ; H <sub>2</sub> and I <sub>2</sub> gas can be recycled; Environmentally friendly process
5. [9]	Tantalum capacitor scraps	Electron beam smelting and refining conducted at 21.6 kW beam power for 3 min	Not reported	99.96%	It is a Ta purity rate (quality) increasing process; high recovery rate
6. [10]	Tantalum capacitor scraps	High-temperature chloride metallurgy by reacting FeCl <sub>2</sub> with tantalum capacitor at 500 °C and 50% FeCl <sub>2</sub> for 2 h scrap to produce TaCl <sub>5</sub>	93.56%	>99%	Mixed control is rate controlling during chlorination; to increase Ta recovery—decrease particle size of reactants and increase surface area of contact; environmentally friendly recovery of Tantalum using non-toxic FeCl <sub>2</sub> (compared to Cl <sub>2</sub> , HCl and CCl <sub>4</sub> ); absence of hazardous gases and liquid waste

(continued)

Table 1 (continued)

S. No. and Reference	Sample	Methodology (optimal conditions)	Recovery rate	Purity rate	Comments
7. [11]	Tantalum capacitor scraps	Pyrolysis of tantalum capacitor scrap at 550 °C, 30 min and 100 ml/min heating rate to separate oil and gas (which can be further used as energy sources) and solid residue as Ta, Ni, Fe, Ag and SiO <sub>2</sub> . Tantalum is further recovered from the solid residue by chloride metallurgy same as [10]	<70% organics conversion. Tantalum recovery must be similar to [10] as 93.56% because same method is used	Same as [10] as 99%	This is a pre-tantalum recovery process to remove organics from tantalum capacitors to increase Ta recovery. This process can be integrated with chloride metallurgy to recover Tantalum; it has disadvantage of low organic conversion <70%
8. [12]	Tantalum capacitor scraps	Chlorination-sintering-chemisorption process to first recover Ta from capacitors as TaCl <sub>5</sub> by chlorinating with FeCl <sub>2</sub> [10]. Then, TaCl <sub>5</sub> is sintered at 700 °C for 6 h to convert to Ta <sub>2</sub> O <sub>5</sub> . Lastly, Ta <sub>2</sub> O <sub>5</sub> /Polyaniline is produced by chemisorption method for its photocatalytic properties and application	>92%	Same as [10] as 99%	Waste utilization, photocatalyst production, and high energy consumption process (because of high temperature and long time required during sintering)

## Hydrometallurgical Recovery

Though pyrometallurgy is more commonly applied for tantalum recoveries from secondary sources, there are various alternate hydrometallurgical routes reported as well. Because of the inherent nature of tantalum to resist corrosion even in aggressive mediums, hydrometallurgical methods for recovering tantalum usually involve recovering elements attached to tantalum first. Hydrometallurgical processes are characterized by high efficiency, resource extensive, high waste or by-product generation and costly processes. Generally, for tantalum recovery, hydrometallurgical methods have to be used in conjunction with other unit processes for complete process flow. Some commonly used methods include acid leaching in leaching reagents like HF, NH<sub>4</sub>F, HNO<sub>3</sub>, HCl, or H<sub>2</sub>SO<sub>4</sub> mediums; solvent extraction using solvents like methyl isobutyl ketone (MIBK), tributyl phosphate, cyclohexane, 2-octanol, and ionic liquids, and ion exchange method. Some methods to hydro-metallurgically recover tantalum from different sources are summarized in Table 2.

## Conclusion

There are various processes to recover tantalum, broadly classified into high-temperature oxidation, pyrolysis, steam gasification, iodization, acid leaching, alkaline leaching, application of ionic liquid, and supercritical water treatment. Pyrometallurgy is energy intensive but produces tantalum of high purity, in short time and may generate less waste by-products. On the other hand, hydrometallurgy routes are less energy intensive but produce a lot of waste which needs to be further handled and may involve use of high quantities of toxic reagents. Both processes have their advantages and limitations. Table 3 lists some differences between pyrometallurgy and hydrometallurgy for tantalum recovery. The selection of recovery strategy for tantalum depends on the waste from which it needs to be extracted. As described in the sections above, tantalum recovery involves a whole process flow with multiple steps to purify and separate other components from the waste scrap.

In case of tantalum coated steel composite, tantalum is attached to one other component which is steel and there may or may not be an interdiffusion layer which depends on the coating deposition method used. Thus, the main considerations here are the steel substrate and composite's interface characteristics. If tantalum is to be recovered with minimum damage to the substrate, pyrometallurgy to extract tantalum as its oxides may be the most efficient method to protect the steel substrate. Tantalum and iron oxidize in oxygen containing environment to develop protective scales of Ta<sub>2</sub>O<sub>5</sub> and oxides of the substrate, respectively. Thermodynamically, Ta<sub>2</sub>O<sub>5</sub> is a very stable phase at high temperatures compared to most metals. Therefore, both tantalum coating and steel substrate will oxidize but at relatively different rates, which can

**Table 2** Hydrometallurgical routes for recovering tantalum from different secondary sources

Author	Sample	Methodology (optimal conditions)	Recovery rate	Purity rate	Comments
1. [13]	Nigerian tantalite ore	Tantalum is selectively leached in 12 M HCl medium for 120 min at 80 °C	67.2%	Not reported	Rate of dissolution is dependent on hydrogen ion concentration; diffusion controlled kinetics; increase in surface area exposure to acid solution increases rate of dissolution
2. [14]	Nigerian tantalite ore	Tantalum is selectively dissolved in 8.06 M HNO <sub>3</sub> medium for 120 min at 80 °C	81.3%	Not reported	Tantalum dissolution increases in nitric acid medium with increase in leaching time, temperature, stirring speed and decrease in particle size; different acid solutions have different oxidizing characteristics and therefore, different tantalum dissolution rates
3. [15]	Mixture of Nb <sub>2</sub> O <sub>5</sub> and Ta <sub>2</sub> O <sub>5</sub> with impurities of Ti, Si, Sn, Fe, Mn	Nb <sub>2</sub> O <sub>5</sub> to Ta <sub>2</sub> O <sub>5</sub> ratio of 2.33:1 is roasted with KOH (2:1 ratio of KOH to sample) at 40 °C for 60 min, followed by leaching with water. Leached solution is purified by evaporation, crystallization, and phase transformation using a dilute acid	93.6%	99.3%	Optimal ratio of Nb:Ta is important for increased leached recovery rate

(continued)



Table 2 (continued)

Author	Sample	Methodology (optimal conditions)	Recovery rate	Purity rate	Comments
4. [16]	Mixture of Ta <sub>2</sub> O <sub>5</sub> and Nb <sub>2</sub> O <sub>5</sub>	First, fluoride solution of samples is made with different fluxes like NH <sub>4</sub> F, HF, Na <sub>2</sub> HPO <sub>4</sub> /NaH <sub>2</sub> PO <sub>4</sub> , H <sub>2</sub> O, followed by separation of Nb and Ta from fluoride solution by 3 different methods: Selective precipitation using p-phenylenediamine, solvent extraction using methyl isobutyl ketone and ion exchange using Amberlite resin and Dowex marathon	73.3% by selective precipitation; 100% by 2 step solvent extraction using 4 M H <sub>2</sub> SO <sub>4</sub> ; 73.4% by ion exchange using Amberlite resin and 52.3% using Dowex marathon	Not reported	Fluoride solution of Nb and Ta using NH <sub>4</sub> F, HF of those oxides are similar to those obtained by HF solvent; fluoride solutions for Ta and Nb extraction are simple, efficient, and economical; oxides of Nb and Ta have higher property differences than Ta and Nb metals, making their separation easier
5. [17]	Tantalum capacitor scraps	Supercritical water (SCW) treatment using supercritical water consisting of H <sup>+</sup> and OH <sup>-</sup> ions that form an acid/base catalyst for decomposing organic compounds. SCW treatment of epoxy resin casing of tantalum capacitor by two methods: Ta metal is recovered directly by supercritical water oxidation at 400 °C, 25 MPa and 1.5 h; Ta powder is recovered by mechanical separation after supercritical water depolymerization at 425 °C, 25 MPa and 2 h	96.26% by supercritical water depolymerization	72.37% by supercritical water depolymerization; 93.18% by supercritical oxidation	Higher rate of organic decomposition in supercritical water oxidation; environmentally friendly process to decompose organic resin of capacitor, and tantalum can be subsequently easily recovered at the most by mechanical separation

(continued)

Table 2 (continued)

Author	Sample	Methodology (optimal conditions)	Recovery rate	Purity rate	Comments
6. [18]	Tantalum capacitor scrap	Organics (epoxy) and wire (Ni-Fe terminal) separated by pyrolysis at 600 °C for 10 min and magnetic separation in pre-treatment step. Tantalum leached using different leaching agents—5% by volume HF; 180 °C, 30 mL/g for 3 h showing the best leaching properties. Solvent extraction using different solvents to separate Ta in organic phase—0.025 M, pH 1 for 1 min with Alamime336 reagent. Stripping of organic phase by 2 M HNO <sub>3</sub> , 1 organic/aqueous ratio for 5 min, followed by chemical precipitation and calcination of Ta to Ta <sub>2</sub> O <sub>5</sub>	Overall recovery rate is 98% 99% using HF; 99.5% extraction using Alamime 336 reagent; 99.4% stripping using HNO <sub>3</sub>	99.9%	High chemical waste generating process and high consumption of acids; low energy consumption; high recovery and purity rate of tantalum
7. [19]	Tantalum dissolved in sulfuric acid medium along with presence of other impurities like Nb, Fe, Ni, Ag and Mn	Tantalum is extracted from sulfuric acid medium selectively by solvent extraction process using a novel Phosphonated task specified ionic liquid (TSIL). Tantalum is further extracted from ionic liquid by dissolution in water at water/ionic liquid ratio of 5, followed by calcination at 900 °C for 4 h to Ta <sub>2</sub> O <sub>5</sub>	90%	Not reported	Ionic liquids are more environmentally friendly than organic solvents; phosphonated task specified ionic liquids are loss 15% in aqueous phase; an alternate solvent to commonly used methyl isobutyl ketone which is explosion hazardous

(continued)

Table 2 (continued)

Author	Sample	Methodology (optimal conditions)	Recovery rate	Purity rate	Comments
8. [20]	Nb-Ta alkaline solution from Maboumine process containing other impurities like Ti, Na and Fe	3-step liquid to liquid solvent extraction 1. Nb and Ta co-extraction using quaternary ammonium in aliphatic diluent 2. Nb selective extraction using oxalic acid and nitration solution at 0.5 M concentration 3. Ta selective extraction using nitric medium at 0.5 M concentration	>20% wt. of Ta as Ta <sub>2</sub> O <sub>5</sub> .nH <sub>2</sub> O		Fluoride-free process; mild alkaline medium for selective extraction of Nb and Ta is presented
9. [21]	Synthetic capacitor leached solution containing Ta <sub>5</sub> (V) and Nb(V)	N-butyl-N-ethyl-piperidinium bis(trifluoromethylsulfonyl)imide and N-octyl-N-ethyl-piperidinium bis(trifluoromethylsulfonyl)imide pure ionic liquids were used to extract tantalum from 1-7 g/L Ta solution of 6 M H <sub>2</sub> SO <sub>4</sub>	>90% by both ionic liquids		The two ionic liquids used here are more environmentally friendly than phosphonated task specified ionic liquids [19] and dissolve less than 1% in aqueous phase
10. [22]	Hydrofluoric acid solution containing Nb, Ta, Fe, SiO <sub>2</sub> , Ti and Mn	Co-extraction of Nb and Ta from hydrofluoric acid-based solution using 25% trioctyl amine in organic to aqueous ratio of 3. Selective extraction of Nb and Ta using HNO <sub>3</sub> , Na <sub>2</sub> CO <sub>3</sub> , and oxalic acid. Best medium for selective extraction of Ta is 10 M HNO <sub>3</sub>	93% after 3 contacts with 10 M HNO <sub>3</sub>	98.08%	And alternate alkaline solvent for selective extraction of Nb and Ta is presented

**Table 3** Comparison of pyrometallurgy and hydrometallurgy techniques for tantalum recovery

Pyrometallurgy techniques	Hydrometallurgy techniques
High energy consumption	Low energy consumption
Short processing period	Long processing period
May produce less amount of waste by-product	Produces large quantity of waste by-product
High efficiency, but can be less selective	High efficiency with high selectivity
May require a smaller number of processing step depending on the method used	Many processing steps required

be optimized. But if the whole tantalum coated steel composite is to be recycled, a combination of hydrometallurgy and pyrometallurgy may be the best method to selectively extract Fe (steel) and Ta.

## References

1. "Fourth Annual Report on Carcinogens (1985) U.S. Department of Health and Human Services, NTP 85-002, p 85
2. USGS Report on Tantalum (2022) U.S. Geological Survey, Mineral Commodity Summaries, 2022.
3. Tantalum-Niobium International Study Center (2020) Beautiful metal. Oxide films on Tantalum and Niobium. TIC Bulletin No 181
4. Reck BK, Graedel TE (2012) Challenges in metal recycling. *Science* 337(6095):690–695
5. Mineta K, Okabe TH (2005) Development of a recycling process for tantalum from capacitor scraps. *J Phys Chem Solids* 66(2–4):318–321
6. Fujita T, Ono H, Dodbiba G, Yamaguchi K (2014) Evaluation of a recycling process for printed circuit board by physical separation and heat treatment. *Waste Manage* 34(7):1264–1273
7. Katano S, Wajima T, Nakagome H (2014) Recovery of tantalum sintered compact from used tantalum condenser using steam gasification with sodium hydroxide. *APCBEE Proc* 10:182–186
8. Lessard JD, Shekhter LN, Gribbin DG, Blagoveshchensky Y, McHugh LF (2015) A new technology platform for the production of electronic grade tantalum nanopowders from tantalum scrap sources. *Int J Refract Metal Hard Mater* 48:408–413
9. Vutova K, Vassileva V, Koleva E, Munirathnam N, Amalnerkar DP, Tanaka T (2016) Investigation of tantalum recycling by electron beam melting. *Metals* 6(11):287
10. Niu B, Chen Z, Xu Z (2017) Method for recycling tantalum from waste tantalum capacitors by chloride metallurgy. *ACS Sustain Chem Eng* 5(2):1376–1381
11. Niu B, Chen Z, Xu Z (2017) Application of pyrolysis to recycling organics from waste tantalum capacitors. " *J Hazard Mater* 335:39–46
12. Niu B, Chen Z, Xu Z (2020) Recycling waste tantalum capacitors to synthesize high value-added Ta<sub>2</sub>O<sub>5</sub> and polyaniline-decorated Ta<sub>2</sub>O<sub>5</sub> photocatalyst by an integrated chlorination-sintering-chemisorption process. *J Clean Prod* 252:117206
13. Baba AA, Adekola FA, Faseki M (2005) A study of the kinetics of the dissolution of a Nigerian tantalite ore in hydrochloric acid. *Ife J Sci* 7(2):221–227
14. Baba AA, Adekola FA, Dele-Ige OI, Bale RB (2007) Investigation of dissolution kinetics of a Nigerian tantalite ore in nitric acid. *J Miner & Mater Charact & Eng* 7(1):83–95

15. Wang X, Zheng S, Xu H, Zhang Y (2009) Leaching of niobium and tantalum from a low-grade ore using a KOH roast–water leach system. *Hydrometallurgy* 98(3–4):219–223
16. Nete M, Purcell W, Nel JT (2016) Hydrometallurgical separation of niobium and tantalum: a fundamental approach. *Jom* 68(2):556–566
17. Niu B, Chen Z, Xu Z (2017) Recovery of tantalum from waste tantalum capacitors by supercritical water treatment. *ACS Sustain Chem Eng* 5(5):4421–4428
18. Chen W-S, Ho H-J, Lin K-Y (2019) Hydrometallurgical process for tantalum recovery from epoxy-coated solid electrolyte tantalum capacitors. *Materials* 12(8):1220
19. Micheau C, Lejeune M, Arrachart G, Draye M, Turgis R, Michel S, Legeai S, Pellet-Rostaing S (2019) Recovery of tantalum from synthetic sulfuric leach solutions by solvent extraction with phosphonate functionalized ionic liquids. *Hydrometallurgy* 189:105107
20. Deblonde GJ-P, Bengio D, Beltrami D, Bélair S, Cote G, Chagnes A (2019) A fluoride-free liquid-liquid extraction process for the recovery and separation of niobium and tantalum from alkaline leach solutions. *Sep Purif Technol* 215:634–643
21. Legeai S, Pellet-Rostaing S (2020) Ionic liquids as extraction media in a two-step eco-friendly process for selective tantalum recovery. *ACS Sustain Chem Eng* 8(4):1954–1963
22. Dutta S, Mukhopadhyay S, Gaddam S, Shenoy KT, Mirji KV (2021) Process development for the separation of niobium and tantalum from fluoride medium using trioctyl amine and application of Taguchi's method to optimize solvent extraction parameters. *Hydrometallurgy* 199:105522

# Reduction Volatilization Behavior of Indium Oxide in Indium-Tin Oxide (ITO) Wastes Under CO/CO<sub>2</sub> Atmosphere



Zijian Su, Yan Wang, Bin Lei, and Yuanbo Zhang

**Abstract** ITO is a vital material in preparing semiconducting film for electronic display screens, which contains 80–95 wt% of indium oxides. However, indium is a rare dispersion in Earth's crust with an average abundance of 0.02 ppm, which is quite difficult to recover extract from primary ores. Then ITO wastes were high-quality secondary resource for indium recovery. In this paper, a novel process for the separation and recovery of indium oxides from ITO waste targets via roasting under CO–CO<sub>2</sub> atmosphere is proposed. The effect of roasting parameters on the indium volatilization and phase transformation was conducted using thermomechanical analysis, XRD, SEM, etc. The results showed that the indium volatilization was 95.2 wt% under optimal experimental conditions. In<sub>2</sub>O<sub>3</sub> was selectively reduced to In<sub>2</sub>O and volatile as gaseous phase above 900 °C, then indium can be separated and collected as disproportionation products.

**Keywords** ITO wastes · Phase transformation · Reduction volatilization

## Introduction

Indium is considered an important strategic resource which associated with other minerals and must be produced as a by-product of other metallurgical processes. In non-ferrous metal smelting, indium was enriched in the slag and ash of Pb–Zn ore; however, the grade was still only 0.1–1.5% [1]. It was difficult to recover from primary ores by mining, mineral processing and smelting process. With the depletion of indium resources and the increasing demand, the extraction of indium from secondary resources is becoming a research priority.

According to researches [2, 3], the production of recycled indium reached more than 1000t in 2021, accounting for 60% of the total indium output. Indium was mainly used in the production of ITO targets (the mixtures consisted with 80–95 wt% In<sub>2</sub>O<sub>3</sub> and 5–20 wt% SnO<sub>2</sub>). However, in the sintering and sputtering process

---

Z. Su · Y. Wang · B. Lei · Y. Zhang (✉)

School of Minerals Processing and Bioengineering, Central South University, Changsha 410083, China

e-mail: [sintering@csu.edu.cn](mailto:sintering@csu.edu.cn)

of ITO targets, the waste target rate was as high as 70% for nodules caused by the generation of  $\text{InO}_x$  and  $\text{SnO}_x$ . Comparing with primary ores, the recycling of ITO scrap targets was more advantageous because of the higher grade of indium (>70%) and the lower number of impurity elements.

The recycling of metal components in ITO waste targets has been widely studied, and the separation and recycling of indium and tin has become the focus. At present, the recovery of indium mainly included hydrometallurgy and pyrometallurgy. The indium and other metal components were leached by acid solution [4]; indium and tin were separated by replacement, extraction, alkali precipitation, and sulfide precipitation, furthermore purified by electrolytic refining [5–8]. However, it consumed a large amount of acid, alkali and extractant, generated waste gas and waste liquid, and even caused serious secondary pollution. The pyrometallurgy for processing ITO wasted targets mainly included vacuum metallurgy and chlorination roasting. The wasted ITO targets could be reduced to In-Sn alloy with CO or  $\text{H}_2$  at 1073 K. Since the saturation vapor pressure of indium and impurities varies greatly under vacuum conditions, the high volatile impurities such as Cd, Zn and Pb could be distilled out at 1223 K, 5 Pa for 2 h, the metallic indium was evaporated at 1323 K, and the low volatile impurities such as Fe, Cu, Ni, and Sn were left in the slag phase, but each ton of indium recovered required 14,000 kWh of electricity [9, 10]. Chlorination reactions were considered for indium separation due to the low boiling point of indium chloride (~673 K) [11]; however, it required a large number of additives and a subsequent purification procedure of metallic indium. In addition, the serious corrosion of equipment was also one of the main reasons limiting its application to industry.

Previous studies showed that  $\text{In}_2\text{O}_3$  could be easily reduced to  $\text{In}_2\text{O}$  and volatilized under the CO– $\text{CO}_2$  atmosphere at high temperature [12]. The indium component could be converted to  $\text{In}_2\text{O}$  and separated from the waste ITO targets, since the saturated vapor pressure of  $\text{In}_2\text{O}$  is much higher than that of metal In and  $\text{In}_2\text{O}_3$ .

In this study, the crushed wasted ITO target was used as the research object. Indium was recovered from the ITO scraps by CVT (chemical vapor transport) method, indium component was separated by gas phase  $\text{In}_2\text{O}$ , and the remaining metal impurities were enriched in the slag phase. In addition, the phase transformation ITO and separation behavior of gaseous intermediates were investigated and characterized using thermodynamic analysis XRD, SEM, ICP, etc. This work provided an efficient and clean pretreatment thought for high-value utilization of waste ITO targets.

## Experimental

### *Materials*

The raw material used in this study was wasted ITO targets obtained from the magnetron sputtering process. The XRD (Bruker D8 advance, Germany) analysis of

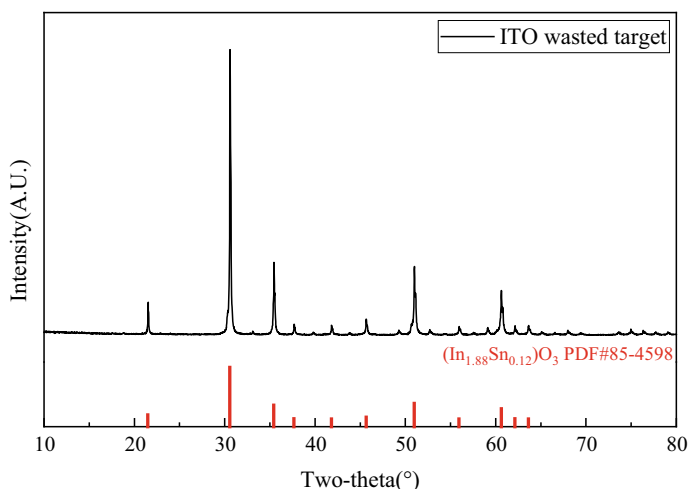


**Fig. 1** XRD pattern of waste ITO target

the wasted ITO target in Fig. 1 showed that the sample was of high purity and matched well with the  $(\text{In}_{1.88}\text{Sn}_{0.12})\text{O}_3$  standard card (PDF# 85-4598), and no diffraction peak of impurities was found.

In order to determine the main chemical components in the waste ITO target, X-ray fluoroscopy (XRF, Axios mAX, PANalytical Co., Ltd., in Holland) analysis was carried out, assaying (wt%) In 72.91, Sn 7.96, Ti 0.22, Al 0.19, Fe 0.07, Zr 0.04, W 0.03, Cu 0.02 as well as Ni 0.01. The results showed that the main components of the waste ITO target were indium and tin. In addition, the impurity elements Ti, Al, Fe, Zr, W, Cu, and Ni introduced with the sintering flux were also found. The contents of impurity elements were extremely low but still higher than the standard of 100 ppm.

## Methods

The experiments were carried out in a horizontal tube furnace. To investigate the effect of roasting parameters on the volatilization of wasted ITO target,  $1.000 \pm 0.005$  g of ground ITO samples weighed, and placed in corundum crucibles, then roasted in the furnace. After roasting for a period of time, the cooled samples were weighed and analyzed for residual indium content by ICP (Thermo fisher Corporation, U.S.). The volatilization can be calculated using the following equation:

$$\gamma = (\text{T}_{\text{In}} \times \text{m}_0 - \text{T}'_{\text{In}} \times \text{m}_1) / \text{T}_{\text{In}} \times \text{m}_0 \times 100\% \quad (1)$$



where  $m_0$  is the mass of ITO samples, g;  $m_1$  is the mass of the sample after roasting, g;  $\gamma$  is the volatilized fraction of indium, wt%;  $T_{In}$  is the total indium content of the wasted ITO target slag, wt%; and  $T'_{In}$  is the total indium content of the sample after roasting, wt%.

## Results and Discussion

### Thermodynamic Analysis

Based on previous studies [13], the reduction of indium and tin was similar, the reaction of  $In_2O_3 \rightarrow In_2O \rightarrow In$  proceed under CO–CO<sub>2</sub> atmosphere with a stepwise reduction. The possible reactions were then presented in the ITO–CO–CO<sub>2</sub> system, assuming that the reactions were carried out at a constant pressure of 1 atm ( $p\theta$ ), and the dominant phase diagrams of In<sub>2</sub>O and SnO were calculated and plotted in Table 1 based on our previous paper.

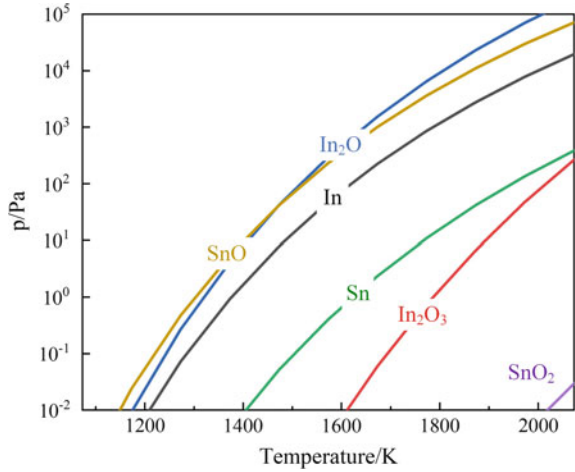
The saturated vapor pressure of main components in the waste ITO target was shown in Fig. 2, including In, Sn, and their oxides. At the same temperature, the saturated vapor pressures of In<sub>2</sub>O and SnO were higher than other phases, and it was easier to transform into the gas phase at 1173–1373 K.

Figure 3 showed that the reduction intervals of indium and tin were different under CO–CO<sub>2</sub> atmosphere, and the reduction temperature of indium was relatively lower, so it was possible to selectively reduce indium and tin to different phases by adjusting the CO content and temperature to achieve indium–tin separation. In region ②, when CO/(CO + CO<sub>2</sub>) exceeded 20%, In<sub>2</sub>O<sub>3</sub> was reduced to In<sub>2</sub>O(g) and volatilized, while SnO<sub>2</sub> was over-reduced to metallic tin. In region ①, when the CO content was too high, In<sub>2</sub>O<sub>3</sub> was easy to being reduced to metal indium, leading to

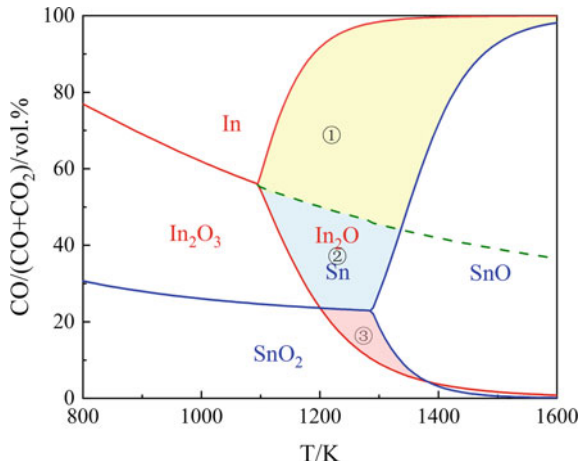
**Table 1** A  $\Delta G_T^\theta$ -T relationship of corresponding reactions SnOx, InOx during the reduction process

Equations	Reaction equations	$\Delta G_T^\theta$ -T (kJ/mol)
(2)	$In_2O_3 + 3CO(g) = 2In + 3CO_2(g)$	$\Delta G_T^\theta = -0.061 T + 73.60$
(3)	$In_2O_3 + 2CO(g) = In_2O(g) + 2CO_2(g)$	$\Delta G_T^\theta = -0.2031 T + 310.56$
(4)	$In_2O(g) + CO(g) = 2In + CO_2(g)$	$\Delta G_T^\theta = 0.142 T - 236.96$
(5)	$SnO_2 + 2CO(g) = Sn + 2CO_2(g)$	$\Delta G_T^\theta = -0.032 T + 15.56$
(6)	$SnO_2 + CO(g) = SnO + CO_2(g)$	$\Delta G_T^\theta = -0.018 T + 15.84$
(7)	$SnO(g) + CO(g) = Sn + CO_2(g)$	$\Delta G_T^\theta = 0.1451 T - 296.68$

**Fig. 2** Saturated vapor pressure diagram of indium tin and their oxides



**Fig. 3** Regional dominance of In, Sn, and their oxide phases under reducing atmospheres



the decrease of the volatilization rate. In region ③, the tin component in the waste ITO target still existed in the form of SnO<sub>2</sub>; however, the low CO content led to the decrease in the reduction reaction, resulting in a low volatilization rate.

***Effect of Parameters on the Volatilization of Indium***

Thermodynamic analysis showed that roasting atmosphere and roasting temperature were the most important factors affecting the separation of indium reduction. The effect of these parameters on the indium volatilization rate was further investigated by

fixing the roasting time to 2 h and the gas flow rate to 4 L/min at different temperatures and atmosphere compositions.

It can be concluded from Fig. 4 that the volatilization rate of indium increased and then decreased with the increase of CO content at a fixed roasting time of 2 h, temperature of 1100 °C, and gas flow rate of 4L/min. When the CO content in the system was high, the generated  $\text{In}_2\text{O}_{(\text{g})}$  would be over-reduced to metallic indium by the excessive CO. Although metallic indium still generated  $\text{In}_2\text{O}_{(\text{g})}$  with  $\text{In}_2\text{O}_3$ , the rapid rate of indium generation would lead to the generation of indium metal irreversible, resulting in lower volatility of indium (Fig. 5).

It was obvious that the volatilization rate of indium increased with the temperature and raised significantly after 1050 °C. Since the temperature reached the melting point of SnO, the generation of  $\text{In}_2\text{O}_{(\text{g})}$  was promoted ( $\text{SnO} + \text{In}_2\text{O}_3 \rightarrow \text{SnO}_2 + \text{In}_2\text{O}_{(\text{g})}$ ), resulting in the volatilization rate of indium increased rapidly. When the temperature was fixed at 1100°C, the volatilization rate of indium reached a maximum of 95.2%.

As shown in Fig. 6, the volatilization rate of indium varied linearly with time after 1 h. In the early stage of the reaction, the low pressure of  $\text{In}_2\text{O}_{(\text{g})}$  promoted the reaction  $\text{In}_2\text{O}_3 + \text{CO}_{(\text{g})} \rightarrow \text{In}_2\text{O}_{(\text{g})} + \text{CO}_{2(\text{g})}$  to occur at a faster reaction rate. With the extension of time, the amount of  $\text{In}_2\text{O}_{(\text{g})}$  generated was consistent with the amount of condensation.

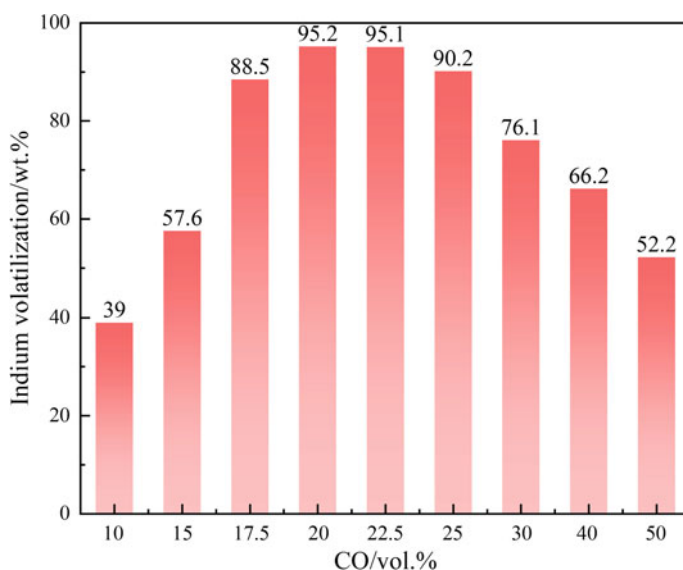
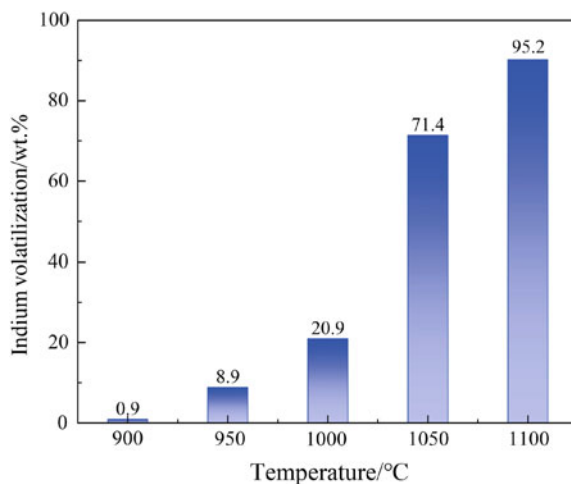
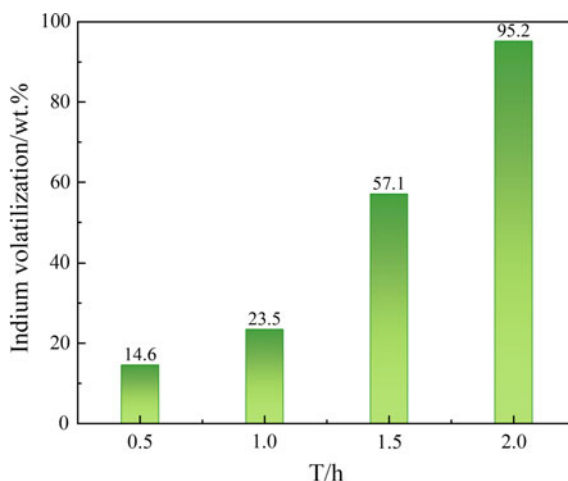


Fig. 4 Effect of CO content on indium volatilization

**Fig. 5** Effect of temperature on indium volatilization



**Fig. 6** Effect of roasting time on indium volatilization



### ***Analysis of Roasting Results and Products***

The XRD analysis of the roasted residual sample was shown in Fig. 7. Under the roasting condition of 1100 °C and 20% CO, the main phase of the residual sample was unreacted  $\text{In}_2\text{O}_3$ , while  $\text{SnO}_2$  was reduced to metallic tin, which was consistent with the results of thermodynamic calculations. With the increase of CO concentration to 40%, the ITO waste target was over-reduced into indium-tin alloy. The reason of poor separation efficiency is that the partial pressure of  $\text{In}_2\text{O}$  is too high to be regulated under the condition of high CO concentration.

As shown in Fig. 8, the samples collected under optimal conditions at 20 vol.% CO consisted of  $\text{In}_2\text{O}_3$  and In, which indicated that  $\text{In}_2\text{O}(\text{g})$  disproportionated during the

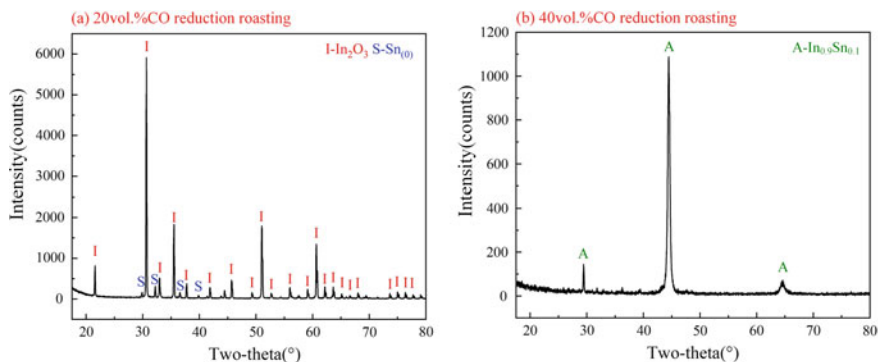


**Fig. 7** XRD patterns of roasting residues

condensation process. According to the research,  $\text{In}_2\text{O}(\text{g})$  is extremely unstable below  $850^\circ\text{C}$ , leading to  $\text{In}_2\text{O} \rightarrow \text{In}_2\text{O}_3 + \text{In}$ . More importantly, there was no diffraction peak of other impurity in the product, indicating that indium component had been separated, and the tin was enriched in the solid phase while the indium was evaporated as gaseous phase.

The SEM (MIRA3 TESCAN, Czech Republic) analysis results also showed the disproportionation reaction occurred during the condensation process. As shown in Fig. 9, the volatilized product was obviously composed of two phases, one was fibrous nanorods mainly composed of  $\text{In}_2\text{O}_3$  collected in the high temperature region, and the other was an octahedron mixture of  $\text{In}_2\text{O}_3$  and metallic In collected in the low

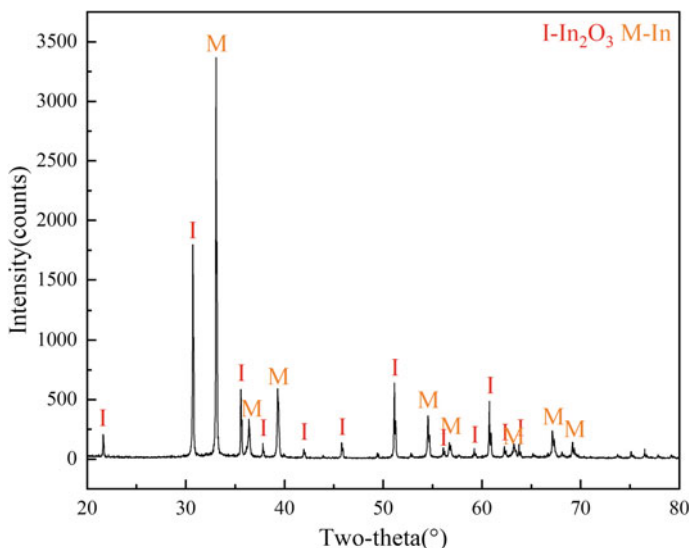


**Fig. 8** XRD patterns of volatiles

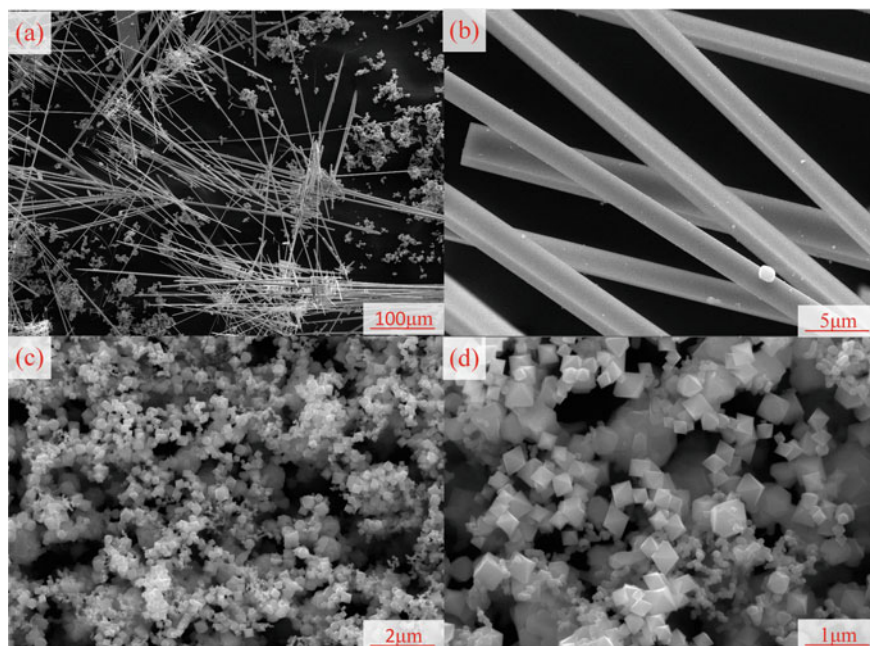


**Fig. 9** SEM analysis of volatile products

temperature region. The SEM results of volatile samples were corresponding to the XRD patterns.

## Conclusions

This study proposed a new strategy for the separation and recovery of indium from waste ITO target under CO–CO<sub>2</sub> atmosphere. According to the thermodynamic analysis results, indium can be selectively volatilized to achieve the separation of indium and tin by adjusting the CO content and temperature; indium can be separated and collected as disproportionation products. Under the selected parameters, the optimum oxidation volatilization rate of indium reached 95.2% for calcination temperature 1100 °C, CO/(CO + CO<sub>2</sub>) content 20%, roasting time 120 min.

**Acknowledgements** The research is financially supported by National Natural Science Foundation of China (No.51904353). The independent exploration and innovation project for graduate students at Central South University (2022ZZTS0544).

## References

1. Pradhan D, Panda S, Sukla L (2018) Recent advances in indium metallurgy: a review. *Min Proc Ext Met Rev* 39(3):167–180
2. USGS (2000–2021) Mineral commodity summaries. Available at. <https://www.usgs.gov/centers/nmic/indium-statistics-and-information>
3. Werner T, Mudd G, Jowitt S (2017) The world's by-product and critical metal resources part III: a global assessment of indium. *Ore Geol Rev* 86:939–956
4. Schuster J, Ebin B (2021) Investigation of indium and other valuable metals leaching from unground waste LCD screens by organic and inorganic acid leaching. *Sep Purif Technol* 279:119659
5. Li Y, Liu Z, Li Q, Liu Z, Zeng L (2011) Recovery of indium from used indium–tin oxide (ITO) targets. *Hydrometallurgy* 105(3–4):207–212
6. Choi D, Yun W, Son Y (2016) Recovery of ITO nano powder from a waste ITO target by a simple co-precipitation method. *RSC Adv* 6(84):80994–81000
7. Su X, Li S, Che Y, Song J, Yang B, He J (2022) Recovery and reuse of spent ITO targets through electrochemical techniques. *J Electrochem Soc* 169(2):023507
8. Fan Y, Liu Y, Niu L, Zhang W, Zhang T (2021) Efficient extraction and separation of indium from waste indium–tin oxide (ITO) targets by enhanced ammonium bisulfate leaching. *Sep Purif Technol* 269:118766
9. Itoh S, Maruyama K (2011) Recoveries of metallic indium and tin from ITO by means of pyrometallurgy. *High Temp Mat Pr-ISR* 30(4):317–322
10. Li D, Dai Y, Yang B, Liu D, Deng Y (2013) Purification of indium by vacuum distillation and its analysis. *J Cent South Univ* 20(2):337–341
11. Lv Y, Xing P, Ma B, Liu B, Wang C, Zhang Y, Zhang W (2019) Separation and recovery of valuable elements from spent CIGS materials. *ACS Sustain Chem Eng*. 7(24):19816–19823
12. Thiel A, Luckmann H (1928) Studien über das Indium. III. Abhandlung. *Z Anorg Alloy Chem* 172(1):353–371
13. Su Z, Zhang Y, Liu B, Zhou Y, Jiang T, Li G (2016) Reduction behavior of SnO<sub>2</sub> in the tin-bearing iron concentrates under CO–CO<sub>2</sub> atmosphere. Part I: effect of magnetite. *Powder Technol* 292:251–259

**Part V**  
**Poster Session**



# Evolution Mechanism of Vanadium-Containing Phases During Sodium Roasting of Vanadium Slag with High Chromium Content



Jie Cheng, Hong-Yi Li, Dong Hai, Xin-Mian Chen, Jiang Diao, and Bing Xie

**Abstract** In order to fundamentally improve the recovery rate of vanadium in the process of sodium roasting-water leaching of vanadium slag with high chromium content, it is very important to study the evolution mechanism of vanadium-containing phases. XRD was used to characterize the phase evolution of vanadium-containing phases with roasting time. At the beginning of roasting, the vanadium-containing phases basically were not changed,  $V^{3+}$  still formed  $FeV_2O_4$  with  $Fe^{2+}$  and  $O^{2-}$ . After 10 min,  $FeV_2O_4$  began to be oxidized,  $V^{3+}$  was oxidized to  $V^{4+}/V^{5+}$ . When the roasting time reached 15 min, the oxidized  $V^{5+}$  started to react with  $Na_2CO_3$  to form soluble vanadate sodium. After 50 min, the diffraction peaks of sodium vanadate increased sharply. After 90 min, almost all  $FeV_2O_4$  was converted to  $Na_3VO_4$ ,  $NaV_3O_8$ , and  $NaVO_3$ .

**Keywords** Vanadium slag with high chromium content · Sodium roasting · Evolution mechanism

## Introduction

Vanadium (V) is a high-value, strategic metal widely applied in national defence, chemical, and metallurgical engineering [1–7]. In China, the V–Ti magnetite ores are smelted in a blast furnace for steelmaking, wherein vanadium-containing slag is intentionally produced as a by-product [8–11]. The vanadium slag with high chromium content then becomes a direct raw material for vanadium extraction. At present, sodium roasting-water leaching is the most generally used technique to extract vanadium from the vanadium slag among many vanadium slag extraction techniques [12, 13]. The vanadium slag roasting with sodium salt is an oxidation

---

J. Cheng · H.-Y. Li (✉) · D. Hai · X.-M. Chen · J. Diao · B. Xie  
College of Materials Science and Engineering, Chongqing University, Chongqing 400044, China  
e-mail: [hongyi.li@cqu.edu.cn](mailto:hongyi.li@cqu.edu.cn)

H.-Y. Li · J. Diao  
National Engineering Research Center for Magnesium Alloys, Chongqing University,  
Chongqing 400044, China

process [14]. Vanadium embedded in the slag presents as  $V^{3+}$ , and with roasting,  $V^{3+}$  is oxidized to  $V^{4+}$  and  $V^{5+}$  and converted to sodium vanadate, which can be dissolved in a subsequent water leaching step [15–18]. However, the vanadium recovery by the sodium roasting-water leaching technique is not very high [19]. Based on the advocated resource conservation and sustainability, the vanadium recovery in the sodium roasting-water leaching process should be improved. The key to improve the vanadium recovery lies in the in-depth understanding of the transformation mechanism of vanadium-containing phases during the sodium roasting of vanadium slag. Only by deeply understanding the evolution path of vanadium-containing phases during the sodium roasting process of vanadium slag, a higher vanadium recovery can be obtained.

Currently, some works have been undertaken to study the roasting mechanism of the vanadium slag. Van et al. reported the oxidation kinetics of  $FeV_2O_4$  over the temperature range of 473–853 K and the oxidation behavior of  $FeV_2O_4$  by oxygen in the appearance of  $Na_2CO_3$  [20]. Li et al. revealed the detailed evolution mechanism of the vanadium-containing phases during sodium roasting of the vanadium slag [12]. Jiang et al. studied the phase evolution of the main components during the calcification roasting of the vanadium slag [21]. Zhang et al. investigated the mechanism of vanadate formation while roasting vanadium with calcium oxide [22]. However, the current research on the evolution mechanisms of vanadium extraction from vanadium slag only stays at the macro level and cannot fundamentally control the evolution of vanadium-containing phases during the roasting process.

In this work, we used X-ray diffraction (XRD) to explore the evolution paths of vanadium-containing phases with the change of roasting time from a microscopic perspective.

## Materials and Methods

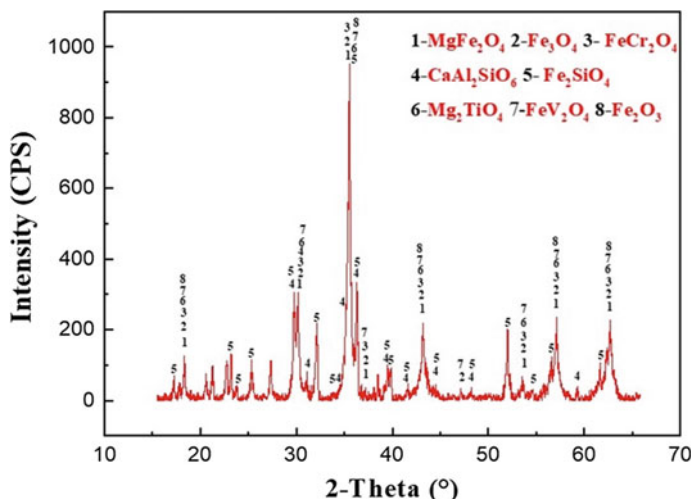
### *Materials and Characterizations*

The vanadium slag with high chromium content used in the experiment was synthesized according to the chemical and phase compositions of vanadium slag with high chromium content produced by Pan-Steel in China. All chemicals used in the study were of analytical grade (Chengdu Kelong Chemicals, China) and were dried at 393 K for 24 h before use to prepare the vanadium slag with a high chromium content in the desired shape for better characterization. The CaO powder was calcined at 1473 K before being used to eliminate  $CO_2$  molecules for purity assurance. The deionized water used in this study was produced by Millipore Aquelix 5, USA.

The chemical composition of the vanadium slag with high chromium content (Table 1) and roasted slags were determined using the X-ray fluorescence (XRF, Shimadzu XRF-1800, Japan) technique. The phase compositions of the vanadium slag with high chromium content (Fig. 1) and roasted slags were determined via

**Table 1** Chemical compositions of the vanadium slag with high chromium content, wt(%)

FeO	SiO <sub>2</sub>	TiO <sub>2</sub>	V <sub>2</sub> O <sub>3</sub>	Al <sub>2</sub> O <sub>3</sub>	MnO	Cr <sub>2</sub> O <sub>3</sub>	MgO	CaO
24.39	29.58	3.30	8.15	10.57	1.69	4.62	15.18	2.52

**Fig. 1** XRD pattern of the vanadium slag with high chromium content

powder XRD (Rigaku D/MAX 2500PC, Japan) analysis using Cu-K $\alpha$  radiation from 10° to 90°. In the vanadium slag with high chromium content, V<sup>3+</sup> ions were surrounded by Fe<sup>2+</sup> and O<sup>2-</sup> ions to form the FeV<sub>2</sub>O<sub>4</sub> phase. Likewise, the valuable metal elements Cr and Ti, in the form of Cr<sup>3+</sup> and Ti<sup>4+</sup>, were combined with Fe<sup>2+</sup>, Mg<sup>2+</sup>, and O<sup>2-</sup> ions to form the phases of (Fe, Mg)Cr<sub>2</sub>O<sub>4</sub> and Mg<sub>2</sub>TiO<sub>4</sub>. In addition, Si<sup>4+</sup> constituted the phase of Fe<sub>2</sub>SiO<sub>4</sub> with Fe<sup>2+</sup> and O<sup>2-</sup> ions and the phase of CaAl<sub>2</sub>SiO<sub>6</sub> with Ca<sup>2+</sup>, Al<sup>3+</sup>, and O<sup>2-</sup> ions.

### *Experimental Procedure*

150 g chemical mixture of FeC<sub>2</sub>O<sub>4</sub>·2H<sub>2</sub>O (67.07 g), SiO<sub>2</sub> (27.70 g), TiO<sub>2</sub> (3.65 g), V<sub>2</sub>O<sub>3</sub> (11.03 g), Al<sub>2</sub>O<sub>3</sub> (5.65 g), MnCO<sub>3</sub> (2.88 g), Cr<sub>2</sub>O<sub>3</sub> (11.02 g), MgO (17.29 g), and CaCO<sub>3</sub> (3.71 g) was charged in an Al<sub>2</sub>O<sub>3</sub> crucible (inner diameter: 53 mm, height: 140 mm). Then, it was placed inside a graphite crucible and melted in the furnace at 1773 K. After holding at this temperature for 30 min, the temperature was dropped to 1300 K at the rate of 10 K min<sup>-1</sup> and held at 1300 K for 1 h. In the next step, the synthetic vanadium slag with high chromium content was cooled to room temperature with the furnace.

After crushing treatment, the cooled vanadium slag with high chromium content sample was taken out of the crucible, and the sample was crushed and ground into powder (less than 74  $\mu\text{m}$ ).  $\text{Na}_2\text{CO}_3$  was mixed with vanadium slag with high chromium content at an  $n(\text{V})/n(\text{Na})$  ratio of 0.3 for roasting at 1073 K. The door of the muffle furnace was not completely closed to maintain a sufficient oxidizing atmosphere. It was stirred every 15 min during the roasting process to prevent the vanadium slag with high chromium content from sintering. After roasting for 2.5, 5, 10, 15, 30, 50, 70, and 90 min, the roasted slags were taken. The roasted slags were cooled by air to room temperature and ground into powders.

## Results and Discussion

### *Evolution Mechanism of Vanadium-Containing Phases During Roasting for 2.5–15 min*

In Fig. 2a, when the sodium roasting time was 2.5 min, the  $\text{FeV}_2\text{O}_4$  phase of vanadium atoms did not change. The phases of  $\text{Fe}_2\text{SiO}_4$  and  $\text{CaAl}_2\text{SiO}_6$  changed significantly. A small amount of  $\text{NaFeSi}_2\text{O}_6$  appeared, indicating that  $\text{Fe}_2\text{SiO}_4$  underwent oxidative decomposition, causing the oxidation of a small amount of  $\text{Fe}^{2+}$  to  $\text{Fe}^{3+}$ . Moreover, during the oxidative decomposition process, Si remained as  $\text{Si}^{4+}$ . In addition, the diffraction peak of  $\text{Na}_2\text{SiO}_3$  appeared. It is speculated that  $\text{Fe}_2\text{SiO}_4$  reacted with  $\text{Na}_2\text{CO}_3$ . The essence is that the bonds of  $\text{Si}^{4+}$ ,  $\text{Fe}^{2+}$ , and  $\text{O}^{2-}$  in  $\text{Fe}_2\text{SiO}_4$  were broken, and  $\text{Si}^{4+}$ ,  $\text{Na}^+$ , and  $\text{O}^{2-}$  could form  $\text{Na}_2\text{SiO}_3$ . Besides, the diffraction peak of  $\text{Na}_{1.74}\text{Mg}_{0.79}\text{Al}_{0.15}\text{Si}_{1.06}\text{O}_4$  also appeared, formed by the reaction of  $\text{CaAl}_2\text{SiO}_6$ ,  $\text{Fe}_2\text{SiO}_4$ , and  $\text{Na}_2\text{CO}_3$ .  $\text{Si}^{4+}$  reacted with  $\text{O}^{2-}$  to form  $\text{SiO}_4^{4-}$ , and together with the alkali metal ions  $\text{Na}^{2+}$ ,  $\text{Ca}^{2+}$ , and  $\text{Al}^{3+}$  generated  $\text{Na}_{1.74}\text{Mg}_{0.79}\text{Al}_{0.15}\text{Si}_{1.06}\text{O}_4$ .

As shown in Fig. 2b, when the sodium roasting time was extended to 5 min, compared with 2.5 min, the diffraction peak of  $\text{CaTiSiO}_5$  appeared, a crystal enriched with Ca and Ti atoms [23]. In the current artificial synthesis method of  $\text{CaTiSiO}_5$ ,  $\text{SiO}_2$  was required as one of the reactants. So, it can be concluded that the silicate phases, including  $\text{Fe}_2\text{SiO}_4$  and  $\text{CaAl}_2\text{SiO}_6$ , are decomposed and oxidized in the initial stage of sodium roasting of the vanadium slag with high chromium content.

In Fig. 2c, after roasting for 10 min, the diffraction peaks of  $\text{FeV}_2\text{O}_4$  changed slightly. A small amount of  $\text{FeVO}_4$  and  $\text{FeV}_3\text{O}_8$  appeared, indicating that  $\text{FeV}_2\text{O}_4$  began to participate in the oxidation reaction.  $\text{V}^{3+}$  was incompletely oxidized to form  $\text{V}^{4+}$  and  $\text{V}^{5+}$ , and in combination with  $\text{Fe}^{3+}$  and  $\text{O}^{2-}$ , formed  $\text{FeVO}_4$  and  $\text{FeV}_3\text{O}_8$ . In addition, a large number of titanium-containing phases such as  $\text{Fe}_{2.75}\text{Ti}_{0.25}\text{O}_4$ ,  $\text{FeTiO}_3$ , and  $\text{TiO}_2$  appeared, indicating that the phase of  $\text{Mg}_2\text{TiO}_4$  underwent effective oxidative and decomposition reactions. Moreover, the diffraction peaks of  $\text{Na}_4\text{SiO}_4$  appeared, indicating that  $\text{Fe}_2\text{SiO}_4$  and  $\text{CaAl}_2\text{SiO}_6$  have been significantly involved in the reaction.

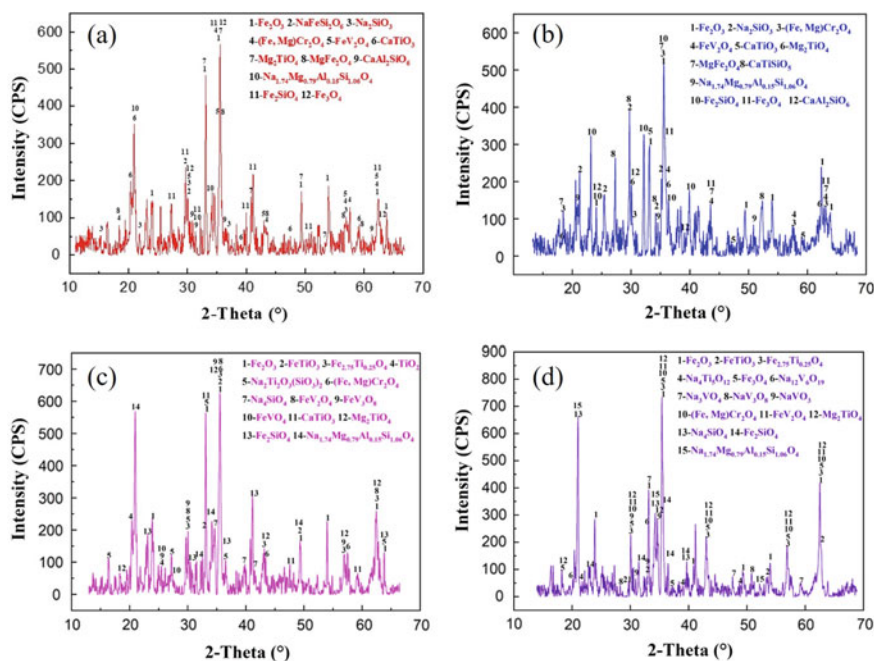


**Fig. 2** XRD analysis of the vanadium slag with high chromium content after roasting for different time. **a** Roasting for 2.5 min; **b** roasting for 5 min; **c** roasting for 10 min; **d** roasting for 15 min

In Fig. 2d, when the sodium roasting time increased to 15 min, the reaction degree of the spinel where vanadium atoms were located was further expanded: not only the outer layer of  $\text{Mg}_2\text{TiO}_4$  reacted but also the  $\text{FeV}_2\text{O}_4$  near the core participated in the reaction.  $\text{FeV}_2\text{O}_4$  was thermally oxidized, and some vanadium atoms were oxidized and decomposed into  $\text{V}^{5+}$ , and reacted with  $\text{O}^{2-}$  and  $\text{Na}^+$  to form many vanadium-containing phases, such as  $\text{Na}_3\text{VO}_4$ ,  $\text{NaV}_3\text{O}_8$ , and  $\text{NaVO}_3$ .

### ***Evolution Mechanism of Vanadium-Containing Phases During Roasting for 30–90 min***

The XRD pattern of the sample after sodium roasting for 30 min (Fig. 3a) shows that the diffraction peaks of  $\text{Na}_3\text{VO}_4$ ,  $\text{NaV}_3\text{O}_8$ , and  $\text{NaVO}_3$  were considerably enhanced. Moreover, the diffraction peak of a new sodium vanadate phase ( $\text{Na}_5\text{V}_3\text{O}_{10}$ ) appeared, formed by the condensation of vanadate sodium. In addition, the diffraction peak of  $\text{FeVO}_4$  also appeared, confirming that  $\text{FeV}_2\text{O}_4$  was first oxidized and then reacted with  $\text{Na}_2\text{CO}_3$ . That is,  $\text{V}^{3+}$  in  $\text{FeV}_2\text{O}_4$  was oxidized to  $\text{V}^{5+}$ ,  $\text{Fe}^{2+}$  was oxidized to  $\text{Fe}^{3+}$ , and then formed  $\text{FeVO}_4$  with  $\text{V}^{5+}$  and  $\text{O}^{2-}$ , and then reacted with  $\text{Na}_2\text{CO}_3$  to form sodium vanadate.

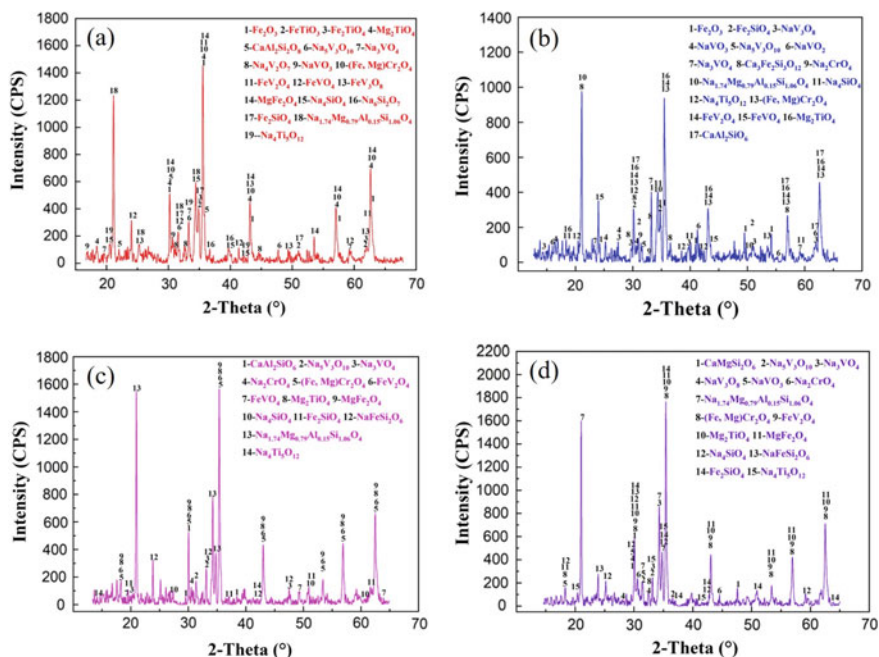


**Fig. 3** XRD analysis of the vanadium slag with high chromium content after roasting for different time. **a** Roasting for 30 min; **b** roasting for 50 min; **c** roasting for 70 min; **d** roasting for 90 min

In Fig. 3(b), after roasting for 50 min,  $\text{FeV}_2\text{O}_4$  wrapped in the outer layer of  $(\text{Fe, Mg})\text{Cr}_2\text{O}_4$  reacted to a certain extent. So,  $(\text{Fe, Mg})\text{Cr}_2\text{O}_4$  in the core of the spinel was exposed. In addition, the diffraction peaks of  $\text{Na}_2\text{CrO}_4$  appeared, indicating that  $(\text{Fe, Mg})\text{Cr}_2\text{O}_4$  started to react with  $\text{Na}_2\text{CO}_3$ , causing the oxidation of  $\text{Cr}^{3+}$  in  $(\text{Fe, Mg})\text{Cr}_2\text{O}_4$ , which lost electrons to become  $\text{Cr}^{6+}$  and reacted with  $\text{Na}^+$  and  $\text{O}^{2-}$  to form  $\text{Na}_2\text{CrO}_4$ . Besides, the diffraction peaks of sodium vanadate increased sharply, proving that  $\text{FeV}_2\text{O}_4$  was in the rapid stage of reaction with  $\text{Na}_2\text{CO}_3$ .

In Fig. 3c, when the sodium roasting time increased to 70 min, the XRD pattern tended to be flat and clear. Among them, the diffraction peaks of  $\text{Na}_3\text{VO}_4$  and  $\text{Na}_5\text{V}_3\text{O}_{10}$ , the oxidized intermediate product ( $\text{FeVO}_4$ ), and the  $\text{Na}_2\text{CrO}_4$  and  $(\text{Fe, Mg})\text{Cr}_2\text{O}_4$  can be clearly found.

As shown in Fig. 3d, when the sodium roasting time was extended to 90 min, the sodium vanadate mainly existed in the form of  $\text{Na}_3\text{VO}_4$ ,  $\text{Na}_5\text{V}_3\text{O}_{10}$ ,  $\text{NaV}_3\text{O}_8$ , and  $\text{NaVO}_3$ , and its diffraction peaks were clear, numerous, and high in intensity. This indicates that sodium vanadate could stably be formed in large quantities. Furthermore, there is no diffraction peak of  $\text{FeVO}_4$ , demonstrating that the reaction speed of  $\text{FeV}_2\text{O}_4$  was very slow, or even stagnant due to the lack of  $\text{Na}_2\text{CO}_3$ . Besides,  $\text{Fe}_2\text{SiO}_4$  did not react completely, and the final reaction products of the olivine phase were:  $\text{Na}_4\text{SiO}_4$ ,  $\text{NaFeSi}_2\text{O}_6$ ,  $\text{CaMgSi}_2\text{O}_6$ , and  $\text{Na}_{1.74}\text{Mg}_{0.79}\text{Al}_{0.15}\text{Si}_{1.06}\text{O}_4$ .

## Conclusion

In this work, the vanadium slag with high chromium content was taken as the research object, and it was aimed to extract vanadium from vanadium slag with a high chromium content in a more efficient and environmentally-friendly way. The change law of the vanadium-containing phases during the sodium roasting process of vanadium slag with high chromium content was deeply analyzed, which laid a theoretical foundation for regulating the evolution of vanadium-containing phases during the sodium roasting process and improving the recovery rate of vanadium. At the beginning of roasting, the phases of  $V^{3+}$  basically were not changed,  $V^{3+}$  still formed  $FeV_2O_4$  with  $Fe^{2+}$  and  $O^{2-}$ . The silicate phases reacted with  $Na_2CO_3$  and formed  $Na_{1.74}Mg_{0.79}Al_{0.15}Si_{1.06}O_4$  and  $Na_2SiO_3$ . After 10 min,  $FeV_2O_4$  began to be oxidized,  $V^{3+}$  was oxidized to  $V^{4+}/V^{5+}$ ,  $Fe^{2+}$  was oxidized to  $Fe^{3+}$ , and  $FeVO_4$  and  $FeV_3O_8$  were formed. When the roasting time reached 15 min, the oxidized  $V^{5+}$  started to react with  $Na_2CO_3$  to form soluble vanadate sodium, such as  $Na_3VO_4$ ,  $NaV_3O_8$ , and  $NaVO_3$ . When roasting time was 50 min,  $(Fe, Mg)Cr_2O_4$  began to be oxidized and underwent sodium reaction with  $Na^+$  and  $O^{2-}$  to form  $Na_2CrO_4$ . When the roasting time was extended to 90 min, almost all  $FeV_2O_4$  was changed to  $Na_3VO_4$ ,  $NaV_3O_8$ , and  $NaVO_3$ .

**Acknowledgements** This work was supported by the National Natural Science Foundation of China [grant No. 52074050].

## References

1. Amarande L, Miclea C, Cioangher M, Grecu MN, Pasuk I (2016) Effects of vanadium doping on sintering conditions and functional properties of Nb-Li co-doped PZT ceramics. Comments on Li location. *J Alloys Compd* 685:159–166
2. Gao F, Olayiwola AU, Liu B, Wang S, Du H, Li J, Wang X, Chen D, Zhang Y (2021) Review of vanadium production part I: primary resources. *Min Proc Ext Met Rev*
3. Lee JC, Kurniawan, Kim EY, Chung KW, Kim R, Jeon H-S (2021) A review on the metallurgical recycling of vanadium from slags: towards a sustainable vanadium production. *J Mater Res Technol* 12:343–364
4. Liang X, Gao G, Liu Y, Zhang T, Wu G (2017) Synthesis and characterization of Fe-doped vanadium oxide nanorods and their electrochemical performance. *J Alloys Compd* 715:374–383
5. Yuan R, Li S, Che Y, He J, Song J, Yang B (2021) A critical review on extraction and refining of vanadium metal. *Int J Refract Met H* 101
6. Liu M, Su B, Tang Y, Jiang X, Yu A (2017) Recent advances in nanostructured vanadium oxides and composites for energy conversion. *Adv Energy Mater* 7
7. Moskalyk RR, Alfantazi AM (2003) Processing of vanadium: a review. *Miner Eng* 16:793–805
8. Liu B, Du H, Wang S-N, Zhang Y, Zheng S-L, Li L-J, Chen D-H (2013) A novel method to extract vanadium and chromium from vanadium slag using molten NaOH-NaNO<sub>3</sub> binary system. *AIChE J* 59:541–552

9. Zhang X, Liu F, Xue X, Jiang T (2016) Effects of microwave and conventional blank roasting on oxidation behavior, microstructure and surface morphology of vanadium slag with high chromium content. *J Alloys Compd* 686:356–365
10. Chen D, Zhao H, Hu G, Qi T, Yu H, Zhang G, Wang L, Wang W (2015) An extraction process to recover vanadium from low-grade vanadium-bearing titanomagnetite. *J Hazard Mater* 294:35–40
11. Zheng H-Y, Sun Y, Lu J-W, Dong J-H, Zhang W-L, Shen F-M (2017) Vanadium extraction from vanadium-bearing titanomagnetite by selective chlorination using chloride wastes (FeCl<sub>3</sub>). *J Cent South Univ* 24:311–317
12. Li H-Y, Fang H-X, Wang K, Zhou W, Yang Z, Yan X-M, Ge W-S, Li Q-W, Xie B (2015) Asynchronous extraction of vanadium and chromium from vanadium slag by stepwise sodium roasting-water leaching. *Hydrometallurgy* 156:124–135
13. Li D-Q, Yang Y, Li H-Y, Xie B (2020) Study on vanadium phase evolution law in vanadium slag during the interface reaction process of sodium roasting. In: Symposium on rare metal extraction and processing held during the 149th TMS annual meeting and exhibition / magnesium technology symposium held during the 149th TMS annual meeting and exhibition, San Diego, CA, 2020, pp 253–264
14. Liu B, Meng L, Zheng S, Li M, Wang S (2018) A novel method to extract vanadium from high-grade vanadium slag: non-salt roasting and alkaline leaching. *Physicochem Probl Mi* 54:657–667
15. Chen L, Wang Z, Qin Z, Zhang G, Yue H, Liang B, Luo D (2021) Investigation of the selective oxidation roasting of vanadium-iron spinel. *Powder Technol* 387:434–443
16. Deng R, Xiao H, Xie Z, Liu Z, Yu Q, Chen G, Tao C (2020) A novel method for extracting vanadium by low temperature sodium roasting from converter vanadium slag. *Chin J Chem Eng* 28:2208–2213
17. Fan H, Duan H, He W, Chen D, Liu T, Long M, Xu P (2018) Sequential extraction of vanadium and chromium from chromium-bearing vanadium slag through two-stage soda roasting-water leaching. *Metall Res Technol* 115
18. Li C, Zhang H, Tao M, Wang X, Li H, Li Y, Tian Y (2021) Efficient separation of silicon and vanadium by sodium roasting-water leaching from vanadium slag and CaV<sub>2</sub>O<sub>6</sub> preparation. *Crystals* 11
19. Li H-Y, Wang K, Wang C, Lin M, Xie B (2019) Atomic atmosphere: a way to understand phase evolution during vanadium slag roasting at the atomic level. *Acta Crystallogr B* 75:927–932
20. Van Vuuren CPJ, Stander PP (2001) The oxidation of FeV<sub>2</sub>O<sub>4</sub> by oxygen in a sodium carbonate mixture. *Miner Eng* 14:803–808
21. Jiang T, Wen J, Zhou M, Xue X (2018) Phase evolutions, microstructure and reaction mechanism during calcification roasting of high chromium vanadium slag. *J Alloys Compd* 742:402–412
22. Zhang J, Zhang W, Zhang L, Gu S (2015) Mechanism of vanadium slag roasting with calcium oxide. *Int J Miner Process* 138:20–29
23. Pantic J, Kremenovic A, Dosen A, Prekajski M, Stankovic N, Bascarevic Z, Matovic B (2013) Influence of mechanical activation on sphene based ceramic material synthesis. *Ceram Int* 39:483–488



# Recovery of Vanadium from Vanadium Slag by Roasting with CaO-MgO Composite Additive



Mingshuai Luo, Junyi Xiang, Qingyun Huang, Shengquin Zhang, and Zenghao Liu

**Abstract** Calcification roasting-acid leaching is a clean vanadium extraction process, but the recovery rate of vanadium is low. Therefore, this study proposed the enhanced extraction process of vanadium slag by calcination with CaO and MgO. The effects of the roasting and leaching process on vanadium recovery and the change of impurity content in vanadium extraction tailings were studied. The results show that under the conditions of roasting temperature of 850°C, roasting time of 2 h, and pH of 2.5, the leaching efficiency of vanadium can reach 93.8% by roasting with the mixture of CaO and MgO. Compared with the calcification roasting-acid leaching process, the leaching efficiency of vanadium can be significantly increased, and the yield of vanadium extraction tailings and the contents of sulfur and calcium also can be reduced by the calcium-magnesium composite roasting process. Such a process shows great potential in improving vanadium recovery and cleaner production.

**Keywords** Vanadium slag · Calcium-magnesium composite roasting · Acid leaching · Leaching efficiency · Vanadium extraction tailings

## Introduction

As a strategic metal [1], vanadium can significantly improve the physical and chemical properties of steel and alloy, and is widely used in metallurgy, aerospace, chemical industry, and other fields. With the development of society, the environmental protection requirements for vanadium extraction from vanadium slag are becoming higher and higher. “High efficiency, clean, and high purity” is the research direction of vanadium extraction process from vanadium slag in the future. At present, vanadium extraction from vanadium slag mainly includes sodium roasting-water leaching process [2] and calcification roasting-acid leaching process [3, 4]. The most widely used process is sodium roasting-water leaching process, which has high vanadium yield but some environmental pollution problems. The calcification roasting-acid

---

M. Luo · J. Xiang (✉) · Q. Huang · S. Zhang · Z. Liu  
Chongqing University of Science & Technology, Chongqing, China  
e-mail: [Xiangjunyi126@126.com](mailto:Xiangjunyi126@126.com)

leaching process is relatively clean [3, 5], but the vanadium yield is slightly lower than that of the sodium roasting process.

Roasting and leaching are the two most important stages in the process of vanadium extraction from vanadium slag. The task of roasting stage is to convert the vanadium spinel in vanadium slag into soluble vanadate by high temperature reconstruction [6], while the task of leaching stage is to dissolve soluble vanadate into solution [7]. However, for the calcification vanadium extraction process, part of vanadium spinel failed to form soluble vanadate during the roasting process, resulting in insufficient vanadium conversion and affecting the subsequent leaching process [8]. In addition, the calcium sulfate precipitate generated by the reaction of calcium vanadate and sulfuric acid in the leaching process can wrap the solid samples, which increases the ion diffusion resistance in the leaching process, thus reducing the vanadium leaching rate [9]. Therefore, improving the conversion rate of soluble vanadate in the roasting process and the leaching rate of vanadate in the leaching process are the key to improve the vanadium recovery [10–12].

In our previous study, it's found that the leaching efficiency of vanadium can be significantly improved by roasting with the mixture of CaO and MgO [13–15]. In this study, the feasibility of calcium and magnesium composite roasting process was analyzed, and the influence of roasting leaching process on the recovery of vanadium and the change of impurity content in the tailings of vanadium extraction were studied.

## Experimental

The sample of vanadium slag used in this study is produced by Panzhihua Iron and Steel Co., LTD. The chemical composition is shown in Table 1. The content of SiO<sub>2</sub> is 14.51%, CaO is 2.58%, V<sub>2</sub>O<sub>5</sub> is 15.29%, and the mass ratio of CaO/V<sub>2</sub>O<sub>5</sub> is 0.168. The additives used in roasting process were analytically pure CaO and MgO, with a purity greater than 99.9%. The water used in the leaching experiment was deionized water, and the concentration of sulfuric acid was 98%.

The XRD pattern of vanadium slag in Fig. 1 shows that in the vanadium slag, Fe<sub>2</sub>TiO<sub>4</sub>, (Mn, Fe)(V, Cr)<sub>2</sub>O<sub>4</sub>, and Fe<sub>2</sub>SiO<sub>4</sub> are the main phases, and Mn<sub>2</sub>V<sub>2</sub>O<sub>7</sub> and Ca<sub>10</sub>V<sub>6</sub>O<sub>25</sub> are the trace phases. SEM images of the vanadium slag in Fig. 1 show that the vanadium slag is mostly irregular bulk particles with loose structure and uneven particle size, most of which are small particles, and a few are large particles with a diameter of about 80 μm.

**Table 1** Chemical analysis of the slag (wt%)

Mg	Al	Si	P	S	Ca	Ti	V	Cr	Mn	Fe	O
1.76	1.84	6.77	0.06	0.09	1.84	8.63	8.57	0.98	5.67	31.00	32.80

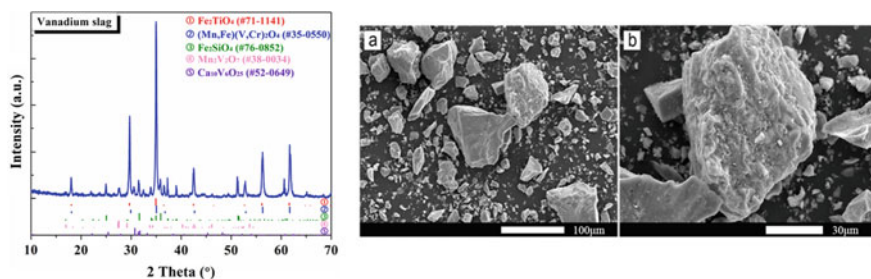


**Fig. 1** XRD patterns and SEM images of vanadium slag sample

The vanadium slag sample was mixed with CaO and MgO powder in a certain proportion, and the mixed vanadium slag sample was obtained by fully mixing in a planetary ball mill. Then, the mixed sample was roasted at 850°C in a muffle furnace for 2 h in a corundum crucible and then removed from the furnace and cooled to room temperature. Finally, the vanadium slag clinker was ball-milling and sieved to 100% particle size less than 75 μm for leaching.

The leaching experiment was carried out in a three-necked flask. The solution was heated to 50 °C before adding vanadium slag clinker. The solid–liquid ratio was maintained at 1:20 (g/mL). The pH of the leaching solution was maintained at 2.5 by continuously adding dilute sulfuric acid. After 60 min of leaching, the slurry was rapidly filtered, and the concentration of vanadium in the filtrate was analyzed by ICP-OES to calculate the leaching rate of vanadium.

## Results and Discussion

Figure 2 shows the XRD patterns of the calcification roasted vanadium slag and calcium-magnesium composite roasted vanadium slag. As shown in Fig. 2, the main phases of the roasted clinker of the two processes are Fe<sub>2</sub>O<sub>3</sub>, Fe<sub>2</sub>TiO<sub>5</sub>, and Mn<sub>2</sub>V<sub>2</sub>O<sub>7</sub>. Compared with calcification roasting, the main phases of vanadate in calcium-magnesium composite roasting clinker i changes from single Ca<sub>2</sub>V<sub>2</sub>O<sub>7</sub> to a mixture of Ca<sub>2</sub>V<sub>2</sub>O<sub>7</sub> and Ca<sub>5</sub>Mg<sub>4</sub>V<sub>6</sub>O<sub>24</sub>.

The effects of calcification roasting and calcium-magnesium composite roasting on the leaching rate of vanadium and other impurities in vanadium slag are presented in Table 2.

Compared with calcification roasting, the leaching rates of Cr and P were significantly reduced by calcium-magnesium composite roasting. Furthermore, the leaching rate of V increased from 87.32 to 92.43%, the leaching rate of Mn increased from 34.77 to 41.09%, the leaching rate of Cr decreased from 1.55 to 1.12%, and the leaching rate of P decreased from 23.79 to 17.59%. However, the composite ratio of calcium and magnesium has little effect on the leaching of iron.

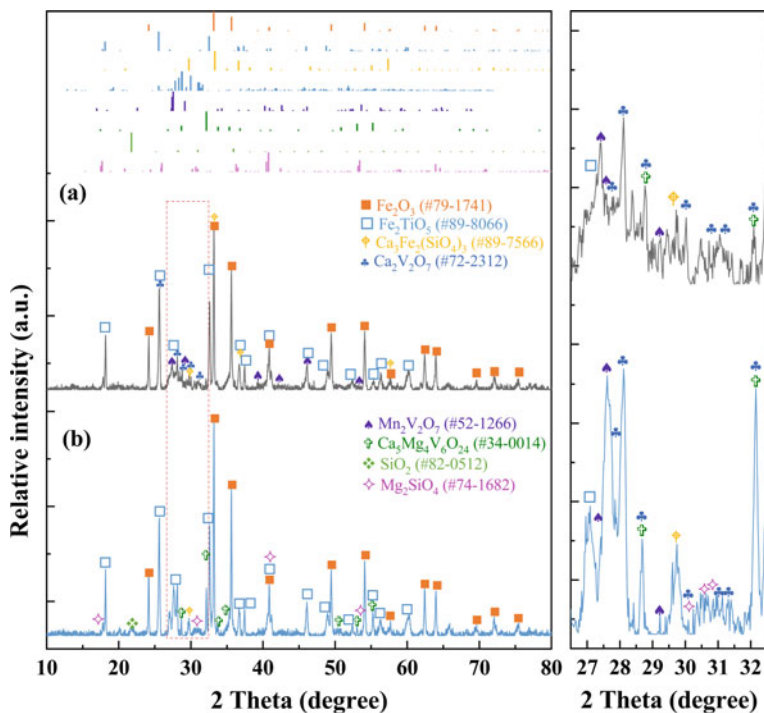


**Fig. 2** XRD patterns of vanadium slag clinker; **a** calcification roasting; **b** calcium-magnesium composite roasting

**Table 2** Comparison of element leaching efficiency between calcification roasting and calcium and magnesium composite roasting (wt%)

Composition (wt%)	V	Cr	P	Mn	Fe	Ca	S
Calcification roasting	87.35	1.55	23.79	34.77	0.2	8.12	3.64
CaO-MgO roasting	93.8	1.13	17.59	41.09	0.24	3.83	1.57

The chemical composition of the vanadium extraction tailings is shown in Table 3. Compared with the calcification roasting process, the content of vanadium in the leached slag decreased significantly after partial replacement of CaO by MgO, the content of sulfur significantly decreased from 5.53 to 2.02%, and the content of Ca directly decreased from 5.83 to 2.74%. However, the content of Mg significantly increased from 0.90 to 2.25% in the leached slag. Furthermore, the yield of the vanadium extraction tailings can be decreased from 92.5 to 89.6% by the calcium-magnesium composite roasting process due to the reduction of calcium sulfate production. Such kind of vanadium extraction tailings can be returned to the sintering process of iron making, so that the harmless treatment of vanadium extraction tailings can be realized.

**Table 3** Chemical composition of the leached residue (wt%)

Process	Mg	Al	Si	P	S	Ca	Ti	V	Cr	Mn	Fe	O	Yield of slag
Calcification roasting	0.90	1.22	4.56	0.03	5.53	5.83	9.11	1.76	1.11	3.36	27.67	38.91	92.5
CaO-MgO roasting	2.25	1.77	6.66	0.06	2.02	2.74	10.18	0.52	1.18	3.28	31.58	37.76	89.6

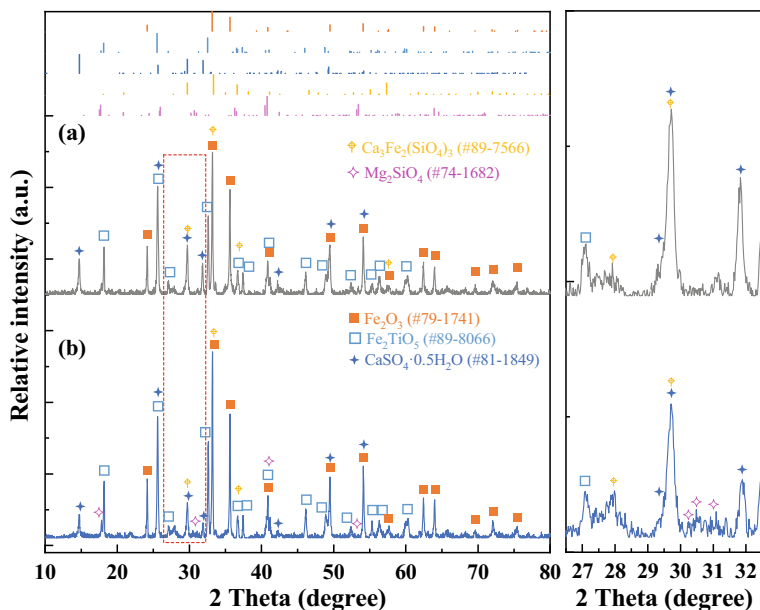


**Fig. 3** XRD patterns of the vanadium extraction tailings by different processes. **a** Calcification roasting; **b** calcium-magnesium composite roasting

The XRD patterns of the extraction tailings of calcification roasting and calcium-magnesium composite roasting clinker are shown in Fig. 3. The main phases of the vanadium extraction tailings are still  $\text{Fe}_2\text{O}_3$  and  $\text{Fe}_2\text{TiO}_5$ . After leaching, the diffraction peaks of  $\text{Ca}_2\text{V}_2\text{O}_7$ ,  $\text{Mg}_2\text{V}_2\text{O}_7$ , and  $\text{Mn}_2\text{V}_2\text{O}_7$  are disappeared as the dissolution of vanadates. The intensity of the diffraction peaks of  $\text{CaSO}_4 \cdot 0.5\text{H}_2\text{O}$  in the leaching residue of calcification roasted vanadium slag, while the intensity of  $\text{CaSO}_4 \cdot 0.5\text{H}_2\text{O}$  diffraction peaks in the leaching residue of calcium-magnesium composite roasted vanadium slag. This further indicates that the concentration of calcium sulfate in the leached slurry can be greatly reduced by calcium-magnesium composite roasting process.

## Conclusions

The following conclusions can be drawn from the present investigation:

- (1) Compared with the calcification roasting process, the content of vanadium in the vanadium extraction tailings can be reduced from 2.25 to 0.52% by calcium-magnesium composite roasting, which realized the efficient leaching of vanadium.

- (2) The calcium-magnesium composite roasting process also significantly reduced the dissolution efficiency of impurities, that is conducive to subsequent vanadium precipitation process.
- (3) Compared with the traditional calcification process, the contents of S and Ca in vanadium extraction tailings are reduced by nearly 50%, and the yield of tailings is reduced by 3%. Such kind of vanadium extraction tailings can be returned to the sintering process of iron making, so that the harmless treatment of vanadium extraction tailings can be realized.

**Acknowledgements** This work was supported by the National Natural Science Foundation of China (No. 52004044), the Natural Science Foundation of Chongqing (cstc2019jcyj-msxmX4117), the Natural Science Foundation of Chongqing (CSTB2022NSCQ-MSX0801), and the Foundation of Chongqing University of Science and Technology (ckrc2022030).

## References

1. Chen DH, Jiu-Jiang LI, Zhao BB, Wang N (2018) The green value outlined of strategic resources on vanadium. *World Nonferrous Metals* (20):1–3
2. Meng Q, Zhang J (2017) Experimental research of sodium salt roasting-vanadium extraction by leaching for a certain kind of vanadium titanomagnetite concentrate from Chaoyang City. *Min Eng* 03(15):34–36
3. Zhang J, Zhang W, Zhang L, Gu S (2015) Mechanism of vanadium slag roasting with calcium oxide. *Int J Miner Process* 138:20–29
4. Wang S, Dutrizac JE, Free ML, Hwang JY, Kim D (2012) Vanadium extraction from high calcium-content vanadium slag by calcification roasting. John Wiley & Sons, Inc., pp 621–627
5. Gao J, Liu XB, Shi ZX (2019) Characteristics of phase transformation and vanadium migration in sodium oxidation roasting of vanadium slag. *Min Metall* 03(28):105–110
6. Chen L, Wang Z, Qin Z, Zhang G, Yue H, Liang B, Luo D (2021) Investigation of the selective oxidation roasting of vanadium iron spinel. *Powder Technol* 387:434–443
7. Yang Z, Li H, Yin X, Yan Z, Yan X, Xie B (2014) Leaching kinetics of calcification roasted vanadium slag with high CaO content by sulfuric acid. *Int J Miner Process* 133:105–111
8. Fu NX, Zhang L, Liu WH, Zhao B, Sui ZT (2018) Mechanism analysis of phase transformation process in calcified roasting of vanadium slags. *Zhongguo Youse Jinshu Xuebao/Chin J Nonferrous Metals* 28(2):377–386
9. Zhang JH, Zhang W, Zhang L, Song-Qing G (2014) Effect of acid leaching on the vanadium leaching rate in process of vanadium extraction using calcium roasting. *J Northeast Univ (Nat Sci)* 11(35):1574–1578
10. Zhang, Xie, Diao, Li (2012) Nucleation and growth kinetics of spinel crystals in vanadium slag. *Ironmaking Steelmaking*, 39(2):147–154
11. Meng LP, Wang SN, Hao DU, Zheng SL (2016) Process mechanism of vanadium-containing slag roasting and alkali leaching. *Chin J Process Eng* 03(16):445–451
12. Shi ZX, Liu JY (2016) Vanadium phase structure and its evolution rule in vanadium extraction by process of calcification roasting-acid leaching. *Min Metall Eng* 06(36):97–99
13. Xiang JY, Wang X, Pei GS, Huang QY, Xue-Wei L (2020) Recovery of vanadium from vanadium slag by composite roasting with CaO/MgO and leaching. *Trans Nonferrous Metals Soc China* 30(11):3114–3123
14. Xiang J, Wang X, Pei G, Huang Q, Lü X (2021) Solid-state reaction of a CaO-V<sub>2</sub>O<sub>5</sub> mixture: a fundamental study for the vanadium extraction process. *Int J Miner Metall Mater* 28(09):1462–1468

15. Xin W, Junyi X, Guishang P, Lanjie L, Qingyun H, Xuewei L (2021) Application of response surface methodology for roasting optimization in composite roasting—Acid leaching vanadium extraction process. *Chem Eng Res Des* 172:254–263(prepublish)



# The Behaviour of Minor Metals in BOF Slag Under Different Additives



G. Haslinger, M. Leuchtenmüller, and S. Steinlechner

**Abstract** In the basic oxygen furnace (BOF) steelmaking process, large quantities of slag are generated, which are sometimes used as by-products. However, in many cases, BOF slag is landfilled and thus seen as waste. Typically contained elements are chromium, manganese, and phosphorus aside from the main slag formers, such as oxides of iron, calcium, and silicon. Following sustainability goals, a major target is the recovery of these elements by modifying the phase formation during cooling to generate artificial minerals which are separable in a subsequent beneficiation step. The paper describes investigations on the formation of mineral phases depending on the additives  $\text{Al}_2\text{O}_3$  and  $\text{TiO}_2$  during slag cooling. The results are compared with the thermodynamic calculation program FactSage. In addition, the enrichment of valuable metals in mineral phases was evaluated with EDX mappings of the scanning electron microscope.

**Keywords** BOF slag · Artificial minerals · Slag modification · Thermodynamic calculations

## Introduction

Pig iron from the blast furnace is treated in the basic oxygen furnace converter (BOF) to produce steel in the primary steelmaking route. Here, 99% pure oxygen is blown onto the hot metal at supersonic speed with a lance. This oxygen reacts with the dissolved carbon to carbon monoxide and carbon dioxide. Other undesirable elements, such as Si, Mn, and P, are oxidized. Besides pig iron, input materials like scrap for cooling and dolomite or lime as slag formers are added [1]. The critical role of the scrap is to cool the system and prevent it from overheating. It is also used as a secondary iron source. With the scrap, impurities like Cu, Ni, As, Pb, Sn, Sb, Mo, and Cr are added to the system [2, 3]. The input charge of the BOF consists of 10–20% steel scrap and 80–90% molten iron [3–5]. The CaO in the lime and dolomite forms

---

G. Haslinger (✉) · M. Leuchtenmüller · S. Steinlechner  
Christian Doppler Laboratory for Selective Recovery for Minor Metals Using Innovative Process Concepts, Montanuniversität Leoben, Franz-Josef-St. 18, 8700 Leoben, Austria  
e-mail: [gerald.haslinger@unileoben.ac.at](mailto:gerald.haslinger@unileoben.ac.at)

the slag together with the oxides  $\text{SiO}_2$ ,  $\text{P}_2\text{O}_5$ ,  $\text{MnO}$ , and  $\text{FeO}$  produced during the process [6]. The tapping is the process's end, where the crude steel is charged through the tapping hole into a steel ladle and then the slag is charged into a slag ladle via the charging opening [7, 8]. This process produces 100–200 kg of slag per tonne of crude steel [9]. With global steel production of 1.380 billion tonnes via the BOF route in 2021, an enormous quantity of BOF steel slag is generated [10]. The major chemical constituents of BOF slag are  $\text{CaO}$  45–60%,  $\text{SiO}_2$  10–15%,  $\text{Fe}_2\text{O}_3$  3–9%,  $\text{MgO}$  3–13%, and  $\text{FeO}$  7–20%. These four compounds form more than 80% of the chemical composition [11, 12]. Minor amounts of  $\text{Al}_2\text{O}_3$  1–5%,  $\text{P}_2\text{O}_5$ ,  $\text{Cr}_2\text{O}_3$ ,  $\text{MnO}$ , and  $\text{TiO}_2$  are also present, originating from the scrap [13–17]. Depending on the steel grade made and the raw materials used, these oxides occur in different concentrations [18]. X-ray diffraction (XRD) analyses reveal the mineralogical composition of BOF slag, whereby the broad spectrum shows the complexity [19, 20]. Predominant mineral phases C2S, C3S, wustite ( $\text{FeO}$ ), and free lime are also revealed. Furthermore, a  $\text{MgO-FeO-MnO}$  phase (RO phase) is present [21]. Table 1 gives an overview of the mineralogical phases in BOF slag.

The mineralogical phases dicalcium silicate (C2S), tricalcium silicate C3S, tetra-calcium aluminoferrite (C4AF), and beta-dicalcium silicate (b-C2S) enable cementitious properties to BOF slag [11, 32, 33]. These mineral phases are essential components of hydraulic binders such as cement [28, 34, 35]. The C2S and C3S phases are generally the major active parts of steel slags. However, the proportion in BOF slags is much lower than in cement, making their hydration rate lower [11]. In conventional cement, the C3S phase is the most active, but it is less present in the slag. During the slow cooling of the slag, most of the C3S decomposes, which also reduces the C3S content in the metastable state. Synchronously, during cooling and crystallization, the more active b-C2S transforms into the less active c-C2S. This fact leads to BOF slag being less hydraulically active than cement. The presence of tricalcium aluminate (C3A) also increases the hydraulic activity of the slag [22]. The wustite ( $\text{FeO}$ ) phases do not react with water, so it behaves inertly. If high iron content is present, the hydraulic properties of the slag are reduced [25]. However,  $\text{MgO}$  forms a wustite type solid solution ( $\text{Mg, Fe, Mn}$ )O called the RO phase during cooling [25, 36]. The free  $\text{CaO}$  content in BOF slags can range from 1–10 wt%; the free  $\text{MgO}$  is less than 2 wt% [25, 37]. The free  $\text{MgO}$  and  $\text{CaO}$  hydrate with water to  $\text{Ca}(\text{OH})_2$  and  $\text{Mg}(\text{OH})_2$ , leading to a volume expansion of 91.7% for  $\text{CaO}$  and 119.6% for  $\text{MgO}$ . These reactions are topochemical; the hydroxides expand outwards, causing stresses and micro-cracks in the slag pieces, which leads to a loss of strength [38].

Adding  $\text{Al}_2\text{O}_3$ -containing materials allows  $\text{CaO}$  and  $\text{FeO}$  to be built into calcium aluminoferrite, such as C4AF and C6AF2 [39]. Therefore, it is possible to transform a harmful mineral phase into a strength-giving compound by oxidation and modification of the slag [39, 40]. Also,  $\text{Al}_2\text{O}_3$  builds a spinel phase with  $\text{FeO}$  and  $\text{MgO}$  [41]. During slow cooling from 1400–1000 °C,  $\text{Fe}_2\text{O}_3$  forms together with  $\text{FeO}$  resp.  $\text{MgO}$  magnetite  $\text{Fe}_3\text{O}_4$  and magnesioferrite  $\text{MgFe}_2\text{O}_4$  [41]. Since Cr is present in the slag in minimal quantities, it is suitable to crystallize it together with Fe and Mg in spinels [13, 14, 16, 17]. In stainless steel slag, the entire  $\text{Cr}_2\text{O}_3$  crystallizes together with  $\text{Al}_2\text{O}_3$ ,  $\text{FeO}$ , and  $\text{MgO}$  in a spinel structure [42, 43]. On the one hand,

**Table 1** Mineralogical phases in BOF slag [21]

Mineral name/trivial name	Chemical	CCN	References
Akermanite	$\text{Ca}_2\text{MgSi}_2\text{O}_7$	C2MS	[22]
Alite	$\text{Ca}_3\text{SiO}_5$	C3S	[6, 15, 18, 22–28]
Brownmillerite	$\text{Ca}_2\text{Fe}_2\text{O}_5$	C2F	[23, 24]
Calcite	$\text{CaCO}_3$	Cc	[15, 23, 25, 29]
Calcium ferrite	$\text{CaFe}_2\text{O}_4$	CF	[26, 27]
Dicalcium aluminoferrite	$2\text{CaO}(\text{Al, Fe})_2\text{O}_3$	C2AF	[29]
Dicalcium aluminosilicate	$\text{Ca}_2\text{Al}_2\text{SiO}_3\text{O}_{12}$	C2AS	[28]
Dicalcium ferrite	$\text{Ca}_2\text{Fe}_2\text{O}_5$	C2F	[6, 15, 18, 22, 24, 25, 27, 30]
a, b, c -Dicalcium silicate	a, b, c- $\text{Ca}_2\text{SiO}_4$	a, b, c-C2S	[6, 18, 22, 23, 25, 26, 28]
Dicalcium silicate-calcium phosphate	$\text{Ca}_2\text{SiO}_4\text{--Ca}_3(\text{PO}_4)_2$	C2S*C3P	[27]
Dolomite	$\text{Ca, Mg}(\text{CO}_3)_2$	C, Mc	[24, 30]
Hematite	$\text{Fe}_2\text{O}_3$	F	[6, 18, 23]
Lime	$\text{CaO}$	C	[18, 22–25, 27, 28, 30]
Manganocalcicite	$(\text{Ca, Mn})\text{CO}_3$	Cc	[24, 30]
Magnesium iron oxide	$\text{Mg}_{0.239}\text{Fe}_{0.761}\text{O}$		[23]
Magnetite	$\text{Fe}_3\text{O}_4$		[25, 27, 28]
Merwinite	$\text{Ca}_3\text{Mg}(\text{SiO}_4)_2$	C3MS2	[24, 30]
Periclase	$\text{MgO}$	M	[25, 28, 31]
Portlandite	$\text{Ca}(\text{OH})_2$		[15, 18, 22–24, 30]
Quartz	$\text{SiO}_2$	S	[25]
RO phase	$\text{MgO-FeO-MnO}$ solid solution		[15, 26–28, 31]
Tetra-calcium Aluminoferrite	$\text{Ca}_4\text{Al}_2\text{Fe}_2\text{O}_{10}$	C4AF	[22]
Wustite	$\text{FeO}$		[23, 25, 27]

enrichment of Cr and Fe should take place with the spinel formation. On the other hand, the magnetic properties of spinels should be made possible by separating them from the C2S, C4AF, and the other CaO-heavy phase [41, 44–46]. In the following, thermodynamic calculations were made to investigate the influence of  $\text{Al}_2\text{O}_3$  and  $\text{TiO}_2$  as additives on BOF slag. Furthermore, the results were tested in a cooling test.

**Table 2** Chemical analysis of the BOF slag [wt-%]

	Al <sub>2</sub> O <sub>3</sub>	CaO	Cr <sub>2</sub> O <sub>3</sub>	MgO	MnO	SiO <sub>2</sub>	P <sub>2</sub> O <sub>5</sub>	TiO <sub>2</sub>	FeO	Fe <sub>2</sub> O <sub>3</sub>	Fe <sub>met</sub>
BOF slag	1.3	36.4	0.32	8.4	7.4	13.5	1.01	0.37	18.77	10.14	0.39

## Material

The investigated slag was obtained from the industry. Table 2 shows the composition of the slag.

The utilised titanium TiO<sub>2</sub> is from ALDRICH with a purity of 99.9%; the aluminium oxide Al<sub>2</sub>O<sub>3</sub> is from ROTH with a purity of 99%.

## Experimental Setup

The first step was to crush and grind the BOF slag. This powder was mixed with the additives and heated to 1450 °C, where it was maintained for 1 h. These mixtures increase the Al<sub>2</sub>O<sub>3</sub> or the TiO<sub>2</sub> content to 15 wt%. Subsequently the mixture was cooled down to 1100 °C with a cooling rate of 0.5 K/min, favouring the formation of crystals [31]. The experiment took place in a nitrogen atmosphere and a corundum crucible.

## Thermodynamic Calculation

The thermodynamic calculations were carried out with FactSage 8.2 in the Equilib function. FToxid was used as the database [47]. The calculation shows the most stable phases of the slag composition and the Cr distribution in the range of 800–1500 °C. The results of the calculation were visualized with a Python code to be able to compare the individual calculations more quickly. Figure 1a shows the stable phases with no treatment of the slag. The slag starts to be solidified at 1550 °C, with MeO\_A#1 as the first phase (RO-phase). C2SP and aC2SA solidified in the second phase, whereby the C2SP phase transforms into Ca<sub>7</sub>P<sub>2</sub>SiO<sub>16</sub> and bC2SA at 1050 °C. bC2SA transforms into bredigite (Ca<sub>7</sub>Mg(SiO<sub>4</sub>)<sub>4</sub>) at 1025 °C. The last solidification of the slag is at 1150 °C, with the phases C2AF and the last RO phase. At 800 °C, most slag consists of the three main phases, RO, bredigite, and C2AF. Also, Ca<sub>4</sub>P<sub>2</sub>O<sub>9</sub> is present. MeO\_A#1 and MeO\_A#2 are also part of the RO phase, consisting mainly of FeO, in which MgO, MnO, Cr<sub>2</sub>O<sub>3</sub>, Fe<sub>2</sub>O<sub>3</sub>, and smaller amounts of CaO are dissolved. The bredigite phase transforms into C2S above 500 °C. Figure 1b shows the distribution of Cr in the slag system. At 1500 °C, most of the Cr is dissolved in the liquid slag. At 1100 °C, the entire Cr is in the RO phase. Figure 2a

is the slag for which the  $TiO_2$  content was calculated at 15%. Due to  $TiO_2$ , about 17% spinel is present at 800 °C in addition to the bredigite, RO phase, and C2AF. This consists of SPINB#1 and SPINB#2, which differ in chemical composition. In SPINB#1, more  $Fe_2O_3$  is present, and the  $Al_2O_3$  content is only 2%, while in SPINB#2, the main phase is  $Al_2O_3$ . The Cr is mainly in the spinels dissolved, with a small amount in the RO phase. Figure 3a shows the slag with 15%  $Al_2O_3$ . Here, at 800 °C, the main phases are bredigite, C2AF, and RO. Only a low amount of spinel phase is present. Half of the Cr is distributed on the spinel, and the other half on the RO phase.

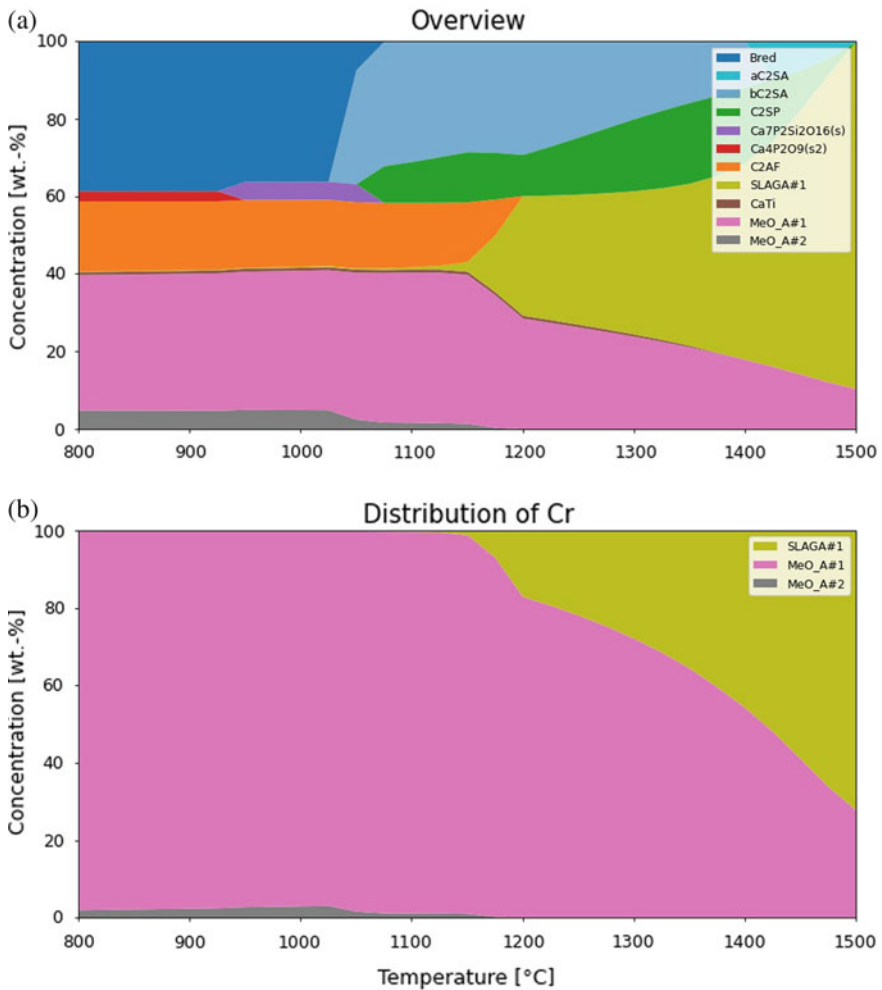


Fig. 1 a Stable phases of the original slag, b Cr-distribution

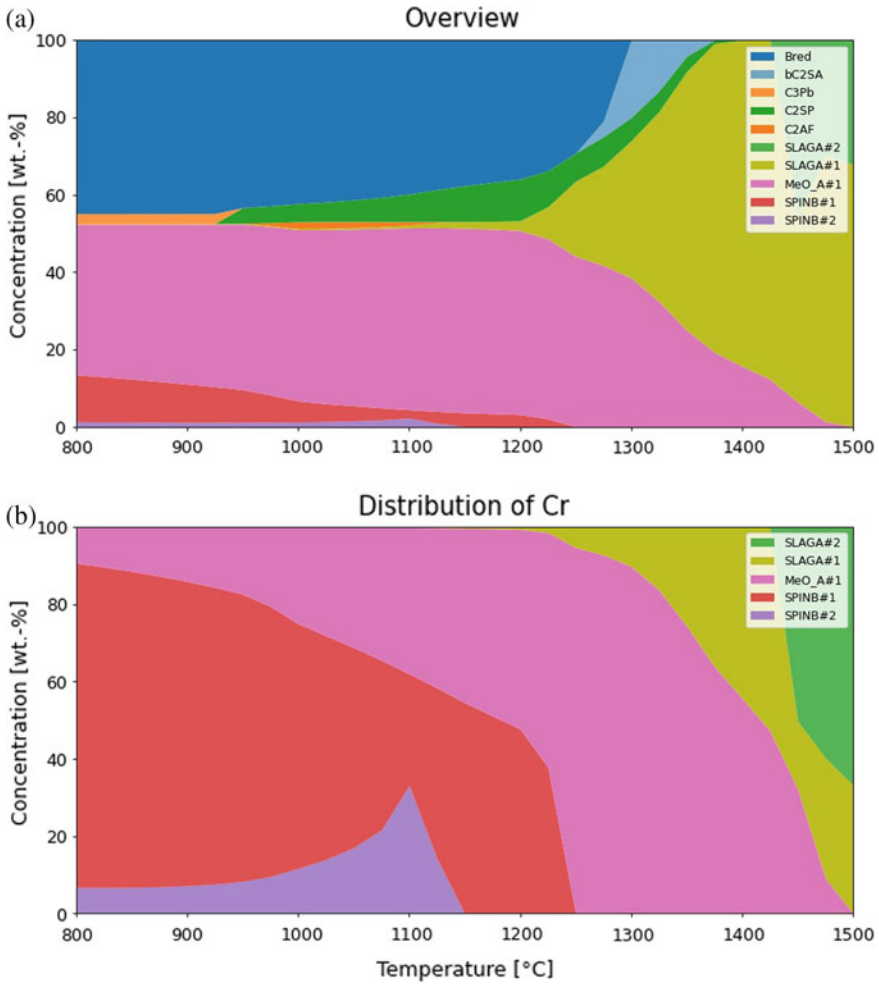
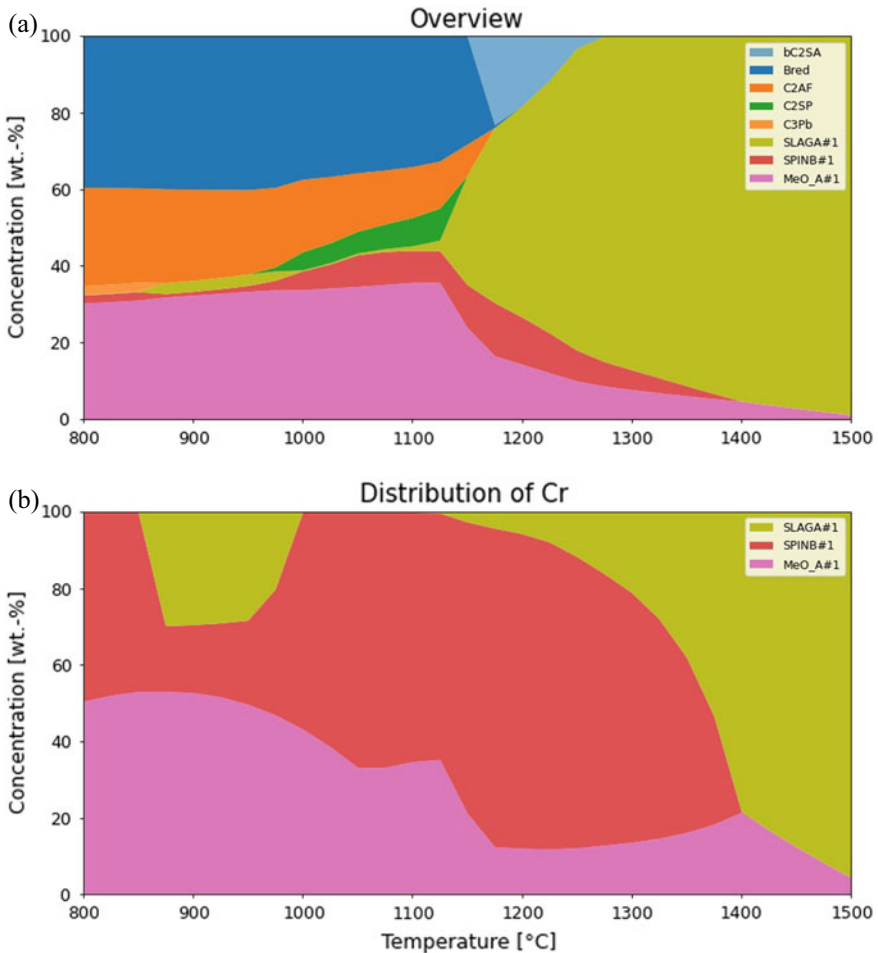


Fig. 2 a Stable phases of the slag with 15% TiO<sub>2</sub>, b Cr-distribution

## Results

For the characterization, a JEOL JSM IT-300 microscope was used. EDX was used to identify the element distribution of mineral phases. The magnification of the images is  $\times 1000$ . All elements are present in oxide form. Figure 4a shows a BSE image of the BOF slag with 15% TiO<sub>2</sub> together with EDX images of the chemical composition. There are three main phases:

- A spinel of the metal oxides of Fe, Al, Mn, and Mg
- A Ca, Si, Al matrix
- A Ca phase with Ti.



**Fig. 3** a Stable phases of the slag with 15% Al<sub>2</sub>O<sub>3</sub>, b Cr-distribution

Cr cannot be assigned to any phase. P is dissolved in the matrix but occurs in higher concentrations with Ca and Si without Al.

Figure 4b shows the BOF slag with 15% Al<sub>2</sub>O<sub>3</sub>. Here, four main phases are recognizable:

- A Fe, Mn, Mg, and Al spinel phase predominates in which Fe content is high?
- A small Fe-, Mn-, Mg-, Al-spinel phase, in which less Fe is present
- A Ca-poor, Al-rich matrix
- A Ca-rich, Al-poor matrix with Si.

Cr and Ti are in the Fe-rich phase, and P is again only present together with Ca.

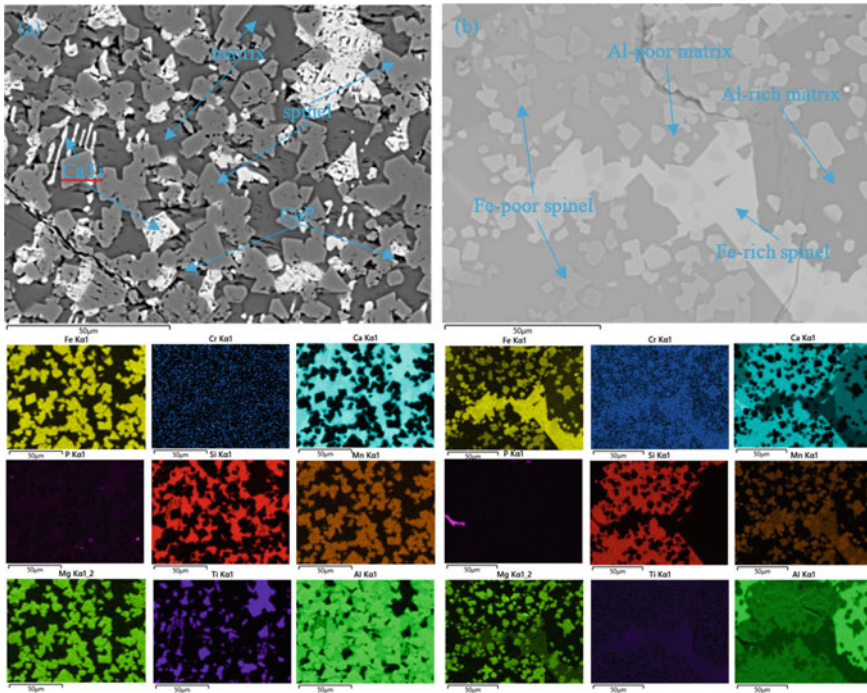


Fig. 4 a slag with 15% TiO<sub>2</sub>, b slag with 15% Al<sub>2</sub>O<sub>3</sub>

The spinel phases can be recognized in Fig. 4a, b due to their characteristic sharp-edged shape.

## Conclusion

The thermodynamic calculations showed that during the treatment of the BOF slag with the additives TiO<sub>2</sub> and Al<sub>2</sub>O<sub>3</sub>, spinels were formed to a certain extent. These spinels could be confirmed in both cases. In the case of TiO<sub>2</sub>, however, contrary to the calculations, only one spinel fraction was detected, whereas, in the case of Al<sub>2</sub>O<sub>3</sub>, a Fe-rich, as well as a Fe-poor spinel fraction, was detected. Cr could not be assigned to any phase in the experiments with TiO<sub>2</sub>. With Al<sub>2</sub>O<sub>3</sub> on the other hand, it is dissolved in the Fe-rich spinel fraction. Furthermore, the calculations showed enrichment of P in the C3P phase, both for TiO<sub>2</sub> and Al<sub>2</sub>O<sub>3</sub>. In both cases, the matrix was formed from the oxides of Ca, Si, and Al, whereby a second matrix without Si is present in the case of the Al<sub>2</sub>O<sub>3</sub> addition.



## References

1. Jiang Y, Ling T-C, Shi C, Pan S-Y (2018) Characteristics of steel slags and their use in cement and concrete—A review. *Resour Conserv Recycl* 136:187–197
2. Spooner S, Davis C, Li Z (2020) Modelling the cumulative effect of scrap usage within a circular UK steel industry—Residual element aggregation. *Ironmaking Steelmaking* 47:(10):1100–1113
3. Voraberger B, Wimmer G, Dieguez Salgado U, Wimmer E, Pastucha K, Fleischanderl A (2022) Green LD (BOF) steelmaking—Reduced CO<sub>2</sub> emissions via increased scrap rate. *Metals* 12(3):466
4. de Beer J, Worrell E, Blok K (1998) Future technologies for energy-efficient iron and steel making. *Annu Rev Energy Environ* 23:1:123–205
5. Brooks G, Madhavan N, Overbosch A, Rhamdhani M, Rout B (2022) Potential for increased scrap melting in a BOF. In: *AISTech 2022 proceedings of the iron and steel technology conference, AISTech 2022 proceedings of the iron and steel technology conference, 2022, AIST, 2022*, pp 441–449
6. Reddy AS, Pradhan RK, Chandra S (2006) Utilization of basic oxygen furnace (BOF) slag in the production of a hydraulic cement binder. *Int J Miner Process* 79(2):98–105
7. Snigdha G, Bharath BN, Viswanathan NN (2019) BOF process dynamics. *Miner Process Extr Metall* 128(1–2):17–33
8. Cavaliere P (2019) Basic oxygen furnace: most efficient technologies for greenhouse emissions abatement. In: Cavaliere P (ed) *Clean ironmaking and steelmaking processes*. Springer International Publishing, Cham, pp 275–301
9. Mahieux P-Y, Aubert J-E, Escadeillas G (2009) Utilization of weathered basic oxygen furnace slag in the production of hydraulic road binders. *Constr Build Mater* 23(2):742–747
10. World Steel Association (2020) *Steel Statistical Yearbook 2020 concise version*
11. Wang Q, Yan P: Hydration properties of basic oxygen furnace steel slag
12. Wang G, Wang Y, Gao Z (2010) Use of steel slag as a granular material: volume expansion prediction and usability criteria. *J Hazard Mater* 184(1–3):555–560
13. Das B, Prakash S, Reddy P, Misra VN (2007) An overview of utilization of slag and sludge from steel industries. *Resour, Conserv Recycl* 50(1):40–57
14. Reuter M, Xiao Y, Boin U (2004) Recycling and environmental issues of metallurgical slags and salt fluxes. In: *VII International conference on molten slags fluxes and salts (2004)*, pp 349–356
15. Lun Y, Zhou M, Cai X, Xu F (2008) Methods for improving volume stability of steel slag as fine aggregate. *J Wuhan Univ Technol-Mater Sci Ed* 23(5):737–742
16. Wang Z, Sohn I (2019) A review on reclamation and reutilization of ironmaking and steelmaking slags. *J Sustain Metall* 5(1):127–140
17. Shen H, Forsberg E (2003) An overview of recovery of metals from slags. *Waste Manag* 23(10):933–949
18. Miraoui M, Zentar R, Abriak N-E (2012) Road material basis in dredged sediment and basic oxygen furnace steel slag. *Constr Build Mater* 30:309–319
19. Yildirim IZ, Prezzi M: Chemical, mineralogical, and morphological properties of steel slag
20. Chen Z, Wu S, Xiao Y, Zhao M, Xie J (2016) Feasibility study of BOF slag containing honeycomb particles in asphalt mixture. *Constr Build Mater* 124:550–557
21. Kambole C, Paige-Green P, Kupolati WK, Ndambuki JM, Adeboje AO (2017) Basic oxygen furnace slag for road pavements: a review of material characteristics and performance for effective utilisation in southern Africa. *Constr Build Mater* 148:618–631
22. Poh HY, Ghataora GS, Ghazireh N (2006) Soil stabilization using basic oxygen steel slag fines. *J Mater Civ Eng* 18(2):229–240
23. Ko M-S, Chen Y-L, Jiang J-H (2015) Accelerated carbonation of basic oxygen furnace slag and the effects on its mechanical properties. *Constr Build Mater* 98:286–293
24. Alanyali H, Çöl M, Yılmaz M, Karagöz Ş (2009) Concrete produced by steel-making slag (basic oxygen furnace) addition in Portland Cement. *Int J Appl Ceram Technol* 6(6):736–748

25. Belhadj E, Diliberto C, Lecomte A (2012) Characterization and activation of basic oxygen furnace slag. *Cement Concr Compos* 34(1):34–40
26. Engström F, Adolfsson D, Yang Q, Samuelsson C, Björkman B (2010) Crystallization behaviour of some steelmaking slags. *Steel Res Int* 81(5):362–371
27. Björkman B, Eriksson J, Nedar L, Samuelsson C (1996) Waste reduction through process optimization and development. *JOM* 48(3):45–49
28. Wang Q, Yan P, Han S (2011) The influence of steel slag on the hydration of cement during the hydration process of complex binder. *Sci China Technol Sci* 54(2):388–394
29. Zhang T, Yu Q, Wei J, Li J, Zhang P (2011) Preparation of high performance blended cements and reclamation of iron concentrate from basic oxygen furnace steel slag. *Resour, Conserv Recycl* 56(1):48–55
30. Yildirim I, Prezzi M Use of steel slag in subgrade applications
31. Tossavainen M, Engstrom F, Yang Q, Menad N, Lidstrom Larsson M, Bjorkman B (2007) Characteristics of steel slag under different cooling conditions. *Waste Manag (New York, NY)* 27(10):1335–1344
32. Shi C, Qian J (2000) High performance cementing materials from industrial slags—A review. *Resour, Conserv Recycl* 29(3):195–207
33. Yi H, Xu G, Cheng H, Wang J, Wan Y, Chen H (2012) An overview of utilization of steel slag. *Procedia Environ Sci* 16:791–801
34. Jiang L, Bao Y, Chen Y, Liu G, Zhang X, Han F, Yang Q (2019) Structural characteristics and hydration kinetics of oxidized steel slag in a CaO-FeO-SiO<sub>2</sub>-MgO system. *High Temp Mater Process* 38(2019):290–300
35. Belhadj E, Diliberto C, Lecomte A (2014) Properties of hydraulic paste of basic oxygen furnace slag. *Cement Concr Compos* 45:15–21
36. Yan J, Wu S, Yang C, Zhao Z, Xie J (2022) Influencing mechanisms of RO phase on the cementitious properties of steel slag powder. *Constr Build Mater* 350:128926
37. Brand AS, Roesler JR (2015) Steel furnace slag aggregate expansion and hardened concrete properties. *Cement Concr Compos* 60:1–9
38. Erlin B, Jana D (2003) Forces of hydration that can cause havoc in concrete. *Concr Int* 51–57
39. Li J, Yu Q, Wei J, Zhang T (2011) Structural characteristics and hydration kinetics of modified steel slag. *Cement Concr Res* 41(3):324–329
40. Murphy JN, Meadowcroft TR, Barr PV (1997) Enhancement of the cementitious properties of steelmaking slag. *Can Metall Q* 36(5):315–331
41. Jiang L, Bao Y, Yang Q, Chen Y, Liu G, Han F, Wei J, Engström F, Deng J (2017) Formation of spinel phases in oxidized BOF slag under different cooling conditions. *Steel Res Int* 88(11):1700066
42. Zeng Q, Li J, Mou Q, Zhu H, Xue Z (2019) Effect of FeO on spinel crystallization and chromium stability in stainless steel-making slag. *JOM* 71(7):2331–2337
43. Zhao Q, Liu C, Cao L, Zheng X, Jiang M (2018) Stability of chromium in stainless steel slag during cooling. *Minerals* 8(10):445
44. Willard MA, Nakamura Y, Laughlin DE, McHenry ME (1999) Magnetic properties of ordered and disordered spinel-phase ferrimagnets. *J Am Ceram Soc* 82(12):3342–3346
45. Harrison RJ, Putnis A (1998) The magnetic properties and crystal chemistry of oxide spinel solid solutions. *Surv Geophys* 19(6):461–520
46. Wang D, Jiang M, Liu C, Min Y, Cui Y, Liu J, Zhang Y (2012) Enrichment of Fe-containing phases and recovery of iron and its oxides by magnetic separation from BOF slags. *Steel Res Int* 83(2):189–196
47. CRCT/GTT (2020) FactSage

# Author Index

## A

Abdallah, Mohamed, 179  
Abdulfattah, Furqan, 239  
Adams, Zachary Kenneth, 27  
Adeboye, Seyi E., 221  
Agava, Rasheed A., 221  
Akanji, Fausat T., 221  
Alabi, Abdul Ganiyu F., 221  
Alabi, Oladunni Oyelola, 239  
Alam, Shafiq, 179  
Allanore, Antoine, 27, 209  
Ambade, Balram, 83, 117  
Anawati, John, 3  
Ayinla, Kuranga I., 221  
Azimi, Gisele, 3

## B

Baba, Alafara A., 221  
Bai, Xianglin, 61  
Baltrusaitis, Jonas, 15  
Bawkar, Shilpa Kalamani, 185  
Bhatti, Ijaz Ahmad, 161  
Boury, Charles, 209  
Bwala, Markus Daniel, 239

## C

Chagnes, Alexandre, 131  
Cheema, Humma Akram, 161  
Cheng, Jie, 271  
Chen, Xin-Mian, 271  
Chileshe, Fredrick, 95  
Chinwego, Chinenye, 33  
Choubey, Pankaj K., 117, 185  
Choubey, Pankaj Kumar, 39, 83  
Cote, Gérard, 131

## D

Diao, Jiang, 271  
Ding, Lingyang, 3  
Dinkar, Om Shankar, 83, 117

## F

Forsberg, Kerstin, 73, 199

## G

Gardner, James, 73  
Green, Sierra R., 209  
Gupta, Akanksha, 247

## H

Hai, Dong, 271  
Hait, Jhumki, 185  
Halleux, Hubert, 131  
Han, Jibiao, 61  
Hara, Yotamu Rainford Stephen, 95  
Haruna, Mohammed S., 221  
Haslinger, G., 287  
Hassan, Suleiman Bolaji, 239  
Hoogendoorn, Billy W., 199  
Huang, Qingyun, 279

## I

Ibrahim, Abdullah S., 221  
Ilyas, Sadia, 161

## J

Jeon, Jong Hyuk, 171  
Jeoung, Hyeong-Jun, 105  
Jha, Manis K., 185

Jha, Manis Kumar, 39, 83, 117  
 Jyothi, Rajesh Kumar, 39, 171

**K**

Kaker, Vasu, 27  
 Kang, Jungshin, 105  
 Karamalidis, Athanasios K., 141  
 Kim, Hyunjung, 161  
 Kim, Sookyung, 227  
 Kim, Youngjae, 105  
 Kim, Young Min, 105  
 Kurniawan, Kurniawan, 227

**L**

Lee, Jae-chun, 227  
 Lee, Jin-Young, 105, 171  
 Lee, Tae-Hyuk, 105  
 Lei, Bin, 259  
 Leuchtenmüller, M., 287  
 Li, Hong-Yi, 271  
 Liu, Zenghao, 279  
 Li, Yong, 61  
 Luo, Mingshuai, 279

**M**

Mangold, Lucas, 131  
 Ma, Wangrui, 61  
 Ma, Yiqian, 73  
 Mishra, Brajendra, 247  
 Mundundu, Janet, 95  
 Musowoya, Mazwi Douglas, 95

**N**

Nilsson, Fritjof, 199

**O**

Okabe, Toru H., 105  
 Olsson, Richard T., 73, 199

**P**

Panda, Rekha, 39, 83, 117, 185  
 Parirenyatwa, Stephen, 95  
 Parween, Rukshana, 117  
 Patel, Madhav, 141  
 Poliseti, Veerababu, 199  
 Powell, Adam, 33

**R**

Raji, Mustapha A., 221  
 Rao, Mudila Dhanunjaya, 153  
 Rokkam, Srujan, 15

**S**

Sayyadi, Musa Gafai, 239  
 Silva, Manoj, 15  
 Singh, Kamalesh Kumar, 153  
 Singh, Nityanand, 39  
 Singh, Pramod K., 185  
 Sjögren, Amanda, 73  
 Sola, Ana Belen Cueva, 171  
 Srivastava, Rajiv Ranjan, 161  
 Steinlechner, S., 287  
 Stinn, Caspar, 27  
 Su, Zijian, 259  
 Svärd, Michael, 73

**T**

Tjus, Kåre, 199  
 Truong, Quang, 15

**W**

Wang, Biao, 61  
 Wang, Shijie, 53  
 Wang, Yan, 259  
 Wu, Xilong, 61

**X**

Xiang, Junyi, 279  
 Xiao, Xiong, 73, 199  
 Xie, Bing, 271

**Y**

Yang, Bin, 61  
 Yang, Quan, 61  
 Yi, Kyung-Woo, 105

**Z**

Zhang, Shengquin, 279  
 Zhang, Yuanbo, 259  
 Zhao, Yu, 61

# Subject Index

## A

Acid leaching, 16, 20, 22, 23, 40, 154, 248, 252, 279, 280  
Ammonium sulfate, 3, 5, 7, 10–12  
Anode slimes, 53, 54, 58  
Artificial minerals, 287

## B

Barite ore, 222–225  
Battery recycling, 199  
Beneficiation, 27, 28, 132, 209, 222, 239–243, 245, 287  
Bimetallic composite, 247  
Bioadsorbent, 185–188, 191–195  
Biomass, 181, 184  
Biosorption, 181, 183  
Bismuth, 53, 54, 56–59  
BOF slag, 287–290, 293, 294

## C

Calcium-magnesium composite roasting, 279, 281, 282, 284, 285  
Capacitor recovery, 247  
Catechol, 141–145, 147–149  
Cellulose, 194, 199, 201, 206, 207  
Characterization, 41, 84, 143, 202, 228, 229, 234, 239–243, 245, 272  
Chitosan, 141–145, 149, 187, 189  
Chloride, 179, 181, 182, 184  
Copper, 53, 54, 57, 58, 61, 67, 68, 84–87, 89, 91–93, 106, 117–119, 121–126, 153–157, 159, 188–190, 193, 195, 210, 249  
Copper cathode, 105–107, 111, 114  
CoSO<sub>4</sub>, 73–80

Critical element, 20, 141, 142  
Crowding, 171–173, 175–177

## D

Desorption, 3–7, 9–12  
Drilling mud, 221, 222, 225

## E

Effluent treatment, 126, 185, 186  
Energy storage, 200, 241  
Enrichment, 28, 61, 63, 65–68, 171–175, 177, 222, 287, 289, 294  
Eutectic freeze crystallization, 73–76  
Evolution mechanism, 271, 272, 274, 275  
Extraction, 15–17, 19–23, 27–29, 31, 40, 54, 73, 74, 118, 124, 126, 131–133, 135, 141, 142, 154, 156–159, 171–175, 177, 203, 243, 245, 248, 252, 254–256, 259, 260, 271, 272, 279, 280, 284

## F

Flotation, 31, 126, 132, 210, 221–223, 225, 242, 243  
Froth flotation, 84, 223, 244

## G

Germanium, 141, 142, 146, 149  
Gold, 53–56, 58, 69, 84, 117, 153–159

## H

Heavy metals, 132, 186–188, 228

Hydrometallurgy, 74, 132, 209, 248, 252, 257, 260  
 Hydrometallurgy processes, 117

**I**

Industrial effluents, 179  
 Industrial electronic waste, 15  
 Ionic clay, 3–5, 7–9, 11, 12  
 ITO wastes, 259, 260, 265

**L**

Lapidolite, 241  
 Leaching, 15–17, 20–23, 28, 39–42, 45–48, 54, 74, 85, 86, 89, 92, 117–119, 121–124, 126, 131, 153–156, 159, 172, 210, 221, 223–225, 228, 237, 242, 252, 253, 255, 271, 272, 279–281, 284  
 Leaching efficiency, 15, 20, 21, 23, 45, 46, 74, 121, 221, 279, 280, 282  
 Lead, 20, 61, 68, 69, 84–87, 89, 91–93, 107, 118, 119, 154, 172, 191–193, 195, 210, 264, 288  
 Lignin, 179, 181–183  
 Li-ion batteries, 73, 74  
 Linear free-energy relationship, 147  
 Lithium, 106, 113, 239–245

**M**

Magnesium metal, 105–108, 113, 114  
 Magnesium oxide resources, 107, 109, 110, 113, 114  
 Metal, 16, 19, 21, 27, 31, 40–45, 53, 54, 56–58, 61–63, 65–70, 74, 75, 79, 83–87, 105–108, 112–114, 117–121, 124, 126, 132–134, 141–143, 147, 148, 154–156, 158, 159, 172–175, 177, 185–195, 200, 208–210, 212, 215, 227–229, 234–237, 239–241, 247–250, 252, 254, 259, 260, 262, 264, 271, 273, 274, 287  
 Metal capture method, 61, 65  
 Mineral processing, 179  
 Mining, 179, 180  
 Modeling, 181  
 Molten salt electrolysis, 106–109  
 Molybdenites flue dust, 161, 162, 166, 168  
 Monazite, 27, 29–31

**N**

NdFeB, 15–17, 19–23

Neodymium, 15, 16, 20, 23, 28, 30, 40, 62  
 Nigeria, 221–223, 225, 239, 240, 243, 245  
 Non-complexing media, 131

**O**

Oil and gas industries, 221, 222, 225

**P**

Palladium, 53–56, 58, 61, 63, 64, 84, 154, 155  
 PCBs, 43, 83–86, 89, 91, 93, 117–124, 126, 153, 154, 156, 158  
 Pegmatite, 240–243, 245  
 Permanent magnet, 16, 39, 40, 43, 44  
 Phase transformation, 253, 259, 260  
 Phosphoric acid, 131–133, 137, 192  
 Platinum, 53, 55, 56, 58, 61–65, 67, 68, 84, 117, 154  
 Platinum group metals (PGMs), 53, 54, 61–70  
 Precipitation, 40, 74, 132, 147–149, 199, 200, 204–207, 254, 255, 260, 285  
 Pre-treatment, 41, 42, 44, 83–85, 117–119, 132, 255  
 Purification, 54, 68, 74, 132, 133, 156, 195, 205, 222, 225, 247–249, 260  
 Pyrolysis, 210, 227–229, 231–237, 248, 251, 252, 255  
 Pyrometallurgy, 65, 132, 248, 252, 257, 260  
 Pyrometallurgy recovery, 70

**R**

Rare earth, 15, 17, 27–31, 39–42, 44, 62, 84, 132, 210  
 Rare earth elements (REEs), 3–12, 15–17, 20, 23, 27–31, 39–41, 43, 45–48, 62  
 Rare earth metals, 33, 34, 36  
 Recover REEs, 39, 40  
 Recovery, 16, 17, 21, 31, 40, 41, 43–46, 48, 53–59, 61–70, 74, 83–85, 91, 93, 117–119, 124, 126, 153, 154, 156–159, 172, 185, 186, 191–193, 195, 218, 227, 228, 237, 240, 242, 247–256, 259, 260, 267, 271, 272, 277, 279, 280, 287  
 Recycling, 15, 16, 28, 33, 39, 61, 62, 64, 65, 68, 73, 74, 84, 117, 118, 153, 171, 185, 199, 200, 208, 210, 228, 236, 247, 248, 260  
 Reduction volatilization, 263  
 Refractory metals, 161, 162

Response surface methodology, 227–229, 237  
Roasting, 28, 39–41, 44–46, 245, 259–267, 271, 272, 274–277, 279–284

## S

Scrap Nd-Fe-B magnets, 39, 40  
SCR catalyst, 171–174, 177  
Secondary recovery, 247  
Selenium, 53, 54, 56–58, 179–184  
Separation, 23, 27, 28, 54, 66–68, 74, 83–86, 91, 93, 119, 126, 132, 142, 149, 153, 172, 173, 175, 177, 186, 195, 209, 210, 218, 222, 227, 228, 236, 237, 242, 247–249, 254, 255, 259, 260, 262, 263, 265, 267  
Slag modification, 287  
Sodium roasting, 271, 272, 274–277, 279, 280  
Solid-phase extraction, 141, 142  
Speciation, 131, 133–137, 172, 174, 175, 177  
Spent automobile catalyst, 62, 65–70  
Spodumene, 240–243, 245  
Sulfidation, 27–31, 209, 210, 212, 215, 218  
Sulfides chemistry, 31, 209, 210

## T

Tantalum, 240, 241, 247–257  
Tantalum recovery, 248, 249, 251, 252, 257  
Thermodynamic calculations, 265, 287, 289, 290, 294  
Tin, 84–87, 91–93, 106, 119, 154, 156–159, 200, 215, 241, 248, 260–263, 265–267

Titanium(IV), 18, 131–139, 142, 172, 200, 274, 290  
Tungsten, 17–19, 95–99, 101, 102, 171–177, 209, 210, 212, 214–218, 247

## U

Uranium, 95–99, 101, 102

## V

Vacuum distillation, 105, 106, 108, 113, 114  
Vanadium, 171–177, 271, 272, 274, 275, 277, 279–282, 284, 285  
Vanadium extraction tailings, 279, 282, 284, 285  
Vanadium slag, 271, 272, 277, 279–282, 284  
Vanadium slag with high chromium content, 271–277

## W

Waste printed circuit boards (WPCBs), 69, 84, 117, 126, 154–156, 159, 227–229, 231–237

## Y

Yttrium, 95–99, 101, 102

## Z

Zambia, 95, 101  
ZnO particle synthesis, 201, 202